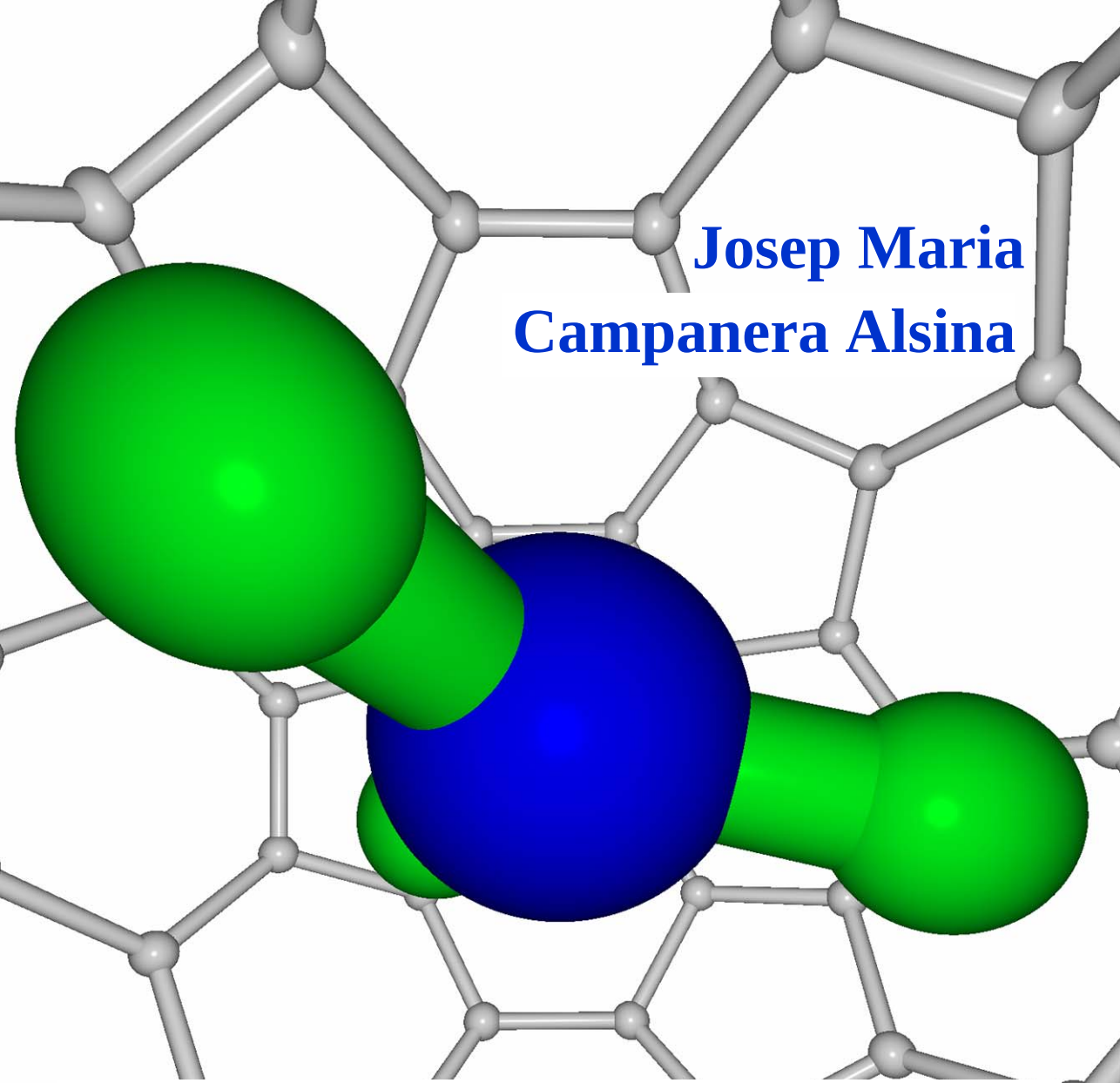

Josep Maria
Campanera Alsina

Theoretical Characterisation of Metallofullerenes

Theoretical Characterisation of Metallofullerenes

Departament de Química Física i Inorgànica
Facultat de Química
Universitat Rovira i Virgili

Theoretical Characterisation of Metallofullerenes

Josep Maria Campanera Alsina

Tarragona, novembre de 2004

Director de la tesi: Josep Maria Poblet Rius
Catedràtic de Química Física
Universitat Rovira i Virgili

Memòria presentada per optar
al títol de Doctor en Química

UNIVERSITAT ROVIRA I VIRGILI

Josep Maria Poblet Rius, catedràtic de Química Física del Departament de Química Física i Inorgànica de la Universitat Rovira i Virgili

Faig constar que la present memòria, que porta per títol:

"**Theoretical Characterisation of Metallofullerenes**"

ha estat realitzada sota la meva direcció al Departament de Química Física i Inorgànica de la Universitat Rovira i Virgili pel llicenciat en Química Josep Maria Campanera Alsina per obtenir el grau de Doctor en Química.

Tarragona, 8 de novembre de 2004.

Dr. Josep Maria Poblet Rius

prefaci

Alguns descobriments importants de la ciència són accidentals. Això fou, certament, el cas del ful·lerè $C_{60.}$ Quan ara fa quatre anys, l'any 2000, vaig iniciar el treball d'investigació sobre els *metal·loful·lerens* m'havien arribat veus de la importància mediàtica d'aquestes noves estructures però no de la intensa història del seu descobriment. Aquesta m'ha fascinat!. Sobretot quan l'any 2003 vaig tenir la possibilitat de fer una estada al grup dels professors Kroto i Taylor de la Universitat de Sussex (Gran Bretanya). Llavors, els textos, sorprenents però inerts, que havia llegit sobre la història del descobriment dels ful·lerens prenien forma en espais coneguts i personatges propers. El 1985, Smalley i Kroto estaven interessats en la composició química de les estrelles gegants vermelles riques en carboni de l'espai exterior. En un dels seus experiments, reproduint aquelles condicions, no van ignorar, però, els grans pics a 720 i 840 *m/e* que havien aparegut en un espectre de masses. Smalley i Kroto tingueren la perspicàcia de reconèixer la gran importància d'aquells pics. Aquell descobriment serendípic, sens dubte, va obrir un nou camp: la ciència dels ful·lerens. La serendipitat en els ful·lerens no havia acabat aquí. Krätschmer i Huffman el 1990, interessants en la producció de grafit, descobreixen un mètode per la producció de grans quantitats de C_{60}. Ja teníem tots els ingredients per triomfar. L'any 1991 la prestigiosa revista *Science* nomenà el ful·lerè C_{60}, *Molècula de l'any* i ja el 1996, Kroto, Smalley i Curl es fan mereixedors del premi Nobel de Química. Avui dia, cada vegada més però, els científics són empesos a focalitzar els seus esforços en la recerca que tindrà ràpids i directes beneficis econòmics. Així sovint els científics perden l'habilitat de perseguir resultats inesperats/casuals que poden dirigir a direccions totalment noves o fins i tot més emocionants. És important, doncs, donar suport i encoratjar a la recerca bàsica sovint conduïda només per la curiositat. Prenguem exemple de la història del descobriment dels ful·lerens.

Tot i que la investigació a l'entorn dels ful·lerens s'ha anat desinflant els últims anys, després d'un començament més que espectacular, el nombre d'aplicacions potencials d'aquestes noves estructures es manté encara ara intacte. Es preveuen aplicacions industrials com a catalitzadors, lubricants, fibres d'alta resistència, interruptors òptics i superconductors. Com a especial utilitat s'ha provat que el C_{60} i els seus derivats (a causa de

la seva gran mida, l'estabilitat i el caràcter hidrofòbic) podrien tenir gran vàlua com a agents terapèutics o de diagnosi en medicina. També s'està estudiants el paper com a repartidors dels principis actius d'un fàrmac pel nostre cos. Una altre aplicació potencial per aquestes estructures és en l'àrea de la ciència dels materials: nanotubs, fibres de carboni, etc. Sens dubte, però fins ara, la gran aportació dels ful·lerens ha estat la possibilitat dels treballs multidisciplinars: químics, físics, matemàtics i biòlegs han hagut de treballar coordinats per tal d'estudiar aquestes noves molècules.

El present treball d'investigació titulat "*Theoretical characterisation of metallofullerenes*" arrenca del treball de l'alumne de doctorat predecessor del grup de Química Quàntica del Departament de Química Física i Inorgànica de la URV, en Jordi Muñoz. Els *metal·loful·lerens* es poden classificar estructuralment de forma molt senzilla segons on el metall es situï respecte la caixa ful·lerènica. Així tenim els *metal·loful·lerens endoèdrics* (a l'interior de la caixa), *heteroèdrics* (a l'estructura carbonada) i *exoèdrics* (a l'exterior). Mitjançant la teoria del funcional de la densitat (DFT) s'han caracteritzat teòricament els compostos més novells i novedosos per cadascuna de les famílies. Hem descrit l'enllaç, l'isomerisme i la reactivitat. La tesi s'estructura en dues grans parts. La primera part (Introducció) conté tres capítols: química de ful·lerens (cap. 1), química computacional per ful·lerens (cap. 2) i abast i objectius de la tesi (cap. 3). Així en aquesta primera part assentem les bases químiques i metodològiques per tal d'entendre els resultats presentats en la segona part. La segona part (resultats) conté els tres capítols fonamentals d'aquesta tesi (cap. 4, 5 i 6), a més d'un altre de conclusions i perspectives (cap. 7). Els tres capítols centrals fan referència a cadascuna de les famílies de metal·loful·lerens: *Trimetallic nitride template (TNT) endohedral metallofullerenes* (chap. 4), *heterohedral metallofullerenes* (chap. 5) *i* $M(PH_3)_2$ *exohedral metallofullerenes* (chap. 6). Aquest treball se sustenta en cinc articles publicats o recentment acceptats en revistes científiques internacionals.

Tot i que majoritàriament el present treball està redactat en anglès no per això he oblidat la meva llengua. Així m'he esforçat al màxim per incloure una introducció al màxim nivell de rigurositat científica en català sobre la química de ful·lerens i la metodologia emprada en la tesi. Aquest atreviment ha necessitat de l'adaptació de noves paraules a la meva llengua provinents de l'anglès: *endoèdric (endohedral), exoèdric (exohedral),*

heteroèdric (heterohedral), piracil·lè (pyracylene), corannul·lè (corannulene) i *pirè (pyrene),* així com, alguns dels seus derivats. Esperem que la meva intuïció hagi funcionat. El meu granet, doncs, al món científic en català. No obstant espero que això no sigui cap impediment per a la comprensió global del treball per part dels lectors i dels membres del tribunal. Si la introducció és en català l'apartat de resultats és íntegrament en anglès. Aquest m'ha permès barallar-me amb una altre llengua que ara conec un pèl més. Un gran repte, sens dubte!

Josep M. Campanera
Tarragona, novembre de 2004

A la meva família,
mare, pare i germà, una abraçada!

[Heu de viure la tesi com un desafiament]
Umberto Eco

[Aquí el meu]
Josep M. Campanera

contents

list of publications

"Bonding within the Endohedral Fullerenes $Sc_3N@C_{78}$ and $Sc_3N@C_{80}$ as Determined by Density Functional Calculations and Reexamination of the Crystal Structure of $\{Sc_3N@C_{78}\}\cdot Co(OEP)\}\cdot 1.5(C_6H_6)\cdot 0.3(CHCl_3)$".
Josep M. Campanera, Carles Bo, Marilyn M. Olmstead, Alan L. Balch and Josep M. Poblet *J. Phys. Chem. A* **2002**, *106*, 12356-12364.

"Open-Cage Fullerene Derivatives with 15-Membered-Ring Orifices".
Georgios C. Vougioukalakis, Kosmas Prassides, Josep M. Campanera, Malcolm I. Heggie and Michael Orfanopoulos *J. Org. Chem.* **2004**, *69*, 4524-4526.

"Mass Spectrometric and Computational Studies of Heterofullerenes ($[C_{58}Pt]^-$, $[C_{59}Pt]^+$) Obtained by Laser Ablation of Electrochemically Deposited Films".
Akari Hayashi, Yongming Xie, Josep M. Poblet, Josep M. Campanera, Carlito B. Lebrilla and Alan L. Balch *J. Phys. Chem. A* **2004**, *108*, 2192-2198.

"Organometallic Derivatives of Fullerenes: A DFT Study of (η^2-C_x){Pt(PH3)2}n (x = 60, 70, 84; n = 1-6)".
Josep M. Campanera, Jordi Muñoz, Jordi Vázquez, Carles Bo and Josep M. Poblet *Inorg. Chem.* **2004**, *43*, 6815-6821.

"Prediction of Heterofullerene Stabilities: a Combined DFT and Chemometric Study of $C_{56}Pt_2$, $C_{57}Pt_2$ and $C_{81}Pt_2$".
Josep M. Campanera, Carles Bo, Alan L. Balch, Joan Ferré and Josep M. Poblet *Chem. Eur. J.* **2004**, in press.

"Analysis of polyaddition levels in *i*-Sc_3NC_{80}".
Josep M. Campanera, Malcolm I. Heggie and Roger Taylor *J. Phys. Chem. A* **2004**, in press.

list of abbreviations and symbols

BE	Binding energy/energia d'enllaç
BSSE	Basis set superposition error
DE	Dissociation energy
DZP	Double-ζ + polarization
EA	Electron affinity/afinitat electrònica
EBE	Encapsulation binding energy
EDDM	Electron density deformation map
EPA	Energy per atom/energia per àtom
HBE	Hydrogenation binding energy
HMO	Hückel molecular orbital
HOMA	Harmonic oscillator model of aromaticity
IBE	Insertion binding energy
IP	Ionization potential/potencial d'ionització
IPR	Isolated pentagon rule
MBO	Mayer bond order
MO	Molecular orbital
PLS	Partial least squares
RE	Relative energy
SE	Substitution energy
TCNE	Tetracyanoethylene
TNT	Trimetallic nitride template
TZP	Triple-ζ + polarization
θ_p	Pyramidalization angle
ΔE_{HOLE}	Hole energy, SE = ΔE_{HOLE} + IBE
ΔE_{DE}	Deformation energy term, BE = $\Delta E_{ST} + \Delta E_{ORB} + \Delta E_{DE}$
ΔE_{ST}	Steric repulsion term, BE = $\Delta E_{ST} + \Delta E_{ORB} + \Delta E_{DE}$
ΔE_{ORB}	Orbital interaction term, BE = $\Delta E_{ST} + \Delta E_{ORB} + \Delta E_{DE}$
ΔE_{INT}	Interaction energy term, $\Delta E_{INT} = \Delta E_{ST} + \Delta E_{ORB}$
ΔE_{Pauli}	Pauli repulsion, $\Delta E_{ST} = \Delta E_{Pauli} + \Delta E_{elstat}$
ΔE_{elstat}	Electrostatic interaction, $\Delta E_{ST} = \Delta E_{Pauli} + \Delta E_{elstat}$

PART I. INTRODUCCIÓ

CAPÍTOL 1

QUÍMICA DE FUL·LERENS

En aquest primer capítol presentem la història de com a partir d'un pic de massa igual a la de 60 carbonis la comunitat científica descobrí unes noves estructures químiques amb propietats i reactivitat desconegudes: els ful·lerens. Aquest pic fou enregistrat en un espectre de masses fortuït l'any 1985 intentant explicar la composició química de l'espai. El nom de ful·lerens els hi ve en honor a l'arquitecte Richard Buckminster Fuller. En Richard dissenyà la famosa cúpula geodèsica de l'exposició universal de Montreal de 1967 que havia permès dilucidar l'estructura del primer i més famós dels ful·lerens, el C_{60} (apartat 1.1). Les estructures que hi havia darrera dels pics de nombre parell de carbonis foren determinades a partir de dues hipòtesis d'estabilitat (apartat 1.2). Primer, corresponien a políedres d'àtoms de carbonis tricoordinats formant caixes closes amb hexàgons i pentàgons (secció 1.2.1), i segon, les estructures no havien de tenir cap parella de pentàgons de carbonis adjacents (regla IPR) (secció 1.2.3). Les dues hipòtesis permeteren plantejar de forma teòrica tots els isòmers possibles que hi havia darrera d'aquells pics de nombre parell de carbonis. Finalment gràcies a l'espectroscòpia de ressonància magnètica nuclear (RMN) de ^{13}C moltes d'aquestes estructures teòriques han estat confirmades experimentalment. En un tercer apartat aglutinem les propietats electròniques i geomètriques que determinen la reactivitat dels ful·lerens (apartat 1.3). Partim de la idea que els ful·lerens presenten una menor estabilitat termodinàmica que les altres dues formes al·lotròpiques de carboni, degut principalment a les conseqüències de la corbatura de la superfície carbonada. Ja en l'últim apartat (1.4) focalitzem el text en els

compostos d'interès pel treball presentat aquí: els metal·loful·lerens, derivats metàl·lics de ful·lerens. Degut a la varietat de propietats i la seva forma, els ful·lerens presenten un grapat de possibilitats de derivatització metàl·lica. Seguint el que serà la columna vertebral d'aquest treball, els dividim estructuralment en: endoèdrics, encapsulament d'unitats metàl·liques a l'interior (1.4.1); heteroèdrics, substitució metàl·lica a la mateixa superfície carbonada (1.4.2); i exoèdrics, derivatització a l'exterior (1.4.3). Creiem que la divisió és força encertada tenint en compte que el tipus d'enllaç organometàl·lic que es dóna en cadascuna de les tres famílies de metal·loful·lerens és força diferent. Així en aquest apartat destaquem els compostos més importants i exemplificadors de cadascuna de les tres famílies que són predecessors als compostos estudiats en aquest treball d'investigació. També en descrivim somerament la geometria i l'enllaç.

1.1 INTRODUCCIÓ

Els ful·lerens són caixes closes de carbonis que contenen només anells pentagonals i hexagonals. El C_{60} icosaèdric és el més conegut i estudiat que a la vegada ens serveix d'arquetipus. La primera aparició de l'estructura del C_{60} en connexió amb un experiment fou proposada per Kroto, Heath, O'Brien, Curl i Smalley el 1985.[1] Aquesta primera aparició de l'estructura del C_{60} era en un intent per explicar l'abundància pronunciada del *clúster* de 60 carbonis aconseguit en experiments de vaporització de grafit mitjançant làser. No obstant, un any abans s'havia començat ja la carrera cap al descobriment d'aquesta nova molècula. En Rohlfing et al. havien obtingut un espectre de masses on el pic de 60 àtoms de carboni era el prominent,[2] també aquell 1984, l'estructura de pilota de carbonis havia estat ja apuntada per Stankevich et al. com una estructura hipotètica d'altres formes al·lotròpiques de carboni.[3] Fins i tot articles molt anteriors d'en Tisza,[4] Jones[5] i Osawa[6] del 1933, 1966 i 1970, respectivament, ja preveien l'estructura de 60 carbonis. Cap dels articles, però, relacionava l'estructura amb l'experimentació tal i com feren en Kroto et al. Posteriorment, la proposta d'en Kroto fou confirmada el 1990 quan en Krätschmer, Lamb, Fostiropoulos i Huffman informaren sobre un mètode per la generació de grans quantitats de C_{60} juntament amb l'evidència espectroscòpica de la seva estructura.[7] Així l'aparició dels articles d'en Kroto i d'en Krätschmer inicià una nova era en la química del carboni la qual ha involucrat químics, físics, matemàtics i científics de gairebé totes les especialitats.[8] Els ful·lerens representen la tercera forma al·lotròpica del carboni, a més a més de les ja conegudes: el diamant i el grafit. El sutge avui produït per la tècnica d'en Krätschmer i Huffman no només produeix C_{60} sinó una gran varietat de caixes de carbonis (C_{36}-C_{96}),[9] nanotubs i moltes altres formes polimèriques de carbonis.[10] El C_{60} fou nomenada "Molècula de l'any" per la revista *Science* el 1991, i el 1996 el Premi Nobel de química recaigué en el seus descobridors: Robert Curl (EUA), Richard Smalley (EUA) and Harold Kroto (GB).

El ful·lerè C_{60}, també conegut com futbolà, *buckminsterfullerene* o [60]-ful·lerè és el constituent més prominent extret d'aquest sutge.[7] El C_{70} és el segon ful·lerè més abundant. Així no és estrany que la majoria de reaccions químiques hagin estat desenvolupades al voltant d'aquestes dues

estructures.[11] Els ful·lerens són actualment versàtils blocs de construcció en química orgànica introduint noves propietats químiques, electròniques i fotofísiques. L'interès en aquestes molècules pot ser copsat en el gran nombre d'articles ja apareguts en la literatura científica. Les caixes ful·lerèniques consisteixen enterament de carbonis sp^2 amb un fort caràcter electroatraient.[12] Això afecta el seu comportament químic, per exemple, reaccionant fàcilment amb nucleòfils. Cal esperar, doncs, que aquestes noves molècules presentin una reactivitat molt semblant a la d'estructures deficients en electrons.

Tenim disponibles a la bibliografia científica textos sobre l'extensa química dels ful·lerens des dels seus inicis fins a l'actualitat. En cito a tall d'exemple els de més vocació generalista on es tracten aspectes tant de reactivitat com d'estructura geomètrica i electrònica: el d'en Cioslowski (*Electronic Strucutre Calculations on Fullerenes and Their Derivatives*),[13] el d'en Taylor (*Lecture Notes on Fullerene Chemistry, a handbook for chemists*)[14], el d'en Hirsch (*The Chemistry of the fullerenes*)[15] i finalment el d'en Kadish i Ruoff (*Fullerenes: chemistry, physics and technology*).[16] Sense oblidar el primer compendi teòric de totes les estructures ful·lerèniques d'en Fowler i en Manolopoulos (*An Atlas of Fullerenes*).[17] El present text ha estat basat en aquests llibres.

1.2 FUL·LERENS LLIURES

1.2.1 Ful·lerens com a poliedres

Els ful·lerens són *clústers* formats d'un nombre parell d'àtoms de carboni. Cada carboni es troba unit a altres tres per formar una caixa closa de només anells pentagonals i hexagonals.[18,19] Aquesta estructura d'enllaç correspon a un políedre: un àtom a cada vèrtex, un enllaç a cada aresta i un anell a cada cara. Una de les millors propietats dels poliedres és el *Teorema d'Euler*,[20] formulat dos-cents anys abans del descobriment dels ful·lerens. El matemàtic suís afirmà que la relació entre els vèrtexs (v), arestes (a) i cares (c) d'un políedre esfèric era: $v + c = a + 2$. Per un políedre corresponent a un ful·lerè C_k, el nombre de vèrtexs és $v = k$ i el nombre d'arestes $a = 3k/2$. El nombre de cares, aïllant en l'anterior fórmula, és per tant $c = k/2+2$. Aquestes afirmacions són vàlides per qualsevol políedre esfèric amb vèrtexs

trivalents. Altres conclusions que es desprenen del teorema són que tots els ful·lerens C_k han de contenir 12 anells pentagonals i (k/2)-10 anells hexagonals. Així, variant el nombre d'anells hexagonals i la distribució dels 12 anells pentagonals podem aconseguir ful·lerens de diferents mides i diferents isòmers del mateix nombre de carbonis. Segons aquesta definició el ful·lerè més petit possible té només 20 carbonis sense cap hexàgon i amb un únic isòmer possible. També s'arriba a la conclusió que pels ful·lerens C_k on k parell i $k > 24$ almenys un isòmer és possible.[21] No només això, a mesura que el nombre de carbonis augmenta el nombre d'isòmers per cada estequiometria també augmenta exponencialment. A tall d'exemple per k = 28, 3; per k = 60, 1812; k = 68, 6332; k = 70, 8149; k = 78, 24109; k = 80, 31924; k = 84, 51592 i k = 100, 285913 isòmers.[17] I això sense tenir en compte els enantiòmers. Tota aquesta variabilitat feu que es busquessin noves regles per acotar el nombre d'isòmers a ser estudiats.

1.2.2 Compromís entre la corbatura i l'estructura electrònica

La primera hipòtesi sobre els pics de nombre parell de carbonis, definint-los com a poliedres, ja limita moltíssim les possibilitats d'aquests nous *clústers* (secció anterior). Aquesta primera hipòtesi és especialment atractiva ja que les caixes closes eviten enllaços penjats que desestabilitzen si les comparem amb fragments de la mateixa mida de xarxes infinites de diamant o grafit. I també, perquè els àtoms tricoordinats satisfan els requeriments de valència millor que no pas les cadenes lineals o els anells monocíclics.[1] El grafit infinit amb carbonis trivalents sense enllaços penjats és termodinàmicament la forma més estable del carboni elemental. De fet, la formació de caixes closes de carbonis porta associada una energia de tensió estèrica deguda a la corbatura de la superfície de carbonis. En algun cas aquesta energia estèrica podria arribar a superar l'energia relacionada amb el tancament de la caixa. Per això, aviat s'entengué la necessitat de trobar regles per la minimització d'aquesta energia de tensió estèrica com a nova hipòtesi per tal de limitar el nombre d'estructures a estudiar.

Tanmateix l'energia desfavorable associada a la corbatura no és l'únic factor important en l'estabilitat de ful·lerens. L'estructura electrònica també té molt a dir en aquesta estabilitat. El model més simple, i a la vegada el més valuós, capaç de distingir els diferents isòmers, l'ha proporcionat la

teoria dels orbitals moleculars de Hückel (*Hückel molecular orbital*, HMO).[22,23] Tenim tres factors importants que determinen l'estructura electrònica dels ful·lerens: (1) són caixes closes, (2) tenen els àtoms de carboni individuals en entorns tricoordinats semblants al grafit (hibridació sp^2) i (3) presenten una esfericitat que allunya lleument els carbonis de la situació d'hibridació sp^2 pura. Si considerem els electrons *1s* localitzats, cada carboni té 4 electrons i 4 orbitals de valència (un *2s* i tres *2p*) per contribuir a l'enllaç del ful·lerè. D'aquests quatre electrons, tres són usats per produir enllaços σ C–C senzills a través de les arestes del políedre i un per prendre part en un sistema d'enllaç π C–C. L'electró π es situa en un orbital radial que podria ser el pur *2p* si l'entorn local fos perfectament pla, però més generalment en els ful·lerens serà un orbital híbrid sp^m.[24] El model HMO permet una simplificació de l'estructura electrònica en la separació d'enllaços σ i π molt valuosa. Pel cas del C_{60}, el model dóna un raonable salt d'energia HOMO-LUMO ($0.7566|\beta|$, comparat a $2|\beta|$ pel benzè) i una energia total de ressonància de $0.5527|\beta|$ per àtom apropant-se al valor del grafit de $0.5761|\beta|$.[25] β és la integral de ressonància. S'ha comprovat que els ful·lerens més estables presenten salts d'energia HOMO-LUMO importants[26] o com a mínim estructures electròniques de capes tancades, així com, altes energia de ressonància electròniques π. Sovint, però, l'augment de l'estabilitat electrònica π i la disminució de la tensió estèrica es troben en competició. Només les estructures de C_{60} i C_{70} mostren resultats òptims respecte ambdós criteris.[27]

1.2.3 Regla dels pentàgons aïllats (IPR)

La conseqüència més important de la minimització de l'energia de tensió estèrica en els ful·lerens és l'aparició de la regla dels pentàgons aïllats (*isolated pentagon rule,* IPR) formulada per en Kroto el 1987[18] i també apuntada per Schmalz el 1988.[19] La regla IPR diu que els ful·lerens més estables són aquells en que tots els 12 pentàgons es troben aïllats. La presència de pentàgons adjacents produeix una severa tensió estèrica que impossibilita la formació d'aquests ful·lerens. Alhora, es té una preferència pel ful·lerens amb un menor nombre de pentàgons adjacents. També s'apuntava com a factor minimitzador de l'energia estèrica, que els pentàgons estiguessin tant allunyats entre si com fos possible, és a dir

uniformement distributs.[18,28] El fet rellevant és que els dos pics més pronunciats en l'espectre de masses inicial (C_{60} i C_{70}) eren els dos primers possibles ful·lerens que complien la regla IPR, és a dir sense pentàgons adjacents. La regla IPR pot ser justificada fàcilment usant idees de la rehibridació dels carbonis. En particular, ha estat discutida en base al grafit i el C_{20}. La tensió estèrica augmenta a mesura que els carbonis s'allunyen de la hibridació ideal sp^2 del grafit per apropar-se a la hibridació sp^3 del C_{20} . Això és degut a la desalineació dels orbitals π en aquesta estructura torsionada. Els carbonis que es troben entre dos pentàgons adjacents (tipus ***E*** a l'apèndix A.1) es troben més piramidalitzats (curvats) i tenen un caràcter sp^3 més marcat que no pas els carbonis entre dos hexàgons (tipus ***A***, ***B***, ***C***) o bé entre un hexàgon i un pentàgon (tipus ***D***). No obstant, la justificació de la regla IPR no només es basa en la tensió estèrica. Resulta que l'energia de ressonància electrònica π també es veu afectada per la presència de pentàgons adjacents. Així, dos pentàgons adjacents tenen un cicle de vuit carbonis de longitud el qual pot ser assumit, en base la regla de Hückel *4n*, de tenir un efecte desestabilitzant sobre tota l'estructura electrònica π. És doncs, especialment significant que ambdós efectes: la tensió estèrica i l'estructura electrònica π donin suport a la regla IPR. També s'ha comprovat que dins de la teoria HMO, la isolació de pentàgons és necessària però no suficient per a tenir una capa electrònica tancada; factor d'estabilitat, com ja hem vist. L'estabilitat dels ful·lerens, doncs, pot ser atribuïda a un balanç entre l'estabilitat electrònica π i la tensió estèrica produïda per la corbatura. Tot i que la regla IPR afavoreix ambdós factors, entre els isòmers IPR d'una mateixa estequiometria sovint l'estabilitat electrònica π i la tensió estèrica segueixen camins diferents. La diferència energètica entre l'únic isòmer del C_{60} que compleix la regla IPR i un isòmer C_{2v} amb dos parells de pentàgons adjacents és d'1.4 eV. Això dóna una energia de penalització de 0.7 eV per cada una de les parelles de pentàgons adjacents i per tant corrobora sobradament la regla IPR.[29]

1.2.4 Isòmers dels ful·lerens IPR

Aplicant la restricció de la regla IPR (1.2.3) sobre la definició de políedre dels ful·lerens (1.2.1), el nombre d'estructures es redueix dràsticament. A tall d'exemple dono només els isòmers IPR dels ful·lerens

més habituals: 1 isòmer IPR pel C_{60}, 1 pel C_{70}, 1 pel C_{74}, 2 pel C_{76}, 5 pel C_{78}, 7 pel C_{80}, 9 pel C_{82} i 24 pel C_{84}.[17] El C_{60} i el C_{70} són els dos primers ful·lerens IPR i entre ells no n'hi ha cap altre. Els ful·lerens amb més de 70 carbonis són anomenats ful·lerens superiors. Malgrat aquestes consideracions teòriques, no tots aquests isòmers s'han observat experimentalment, però els que ho han estat, corresponen amb algun dels isòmers IPR pre-establerts teòricament. Ens centrarem a discutir únicament sobre les sis estequiometries relacionades amb el treball: C_{60}, C_{68}, C_{70}, C_{78}, C_{80} i C_{84}. Tots ells són ful·lerens IPR excepte el C_{68}. La numeració i corresponent simetria dels isòmers segueix la que proposaren Fowler i Manolopoulos, la qual és bastament acceptada per la comunitat científica.[17] Així, com a exemple de la nomenclatura, l'únic isòmer IPR del C_{60} s'escriu com I_h-C_{60}:**1**, referint-se a la simetria, estequiometria i numeració isomeral, respectivament.

El primer ful·lerè en ser caracteritzat fou el I_h-C_{60}:**1** (per abreujar simplement C_{60}) el qual originàriament fou identificat per les seves quatre bandes d'absorció IR per en Krätschmer et al. el 1990,[7] i molt aviat per una sola senyal en l'espectre de RMN de ^{13}C per en Taylor et al. el mateix any.[30] L'estructura del C_{60} es mostra en l'apèndix A.2. Aquest segon article d'en Taylor també informà sobre la detecció del segon ful·lerè més prolífic el D_{5h}-C_{70}:**1** (apèndix A.4). L'espectre de RMN de ^{13}C del C_{70} consistí en 5 línies amb una integració de senyals 3 x 10 i 2 x 20, com era d'esperar per una simetria D_{5h}.[30] No existeix cap isòmer IPR de les 6332 estructures ful·lerèniques possibles del C_{68}.[17] No obstant l'isòmer D_3-C_{68}:**6140** ha estat identificat en l'estructura del *metal·loful·lerè*: $Sc_3N@C_{68}$. Tot i no ser un ful·lerè IPR, aquest és l'isòmer amb un menor nombre de pentàgons adjacents – només 3 parelles – que li confereixen una estabilitat per sobre de la resta.[31] El segon ful·lerè superior en ser caracteritzat fou el C_{78}. L'any 1991 s'identificà una barreja de tres dels cinc isòmers IPR del C_{78} a partir de l'espectre de RMN de ^{13}C.[32] El més sorprenent fou que la quantitat relativa de cada isòmer en la mescla era sensible a les condicions experimentals. Així les observacions suggerien que era possible tenir estabilitats termodinàmiques semblants per diversos isòmers, i a més a més que els factors cinètics també jugaven un paper important en el procés de formació dels ful·lerens.[33] La barreja estava formada per D_3-C_{78}:**1**, C_{2v}-C_{78}:**2** i $C_{2v'}$-C_{78}:**3**. Les energies relatives (en kJ/mol) dels cinc isòmers IPR segueixen el

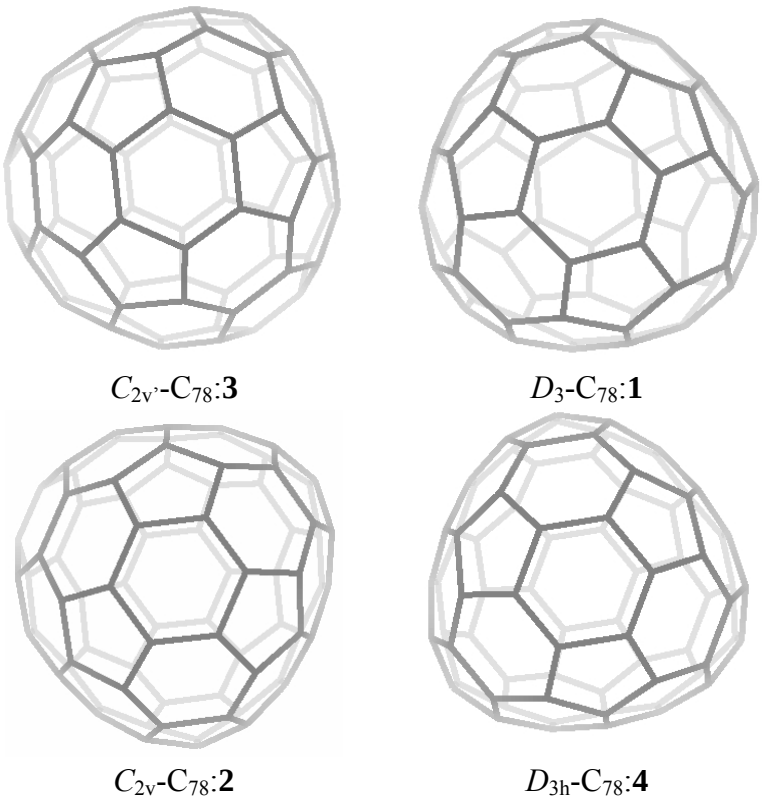

$C_{2v'}$-C_{78}:**3** D_3-C_{78}:**1**

C_{2v}-C_{78}:**2** D_{3h}-C_{78}:**4**

Figura 1.1 Estructura geomètrica de 4 dels 5 isòmers IPR del C_{78}. L'estructura del cinquè isòmer, el $D_{3h'}$-C_{78}:**5**, es pot visualitzar en l'apèndix A.5. El $C_{2v'}$-C_{78}:**3** és l'isòmer més estable termodinàmicament mentre que el $D_{3h'}$-C_{78}:**5** és el que es troba encapsulant l'Sc_3N en l'endohedre $Sc_3N@C_{78}$. Les estructures estan ordenades de més a menys estables.

següent ordre $C_{2v'}$-C_{78}:**3** (0) > D_3-C_{78}:**1** (14) > C_{2v}-C_{78}:**2** (17) > $D_{3h'}$-C_{78}:**5** (30) > D_{3h}-C_{78}:**4** (85).[34] Tots ells estan dibuixats en la Figura 1.1. Pel que respecta al C_{80} s'han publicat encara pocs estudis ja que no fou detectat fins el 1996. Concretament de les 7 estructures IPR teòriques: D_{5d}-C_{80}:**1**, D_2-C_{80}:**2**, C_{2v}-C_{80}:**3**, D_3-C_{80}:**4**, $C_{2v'}$-C_{80}:**5**, D_{5h}-C_{80}:**6** i I_h-C_{80}:**7** només dues han estat aïllades i caracteritzades: la D_2-C_{80}:**2** i la D_{5d}-C_{80}:**1** (veure Figura 1.2). Teòricament hem corroborat que els dos isòmers trobats experimentalment són els més estables i gairebé isoenergètics i que la diferència entre el més

estable (D_{5d}-C_{80}:**1**) i el menys estable (I_h-C_{80}:**7**) és de només de 0.5 eV. La cursa per la dilucidació dels isòmers del C_{84} començà el 1992. Tota l'experimentació indica que es produeix una barreja en equilibri 2:1 dels isòmers D_2-C_{84}:**22** i D_{2d}-C_{84}:**23**, la qual dóna un espectre de RMN de ^{13}C de 31 línies d'igual intensitat i una línia de la meitat d'intensitat. Aquesta assignació, de fet, és força subtil perquè hi ha altres tres isòmers de simetria D_2 entre els 24 isòmers IPR possibles del C_{84} que donarien un patró de RMN idèntic. Però el fet que la mescla d'isòmers es doni en un equilibri 2:1 implica un equilibri de les dues formes isoenergètiques més estables que sense ambigüitats corresponen als isòmers D_2-C_{84}:**22** i D_{2d}-C_{84}:**23** tal i com ha estat comprovat per càlculs teòrics.[33,35]

1.2.5 Obtenció experimental

Aquests i altres ful·lerens superiors han estat sintetitzats seguint el mètode d'en Taylor.[30] L'aplicació d'una descàrrega elèctrica sobre un arc de carboni grafit en atmosfera d'heli o argó provoca la vaporització del carboni i la formació d'un sutge. Aquest procés es realitza en l'aparell anomenat de Krätschmer-Huffman. El sutge conté una varietat extraordinària d'espècies carbonades moleculars i polimèriques. Els ful·lerens continguts en el sutge són extrets en un dissolvent i posteriorment separats per cromatografia d'alta resolució (HPLC). Les principals variacions són respecte el mètode de producció del sutge (descàrrega elèctrica o resistència de calor) i en els solvents usats en l'extracció. Val a dir que el ful·lerens també poden ser produïts a partir de la combustió o piròlisis de compostos aromàtics policíclics.[36] Aquesta nova tècnica ha estat millorada recentment per Scott et al. permeten una síntesi mes controlable i racional que pel mètode anterior.[37] Jugant amb aquests paràmetres altres ful·lerens superiors han estat sintetitzats, com ara: C_{76}, C_{82}, C_{90}, C_{94} i C_{96}. Aquests completen una mica més el mapa de ful·lerens previstos teòricament.

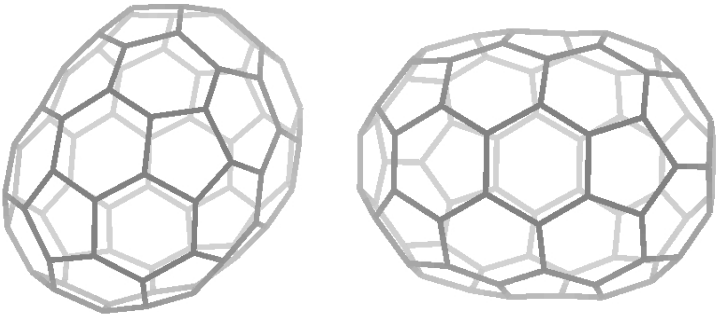

D_{5d}-C_{80}:**1**

D_{2}-C_{80}:**2**

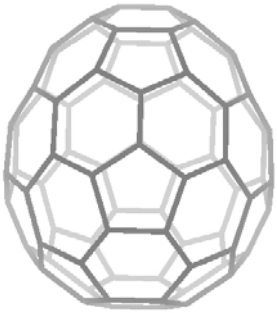

C_{2v}-C_{80}:**3**

$C_{2v'}$-C_{80}:**5**

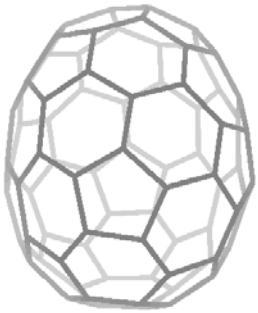

D_{3}-C_{80}:**4**

D_{5h}-C_{80}:**6**

Figura 1.2 Estructura geomètrica de 6 dels 7 isòmers IPR del C_{80}. L'estructura del setè isòmer, el I_h-C_{80}:**7**, es pot visualitzar en l'apèndix A.6. El D_{5d}-C_{80}:**1** és l'isòmer més estable termodinàmicament mentre que el I_h-C_{80}:**7** és el que es troba encapsulant l'Sc_3N en l'endohedre $Sc_3N@C_{80}$. Les estructures estan ordenades de més a menys estables.

Taula 1.1 Caracterització electrònica i geomètrica dels isòmers IPR més estables entre el C_{60} i el C_{84} i alguns altres ful·lerens d'interès pel treball d'investigació [a]

ful·lerè	EPA [b]	Radi Caixa	Salt HOMO-LUMO	HOMA [c]	IP [d]	EA [d]
I_h-C_{60}:**1**	–7.35	3.551	1.66	0.274	7.56 / 7.57*	2.89 / 2.85*
D_3-C_{68}:**6140**	–7.33	3.783	0.51	0.356	7.11*	3.71*
D_{5h}-C_{70}:**1**	–7.39	3.837	1.71	0.362	7.46	2.90
D_2-C_{76}:**2**	–7.40	4.002	1.07	0.322	6.09	3.16
$C_{2v'}$-C_{78}:**3**	–7.41	4.052	0.76	0.350	6.88	2.43
$D_{3h'}$-C_{78}:**5**	–7.41	4.052	0.62	0.356	6.88*	3.49*
D_{5d}-C_{80}:**1**	–7.40	4.106	0.12	0.342	6.41	3.64
I_h-C_{80}:**7**	–7.40	4.103	0.00	0.464	6.92*	3.75*
C_2-C_{82}:**3**	–7.41	4.154	0.23	0.324	6.79	3.43
D_2-C_{84}:**22**	–7.43	4.200	1.03	0.373	7.01	3.40
D_{2d}-C_{84}:**23**	–7.43	4.199	1.10	0.373	7.06	3.36

[a] Energia en eV i geometries en Å. [b] Energia per àtom (EPA). [c] *Harmonic oscillator model of aromaticity* (HOMA). [d] * és indicatiu de potencial d'ionització (IP) o afinitat electrònica (EA) vertical.

1.3 CARACTERITZACIÓ

1.3.1 Estabilitat en l'increment de carbonis

Hem volgut comparar l'estabilitat de cada una de les estequiometries que intervenen en el treball comparant l'energia d'enllaç per àtom (EPA) (Taula 1.1 i Figura 1.3). Hem considerat l'isòmer IPR més estable de cadascuna de les estequiometries ful·lerèniques entre el C_{60} i el C_{84}: I_h-C_{60}:**1**, D_{5h}-C_{70}:**1**, D_2-C_{76}:**2,** $C_{2v'}$-C_{78}:**3**, D_2-C_{80}:**2**, C_2-C_{82}:**3** i D_2-C_{84}:**22**; així com l'estructura no IPR del ful·lerè D_3-C_{68}:**6140** i algunes altres estructures que intervenen fortament en el present treball d'investigació: $D_{3h'}$-C_{78}:**5**, I_h-C_{80}:**7** i D_{2d}-C_{84}:**23**. Tot i que les diferències són petites, en la sèrie dels isòmers IPR s'observa clarament que els ful·lerens més grans són significativament més estables que el C_{60} en base a l'EPA. Així l'EPA pel C_{60} és –7.35 eV mentre que per l'isòmer més estable del C_{84} (D_2-C_{84}:**22**) és de –7.43 eV.

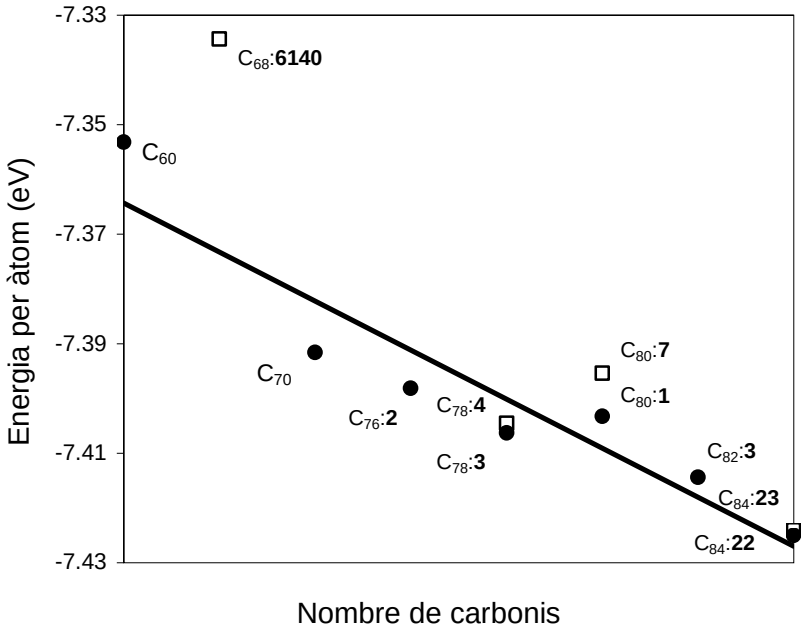

Figura 1.3 Energia per àtom (EPA) pels isòmers IPR més estables de les estequiometries compreses entre el C_{60} i el C_{84} (cercles plens) i alguns altres isòmers involucrats en aquest treball (quadrats buits). La línia de tendència té en només compte el primer grup d'isòmers.

Aquesta tendència és consistent amb la previsió que l'estabilitat s'incrementarà a mesura que la superfície carbonada esdevingui més plana i per tant la tensió estèrica disminueixi. Això succeirà quan la mida dels ful·lerens augmenti. Així doncs, la gran preferència per la formació dels ful·lerens de C_{60} i C_{70} indicaria que els factors cinètics jugarien un paper important, ja que el ful·lerens més estables termodinàmicament no són els obtinguts amb més rendiment experimentalment. Aquests valors també mostren una estabilitat inferior al diamant i el grafit.[14] També ressalta la forta disminució de l'estabilitat en el cas del ful·lerè no IPR D_3-C_{68}:**6140** de 0.02 eV per àtom, tal i com ja havíem predit en seccions anteriors.

1.3.2 Propietats geomètriques

Només existeixen quatre tipus d'enllaços C–C en els ful·lerens que compleixen la regla IPR (veure'ls a apèndix A.1). Els enllaços C–C es diferencien per la seva topologia, que a la vegada, els confereix unes propietats singulars: distància d'enllaç, angle de piramidalització (θ_p) i ordre d'enllaç. L'angle de piramidalització és una mesura introduïda per Haddon i Raghavarachi[38] i representa una mesura de la corbatura de la superfície ful·lerènica. Els ordres d'enllaç de Mayer (*Mayer bond order*, MBO) ens donen una indicació sobre la fortalesa de l'enllaç tant σ com π. A la secció 4.7.2 hi haurà més detalls teòrics tant de l'angle de piramidalització com de l'ordre d'enllaç Mayer. Els enllaços formats per l'acoblament de dos hexàgons són anomenats de tipus 6:6. Dins d'aquest primer grup, els de tipus piracil·lènic (tipus ***A***) corresponen a un enllaç C–C 6:6 que fa de pont entre dos pentàgons. Si l'enllaç C–C 6:6 fa de pont entre dos hexàgons s'anomena de tipus pirènic (tipus ***C***) i si ho fa entre un hexàgon i un pentàgon és de tipus ***B*** (segons el nostre coneixement sense cap nom especial). Finalment, trobem l'enllaç C–C format per l'acoblament d'un hexàgon i un pentàgon anomenat C–C 6:5 coranul·lènic (tipus ***D***). Pels ful·lerens no IPR poden aparèixer altres tipologies d'enllaç com ara l'***E*** i l'***F*** del ful·lerè D_3-C_{68}:**6140**. A l'apèndix trobem la caracterització de tots els diferents tipus d'enllaços C–C dels ful·lerens lliures que estan involucrats en el present treball. Les distàncies C–C més curtes i de caràcter doble es donen en la tipologia piracil·lènica ***A*** (~ 1.39 Å) que a la vegada són els que permeten també una piramidalització més elevada (θ_p > 11º). En contraposició, trobem els enllaços de tipus pirènics ***C*** que se situen en les part més planes de les estructures ful·lerèniques amb distàncies C–C senzilles al voltant de 1.47 Å i amb una piramidalització de ~ 8.6º o fins i tot inferior a 7º en algun cas. Com a casos intermitjos tenim els enllaços de tipus ***B*** i ***D*** que presenten distàncies i angles de piramidalització entre 1.41-1.45 Å i 9-11º, respectivament. Cada tipologia d'enllaç ocupa el seu espai determinat en la caixa ful·lerènica. Es interessant adonar-se que els enllaços que se situen exteriorment dels pentàgons (tipus ***A*** i ***B***), en línies generals, són més curts i de major caràcter doble que no pas els propis del pentàgon (tipus ***D***). Allargant les distàncies C–C i piramidalitzant els carbonis pentagonals es minimitza la tensió estèrica produïda per la inclusió dels

pentàgons. La conseqüència d'aquesta localització serà que els ful·lerens es comporten més com alquens que no pas com compostos aromàtics. La caracterització dels diferents grups d'enllaços C–C veurem que és un pas inicial primordial per l'estudi de reactivitat *heteroèdrica* i sobretot *exoèdrica* dels ful·lerens.

Una altra propietat geomètrica és el radi de caixa. Tenim llistat els radis de caixa pels isòmers considerats a la Taula 1.1. El radi de caixa augmenta a mesura que augmenten el nombre de carbonis i ens dóna una idea sobre la grandària de la cavitat interior. Més endavant veurem com també pot arribar a ser una mesura de la distorsió que pateix el ful·lerè a mesura que rep transformacions químiques.

1.3.3 Estructura electrònica

Els orbitals moleculars del ful·lerè C_{60} poden ser classificats en dos tipus, π i σ. Els orbitals tipus π posseeixen una superfície nodal que coincideix pràcticament amb la superfície creada pels àtoms de carboni, mentre que en els orbitals tipus σ aquesta superfície nodal és inexistent. Com a primer model d'estudi, l'energia dels orbitals tipus π pot ser obtinguda a partir de la teoria HMO del sistema de 60 carbonis disposats en una caixa closa. Aquesta estructura electrònica rendeix un HOMO pentadegenerat h_u, un LUMO tridegenerat t_{1u} i un LUMO+1 també tridegenerat t_{1g} molt proper en energia a l'anterior.[25,39] Aquest esquema dels orbitals frontera és també sostingut per nivells de teoria més sofisticats: HF/6-31G*[41] i DFT-LDA.[42] La separació energètica HOMO-LUMO (1.66 eV), sense ser molt elevada, és suficient per conferir certa estabilitat a la molècula. Aquest no és un fet aïllat del C_{60} sinó que la resta d'isòmers més estables també contenen considerables salts HOMO-LUMO tal i com es veu a la Taula 1.1. Aquesta característica és d'enorme importància per entendre les propietats dels ful·lerens com a semiconductors.[43] Els orbitals HOMO h_u representen interaccions π enllaçants en els enllaços C–C 6:6 i π antienllaçants en els C–C 6:5. Mentre que els LUMO i LUMO+1 tridegenerats representen una situació inversa. Per tant, és d'esperar que l'ocupació dels h_u produeixi un escurçament dels enllaços C–C 6:6 i un allargament dels C–C 6:5 del C_{60}. D'aquí prové la famosa alternança en les distàncies C–C i la prova que els electrons π no es troben deslocalitzats

sobre tots els enllaços de manera homogènia.[44] L'enllaç C–C 6:6 i 6:5 mesuren 1.397 i 1.452 Å, respectivament pel C_{60}. Els valors experimentals donats per mesures de difracció electrònica en fase gas foren 1.401 Å i 1.458 Å, respectivament.[45] Per altra banda una suposada ocupació dels LUMO t_{1u} i t_{1g} ha de tenir l'efecte contrari i per tant afavorir la igualtat entre els enllaços i així augmentant d'aquesta manera l'aromaticitat. Efectivament, càlculs sobre l'anió C_{60}^{12-} ($Li_{12}C_{60}$) corroboren un allargament fins a 1.45 Å dels enllaços C–C 6:6 piracil·lènics i un escurçament dels C–C 6:5 coranul·lènics fins 1.44 Å, així doncs, essent ambdós pràcticament iguals.[46] Aquest comportament d'igualació de la distància dels diferents enllaços quan els ful·lerens reben electrons també ha estat observada en els ful·lerens superiors.[13] En resum, l'alternança entre les distàncies C–C 6:6 i el 6.5 en el C_{60} es pot explicar en termes d'estructura electrònica així com amb arguments de tensió estèrica com s'ha fet en la secció 1.2.6. Altre cop ens apareix aquesta dualitat entre factors geomètrics i electrònics tal i com havia aparegut en les primeres seccions (1.2.1-1.2.3) per explicar l'estabilitat dels ful·lerens lliures.

1.3.4 Aromaticitat

Sobre l'aromaticitat dels ful·lerens hi ha hagut molta controvèrsia i en particular sobre la del C_{60} que inicialment es postulà com possiblement superaromàtic. L'aromaticitat[47] s'associa a la deslocalització cíclica d'electrons que provoca una estabilització extra en el cas de compostos aromàtics i una desestabilització en el cas dels antiaromàtics. Actualment el C_{60} es considerat poc aromàtic per diversos aspectes: (1) les diferents energies que calculen la deslocalització electrònica π revelen que no és més aromàtic que l'heptacè,[48] (2) el seu feble diamagnetisme, (3) l'alta alternança entre les distàncies C–C de tipus 6:6 i 6:5 i (4) finalment la reactivitat química és més propera a la dels alquens deficients en electrons que no pas a la del benzè. L'aromaticitat dels ful·lerens icosaèdrics (C_{20}, C_{60} i C_{80}) depèn del nombre d'electrons deslocalitzats a la capa de valència. La màxima aromaticitat esfèrica pot només ser assolida amb $2(N+1)^2$ electrons omplint completament aquesta capa.[49] La regla $2(N+1)^2$ representa l'anàloga esfèrica de la regla de Hückel pel compostos plans. Així l'aromaticitat del C_{60} s'estimula quan 12 electrons s'afegeixen a l'estructura electrònica, N=5

per la regla $2(N+1)^2$. La reducció afavoreix a l'igualació de les distàncies C–C per les raons explicades en la secció anterior. El C_{70} presenta una zona central força aromàtica (enllaços Ce–Ce, Cd–Ce i Cd–Cd, veure apèndix A.4) i una zona als pols on es localitzen els dobles/simples enllaços (enllaços Ca–Ca, Ca–Cb, Cb–Cc i Cc–Cc). S'han proposat molts criteris per mesurar l'aromaticitat però actualment quatre tipus han provat la seva efectivitat: criteris energètics, electrònics, magnètics i geomètrics. Avui dia, l'energia d'estabilització aromàtica (*aromatic stabilisation energy*, ASE)[50] és un criteri energètic per avaluar l'aromaticitat, com a criteri electrònic últimament s'ha imposat l'índex de deslocalització para (*para delocalisation index*, PDI)[51] i com a criteri magnètic tenim el desplaçament químic independent nuclear (*nuclear independent chemical shift*, NICS).[52] Nosaltres sense voler entrar molt a fons en l'aromaticitat ens hem centrat únicament en l'aromaticitat geomètrica a partir de l'índex HOMA (*harmonic oscillator model of aromaticity*).[53] L'HOMA avalua l'aromaticitat a partir de l'alternança de la longitud dels enllaços C–C i també del valor absolut d'aquestes distàncies. Per més detalls veure la secció 5.3.1. L'estabilitat produïda per l'aromaticitat serà un factor clau en l'estabilitat relativa dels regioisòmers dels *ful·lerens heteroèdrics*. A la Taula 1.1 tenim llistat els HOMA dels ful·lerens lliures involucrats en la tesi. Com es pot observar l'aromaticitat no depèn de la grandària del ful·lerè sinó de la topologia i distribució dels enllaços que conté cadascun dels isòmers. El I_h-C_{80}:**7** s'erigeix com el més aromàtic (HOMA = 0.464). No és d'estranyar ja que és el que presenta major igualtat en les distàncies dels seus enllaços: el 6:6 tipus ***B*** mesura 1.428 Å i el 6:5 tipus ***D*** mesura 1.438 Å (Apèndix A.6). En canvi, el I_h-C_{60}:**1** li correspon el valor menys aromàtic de 0.274 que a la vegada coincideix amb el que presenta major alternança entre els seus enllaços 6:6 i 6:5.

1.3.5 Propietats físiques

A la Taula 1 també hem llistat els potencials d'ionització (IP) i les afinitats electròniques (EA) dels ful·lerens lliures considerats. La variació en l'afinitat electrònica és paral·lela a les energies dels orbitals LUMO.[54] Els ful·lerens lliures en general presenten orbitals LUMO força estabilitzats, és a dir, baixos en energia, fet que explica la seva facilitat a acceptar electrons i

ser fàcilment reduïts.[55] L'estabilitat dels orbitals LUMO s'associa a la piramidalització dels carbonis.[56] La facilitat en la reducció fa que els ful·lerens actuïn com a bons agents oxidants i per exemple són capaços d'oxidar l'àcid sulfhídric a sofre.[58] L'EA dels dos ful·lerens més coneguts el C_{60} i el C_{70} és de 2.65 i 2.73 eV, respectivament. Com es pot observar en la Taula 1.1 les EAs dels ful·lerens més grans augmenten lleugerament respecte el C_{60} i C_{70}. Els ful·lerens també presenten una alta estabilitat dels orbitals HOMO que els hi confereixen una alta estabilitat davant l'oxidació. L'IP del C_{60} i del C_{70} és, doncs, força elevat, de 7.56 i 7.46 eV, respectivament. Pels ful·lerens superiors s'obtenen valors menors, per exemple, 7.01 eV pel D_2-C_{84}:**22**. Així els ful·lerens superiors són millors electrodonadors i també millors electroacceptors que el C_{60} o el C_{70}. S'argumenta que els ful·lerens superiors tenen una proporció més gran d'anells hexagonals i per tant posseeixen una estructura electrònica més propera a la del grafit, la qual té aquestes propietats.[13] Malgrat el fet que els ful·lerens superiors siguin millors electroacceptors que el C_{60}, és poc probable que formin anions altament carregats. Això és degut a que, a diferència del C_{60}, aquests normalment no posseeixen LUMOs degenerats. De les dades de la Taula 1.1 es desprèn també que els IPs i les EAs són lleugerament sensibles a la topologia de cada un dels isòmers, així l'IP i l'EA del D_{5d}-C_{80}:**1** i del I_h-C_{80}:**7** difereixen en 0.51 eV i 0.11 eV, respectivament. El mateix passa entre els dos isòmers llistats del C_{78} i del C_{84}.

1.3.6 Reactivitat química

En Hirsch ha redactat magnífics compendis de reactivitat orgànica de ful·lerens.[59] Els dos principals tipus de reaccions químiques primàries que són possibles són: reaccions d'addició i reaccions *redox*. Aquest sol fet ja ens dóna idea que la reactivitat dels ful·lerens és significativament diferent a la dels clàssics aromàtics plans. La reactivitat dels ful·lerens s'aproxima força a la de les poliolefines electrodeficients, on la principal transformació química és l'addició 1,2 als enllaços 6:6 piracil·lènics (o de major caràcter doble). Especialment es donen atacs nucleòfics i radicalaris obtenint adductes hidrogenats, alquilats, arilats, alquinilats, sililats, aminats i fosforats. Així les addicions es donen en una coordinació η^2 als enllaços,

més que no pas, coordinacions η^5 i η^6 a les cares. En cas d'addicions amb un alt grau d'impediment estèric també es produeixen addicions 1,4. La completa caracterització dels mono- i poliadductes resultat de les cicloaddicions ha permès un gran increment del coneixement de la química de ful·lerens. Aquestes es donen exclusivament en els enllaços de major caràcter doble com els 6:6 piracil·lènics del C_{60}, excepte en les addicions de nitrens que es poden donar en els 6:5 del C_{60}.[60] Aquests enllaços actuen com a dienòfils. Encara que la reducció dels ful·lerens és molt més fàcil que la seva oxidació, també s'han portat a terme una varietat d'addicions electrofíliques i funcionalitzacions oxidatives. Així els ful·lerens halogenats i oxigenats són també força comuns. Aquestes funcionalitzacions *exoèdriques* representen el conjunt de compostos més ben estudiats i caracteritzats de la química de ful·lerens. La força conductora per aquesta reactivitat *exoèdrica* és la reducció de la tensió estèrica deguda a la rehibridació dels carbonis sp^2 a sp^3. Ara bé, en els últims anys s'han realitzat grans esforços en la derivatització a l'interior dels ful·lerens i a la superfície carbonada. Els primers se sintetitzen a partir de reaccions d'encapsulament i els segons mitjançant reaccions de substitució.

1.4 METAL·LOFUL·LERENS

Inicialment la química de ful·lerens fou una química purament orgànica, tal i com expliquem en l'apartat anterior, i no s'explorà intensament la modificació química a través de la reacció amb compostos metàl·lics fins a mitjans dels anys 90. Tenim geomètricament tres maneres de modificar un ful·lerè mitjançant la reacció amb una unitat metàl·lica: (1) per encapsulament a l'interior de la caixa ful·lerènica (anomenats *metal·loful·lerens endoèdrics*), (2) per incorporació a l'estructura carbonada en una substitució (*metal·loful·lerens heteroèdrics*) i finalment (3) per derivatització externa a la superfície (*metal·loful·lerens exoèdrics*). En anglès respectivament són anomenats: *endohedral metallofullerenes*, *heterohedral metallofullerenes* i *exohedral metallofullerenes*. Els aspectes de la reactivitat organometàl·lica dels ful·lerens ha estat coberta magníficament per tres articles, força antics però molt ben estructurats i aclaridors, d'en Stepens[61], en Bowser[62] i en Hammond[63].

1.4.1 Endoèdrics

Ja des del principi, en l'aparició de l'ió $C_{60}La^+$, es pensà en la possibilitat d'encabir àtoms, ions i petites molècules a l'interior dels ful·lerens.[64] S'han anomenat *ful·lerens endoèdrics,* o bé *ful·lerens empresonats (incar-fullerenes)* o fins i tot *endoedres* per escurçar, a aquelles estructures on s'ha aconseguit aquest tipus de derivatització. Les espècies resultants d'aquests encapsulaments es poden classificar en dues categories.[65] En els *compostos endoèdrics* trobem una barreja orbitàl·lica significativa entre l'hoste (petita unitat metàl·lica) i l'amfitrió (caixa ful·lerènica) que dóna lloc a un enllaç químic directe. Aquest seria el cas de molècules hoste grans o bé de ful·lerens de caixes petites com ara l'M@C_{28}, M = Mg, Al, Si, S, Ca, Si, Ti, Ge, Zr i Sn.[66] Seguirem la nomenclatura àmpliament emprada en la bibliografia científica en la que el símbol @ identifica A empresonat dins a B en A@B. No obstant, la nomenclatura IUPAC seria *i*-AB. Per altra banda, en els *complexos endoèdrics* la barreja és negligible i l'enllaç entre ambdues parts es dominat per efectes electrostàtics i de polarització.[67] Exemple d'aquest últim tipus són l'encapsulament de gasos nobles,[68] metalls alcalins, alcalinoterris,[69] metalls de transició[70] i molècules diatòmiques[71] en el C_{60} i altres ful·lerens. Aquests seran els que centraran la nostra atenció. Avui dia s'han detectat *complexos endoèdrics* monometàl·lics de gairebé tota la sèrie dels alcalins, alcalinoterris, lantànids, actínids i grup 1 (Sc, Y, La, Ac) amb una gran varietat de caixes C_k (k = 60, 70, 72, 74, 76, 80, 82, 84). També es té constància de l'encapsulament dimetàl·lic d'Sc, La, Ce, Pr, Y i U en caixes de C_k (k = 60, 74, 76, 80, 82, 84) i fins i tot de trimetàl·lics d'Sc dins el C_{82} i C_{84}. L'enllaç entre els metalls i la caixa ful·lerènica ve caracteritzat per un model iònic de transferència electrònica del metall a la caixa. Així els *metal·loful·lerens endoèdrics* sovint són referits com a superàtoms en el sentit de tenir un centre carregat positivament i una caixa carregada negativament.[72] En general, l'estat d'oxidació +3 s'aplica a Sc, Y, La, Ce, Pr, Nd, Gd, Tb, Ho, Er, Lu i l'estat d'oxidació +2 a Ca, Sr, Sm, Eu, Tm i Yb.[73] En el cas, però, de l'encapsulament de gasos nobles la transferència electrònica és inexistent. La principal problemàtica d'aquests primers *metal·loful·lerens endoèdrics*, dits també *clàssics*, és el baix rendiment obtingut a partir del sutge del mètode de Krätschmer-Huffman i l'alta

sensibilitat a l'aire. Això no ha permès una caracterització completa ni l'obtenció de grans quantitats per ser estudiades ni estructuralment ni espectroscòpicament. Així els primers indicis que els metalls es trobaven a l'interior no venen d'estudis de raigs-X (els quals ho determinen sense ambigüitats) sinó del tipus reactivitat observada.

Últimament la diversitat dels *complexos endoèdrics* ha augmentat amb l'aparició dels insòlits $Sc_3N@C_{68}$,[31] $Sc_3N@C_{78}$[74] i $Sc_3N@C_{80}$[75]. Aquests són els primers *metal·loful·lerens endoèdrics* que inclouen 4 àtoms al seu interior. En l'$Sc_3N@C_{80}$ es trobà que l'hoste s'encapsulava de forma plana mantenint una alta simetria del ful·lerè. El ful·lerè era estabilitzat com a resultat d'una transferència de càrrega entre el nitrur i la caixa. S'aposta per un model clarament iònic: $Sc_3N^{6+}@C_{80}^{6-}$. L'estudi en profunditat d'aquest nou grup de compostos serà l'origen del capítol 4.

1.4.2 Heteroèdrics

Els derivats de ful·lerens en que alguns àtoms de l'estructura ful·lerènica són substituïts per heteroàtoms són possibles. Són els anomenats *heteroful·lerens* o bé *ful·lerens heteroèdrics*. No és d'estranyar que els primers substituts del carboni fossin elements molt propers a ell: nitrogen, bor i silici. Efectivament, els primers *ful·lerens heteroèdrics* detectats espectroscòpicament foren els que contenen nitrogen (azaful·lerens) i que actualment són els més estudiats ja que poden ser obtinguts en quantitats macroscòpiques.[76] Mentrestant, els boraful·lerens només han estat detectats en espectres de masses.[77] Consideracions de valència en el cas del nitrogen dicten que els productes han de ser radicals (creant la possibilitat per la dimerització donant compostos com $(C_{59}N)_2$[78] i $(C_{69}N)_2$),[79] tenir hidrògens addicionals $(C_{59}NH)$[80] o contenir més d'un heteroàtom ($C_{58}N_2$). En aquest últim cas, on és possible una multisubstitució, es presenta també un interessant cas de regioisomerisme. En tots els casos s'ha constatat una menor estabilitat dels ful·lerens amb dopatge respecte els totalment carbonats. Des del començament, els *ful·lerens heteroèdrics* han estat considerats molècules interessants, principalment perquè es visionà que una modificació de l'estructura de la caixa provocaria una nova estructura electrònica, funcionalitat química i sobretot l'exhibició d'unes noves propietats. No obstant, actualment la presència de *metal·loful·lerens*

heteroèdrics és ben minsa i reduïda. Només tenim constància de la detecció en espectres de masses d'algunes estequiometries que incorporen Pt i Ir: $C_{58}M$, $C_{59}M$, $C_{56}M_2$ i $C_{57}M_2$ (M = Pt i Ir).[81] Aquestes estructures seran estudiades en profunditat en aquest treball en el capítol 5.

1.4.3 Exoèdrics

Els compostos on la derivatització química es dóna a l'exterior de la caixa ful·lerènica són anomenats *ful·lerens exoèdrics*. Aquests són possiblement els ful·lerens organometàl·lics més ben estudiats dels tres famílies. Els ful·lerens reaccionen fàcilment amb una gran quantitat de centres metàl·lics rics en electrons per formar complexos estables. En cas de centres metàl·lics impedits estèricament o no tant rics en electrons l'estabilitat, però, dels subsegüents complexos es redueix dràsticament. Molts d'ells són de fàcil síntesi i han estat ja caracteritzats estructuralment. El primer a ser completament caracteritzat fou el 1,2-$C_{60}(OsO_4)$(4-t-$BuC_5H_4N)_2$ per Hawkins el 1991.[82] Des del punt de vista estructural poden ser dividits en dos grans grups: els complexos σ enllaçats i els π enllaçats.[61] Els primers no han tingut gaire èxit i solen ser utilitzats com a intermedis per la preparació d'altres *metal·loful·lerens*. Exemples en tenim en: l'anterior èster d'osmi 1,2-$C_{60}(OsO_4)$(4-t-$BuC_5H_4N)_2$, el $C_{60}(Bu^t)(Li)$,[83] el $C_{60}S_2Fe_2(CO)_6$[84] i el $C_{60}\{Re(CO)_5\}_2$[85]. Els *metal·loful·lerens exoèdrics* π enllaçats formen un enllaç de tipus coordinatiu entre el centre metàl·lic i un dels seus enllaços C–C de major caràcter doble. Aquest enllaç es dominat fortament per la retrodonació del metall a la caixa. L'alta electroafinitat de les caixes ful·lerèniques facilita aquesta retrodonació. Així, la reactivitat dels ful·lerens és més similar a la del tetracianoetilè ($C_2(CN)_4$) que no pas a la del benzè o fins i tot a la del etilè. Exemples de *metal·loful·lerens exoèdrics* π són els complexos d'iridi, platí i ruteni. Els d'iridi deriven del compost de Vaska $Ir(CO)Cl(PR_3)_2$ per donar compostos de fórmula general (η^2-C_{60})$Ir(CO)Cl(PR_3)_2$, mentre que els de Pt deriven del desplaçament de l'etilè per part dels ful·lerens: (η^2-C_2H_4)$M(PR_3)_2$ + C_{60} → (η^2-C_{60})$M(PR_3)_2$ + C_2H_4 (M = Ni, Pd, Pt).[86] Els *complexos exoèdrics* π enllaçats de fórmula general (η^2-C_k)$\{M(PH_3)_2\}_n$ (M = Pt, Pd, Ni; k = 60, 70, 84; n =1, 2, 4, 6) seran objecte d'estudi en profunditat en el capítol 6.

REFERÈNCIES I NOTES

[1] Kroto, H. W.; Heath, J. R.; O'Brien, S. C.; Curl, R. F.; Smalley, R. E. *Nature* **1985**, *318*, 162.
[2] Rohlfing, E. A.; Cox, D. M.; Kaldor, A. *J. Chem. Phys.* **1984**, *81*, 3322.
[3] Stankevich, I. V.; Nikerov, M. V.; Bochvar, D. A. *Russ. Chem. Rev.* **1984**, *53*, 640.
[4] Tisza, L. Z. *Phys.* **1933**, *82*, 48.
[5] Jones, D. E. H. *New Science* **1966**, *32*, 245.
[6] Osawa, E. *Kagaku (Kyoto)* **1979**, *25*, 854.
[7] Krätschmer, W.; Lamb, L. D.; Fostiropoulos, K.; Huffman, D. R. *Nature* **1990**, *347*, 354.
[8] Braun, T. *Angew. Chem. Int. Ed. Engl.* **1992**, *31*, 588.
[9] Achiba, K.; Kikuchi, Y.; Aihara, T.; Wakabayashi, Y.; Miyake, M.; Kainosho *The chemical Physics of Fullerenes 10 (and 5) Years later*, N. A. Series, Editor W. Andreoni, Berlin, **1996**, pag. 139.
[10] (a) Ugarte, D. *Nature* **1992**, *359*, 707. (b) Bethume, D. S.; Kiang, C. H.; de Vries, M. S. *Nature*, **1993**, *363*, 605. (c) Iijima, S. *Nature*, **1991**, *354*, 56.
[11] Taylor, R. *Nature*, **1993**, *363*, 685.
[12] Bent, H. A. *Chem. Rev.* **1961**, *61*, 275.
[13] Cioslowski, J. *Electronic Structure Calculations on Fullerenes and Their Derivatives*, Oxford University Press, Oxford, **1995**.
[14] Taylor, R. *Lectrure notes on fullerene chemistry, a handbook for chemists*, London Imperial College Press, London, **1999**.
[15] Hirsch, A.; Rubin, Y.; Hummelen, J. C.; Bellavia-Lund, C.; Wudl, F.; Thilgen, C.; Diederich, F.; Prato, M.; Terrones, M.; Hsu, W. K.; Kroto, H. W.; Walton, D. R. M. *The Chemistry of fullerenes*, G. Thieme, Stuttgart, **1994**.
[16] Kadish, K. M.; Ruoff, R. S. *Fullerenes: chemistry, physics, and technology*, John Wiley & sons, New York, **2000**.
[17] Fowler, P. W.; Manoloupoulus, D. E. *An Atlas of Fullerenes*, Oxford University Press, Oxford, **1995**.
[18] (a) Kroto, H. W. *Nature* **1987**, *329*, 529.
[19] (a) Schmalz, T. G.; Seitz, W. A.; Klein, D. J.; Hite, G. E. *J. Am. Chem. Soc.* **1988**, *110*, 1113. (b) Klein, D. J.; Seitz, W. A.; Schmalz, T. G. *Nature*, **1986**, *323*, 703.
[20] Lakatos, I. *Proofs and refutations* Cambridge University Press, Cambridge, **1976**.
[21] Fowler, P. W.; Cremona, J. E.; Steer, J. I. *Theor. Chim. Acta*, **1988**, *73*,1.

[22] Com a exemple veure: Streitwieser, A. *Molecular orbital theory for organic chemists*, Willey, NewYork, **1961**.

[23] Podeu trobar una petita descripció de la teoria HMO a l'apartat 2.2 del següent capítol.

[24] Haddon, R. C. *Science* **1993**, *261*, 1545.

[25] Davidson, R. A. *Theor. Chim. Acta* **1981**, *58*, 193.

[26] Aihara, J.; Yoshida, M. *J. Mol. Graphics Model* **2001**, *19*, 194.

[27] Fowler, P. W.; Austin, S. J.; Manolopoulos, D. E. *Competing factors in fullerene stability, a Chemistry and physics of the fullerenes*, Prassides, K., ed. Kluwer, Dordrecht, **1994**.

[28] Raghavachari, K. *Chem. Phys. Lett.* **1992**, *190*, 397.

[29] Zhang, B. L.; Wang, C. Z.; Ho, K. M.; Xu, C. H.; Chan, C. T. *J. Chem. Phys.* **1992**, *97*, 5007.

[30] Taylor, R.; Hare, J. P.; Abdul-Sada, A. K.; Kroto, H. W. *J. Chem. Soc.; Chem. Comm.* **1990**, 1423.

[31] Stevenson, S.; Fowler, P. W.; Heine, T.; Duchamps, J. C.; Rice, G.; Glass, T.; Harich, K.; Hadju, E.; Bible, R.; Dorn, H. C. *Nature*, **2000**, *408*, 428.

[32] Diederich, F.; Whetten, C.; Thilgen, C.; Ettle, R.; Chao, I.; Alvarez, M. M. *Science* **1991**, *254*, 1768.

[33] Kikuchi, K.; Nakahara, N.; Wakabayashi, S.; Suzuki, S.; Shiromaru, H.; Miyake, Y.; Saito, K.; Ikemoto, I.; Kainosho, M.; Achiba, Y. *Nature* **1992**, *357*, 142.

[34] Raghavachari, K.; Rohlfing, C. M. *Chem. Phys. Lett.* **1993**, *208*, 436.

[35] (a) Manolopoulos, D. E.; Fowler, P. W.; Taylor, R.; Kroto, H. W.; Walton, D. R. M. *J. Chem. Soc. Faraday Trans.* **1992**, *88*, 3117. (b) Diederich, F.; Whetten, R. L. *Acc. Chem. Res.* **1992**, *25*, 119.

[36] (a) Howard, J. B.; McKinnon, J. T.; Makarovsky, Y.; Lafleur, A. L.; Johnson, M. E. *Nature*, **1993**, *366*, 729. (b) Howard, J. B.; Lafleur, A. L.; Makarovsky, Y.; Mitra, S.; Poe, C. J.; Yadav, T. K. *Carbon* **1992**, *30*, 1183. (c) Taylor, R.; Langley, G. J.; Kroto, H. W.; Walton, D. M. *Nature* **1993**, *366*, 729. (d) Taylor, R.; Langley, G. J. *Proc. Electrochem. Soc.* **1994**, *94*, 68.

[37] Scott, L. T.; Boorum, M. M.; McMahon, B. J.; Hagen, S.; Mack, J.; Blank, J.; Wegner, H., de Meijere A. Science, 2002, 295, 1500.

[38] Haddon, R. C.; Raghavachari, K. *Electronic structure of the Fullerenes: Carbon Allotropes of Intermediate Hybridazation in Buckminsterfullerenes* VCH Publishers, New York, **1993**.

[39] (a) Haddon, R. C.; Brus, L. E.; Raghavachari, K. *Chem. Phys. Lett.* **1986**, *125*, 459. (b) Dias, J. R. *J. Chem. Ed.* **1989**, *66*, 1012. (c) Byers Brown, W. *Chem. Phys. Lett.* **1987**, *136*, 128. (d) Fowler, P. W.; Woolrich, J. *Chem. Phys. Lett.* **1986**, *127*, 78. (e) Braga, M.; Rosén, A.; Larsson, S. *Z. Phys. D* **1991**, *19*, 435.

[41] Fowler, P. W.; Lazzeretti, P.; Zanasi, R. *Chem. Phys. Lett.* **1990**, *165*, 79.
[42] Rosén, A.; Wästberg, B. *Surf. Sci.* **1992**, *269*, 1121.
[43] Saito, S.; Sawada, S.; Hamada, N.; Oshiyama, A. *Mater. Sci. Eng. B- Solid State M* **1993**, *19*, 105.
[44] Kortan, A. R.; Kopylov, N.; Glarum, S. H.; Gyorgy, E. M.; Ramírez, A. P.; Fleming, R. M.; Thiel, F. A.; Haddon, R. C. *Nature* **1992**, *355*, 529.
[45] Hedberg, K.; Hedberg, L.; Bethune, D. S.; Brown, C. A.; Dorn, H. C.; Johnson, R. D.; de Vries, M. *Nature*, **1991**, *254*, 410.
[46] (a) Andreoi, W.; Gygi, F.; Parinelo, M. *Phys. Rev. Lett.* **1992**, *68*, 823. (b) Kohanoff, J.; Andreoni, W.; Parinello, M. *Chem. Phys. Lett.* **1992**, *198*, 472.
[47] (a) Minkin, V. I. ; Glukhoutsev, M. N.; Simkin, B. Y. *Aromaticity and antiaromaticity. Electronic and Structural Aspects* John Wiley & Sons inc, London. (b) Krygowsky, T. M.; Cyranski, K. *Chem. Rev.* **2001**, *101*, 1385.
[48] Aihara, J.; Hosoya, H. *Bull. Chem. Soc. Jpn.* **1988**, *61*, 2657.
[49] (a) A. Hirsch, Z. Chen, H. Jiao, *Angew. Chem.* **2000**, *39*, 112. (b) *Angew. Chem. Int. Ed. Engl.* **2000**, *39*, 3915. (c) Z. Chen, H. Jiao, A. Hirsch, W. Thiel, *Chem. Phys. Lett.* **2000**, *329*, 47. (d) M. Bühl, A. Hirsch, *Chem. Reviews* **2001**, *101*, 1153. (e) Z. Chen, H. Jiao, A. Hirsch, W. Thiel, *J. Org. Chem.* 2001, *66*, 3380. (f) Z. Chen, J. Cioslowski, N. Rao, D. Moncrieff, M. Bühl, A. Hirsch, W. Thiel, *Theor. Chim. Acta* 2001, *106*, 106. (g) Z. Chen, H. Jiao, A. Hirsch, T. Thiel, *J. Mol. Model.* **2001**, *7*, 161.
[50] (a) George, P.; Trachtman, M.; Bock, C. W.; Brett, A. M. *J. Chem. Soc., Perkin Trans. II* **1997**, 1036. (b) Glukhovtsev, M. N.; Schleyer, P. *Chem. Phys. Lett.* **1992**, *198*, 547. (c) Suresh, C. H.; Koga, N. *J. Org. Chem.* **2002**, *67*, 1965.
[51] (a) Poater, J.; Fradera, X.; Duran, M.; Solà, M. *Chem., Eur. J.* **2003**, *9*, 400. (b) Poater, J.; Fradera, X.; Duran, M.; Solà, M. *Chem., Eur. J.* **2003**, *9*, 1113.
[52] Subramanian, G.; Schleyer, P. v. R.; Jiao, H. *Angew. Chem., Int. Ed. Engl.* **1996**, *35*, 2638.
[53] (a) Kruszewski, J.; Krygowski, T. M. *Tetrahedron Lett.* **1972**, *3839*. (b) Krygowski, T. M. *J. Chem. Inf. Comp. Sci.* **1993**, *33*, 70.
[54] Boltalina, O. V.; Dashkova, E. V.; Sidorov, L. N. *Chem. Phys. Lett.* **1996**, *256*, 253.
[55] Elser, V.; Haddon, R. C. *Nature* **1987**, *325*, 792.
[56] (a) Solà, M.; Mestres, J.; Duran, M. *J. Phys. Chem.* **1995**, *99*, 10758. (b) Haddon, R. C. *Acc. Chem. Res.* **1988**, *21*, 243. (c) Haddon, R. C. *Science* **1993**, *261*, 1545.
[58] Darwish, A. D.; Kroto, H. W.; Taylor, R.; Walton, D. R. M. *J. Chem. Soc., Chem. Commun.* **1994**, 15.

[59] (a) Hirsch, A. *Principles of Fullerene Reactivity.* Topics in Current Chemistry, **1999**, 199, pag 1-65. (b) Hirsch, A. *J. Phys. Chem. Solids* **1997**, *58*, 1729. (c) Hirsch, A. *Synthesis*, **1995**, 895.

[60] Cases, M.; Duran, M.; Mestres, J.; Martín, N.; Solà, M. *Fullerenes for the New Millennium*, Kadish, K. M.; Kamat, P. V., Guldi, D. Eds., Pennington: Electrochemical Society Inc., Washington DC, Vol 11, **2001**, 244.

[61] Stephens, A. H. H.; Green, M. L. H. *Adv. Inorg. Chem.* **1997**, *44*, 1.

[62] Bowser, J. R. *Adv. Organomet. Chem.* **1994**, *36*, 57.

[63] Hammond, G. S.; Kuck, V. J. *ACS Symposium Series 481*, Am. Chem. Soc., Washington, DC, **1992**.

[64] Heath, J. R.; O'Brien, S. C.; Zhang, Q.; Liu, Y.; Curl, R. F.; Kroto, H. W.; Tittel, F. K.; Smalley, R. E. *J. Am. Chem. Soc.* **1985**, *107*, 7779.

[65] Cioslowski, J. Raghavarachi, K. *J. Chem. Phys.* **1993**, *98*, 8734.

[66] Guo, T.; Smalley, R. E.; Scuseria, G. E. *J. Chem. Phys.* **1993**, *99*, 352.

[67] Cioslowski, J.; Fleischmann, E. D. *J. Chem. Phys.* **1991**, *94*, 3730.

[68] Cioslowski, J. *Ab Initio Electronic Strucuture Calculations on Endohedral Complexes of the C_{60} Cluster, in Spectroscopic and Computational Studies of Supramamolecular Systems* (J. E.D. Davies, ed.) Luwer Academic Publishers, Dordrecht, **1992**, chap. 10, p.269.

[69] Broclawik, E.; Eilmes, A. *J. Chem. Phys.* **1998**, *108*, 3498.

[70] Suzuki, S.; Kawata, S.; Shiromaru, H.; Yamauchi, K.; Kikuchi, K.; Kato, T.; Achiba,Y. *J. Chem. Phys.* **1992**, *96*, 7159.

[71] Cioslowski, J. *J. Am. Chem. Soc.* **1991**, *113*, 4139.

[72] Nagase, S.; Kobayashi, K. *J. Chem. Soc., Chem. Commun.* **1994**, 1837.

[73] Moro, L.; Ruoff, R. S.; Becker, C. H.; Lorents, D. C.; Malhotra, R. *J. Phys. Chem.* **1993**, *97*, 6801.

[74] Olmstead, M. M.; Bettencourt-Dias, A.; Duchamp, J. C.; Stevenson, S. Marciu, D.; Dorn, A. C.; Balch, A. L. *Angew. Chem., Int. Ed. Engl.* **2001**, *40*, 1223.

[75] Stevenson, S.; Rice, G.; Glass, T.; Harich, K.; Cromer, F.; Jordan, M. R.; Craft, J.; Hadju, E.; Bible, R.; Olmstead, M. M.; Maltra, K.; Fisher, A. J.; Balch, A. L.; Dorn, H. C. *Nature*, **1999**, 401, 55.

[76] (a) Pradeep, T.; Vijayakrishnan, V.; Santra, A. K.; Rao, C. N. R. *J. Phys. Chem.* **1991**, *95*, 10564. (b) Yu, R. et al. *J. Phys. Chem.* **1995**, *99*, 1818. (c) Mattay, J. et al. *J. Phys. Chem.* **1995**, *51*, 6997.

[77] (a) Guo, T.; Jin, C.; Smalley, R. E. *J. Phys. Chem.* **1991**, *95*, 4948. (b) Chai et al. J. *Phys. Chem.* **1991**, *85*, 7564. (b) Cao, B.; Zhou, X.; Shi, Z.; Gu, Z.; Xiao, H.; Wang, J. *Fullerene Sci. & Technol.* **1998**, *6*, 639.

[78] Hummelen, J. C.; Knight, B.; Pavlovich, J.; Gonzalez, R.; Wudl, F. Science, **1995**, *269*, 1554.

[79] Nuber, B.; Hirsch, A. *Chem. Commun.* **1996**, 1421.
[80] Keshavaraz-K, M. et al. *Nature*, **1996**, *383*, 147.
[81] (a) Branz, W.; Billas, I. M. L.; Malinowski, N.; Tast, F.; Heinebrodt, M.; Martin, T. P. *J. Chem. Phys*. **1998**, *109*, 3425. (b) Billas, I. M. L.; Branz, W.; Malinowski, N.; Tast, F.; Heinebrodt, M.; Martin, T. P.; Massobrio, C.; Boero, M.; Parrinello, M. *NanoStruct. Mat.* **1999**, *12*, 1071. (c) Poblet, J. M.; Muñoz, J.; Winkler, K.; Cancilla, M.; Hayashi, A.; Lebrilla, C. B.; Balch, A. L. *Chem. Comm.* **1999**, 493. (d) Balch, A. L.; Costa, D. A.; Winkler, K. *J. Am. Chem. Soc.* **1998**, *120*, 9614. (d) Hayashi, A.; de Bettencourt-Dias, A; Winkler, K.; Balch, A. L. *J. Mater. Chem.* **2002**, *12*, 2116.
[82] Hawkins, J. M.; Meyer, A.; Lewis, T. A.; Loren, S.; Hollander, F. J. *Science* **1991**, *252*, 312.
[83] Fagan, P. J.; Krusic, P. J.; Evans, D. H.; Lerke, S. A.; Johnston, E. *J. Am. Chem. Soc.* **1992**, *114*, 9697.
[84] Westmeyer, M. D.; Galloway, C. P.; Rauchfuss, T. B. *Inorg. Chem.* **1994**, *33*, 4615.
[85] Zhang, S.; Brown, T. L.; Du, Y.; Shapley, J. R. *J. Am. Chem. Soc.* **1993**, *115*, 6705.
[86] Fagan, P. J.; Calabrese, J. C.; Malone, B. *Science* **1991**, *252*, 2252.

CAPÍTOL 2

QUÍMICA COMPUTACIONAL PER FUL·LERENS

En aquest segon capítol presentem de forma molt genèrica una perspectiva de la química computacional i els seus aspectes teòrics basats en la química quàntica. Cal tenir en compte que farem èmfasi en aquelles teories més involucrades en la química de ful·lerens. Aclarim també que la formulació matemàtica usada no pretén la completesa ni el rigor més estricte. Per aquest altre objectiu hi ha disponible una nombrosa bibliografia. Així només discutim els aspectes més rellevants de cada una de les teories necessaris per l'entesa dels resultats dels capítols centrals de resultats (capítols 4-7). Després de presentar la química computacional i teòrica a la introducció (apartat 2.1), en el següent apartat (2.2) ens centrem en els principals mètodes semiempírics de baix cost computacional que han estat usats àmpliament en els inicis de la química de ful·lerens. En l'apartat 2.3 descrivim de forma molt elemental la formulació i els principis de la coneguda i bàsica aproximació Hartree-Fock (HF). Ja en l'apartat 2.4 repassem els trets més importants de l'altre teoria ab initio: la teoria del funcional de la densitat (DFT). En l'apartat 2.5 descrivim els detalls computacionals dels càlculs presentats a la tesi. Ens centrem en la descripció dels funcionals i les funcions de bases. Finalment en l'apartat 2.6 presentem un compendi de les eines teòriques i computacionals més emprades en el treball d'investigació per a l'anàlisi i interpretació de les dades obtingudes.

2.1 INTRODUCCIÓ

La química computacional és una branca de la ciència computacional. En general, la ciència computacional usa tota la informació coneguda sobre un problema i la incorpora en un model matemàtic basat en alguna teoria. La ciència computacional investiga metodologies sobre la millor resolució del model matemàtic plantejat per la teoria. El model matemàtic donarà informació extra la qual ajudarà a entendre el problema, a fer hipòtesis i a fer prediccions. Avui dia, la ciència computacional està àmpliament estesa en camps com: la química, la física, l'enginyeria i la meteorologia. En concret, la química computacional és capaç de generar informació valuosíssima com ara: estructures geomètriques i propietats moleculars tant físiques com químiques.

La química computacional ha usat diverses teories, cadascuna d'elles amb un grau variat de sofisticació, en la recerca de l'estructura electrònica dels ful·lerens i els seus derivats. Alguns d'aquests mètodes necessiten càlculs complexos i feixucs que només poden ser portats a terme per programes comercials com ara el GAUSSIAN[1], el TURBOMOLE[2], l'ADF[3,4] i l'AIMPRO[5]. Altres però, com per exemple els semiempírics, no requereixen ni tant sols d'una calculadora. Des del punt de vista de l'investigador el compromís entre el cost computacional i la precisió de les dades obtingudes és la consideració més important per determinar quin mètode/teoria hauria de ser usada. Per aquesta raó, és molt important conèixer les limitacions de cada aproximació teòrica abans de llençar-se a calcular amb certa confiança.

En la química computacional tenim involucrades tres tipus de metodologies amb característiques força específiques. (1) Els mètodes *ab initio*, definits com a un conjunt de mètodes en el qual l'estructura molecular pot ser calculada usant no res més que la famosa equació Schrödinger, les constants fonamentals i les dades dels àtoms. (2) Els mètodes semiempírics usen, en canvi, aproximacions al model matemàtic plantejat anteriorment a partir de dades experimentals. (3) Finalment el tercer grup són els englobats dins la mecànica molecular, la qual usa la física clàssica per explicar i interpretar el comportament dels àtoms i les molècules en contraposició als mètodes *ab initio* i els semiempírics que són basats en la teoria de la mecànica quàntica.

En aquesta introducció seran abordats només els mètodes basats en la mecànica quàntica per ser els relacionats amb la metodologia emprada en el present treball d'investigació. Cal dir, però, que els mètodes basats en la mecànica molecular han estat utilitzats satisfactòriament sobretot en els primers anys de la descoberta dels ful·lerens perquè permetien abordar problemes que per la mecànica quàntica eren impensables en aquell temps. Cal citar per exemple els mètodes QCFF[6], MMP2[7] i MM3[8].

La mecànica quàntica es basa en trobar ja sigui *ab initio* o bé semiempíricament les solucions a l'equació de valors i vectors propis d'Schrödinger (equació 2.1), que per un sistema compost per N electrons i M nuclis pren la forma:

(2.1) $$H\Psi = E\Psi$$

(2.2) $$H = -\frac{1}{2}\sum_{I=1}^{M} m_I^{-1}\nabla_I^2 - \frac{1}{2}\sum_{i=1}^{N}\nabla_i^2 + \frac{1}{2}\sum_{I\neq J=1}^{M} Z_I Z_J \left|R_I - R_J\right|^{-1} - \sum_{I=1}^{M}\sum_{i=1}^{N} Z_I \left|R_I - r_i\right|^{-1} + \frac{1}{2}\sum_{i\neq j=1}^{N} \left|r_i - r_j\right|^{-1}$$

on H és l'operador hamiltonià independent del temps, Ψ la funció d'ona del sistema, E l'energia del sistema i els cinc termes de l'equació 2.2 descriuen, respectivament, l'energia cinètica dels nuclis, l'energia cinètica dels electrons, la repulsió entre els nuclis, l'atracció entre els electrons i els nuclis i finalment la repulsió electró-electró. L'equació 2.2 està escrita en unitats atòmiques. m_I, Z_I i R_I són, respectivament, la massa, el número atòmic i la posició instantània del nucli I; mentres r_i denota la posició instantània de l'electro i. Tot i que la solució de l'equació 2.1 només és possible per sistemes monoelectrònics com l'hidrogen, la comunitat científica no ha esmerçat esforços per trobar solucions també pels sistemes polielectrònics (encara que aproximades). El primer pas de totes les teories és l'aproximació de Born-Oppenheimer de separació del moviment nuclear i electrònic que aporta una simplificació més que acceptable.[9] Aquesta primera aproximació permet només centrar-nos en la resolució d'un problema únicament electrònic: $H_e\Psi_e = E_e\Psi_e$, on H_e és l'hamiltonià electrònic per una disposició determinada dels nuclis, Ψ_e és la funció d'ona únicament electrònica i E_e l'energia únicament electrònica.

Els mètodes *ab initio* han necessitat per una banda la incorporació de noves metodologies i per altra la millora de la capacitat de càlcul de les màquines per lliurar millors solucions per molècules cada com més grans. Per altra banda els mètodes semiempírics no han abordat directament les costoses integrals que es desprenen de la resolució de l'equació 2.1 ja que aquestes han estat negligides o bé substituïdes per dades experimentals permetent càlculs a menor cost computacional i de major envergadura.

Trobem magnífics textos introductoris a la química computacional i les seves bases mecanoquàntiques en els compendis de *Química teórica y computacional* dels cursos de doctorat espanyol de la matèria,[10] de l'*European Summerschool in Quantum Chemistry*[11] i els llibre d'en Levine[12] i en Szabo.[13]

2.2 MÈTODES SEMIEMPÍRICS

La mecànica quàntica semiempírica permet en un principi l'avaluació de les mateixes propietats que els mètodes *ab initio*: estructures, energies, estats electrònics, distribucions de càrrega, distribucions d'spín, etc. Un d'aquest primers mètodes fou el formalisme dels orbitals moleculars de Hückel (*Hückel molecular orbitals*, HMO)[14] en el qual només els electrons π dels carbonis insaturats són tinguts en compte. Evidentment, estem parlant d'un model altament simplificat on l'estructura d'enllaços σ ja és coneguda. Aquest mètode permeté els primers passos en l'entesa de l'estructura electrònica dels ful·lerens tal i com hem vist en el capítol anterior. L'operador Hamiltonià, en aquest cas, és compost de la matriu de Hückel donada per:

$$H = \beta A + \alpha 1 \tag{2.3}$$

on α i β són paràmetres empírics que corresponen a les integrals de coulomb i de ressonància, respectivament, però que mai són avaluades. *A* és la matriu de connectivitats que val 0 excepte per dos àtoms units a través d'un enllaç que val 1. L'energia electrònica total π i els ordres d'enllaç π són fàcilment calculats a partir de tots els orbitals ocupats. Tot i la cruesa d'aquesta primera teoria, ja permeté avaluar l'aromaticitat dels ful·lerens mitjançant mesures de l'energia de ressonància de Dewar (*Dewar ressonance energy*,

DRE)[15] o l'energia de ressonància topològica (*topological ressonance energy*, TRE)[16]. Una millora significativa del mètode HMO fou la introducció de la dependència de les integrals de ressonància β respecte a les distàncies d'enllaç i la corbatura dels ful·lerens. En aquest nou mètode, anomenat variable β-HMO,[17] els elements fora de la diagonal de la matriu de Hückel són donats per:

(2.4) $$H_{IJ} = \beta_{IJ} A_{IJ}$$

on el paràmetre β_{IJ} recull aquesta dependència. Finalment la millora i generalització final s'aconsegueix per la teoria de Hückel estesa (*extended Hückel theory*, EHT)[18] en la qual la matriu hamiltoniana utilitza la informació de tots els electrons de valència.

L'AM1,[19] MNDO[20] i PM3[21] són altres mètodes semiempírics que són capaços de reproduir una àmplia varietat de propietats moleculars electròniques i geomètriques per un gran nombre de derivats ful·lerènics. Les dades provinents dels mètodes semiempírics donen una bona entesa amb les dades experimentals en la majoria de casos. Però clar, aquests mètodes necessiten informació prèvia contrastada i adaptada a les molècules en estudi abans d'iniciar qualsevol càlcul.

2.3 APROXIMACIÓ HARTREE-FOCK (HF)

La teoria Hartree-Fock (HF) i també la teoria del camp autoconsistent (*self-consistent field*, SCF) són fonamentals per entendre tota la teoria de l'estructura electrònica de les molècules. El HF es basa en la teoria dels orbitals moleculars la qual postula que el moviment de cada electró pot ser descrit per una simple funció (orbital) d'una partícula que no depèn explícitament dels moviments instantanis dels altres electrons. Aquests orbitals només tenen significat matemàtic i, per tant, són només una aproximació a la realitat (excepte per sistemes monoelectrònics). Així, l'aproximació HF sovint proporciona un bon punt d'inici per mètodes teòrics més elaborats com la interacció de configuracions o la teoria del funcional de la densitat (DFT).

El punt de partença és escriure la funció d'ona com a producte de funcions d'ona monoelectròniques *spin-orbital*, χ_i:

(2.5) $$\Psi_e (1, ...,N) = \chi_{1,\alpha}(1)\, \chi_{1,\beta}(2)... \chi_{N,\beta}(N)$$

Aquesta és la funció d'ona electrònica d'una molècula de capa tancada d'N electrons en la qual l'electró 1 ocupa l'orbital molecular χ_1 amb *spin* α, l'electró 2 ocupa l'orbital molecular χ_1 amb *spin* β, i així endavant. Tanmateix, la funció d'ona ha de complir el principi d'antisimetria de Pauli i, en conseqüència, ha de canviar el signe en la permuta de qualsevol parell d'electrons. Per assolir-ho la funció d'ona s'escriu en forma d'un determinant, el determinat d'Slater, que conté la suma de totes les possibles permutacions:

(2.6) $$\Psi_e = | \chi_1\chi_{2...}\, \chi_N\rangle$$

D'acord amb el principi variacional els millors *spin-orbitals* són aquells que minimitzen l'energia electrònica:

(2.7) $$E_e = \langle\Psi_e | H_e | \Psi_e\rangle \geq E_o$$

Podem variar sistemàticament els *spin-orbitals* χ_i fins que l'energia E_e arribi al mínim, E_o. L'equació pel millor *spin-orbital* s'obté de l'equació Hartree-Fock:

(2.8) $$f_i\chi_i = \varepsilon_i\chi_i$$

on f_i és l'hamiltonià monoelectrònic, o també dit operador de Fock, que inclou l'energia cinètica electrònica, l'energia potencial d'un electró atret pels nuclis i la repulsió d'aquest electró i amb cadascun de la resta d'electrons. L'operador de Fock es desglossa de la següent manera:

(2.9) $$f_i = h_i + \sum_b 2J_{b,i} - K_{b,i}$$

h, J_b i K_b són els hamiltonians de *core*, de Coulomb i d'intercanvi, respectivament. La segona part de (2.9) és el terme d'interacció electrònica de l'operador de Fock i sense ell seria simplement el sumatori d'equacions

monoelectroníques d'Schrödinger. J_b té una fàcil interpretació relacionada amb la repulsió coulòmbica que sent l'electró *i* en la presència de la resta d'electrons, mentre el terme d'intercanvi, K_b, és un terme atractiu de no fàcil interpretació física degut a la seva relació amb la natura antisimètrica de la funció d'ona determinantal. Aquests dos termes són els que aporten més complicació en la resolució de l'equació d'Schrödinger polielectrònica i seran sempre el cavall de batalla en totes les metodologies. Els mètodes semiempírics o bé els negligeixen o bé usen paràmetres enlloc seu. Així, aquestes dues expressions (J_b i K_b) han estat cabdals en l'evolució de la química computacional.

El mètode HF comença amb un conjunt aproximat d'orbitals per tots els electrons del sistema. S'escull un electró i es calcula el potencial en el que mou simplement congelant la distribució de la resta d'N-1 electrons. Usant aquest potencial vingut de la distribució mitjana es resol l'equació d'Schrödinger la qual donarà un nou orbital. Aquest procediment es repeteix per tota la resta d'electrons del sistema usant els electrons en els orbitals congelats com a originadors del potencial. Al final d'un cicle, hi ha un nou conjunt d'orbitals. El procés es repeteix fins que dos conjunts consecutius no presentin variació, que serà quan l'energia del sistema també sigui mínima. Per això, l'aproximació HF es coneix també com a mètode del camp autoconsistent (SCF).

Roothaan introduí l'ús d'un conjunt complet de funcions de base per descriure els orbitals i poder resoldre les complicades equacions diferencials que apareixien en l'aproximació HF. Així, a partir de llavors els orbitals de Hartree-Fock (χ_i) eren construïts a partir de combinacions lineals d'aquestes funcions de base. N'hi ha de diversos tipus. Un conjunt complet de funcions de base són les tipus Slater (*Slater type orbital,* STOs) definides com: $\chi^{\mathrm{STO}} = Nx^l y^m z^n e^{-\zeta r}$ mentre que l'altre tipus són les tipus Gaussian (*Gaussian type orbital*, GTOs): $\chi^{\mathrm{GTO}} = Nx^l y^m z^n e^{-\zeta r^2}$. *x*, *y* i *z* descriuen la part angular de l'orbital i el factor ζ afecta la funció radial i fixa com de comprimit és l'orbital. Com es pot veure l'única diferència entre ambdós tipus és en la dependència respecte d'*r* del terme exponencial. Això té grans implicacions metodològiques. Mentre les GTOs possibiliten un càlcul eficient de les integrals moleculars multicèntriques mitjançant procediments analítics, les STOs només ho permeten per procediments numèrics. No obstant, aquest avantatge és contrarrestat pel fet que són necessàries tres GTOs per

aconseguir la mateixa precisió que una STO. Això és degut a que les STOs reprodueixen més fidelment el comportament electrònic al voltant del nucli. Les funcions de base són també classificades segons la seva qualitat. Això depèn del nombre de funcions que descriuen cada orbital atòmic. En general quantes més funcions són afegides per descriure les particularitats de cada orbital més bones són les bases i més costós també és el càlcul.

2.4 TEORIA DEL FUNCIONAL DE LA DENSITAT (DFT)

La teoria del funcional de la densitat (DFT) es diferencia molt bé dels mètodes clàssics, com ara el mètode Hartree-Fock, per un enfoc diferent a l'hora de resoldre l'equació d'Schrödinger i també des d'un punt de vista tècnic per un menor cost computacional. La DFT es basa en el fet que l'estat fonamental d'una molècula es determina únicament per la corresponent densitat electrònica.

Hohenberg i Kohn estabiren les bases de la teoria DFT[22] els anys 60. Formularen que l'hamiltonià electrònic per *N* electrons i *M* nuclis era:

(2.10) $$H = T + V + W$$

on *T* és l'energia cinètica electrònica, *W* l'energia d'interacció electró-electró i *V* és el potencial d'interacció nucli-electró definit per l'equació 2.11:

(2.11) $$V=\sum_{i=1}^{N} v(r_i) \text{ on } v(r_i)=-\sum_{I=1}^{M} Z_I r_{iI}^{-1}$$

on $v(r_i)$ és el potencial sobre l'electró *i* degut a tots els nuclis *I* de càrrega Z_I. *V* és funció de tots els electrons i per tant pot expressar-se en funció de la densitat electrònica, ρ:

(2.12) $$V[\rho] = \int \rho(r) v(r) \mathrm{d}r$$

El primer teorema de Hohenberg i Kohn estableix que l'energia del estat fonamental no degenerat d'un sistema d'*N* electrons es troba totalment

determinat per la seva densitat electrònica. Així, establim una relació directe entre la densitat electrònica i l'energia, i en conseqüència, amb les propietats del sistema. No tant sols això, a més a més, el valor propi de cada operador de l'equació (2.10) serà també un funcional únic de la densitat. Així intentarem escriure T i W també en funció de la densitat. Així doncs arribem a la separació final que es fa en la DFT:

(2.13) $$E[\rho] = T[\rho] + V[\rho] + W[\rho]$$

El segon teorema de Hohenberg i Kohn estableix que l'energia del sistema ($E[\rho]$) adquireix un valor mínim (E_o) per la densitat exacte del sistema (ρ_o). Així doncs, en la DFT també es compleix, a igual que en els mètodes formulats a partir de la funció d'ona, el principi variacional.

(2.14) $$E_o[\rho_o] \leq E[\rho]$$

D'aquí arribem a l'equació fonamental d'aquesta teoria:

(2.15) $$\mu = \frac{\delta E[\rho]}{\delta \rho}$$

on μ representa la minimització de l'energia $E[\rho]$ respecte la densitat electrònica, ρ.

De l'equació (2.13) només $V[\rho]$ té funcional conegut. Tant el terme $T[\rho]$ com el $W[\rho]$ han de ser desgranats per tal de trobar formes conegudes als seus funcionals. Tenint en compte que l'energia d'interacció electró-electró, $W[\rho]$, es pot dividir en l'energia de repulsió clàssica de Coulomb, $W_{CLA}[\rho]$, que ve donada per l'expressió:

(2.16) $$W_{CLA}[\rho] = \frac{1}{2}\int\int \frac{\rho(r_1)\rho(r_2)}{|r_1 - r_2|} dr_1 dr_2$$

i una part que conté totes les parts no clàssiques de l'interacció, W_{NCLA}, tenim que:

(2.17) $$E[\rho] = T[\rho] + V[\rho] + W_{CLA}[\rho] + W_{NCLA}[\rho]$$

El funcional $W_{NCLA}[\rho]$ tampoc és conegut.

L'altre problema és la desconeixença del funcional de l'energia cinètica, T [ρ]. Aquest es resolgué separant-lo en dues parts: una part cinètica deguda a un sistema de referència amb electrons no interaccionants T_S [ρ] i una part de correlació, T_C [ρ]. Així doncs, T [ρ] = T_S [ρ] + T_C [ρ]. On T_S [ρ] té fàcil solució mentre T_C [ρ] resta desconegut. La nova separació de l'energia és:

(2.18) $$E[\rho] = T_S[\rho] + T_C[\rho] + V[\rho] + W_{CLA}[\rho] + W_{NCLA}[\rho]$$

On tots els termes són coneguts excepte T_C [ρ] i W_{NCLA} [ρ], que de fet, inclouen tota la correlació i l'intercanvi electrònic. La suma dels dos termes desconeguts s'anomena W_{XC} [ρ], (W_{XC} [ρ]= T_C [ρ] + W_{NCLA} [ρ]). El terme W_{XC} [ρ], com en el mètode HF, serà el més costós de calcular i cavall de batalla de tota la metodologia DFT.

Inicialment els mètodes buscaven fórmules explícites pels funcionals, però Kohn i Sham[23] proposaren un mètode autoconsistent d'orbitals monoelectrònics molt semblant al SCF del HF. Aquest considera un sistema de referència de N electrons sense interaccionar.

(2.19) $$f_S^{KS} = -\frac{1}{2}\sum_{i=1}^{N}\nabla_i^2 + \nu_S(r_i)$$

on f_S^{KS} és l'operador de Kohn-Sham i el potencial $\nu_S(r_i)$ s'agafa com el potencial efectiu de Kohn-Sham $\nu_{eff}(r_i)$ que fa possible que el sistema de referència de partícules independents doni una densitat electrònica idèntica a la del sistema real. Així podem reproduir la densitat electrònica exacte resolent el sistema de N equacions monoelectròniques. Finalment arribem a les equacions de Kohn-Sham, totalment anàlogues a les equacions de Fock en el HF:

(2.20) $$f_S^{KS}\varphi_j = \varepsilon_j\varphi_j$$

on φ_j són els orbitals de Kohn-Sham normalitzats que s'expressen com una combinació lineal de les funcions monoatòmiques, χ_u, equació 2.21a. Aquests orbitals φ_j estan profundament relacionats amb la densitat electrònica a través de l'equació 2.21b.

(2.21a) $$\varphi_j = \sum_u c_{uj}\chi_u \quad ; \quad (2.21b) \qquad \rho(r)=\sum_j \left|\varphi_j(r)\right|^2$$

Arribats en aquest punt, el mètode seria exacte si coneguéssim el funcional de correlació i intercanvi, W_{XC}. Lamentablement no el coneixem i estem obligats a realitzar aproximacions. N'existeixen dues:

Aproximació de la densitat local (local density approximation, LDA).[24] Aquí suposem que tenim un gas uniforme d'electrons. Això fa que puguem dividir l'energia de correlació i d'intercanvi en dos termes separats. L'energia d'intercanvi W_X s'escriu en funció de la densitat mitjançant el mètode X_α i l'energia de correlació, W_C, es calcula segons la parametrització de Vosko-Wilk-Nusair (VWN)[25] (equació 2.22). S'observa, no obstant, que aquesta aproximació té certa tendència a sobreestimar les energies d'enllaç.

(2.22) $W_{XC} = W_C + W_X$ on W_C (mètode X_α) i W_X (parametrització VWN)

Aproximació de gradients generalitzats (generalised gradients approximation, GGA). Aquí considerem les fluctuacions locals de la densitat. Així W_{XC} és funció de la ρ i del gradient de la densitat. Normalment aquests mètodes parteixen del funcional d'intercanvi i correlació del LDA, al qual se li afegeixen termes de correcció de gradient GGA. Un exemple d'aquest funcional és el de Becke[26] que inclou la correcció en l'energia d'intercanvi, W_X, mentre el funcional de Perdew[27] corregeix l'energia de correlació, W_C.

Dins la DFT també hi ha un tercer tipus de funcionals anomenats híbrids que incorporen correccions a la correlació i a l'intercanvi. Per exemple el de Lee-Yang-Parr (LYP)[28] per la correlació, que combinat amb el mètode dels tres paràmetres d'en Becke[29] porta al popular funcional

d'intercanvi-correlació, B3LYP. Aquestos s'introduïren amb l'objectiu d'incloure l'energia d'intercanvi exacte vinguda del mètode HF.

El gran coll d'ampolla del HF és la introducció de la correlació electrònica de forma assequible. La DFT representa una alternativa a la introducció dels efectes de la correlació electrònica en la resolució de l'equació d'Schrödinger electrònica. Així doncs, no és d'estranyar que en els últims anys l'aplicació dels mètodes basats en la DFT s'hagin popularitzat moltíssim entre els químics computacionals. Aquests permeten l'estudi de sistemes de talla mitjana i gran a un cost computacional acceptable, que d'altre manera serien inabordables. A més a més, s'ha comprovat que la precisió en la predicció de geometries és bona i comparable als mètodes post HF molt més costosos. En resum, pels grans sistemes ful·lerènics que inclouen metalls, la DFT representa una metodologia adequada i òptima per assolir bona precisió en els càlculs i a la vegada que amb un cost computacional més que acceptable.

2.5 DETALLS COMPUTACIONALS

2.5.1 Funcionals de la densitat

Per tal d'assolir una consistència general en tot el treball s'ha mantingut no tant sols la mateixa metodologia sinó també la mateixa precisió computacional i així fer comparables els resultats. En alguns casos però s'han hagut d'introduir petits canvis en la metodologia forçats per la necessària millora dels resultats.

Els càlculs DFT presentats han sigut portats a terme amb el paquet de programes ADF (*Amsterdam density function*, versions 2000 i 2004). Entre la varietat de funcionals, s'ha escollit per la seva provada reputació l'aproximació de la densitat local LDA amb correccions GGA. L'energia d'intercanvi es calcula mitjançant l'aproximació a un gas uniforme d'electrons (mètode X_α=3/4)[30] i l'energia de correlació ve donada per la parametrització d'en Vosko-Wilk-Nusair (VWN). També hem inclòs correccions de gradient (GGA) als funcionals d'intercanvi i de correlació: el funcional Becke pel primer cas i el funcional Perdew pel segon.

Taula 2.1 Versió de l'ADF emprada i formalisme aplicat en les correccions relativistes en cadascun dels capítols

Capítol	Versió ADF	Formalisme de les correccions relativistes
4 [a]	2000.02	*Pauli*
5	2000.02	*ZORA*
6	2004.01	*ZORA*

[a] Llevat de l'apartat 4.7 que s'ha usat ADF2004.01

Degut a l'ús de metalls de transició com ara Sc, La, Y, Pt, Ir i Os s'han tingut en compte els efectes relativistes en els nostres càlculs. L'ADF dóna la possibilitat d'usar dos formalismes alhora d'incloure correccions relativistes: el *Pauli*[31] i el *ZORA*[32]. El formalisme *Pauli* representa un primer pas per la inclusió dels efectes relativistes, de fet, s'anomena com a quasirelativista. En canvi, el formalisme *ZORA* es basa en correccions de primer ordre sobre l'hamiltonià, el qual es resol de forma relativista amb la necessitat d'unes funcions de base específiques per aquesta metodologia. El formalisme ZORA es especialment útil en el cas d'àtoms pesats.

El capítol 4 està basat en càlculs DFT de l'ADF2000.02 excepte l'apartat 4.7 que es realitzà en ADF2004.01. Usem correccions relativistes *Pauli*. El capítol 5 es continua usant l'ADF2000.02 però ara millorem les correccions relativistes usant el formalisme ZORA per una bona descripció dels àtoms pesats com ara el platí, l'iridi i l'osmi. Els resultats del capítol 6 foren obtinguts ja amb l'última versió de l'ADF, l'ADF2004.01, amb correccions relativistes també ZORA (Taula 2.1).

2.5.2 Funcions de base

Una manera de simplificar els càlculs quan tenim involucrats àtoms pesats és descartar alguns electrons de cada àtom i calcular-los prèviament. Descartem els més interns i inerts, anomenats electrons de *core*. Aquests poden ser considerats congelats ja que són tractats mitjançant potencials de *core* efectius. L'energia d'aquests electrons es calcula com un pas previ del procediment de càlcul. En el procediment de resolució de la densitat electrònica total aquests electrons no participen ni molt menys en l'enllaç en l'extensió en que ho fan els electrons de València. Les correccions relativistes també són aplicades als electrons de *core* a través del potencials de *core* corregits. Aquests potencials són generats pel programa auxiliar

Taula 2.2 Llista completa dels elements que apareixen en els càlculs dels capítols 4-6 amb els seus respectius electrons de *core.* Tots els electrons de València són descrits per conjunts de base STO de qualitat triple-ζ + polarització (TZP) [a]

Element	*Electrons de core*	*Element*	*Electrons de core*
H [b]	--	*Y, Pd*	1s-3spd
C, [b] *N, O, F* [b]	1s	*La*	1s-4spd
P, Sc, Ti, Ni	1s-2sp	*Pt, Ir, Os*	1s-4spdf

[a] Llevat dels casos que s'indica. [b] Doble-ζ + polarització (DZP) en l'apartat 4.8 així com en alguns casos del capítol 6.

DIRAC[3,4] inclòs en el paquet ADF. Tots els electrons inclosos en el *core* són descrits per un simple STO. A la Taula 2.2 tenim llistats els electrons tractats com a capes *core* congelades per tots els àtoms del treball.

L'elecció de les funcions de base utilitzades en aquest treball radica en el bon balanç entre precisió i cost computacional. Ja havíem comentat que n'hi havia de dos tipus: les STO i les GTO. En aquest treball hem usat conjunts de base STO de qualitat triple-ζ + polarització (TZP) per descriure els orbitals de València de tots els àtoms.[33] Aquesta nomenclatura indica que s'usen tres orbitals STO per descriure cada orbital de València. La polarització indica que les nostres funcions de base inclouen STOs per descriure els primers orbitals buits de cada àtom. Només en dos casos hem usat conjunts de base STO de qualitat menor, doble-ζ + polarització (DZP): pel carboni, fluor i hidrogen de l'apartat 4.8 i per alguns càlculs addicionals del capítol 6 que queden indicats clarament en els textos. En les seccions 4.7 i 4.8 s'estudia la reactivitat exterior de les molècules *endoèdriques* $Sc_3N@C_k$ (k = 68, 78, 80). La necessitat d'alleugerir les funcions de base era una obligació ja que en molts casos es sobrepassava el centenar d'àtoms.

2.6 EINES PER A L'ANÀLISI

Presentem tot seguit les eines més emprades per a l'anàlisi i interpretació de les dades computacionals obtingudes. Altres eines són només comentades en el text quan correspongui (per exemple els diagrames d'interacció de fragments).

2.6.1 Descomposició de l'energia d'enllaç (BE)

Al llarg de la tesi s'han realitzat nombrosos anàlisis de la interacció dels metalls amb els lligands per tal de caracteritzar i diferenciar els tipus d'enllaços metall-lligand que tenim present en els *metal·loful·lerens*. En tots els casos s'ha utilitzat el mètode de l'estat de transició estès (*extended transition state*, ETS) desenvolupat per Ziegler i Rauk,[34] que és una continuació de la descomposició de l'energia proposada per en Morokuma.[35] Segons aquest mètode, l'energia d'enllaç (*bonding energy*, BE) entre dos fragments A i B pot ser descomposta en tres contribucions:

(2.23) $$BE = \Delta E_{DE} + \Delta E_{ST} + \Delta E_{ORB}$$

ΔE_{DE} és l'energia de preparació dels fragments o també dita de deformació. Representa l'energia necessària per deformar els fragments des de la seva geometria d'equilibri fins a la geometria que presenten en el compost final i també per promocionar, si cal, els electrons des de la configuració fonamental fins a la configuració electrònica present en el compost final. Així és un terme desestabilitzant. El segon terme, ΔE_{ST}, és el terme estèric i representa la interacció entre els fragments deformats amb les densitats electròniques que cada un dels fragments tindria en absència de l'altre fragment. Aquest terme a la vegada sol ser descompost en dos: l'energia de repulsió de Pauli, ΔE_{Pauli}, i la interacció electrostàtica, ΔE_{elstat}, ($\Delta E_{ST} = \Delta E_{Pauli} + \Delta E_{elstat}$). ΔE_{Pauli} representa la repulsió entre els orbitals ocupats d'ambdós fragments, mentre que ΔE_{elstat} comprèn tota la resta de termes electrostàtics entre fragments: interaccions nucli-nucli, nucli-electró i electró-electró. A la distància normal d'enllaç, ΔE_{elstat} està clarament dominat per les interaccions nucli-electró i així és un terme estabilitzant. L'últim terme és la interacció orbitàl·lica, ΔE_{ORB}, i representa l'estabilització produïda en un sistema quan es permet la relaxació de les densitats electròniques dels fragments. Aquest terme inclou la transferència de càrrega i la polarització que té lloc durant la formació de l'enllaç. ΔE_{ORB} presenta moltes possibilitats d'anàlisi ja que pot ser descomposta segons les espècies irreduïbles de simetria de la molècula. Això, per exemple, ens permet separar entre interaccions σ i π o bé entre orbitals de donació i

retrodonació. Sovint la suma de ΔE_{ST} i ΔE_{ORB} s'anomena ΔE_{INT}, energia d'interacció.

2.6.2 Càrregues atòmiques

Encara que les càrregues atòmiques no són una magnitud observable, els seus valors poden ser de gran utilitat per indicar tendències en les transferències de càrrega entre fragments. No hi ha cap oportunitat experimental per mesurar la càrrega d'un àtom en una molècula. Encara que hi ha una gran quantitat de mètodes per obtenir càrregues atòmiques, l'anàlisi de poblacions de Mulliken[36] és el mètode estàndard usat. La càrrega neta d'un àtom es calcula com:

(2.24) $$q_A = Z_A - \Sigma\,(PS)$$

On Z_A és la càrrega nuclear, P és la matriu densitat electrònica i S és la matriu solapament. Aquesta partició de la càrrega és altament dependent del conjunt de funcions de base escollides entre altres deficiències serioses. Així doncs, el valor absolut de les càrregues atòmiques no té cap sentit i tant sols quan es comparen en les mateixes condicions porten a conclusions fiables. En alguns casos s'han usat per avaluar la transferència entre el fragment metàl·lic i el lligand.

2.6.3 Mapes de deformació de la densitat electrònica (EDDM)

Aquesta eina està força relacionada amb el punt anterior. Es tracta també d'una eina computacional de caràcter qualitatiu que ha estat usada en el capítol 4. Obtenir mapes de deformació de la densitat electrònica (*electron density deformation map*, EDDM)[37] permet visualitzar fàcilment quin ha estat el moviment electrònic en un pla de la molècula. El fonament dels EDDM rau en les transferències electròniques i la polarització ocorregudes un cop dos fragments es deixen interaccionar. La densitat deformada es calcula a partir de la resta entre la densitat final del nostre complex ρ_{comp} i la densitat de cada un dels dos fragments lliure ρ_1 i ρ_2:

(2.25) $$\Delta\rho = \rho_{comp} - [\rho_1 + \rho_2]$$

Així un mapa d'aquesta magnitud en cada punt de l'espai de la nostra molècula detecta regions d'acumulació o bé de despoblament de càrrega després de la interacció entre ambdós fragments per donar el complex final.

2.6.4 Àtoms a les molècules (AIM)

Un espai de particionament alternatiu al mètode de Mulliken l'ofereix la teoria dels *àtoms a les molècules* (*atoms in molecules,* AIM).[38] En aquesta aproximació es postula que els àtoms a les molècules són rodejats per superfícies de flux zero en la densitat electrònica. Aquest postulat addicional mecanoquàntic proporciona un formalisme autoconsistent capaç de donar una clara interpretació física de les interaccions entre àtoms o fragments. En particular, les interaccions dominants (com ara enllaços químics o fortes repulsions estèriques) són delimitades dins les molècules per línies d'interacció atractores que passen a través dels punts crítics d'enllaç (*bond critical points,* bcp). En aquests punts crítics d'enllaç, la $\rho(r)$ presenta un màxim local respecte dues direccions ortogonals i un mínim respecte la tercera. Són també anomenats punts crítics d'enllaç (3,−1). Altres tipus d'enllaços són els anomenats punts crítics de caixa i punts crítics d'anell. Gràcies al progressos recents en les tècniques computacionals[39] aquests punts crítics poden ser localitzats rutinàriament fins i tot en molècules grans com ara els ful·lerens. En el capítol 5 en presentem una bona aplicació en els *metal·loful·lerenes heteroèdrics* —$C_{56}Pt_2$ i $C_{57}Pt_2$— amb l'ajuda del programa XAIM.[40]

2.6.5 Anàlisi multivariant de dades

Les dades químiques són normalment multidimensionals. És a dir, un objecte pot ser definit mitjançant diversos descriptors. Aquest tipus de dades són anomenades multivariants. Per exemple, els objectes podrien ser compostos químics i els descriptors propietats moleculars que especifiquen l'estructura química. En anàlisi multivariant de dades, els objectes i els descriptors són representats per la matriu $\boldsymbol{X}$ la qual té n files corresponent als objectes i m columnes corresponent als descriptors de cada objecte. A més a més, cada objecte tindrà una o més propietats que voldran ser

estudiades: activitat biològica, estabilitat relativa, tipologia de l'objecte, etc. Aquestes propietats s'ordenen en la matriu ***Y***. Per tant, la matriu ***X*** conté les variables independents (*n* objectes x *m* var. indep.) mentre que la ***Y*** conté la variable dependents (*n* objectes x 1 var. dep.). L'anàlisi multivariant de dades es pot dividir en dues grans etapes. La primera consisteix en construir un model regressió que relacioni la matriu ***X*** amb la ***Y***. Ho anomenem calibratge. Aquest model de regressió dilucidarà l'estructura intrínseca de les dades d'***X***. És a dir m'informarà sobre quins descriptors (variables independents) són els més importants i com estan relacionats entre ells. La segona etapa usa el model de regressió construït anteriorment per fer prediccions. Donat un objecte definit per una sèrie de descriptors mesurats (variables independents) estaré interessat en calcular o estimar el valor de la propietat dependent desconeguda. Existeixen diferents metodologies per dur a terme un anàlisi multivariant: la regressió lineal multivariant (*multivariate linear regression*, MLR), la regressió per components principals (*principal component regression*, PCR) i la regressió per mínims quadrats parcials (*partial least squares*, PLS). Altres etapes de l'anàlisi multivariant de dades de caràcter més tècnic són el pretractament inicial de les dades i la validació del nostre model. És a dir assegurar-se que el nostre model construït per MLR, PCR o bé PLS predirà bé per dades semblants a les usades en el calibratge. A la bibliografia tenim disponibles nombrosos llibres sobre l'anàlisi multivariant de dades, sovint integrats en llibres de quimiometria.[41] Tot seguit només farem uns petits esbossos conceptuals sobre les principals metodologies.

El model més senzill és la regressió lineal multivariant, MLR. Donada una matriu ***X*** de variables independents podem construir un model lineal per modelar el valor de la matriu de la variable dependent ***Y***. El model és: $\boldsymbol{Y} = \boldsymbol{X}\, b$ on b és una matriu de coeficients que s'ajusten segons la regla dels mínims quadrats. La regressió per components principals, PCR, va una mica més enllà. Inicialment el PCR crea un nou conjunt de variables independents més petit que el conjunt inicial però mantenint tota la informació de la matriu inicial ***X***. És a dir, el PCR transforma un conjunt de variables correlacionades amb un conjunt de noves variables no correlacionades anomenades *components principals*. Cal apreciar que les variables correlacionades aporten informació redundant al model i per tant poder ser simplificades. En l'anàlisi multivariant de dades només la

variabilitat (canvi de valor relatiu de les variables en els objectes i entre els objectes) aporta informació valuosa al model. De fet, aquestes noves variables (*components principals*) són combinacions lineals de les originals. El primer *component principal* (PC1) descriu la màxima variabilitat de les dades d'$\boldsymbol{X}$ mentre que el segon component principal (PC2) recull la màxima variabilitat deixada pel PC1 i així endavant. La matriu $\boldsymbol{X}$ (*n* objectes i *m* descriptors) en el PCR es descompon en dues matrius més petites: una de puntuacions (*scores*) $\boldsymbol{T}$ (*n* objectes i *d* variables) i una matriu de pesos (*loadings*) $\boldsymbol{P}$ (*d* objectes i *m* variables), on $\boldsymbol{X} = \boldsymbol{T}\,\boldsymbol{P}^{\mathrm{T}}$. L'algoritme usat per portar a terme aquesta descomposició de la matriu $\boldsymbol{X}$ és el NIPALS (*nonlinear iterative partial least squares*). Les puntuacions, de fet, són els valors que prenen les noves variables per cadascun dels objectes mentre que els pesos són les importàncies de cada antiga variable per formar les noves variables. El següent pas en el PCR és agafar la matriu de valors de les noves variables independents (matriu $\boldsymbol{T}$) i usar el mètode MLR per construir el model de calibratge entre la nova matriu $\boldsymbol{T}$ i la $\boldsymbol{Y}$; segons $\boldsymbol{Y} = \boldsymbol{T}\,b$. Finalment tenim el model construït a partir de la regressió per mínims quadrats parcials (PLS). S'assembla molt al PCR però amb l'avantatge que s'imposa que les noves variables independents (aquí anomenades *variables latents*) expliquin la màxima variabilitat de la matriu de variables dependents $\boldsymbol{Y}$. L'algoritme per calcular el PLS és el SIMPLS. D'aquesta manera el PLS és el mètode idoni per fer prediccions. Una aplicació del PLS es presenta en el Capítol 5. Predirem l'estabilitat relativa dels regioisòmers del heteroful·lerè $C_{81}Pt_2$ a partir d'informació geomètrica dels regioisòmers del heteroful·lerè $C_{57}Pt_2$.

REFERÈNCIES I NOTES

[1] Gaussian 03, Revision A.1, Frisch, M. J.; Trucks, G. W.; Schlegel, H. B.; Scuseria, G. E.; Robb, M. A.; Cheeseman, J. R.; Montgomery, J. A.; Vreven, T.; Kudin, K. N.; Burant, J. C.; Millam, J. M.; Iyengar, S. S.; Tomasi, J.; Barone, V.; Mennucci, B.; Cossi, M.; Scalmani, G.; Rega, N.; Petersson, G. A.; Nakatsuji, H.; Hada, M.; Ehara, M.; Toyota, K.; Fukuda, R.; Hasegawa, J.; Ishida, M.; Nakajima, T.; Honda, Y.; Kitao, O.; Nakai, H.; Klene, M.; Li, X.; Knox, J. E.; Hratchian, H. P.; Cross, J. B.; Adamo, C.; Jaramillo, J.; Gomperts, R.; Stratmann, R. E.; Yazyev, O.; Austin, A. J.; Cammi, R.; Pomelli, C.; Ochterski, J. W.; Ayala, P. Y.; Morokuma, K.; Voth, G. A.; Salvador, P.; Dannenberg, J. J.;

Zakrzewski, V. G.; Dapprich, S.; Daniels, A. D.; Strain, M. C.; Farkas, O.; Malick, D. K.; Rabuck, A. D.; Raghavachari, K.; Foresman, J. B.; Ortiz, J. V.; Cui, Q.; Baboul, A. G.; Clifford, S.; Cioslowski, J.; Stefanov, B. B.; Liu, G.; Liashenko, A.; Piskorz, P.; Komaromi, I.; Martin, R. L.; Fox, D. J.; Keith, T.; Al-Laham, M. A.; Peng, C. Y.; Nanayakkara, A.; Challacombe, M.; Gill, P. M. W.; Johnson, B.; Chen, W.; Wong, M. W.; Gonzalez, C. and Pople, J. A. Gaussian, Inc., Pittsburgh PA, **2003**.

[2] Ahlrichs, R.; Bär, M.; Häser, M.; Horn, H.; Kölmel *Chem. Phys. Lett.* **1989**, *162*, 165.

[3] (a) ADF 2000.02. Department of Theoretical Chemistry. Vrije Universiteit. Amsterdam. Hwww.scm.comH. (b) Baerends, E. J.; Ellis, D. E. ; Ros, P. *Chem. Phys.* **1973**, *2*, 41. (c) Versluis, L.; Ziegler, T. *J. Chem. Phys.* **1988**, *88*, 322. (d) te Velde, G. ; Baerends, E. J. *J. Comput. Phys.* **1992**, *99*, 84. (e) Guerra, C. F.; Snijders, J. G.; te Velde, G.; Baerends, E. J. *Theor. Chem. Acc.* **1998**, *99*, 391.

[4] ADF2004.01, SCM, Theoretical Chemistry, Vrije Universiteit, Amsterdam, The Netherlands, Hwww.scm.comH; te Velde, G.; Bickelhaupt, F. M.; Gisbergen, S. J. A. van; Fonseca Guerra, C.; Baerends, E. J.; Snijders, J. G.; Ziegler, T. 'Chemistry with ADF', *J. Comput. Chem.* **2001**, *22*, 931; Fonseca Guerra, C. ; Snijders, J. G.; te Velde, G.; Baerends, E. J. *Theor. Chem. Acc.* **1998**, *99*, 391.

[5] Jones, R.; Briddon, P. R. *Semicond. Semimet.* **1998**, *51A*, 287.

[6] Warshel, A.; Karplus, M. *J. Am. Chem. Soc.* **1972**, *94*, 5612.

[7] Kao, J.; Alligner, N. L. *J. Am. Chem. Soc.* **1977**, *99*, 975.

[8] (a) Alligner, N. L.; Yuh, Y. H. ; Lii, J. H. *J. Am. Chem. Soc.* **1989**, *111*, 8553. (b) Lii, J. H.; Alligner, N. L. *J. Am. Chem. Soc.* **1989**, *111*, 8566. (c) Lii, J. H.; Alligner, N. L. *J. Am. Chem. Soc.* **1989**, *111*, 8576. (d) Alligner, N. L.; Li, F.; Yan, L. *J. Comp. Chem.* **1990**, *11*, 848.

[9] Born, M.; Oppenheimer, R. *Ann. Physik* **1927**, *84*, 457.

[10] Andrés, J.; Bertrán, J. *Química Teórica y Computacional*, Col·lecció "Ciències Experimentals", Universitat Jaume I de Castelló, **2000**.

[11] Ros, B. O.; Widmark, P. O. *European Summerschool in Quantum Chemistry, Books I, II and III*, Lund University, **2000**.

[12] Levine, I. N. Química Cuántica, Editorial AC, Madrid, 1986.

[13] Szabo, A.; Ostlund, N. S. *Modern Quantum Chemistry. Introduction to Advanced Electronic Structure Theory,* McGraw-Hill, New Cork, **1989**.

[14] (a) Hückel, E. *Z. Physik* **1931**, *70*, 204. (b) Hückel, E. *Z. Physik* **1931**, *72*, 310. (c) Hückel, E. *Z. Physik* **1932**, *76*, 628.

[15] Dewar, M. J. S.; de Llano, C. *J. Am. Chem. Soc.* **1969**, *91*, 789.

[16] Gutman, I.; Milun, M.; Trinajstic, N. *J. Am. Chem. Soc.* **1977**, *99*, 1692.

[17] Coulson, C. A.; Golçbiewski, A. *Proc. Phys. Soc.* **1961**, *78*, 1310.

[18] Hoffmann, R. *J. Chem. Phys.* **1963**, *39*, 1397.
[19] Dewar, M. J. S.; Zoebisch, E. G.; Haly, E. F.; Stewart, J. J. P. *J. Am. Chem. Soc.* **1985**, *107*, 3902.
[20] Dewar, M. J. S.; Thiel, W. *J. Am. Chem. Soc.* **1977**, *99*, 4907.
[21] (a) Stewart, J. J. P. *J. Comput. Chem.* **1989**, *10*, 209. (b) Stewart, J. J. P. *J. Comput. Chem.* **1989**, *10*, 221.
[22] Hohenberg, P. Kohn, W. *Phys. Rev. B* **1964**, *136*, 864.
[23] Kohn, W.; Sham, L. *J. Phys. Rev. A* **1965**, *140*, 1133.
[24] Jones, R. O.; Gunnarsson, O. *Rev. Mod. Phys.* **1989**, *61*, 689.
[25] Vosko, S. H.; Wilk, L.; Nusair, M. *Can. J. Phys.* **1980**, *58*, 1200.
[26] Becke, A. D.; *J. Chem. Phys.* **1986**, *84*, 4524. *Phys. Rev. A.* **1988**, *38*, 3098.
[27] (a) Perdew, J. P. *Phys. Rev. B* **1986**, *33*, 8822. (b) *Phys. Rev. B* **1986**, *34*, 7406.
[28] Lee, C.; Yang, W.; Parr, R. G. *Phys. Rev. B.* **1988**, *37*, 785.
[29] Becke, A. D. *J. Chem. Phys.* **1993**, *98*, 5648.
[30] Slater, J. C. *Quantum Theory of Molecules and Solids* Vol. 4, McGraw-Hill, New York, **1974**.
[31] (a) Snijders, J. G.; Baerends, E. J. *Molecular Physics* **1978**, *36*, 1789. (b) Snijders, J. G.; Baerends, E. J.; Ros, P. *Molecular Physics* **1979**, *38*, 1909. (c) Ziegler, T.; Snijders, J. G.; Baerends, E. J. *J. Chem. Phys.* 1981, *74*, 1271. (d) DeKock, R. L.; et al. *Chem. Phys. Let.* **1984**, *105*, 308. (e) DeKock, R. L.; et al. *J. Am. Chem. Soc.* **1984**, *106,* 33387. (f) Boerrigter, P. M., *Spectroscopy and bonding of heavy element compounds*, Vrije Universiteit, **1987**, pag. 233. (g) Boerrigter, P. M.; Buijse, M. A.; Snijders; J. G. *Chemical Physics* **1987**, *111*, 47. (h) Boerrigter, P. M.; Baerends, E. J; Snijders J. G. *Chemical Physics* **1988**, *122*, 357. (i) Ziegler, T.; et al. *J. Phys. Chem.* **1989**, *93,* 3050. (j) Li, J.; Schreckenbach, G.; Ziegler, T. *J. Am. Chem. Soc.* **1995**, *117*, 486.
[32] (a) van Lenthe, E.; Ehlers, A.E.; Baerends, E. J. *J. Chem. Phys.* **1999**, *110*, 8943. (b) van Lenthe, E.; Baerends, E.J.; Snijders, J. G. *J. Chem. Phys.* **1993**, *99*, 4597. (c) van Lenthe, E.; Baerends, E. J.;Snijders, J. G. *J. Chem. Phys.* **1994**, *101*, 9783. (d) van Lenthe, E.; Snijders, J.G.; Baerends, E. J. *J. Chem. Phys.* **1996**, *105*, 6505. (e) van Lenthe, E.; et al. *J. Quant. Chem.* **1996**, *57*, 281
[33] Snijders, J. G.; Baerends, E. J.; Vernooijs, P. *At. Nucl. Data Tables*, **1982**, *26*, 483; Vernooijs, P.; Snijders, J. G.; Baerends, E. J. *"Slater type basis functions for the whole periodic system"*, Internal Report, Free University of Amsterdam, The Netherlands, **1981**.
[34] (a) T. Ziegler, A. Rauk, *Teor. Chim. Acta* **1977**, *46*, 1. (b) T. Ziegler, A. Rauk, *Inorg. Chem.* **1979**, *18*, 1558.
[35] (a) Morokuma, K. *J. Chem. Phys.* **1971**, *55*, 1236. (b) Kitaura, K.; Morokuma, K. *Int. J. Quantum. Chem.* **1976**, *10*, 325.

[36] (a) Mulliken, R. S. *J. Chem. Phys.* **1955**, *23*, 1833. (b) Mulliken, R. S. *J. Chem. Phys.* **1955**, *23*, 1841. (c) Mulliken, R. S. *J. Chem. Phys.* **1955**, *23*, 2338. (d) Mulliken, R. S. *J. Chem. Phys.* **1955**, *23*, 2343.

[37] (a) Coppens, P.; Stevens, E. D. *Adv. Quantum Chem.* **1977**, *10*, 1. (b) Coppens, P.; Hall, M. B. *Electron distributions and the chemical bond*, Plenum Press, NewYork, **1982**. (c) Breitenstein, M.; Dannhöl, H.; Meyer, H.; Schweig, A.; Seeger, R.; Seeger, U.; Zittlau, W. *Int. Rev. Phys. Chem.* **1983**, *3*, 335. (d) Bader, R. F. W.; Nguyen-Dang, T. T. *Adv. Quantum Chem.* **1981**, *14*, 63.

[38] Bader, R. F. W. *Atoms in Molecules. A quantum Theory*, Claredon Press, Oxford, **1990**.

[39] Cioslowski, J.; Nanayakkara, A. *Chem. Phys. Lett.* **1994**, *219*, 151.

[40] Xaim was developed by J. C. Ortiz and C. Bo. Universitat Rovira i Virgili. Tarragona. Spain. Xaim is freely available from Hwww.quimica.urv.es/XAIMH.

[41] (a) Massart, D. L.; Vandeginste, B. G. M.; Buydens, L. M. C.; de Jong, S.; Lewi, P. J.; Smeyers-Verbeke, J. *Handbook of Chemometrics and Qualimetrics*; Elsevier Science; Amsterdam, **1998**; Parts A and B. (b) Martens, H.; Naes, T. *Multivariate Calibration*; John Wiley & Sons, Inc; Chichester, **1989**.

CAPÍTOL 3

ABAST I OBJECTIUS DE LA TESI

El treball d'investigació aquí presentat segueix una divisió molt clara: la divisió estructural dels metal·loful·lerens. El capítol 4 pels metal·loful·lerens endoèdrics: $Sc_3N@C_k$ (k = 68, 78, 80), el capítol 5 pels metal·loful·lerens heteroèdrics: $C_{59}Pt$, $C_{58}Pt$, $C_{57}Pt_2$, $C_{56}Pt_2$ i el capítol 6 pels metal·loful·lerens exoèdrics: $(\eta^2\text{-}C_k)\{M(PH_3)_2\}_n$ (k = 60, 70, 84; M = Pt, Pd, Ni; n = 1, 2, 4, 6). En cadascun dels tres capítol s'ha treballat sobre les estructures més novedoses i novells dels metal·loful·lerens. Els objectius generals han estat fer un pas endavant en l'enteniment tant electrònic com estructural d'aquestes noves molècules. Dins aquest objectiu, no tant sols s'ha buscat la novetat en els continguts sinó també en la forma com s'aconsegueixen. Així l'ús de tècniques quimiomètriques per a l'anàlisi dels resultats en el capítol 5 és el màxim exponent d'aquesta filosofia. Tot seguit passo a descriure els objectius particulars de cadascun dels capítols.

3.1 METAL·LOFUL·LERENES ENDOÈDRICS

El treball arrenca a partir de la detecció i caracterització dels últims *metal·loful·lerens endoèdrics* a inicis de l'any 2000: $Sc_3N@C_k$ (*k* = 68, 78, 80). El capítol 4 que versa sobre aquests *metal·loful·lerens endoèdrics* de nitrur d'escandi vol ser un estudi teòric global sobre les seves característiques d'enllaç, estructurals, isomèriques, físiques i de reactivitat. Els principals resultats estaran relacionats amb els següents punts:

Caracterització de l'enllaç entre la unitat metàl·lica i la caixa ful·lerènica. Mitjançant la construcció de diagrames d'interacció d'orbitals entre ambdós fragments veurem que la interacció presenta un caràcter fortament iònic. Aquesta primera idea serà reforçada amb la descomposició de l'energia d'enllaç i el càlcul de la transferència electrònica entre ambdós fragments.

Isomerisme en $Sc_3N@C_k$ (k = 68, 78, 80). Ja que en el complex $Sc_3N@C_{80}$ s'havia demostrat experimentalment l'alta mobilitat de l'hoste Sc_3N, ens proposem estudiar l'estabilitat relativa dels diferents isòmers vinguts de la rotació del nitrur d'escandi a l'interior de les caixes de C_{68}, C_{78} i C_{80}.

Propietats físiques. Càlcul dels potencials d'ionització, afinitats electròniques i salts d'energia HOMO-LUMO pels *endoedres* $Sc_3N@C_k$ (*k* = 68, 78, 80). Comparativa amb les caixes lliures de C_{68}, C_{78} i C_{80} així com amb els anàlegs *mono-* i *dimetal·loful·lerens endoèdrics clàssics* $M_n@C_k$.

Altres membres de la família. S'han aconseguit sintetitzar altres *metal·loful·lerens endoèdrics* de la mateixa estructura només variant l'àtom d'escandi: $Sc_nM_{3-n}N@C_k$ (*n* = 0-3; M = Sc, La, Y; *k* = 68, 78, 80). L'objectiu principal serà aclarir certes controvèrsies a l'entorn de l'estat d'oxidació d'aquest segon metall, M. També avaluarem l'efecte energètic, electrònic i geomètric del canvi de l'escandi per metalls més voluminosos com La i Y.

Hi haurà noves caixes capaces d'encapsular l'Sc_3N? Fins ara només els ful·lerens D_3-C_{68}:**6140**, $D_{3h'}$-C_{78}:**5**, I_h-C_{80}:**7** i D_{5h}-C_{80}:**6** són capaços d'empresonar l'Sc_3N. Resulta que aquests isòmers no es troben experimentalment de forma lliure ni tampoc són els més estables de la seva estequiometria. Investigarem per què només aquests isòmers i no cap altre isòmer IPR entre el C_{60} i el C_{84} ha sigut capaç de fer-ho.

Reactivitat exoèdrica. Què ha canviat en la reactivitat dels enllaços C–C exteriors un cop s'ha produït l'encapsulament? En un primer treball volem ser capaços de corroborar i predir els enllaços C–C més reactius front a una cicloaddicció [4 + 2] de 1,3-butadiè a la superfície carbonada de $Sc_3N@C_k$ (k = 68, 78, 80). Ens valdrem de factors ja coneguts com a determinants en la reactivitat *exoèdrica*: la piramidalització dels carbonis, la distància d'enllaç C–C i l'ordre d'enllaç C–C. En un segon treball determinarem l'isòmer més estable de l'estequiometria experimental $Sc_3N@C_{80}F_{52}$. Serà interessant veure els canvis produïts per l'addició de 26 molècules de F_2 damunt la superfície i el seu efecte sobre l'estabilitat de la molècula total. En ambdós casos compararem la reacció en els *endoedres* $Sc_3N@C_k$ (k = 68, 78, 80) i les seves respectives caixes lliures C_k (k = 68, 78, 80).

3.2 METAL·LOFUL·LERENES HETEROÈDRICS

La recerca en *metal·loful·lerens heteroèdrics* es troba simplement en els seus inicis. Tot just s'han detectat en espectres de masses les espècies $C_{59}Pt$, $C_{58}Pt$, $C_{57}Pt_2$, $C_{56}Pt_2$ i algunes homologues amb pèrdues d'unitats C_2. Alguns derivats d'Ir també. Se sap que els metalls se situen en l'estructura carbonada pel tipus de reactivitat i ja poca cosa més se'n sap.

Proposta d'enllaç entre el metall Pt i l'estructura carbonada C_{58}. Mitjançant la descomposició detallada de l'energia de substitució en el *clúster* més simètric C_{2v}-$C_{58}Pt$ intentem desengranar el complex enllaç Pt–ful·lerè. Aquest exemple creiem que serà representatiu per la resta d'estequiometries. Ens valdrem també de models més senzills per racionalitzar-lo, com ara el D_{4h}-$C_{24}H_{12}Pt$. Els diagrames d'interacció de

fragments també ens seran útils per localitzar els orbitals metàl·lics dins l'estructura final.

Estabilitat de monoheteroful·lerens. Volem esbrinar els factors energètics, electrònics i geomètrics que afecten l'estabilitat relativa dels compostos C_kM (k = 58, 59, M = Pt, Ir, Os, Ti) on pel $C_{58}M$ el metall substitueix dos carbonis i pel $C_{59}M$ només un. Com a factor energètic tindrem la informació provinent de la descomposició de l'energia de substitució. L'estructura electrònica particular de cada compost també aportarà pistes sobre l'estabilitat: salts HOMO-LUMO, transferències de càrrega, etc. I com a factors geomètrics tindrem en compte: el radi de caixa, les distàncies M–C i l'índex d'aromaticitat HOMA.

Habilitat de coordinació de l'etilè. S'ha detectat experimentalment la coordinació del 1,3-butadiè a la superfície dels *metal·loful·lerens heteroèdrics*. Usarem l'etilè com a model. Caracteritzarem mínimament l'enllaç $C_{58}M–C_2H_4$ i n'avaluarem les característiques energètiques i geomètriques.

Estabilitat de diheteroful·lerens. Degut a la existència d'una gran quantitat de regioisòmers possibles per les estructures $C_{57}Pt_2$ i $C_{56}Pt_2$, haurem d'usar noves tècniques d'anàlisi per tal de trobar el regioisòmer més estable de cada estequiometria. A la vegada aquesta recerca ens permetrà trobar quins són els factors que influeixen en l'estabilitat relativa dels mencionats regioisòmers. Els factors estudiats són de dos tipus: topològics (Separació Pt–Pt, nombre d'enllaços C–C, tipus d'enllaç C–C substituït i número d'anells amb metalls) i estructurals (distàncies d'enllaç C–C 6:6, C–C 6:5 i Pt–C així com els valors d'HOMA i els radis de caixa). Per manejar i destriar entre tants factors usarem l'anàlisi multivariant de dades. En concret la tècnica del PLS (*partial least squares*). Aquesta ens permetrà fins i tot fer prediccions d'estabilitat relatives d'altres heteroful·lerens.

Propietats físiques. Calcularem i compararem els potencials d'ionització i les afinitats electròniques del *metal·loful·lerens heteroèdrics* amb les caixes lliures (C_{60}) i amb els seus anàlegs no metàl·lics de nitrogen i bor.

3.3 METAL·LOFUL·LERENES EXOÈDRICS

Els *metal·loful·lerens exoèdrics* (η^2-C_k)$\{M(PH_3)_2\}_n$ (k = 60, 70, 84; M = Pt, Pd, Ni; n = 1, 2, 4, 6), a diferència dels dos grups anteriors, han estat completament determinats estructuralment i nombrosos estudis ja han estat presentats a la comunitat científica descrivint les propietats físiques i químiques. Els objectius en aquesta part són, doncs, més modestos. Refem els càlculs a nivells de computació molt més elevats focalitzant-nos en les relacions entre l'energia i l'estructura. L'addició d'unitats metàl·liques a ful·lerens superiors com ara el C_{70} i el C_{84} també centraran la nostra atenció. Finalment un dels objectius força perseguits serà la sistematització de la predicció dels punts exoèdrics més reactius mitjançant l'anàlisi de: la piramidalització dels enllaços C–C, la distància C–C i l'ordre d'enllaç C–C.

Repàs de l'enllaç coordinatiu entre la unitat metàl·lica i el ful·lerè. Per tal d'explicar l'enllaç metàl·lic en l'estructura (η^2-C_{60})$Pt(PH_3)_2$ el comparem respecte al model més senzill al qual s'assembla: l'enllaç entre un alquè deficient d'electrons, $C_2(CN)_4$, i la unitat metàl·lica $Pt(PH_3)_2$. Ambdós enllaços segueixen el model de Dewar-Chatt-Duncanson.

Complexos de monoaddició de C_{60}. Dedicarem esforços en trobar metodologies per tal de reduir el cost computacional d'aquest compostos, ja que en les poliaddicions en molts casos es superen el centenar d'àtoms. Alguns autors proposen el modelatge del ful·lerè C_{60} com a C_2H_4 o bé $C_{14}H_8$, però, nosaltres investigarem com pot afectar la reducció de les funcions de base en la geometria i l'energia d'enllaç.

Complexos de poliaddició de C_{60}. El principal objectiu serà quantificar els canvis produïts per la poliaddició sobre el C_{60}: canvi en les energies d'enllaç a mesura que unitats metàl·liques es van afegint i canvi en la piramidalització dels carbonis enllaçats.

Complexos de monoaddició de C_{70} i C_{84}. El C_{70} i el C_{84} presenten una diversitat d'enllaços C–C que ens permetrà diferenciar-los i adonar-se'n dels factors importants en la seva reactivitat.

Predicció dels punts més reactius davant les reaccions d'addició. L'experiència acumulada dels punts anteriors ens permetrà racionalitzar la predicció dels enllaços més reactius davant la reactivitat exoèdrica tenint en compte la seva tipologia, distància C–C, piramidalització i ordre d'enllaç.

PART II. RESULTS

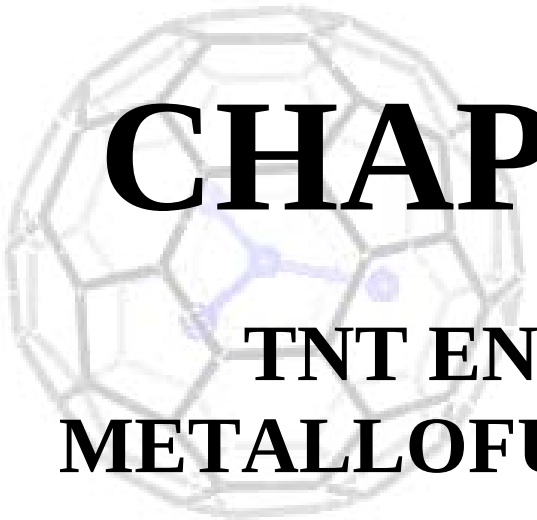

CHAPTER 4

TNT ENDOHEDRAL METALLOFULLERENES

Fullerenes containing a trimetallic nitride template (TNT) within the cage are a particularly interesting class of endohedral metallofullerenes (also termed incarfullerenes). Hereafter, they will be referred to as TNT endohedral metallofullerenes. Not only are the cage properties modified by the presence of the incarcerated group but, almost uniquely amongst endohedral metallofullerenes, they are quite stable. Furthermore, they can be produced in multimilligram quantities, and these amounts should increase in the future. The electronic effect of the TNT group is such that some fullerenes of sizes and symmetry that are otherwise relatively unstable become available for investigation. Classical endohedral metallofullerenes contain a large variety of stoichiometries that are the combination of fullerene cages with different numbers and varieties of incarcerated metals. In C_{28}, for example, there is only one metal atom whereas in the higher C_{84} fullerene there are as many as three. TNT endohedral metallofullerenes are the first time that a four-atom metal unit has been encapsulated inside a fullerene cage. These TNT metallofullerenes mostly have the following stoichiometries: $Sc_{3-n}M_nN@C_k$ (n = 0-3, M = Y, La and lantahnides; k = 68, 78, 80). They are prepared using a modified Krätschmer-Huffman arc generator under N_2 atmosphere. The main advantage they have over classical endohedral metallofullerenes is that the structure can be determined by a single crystal X-ray diffraction study. This is an important advance because crystallization has long been a bottleneck in the structural determination of classical endohedral metallofullerenes, whose metals can present different oxidation states and geometrical positions in a single

stoichiometry. Also, because these TNT endohedral metallofullerenes can be synthesized in high yields and consequently they have already been fully characterized. Now they are about to be exohedrally functionalized. So, these new endohedral metallofullerenes have attracted special interest as new spherical molecules with novel properties ever since they were first detected in 1999.

This chapter is structured in the same way as chapters 5 and 6. All three chapters consist of four different parts. They start with an introduction to the experimental and theoretical studies which provide valuable information about the aspects that will be dealt with in the future sections and then go on to discuss the kind of metal bond between the metal unit and the carbon cage. Subsequently they describe their isomerism, properties and reactivity, and the chapters end with a section of concluding remarks.

In this chapter, section 4.1 starts with a comprehensive review of all the experimental and theoretical studies of the $Sc_3N@C_k$ (k = 68, 78, 80) complexes. Section 4.2 uses the fragment molecular orbital method to conclude that an ionic bond between the TNT unit and the cage explain the most important electronic behavior and geometry of these new endohedral metallofullerenes. Section 4.3 deals with the rapid motion of the TNT unit inside the cage and studies several isomers of $Sc_3N@C_k$ (k = 78, 80) constructed by the Sc_3N rotation. Section 4.4 compares the physical properties of the $Sc_3N@C_k$ (k = 68, 78, 80) complexes with those of free fullerenes and classical endohedral metallofullerenes. The wide variety of TNT units encapsulated inside the fullerene cages is discussed in section 4.5. We pay particular attention to the effects of increasing the ionic radii and decreasing the electronegative character when Sc atoms are replaced progressively by Y and La atoms. Section 4.6 is the biggest step forward in this area: it describes an easy way of determining which fullerenes will be capable of encapsulating TNT units. At the end of the chapter, we investigate the exohedral reactivity of these TNT endohedral metallofullerenes via [4 + 2] cycloaddition reactions (section 4.7) and hydrogentation/fluorination reactions (section 4.8).

4.1 INTRODUCTION

4.1.1 Experimental part

Many fullerenes with encapsulated metals and nonmetals have been reported, but they are typically formed in low yields (< 0.5 %) with multiple isomers of low symmetry, which have prevented progress in the exploration of the chemical and physical properties. However, a new family of trimetallic nitride template (TNT) endohedral metallofullerenes have been reported recently in relatively higher yields with a general formula of $A_{3-n}B_nN@C_k$ (n = 0-3; A, B = group III, IV and rare-earth metals; k = 68, 78, 80). The archetypal examples, in the chronological order of their first reported synthesis are: $Sc_3N@C_{80}$,[1] $Sc_3N@C_{68}$[2,3] and $Sc_3N@C_{78}$[4]. These new endohedral metallofullerenes were prepared by the Krätschmer-Huffman arc fullerene preparation with graphite rods doped with A_2O_3 and B_2O_3 oxides in a dynamic atmosphere of helium and nitrogen in relative yields of 8:1:1, respectively. In fact, the first of these fullerenes, $Sc_3N@C_{80}$, is the third most abundant fullerene and is only exceeded by C_{60} and C_{70}. After the soot is produced, these TNT endohedral metallofullerenes are isolated through a three-step high-pressure liquid chromatography (HPLC) procedure.[5]

The macroscopic quantities of TNT endohedral metallofullerenes make them available for chemical and physical characterization. $Sc_3N@C_{80}$ has been characterized by ^{13}C, ^{14}N and ^{45}Sc NMR spectroscopy, UV/vis spectroscopy and single-crystal X-ray diffraction of the cocrystallized solid: $Sc_3N@C_{80}\cdot Co^{III}$-(OEP)$\cdot 0.5C_6H_6\cdot 1.5CHCl_3$ (OEP is the dianion of octaethylporphyrin).[1,6] ^{13}C NMR analysis revealed that the Sc_3N moiety is planar encapsulated in the highly symmetric I_h-C_{80}:**7** isomer. The cage is stabilized as a result of electron charge transfer between the TNT unit and the fullerene cage. The ^{13}C NMR results also suggested that internal motion of the Sc_3N unit yields a time-averaged electronic environment that preserves the overall I_h symmetry for the carbon cage. The encapsulated Sc_3N unit is not localized at any specific internal bonding sites. The ^{45}Sc NMR spectrum exhibited a single symmetric line which is also indicative of a dynamic structure.[1] On the other hand, the rotational modes from temperature-dependent Raman and infrared spectroscopy studies gave a

direct evidence of the formation of a $Sc_3N–C_{80}$ bond, which significantly reduces the symmetry.[7] It is important to notice that the relaxation times of the vibrational excitations are shorter than those of the magnetic resonance methods. These UV/vis and Raman studies have been extended to a variety of $M_3N@C_{80}$ (M = Y, Tb, Ho, Er) complexes.[8] Recently, the isolation of a new isomer of $Sc_3N@C_{80}$, which corresponds to the Sc_3N encapsulation inside the D_{5h}-C_{80}:**6** isomer, has been characterized by HPLC, mass spectroscopy and ^{13}C NMR.[9] Neither of these C_{80} isomers has been isolated as empty fullerenes and are not even the most stable isomers among the 7 distinct isomers that satisfy the so-called isolated pentagon rule (IPR).[10] In the case of $Sc_3N@C_{78}$ the ^{13}C NMR analysis revealed that the D_{3h}-C_{78}:**5** isomer encapsulates the planar Sc_3N. This isomer has not been calculated as the most stable or it has never isolated as an empty cage. It is very interesting to see that the empty fullerene isomers isolated so far are often different from the carbon cages found in isolable metallofullerenes. On the other hand, the $Sc_3N@C_{68}$ molecule is an exception to the IPR rule: it has three pentalenes (fused pentagons). The TNT unit in each complex is oriented differently with respect to the fullerene cage. Whereas in $Sc_3N@C_{78}$ the metals reside over the set of C27–C28 bonds, a pyracylene C–C bond type (Appendix A.5), the X-ray characterization for $Sc_3N@C_{80}$ and $ErSc_2N@C_{80}$[11] shows that the metals reside over individual carbons in the latter and near the center of 6:5 C–C bonds in the former. Pyracylene C–C bonds consist of 6:6 ring junctions abutted by two hexagons (see Appendix A.1 for the different C–C bond types in IPR fullerenes). Special attention has been paid to Lutetium-based TNT endohedral metallofullerenes, $Lu_{3-n}A_nN@C_{80}$ (n = 0-2; A = Ga, Ho), because they may prove useful as multifunctional contrast agents for X-ray, MRI and radiopharmaceuticals, thereby eliminating the need for three separate agents.[12]

The chemistry of the TNT metallofullerenes may become a substantial area of fullerene research, and it is particularly interesting not only because of the electronic effect of the incarcerated molecule, but because unusual C–C bonding characteristics may exist on the modified fullerene surface. Unfortunately, little is known about the exohedral reactivity of TNT endohedral metallofullerenes. Recently, however, the first organic derivative of the most common TNT endohedral metallofullerene,

$Sc_3@C_{80}$, has been successfully synthesized and characterized by functionalizing the exterior of the cage via the [4 + 2] cycloaddition reaction with 6,7-dimethoxyisochroman-3-one.[13,14] The addition product occurs across a 6:5 rather than a 6:6 C–C bond and has a mirror plane of symmetry as observed from the ^{13}C spectrum. The formation of water-soluble fullerenols $Sc_3N@C_{80}(OH)_nO_n$ (n = *ca.* 10) have also been reported (the value of n is very approximate as no structural characterization was obtained).[15] Finally, experiments have been carried out with the hydrogenation and fluorination of $Sc_3N@C_{80}$ but the results about the number of H or F atoms added to the fullerene surface are unclear.[16] The $Sc_3N@C_{78}$ has also been functionalized with a ^{13}C-labeled reagent to afford mono-, di- and triadducts. ^{13}C and ^{1}H NMR data about the monoadduct suggests that the addend is added to an asymmetric site in the C_{78} carbon cage.[17]

4.1.2 Theoretical part

The electronic distribution for $Sc_3N@C_{80}$ is $(Sc^{3+})_3N^{3-}@C_{80}^{6-}$. Electronic structure calculations showed that the stability of the I_h-C_{80}:**7** isomer increases markedly when six electrons are added to the cage.[18] As a result, the I_h isomer becomes the most stable structure for C_{80}^{6-}.[19] Seven isomeric structures of C_{80} (with symmetries and numbering: D_{5d}-C_{80}:**1**, D_2-C_{80}:**2**, C_{2v}-C_{80}:**3**, D_3-C_{80}:**4**, $C_{2v'}$-C_{80}:**5**, D_{5h}-C_{80}:**6** and I_h-C_{80}:**7**) fulfill the IPR.[20] Two empty cage isomers, D_2-C_{80}:**2** and D_{5d}-C_{80}:**1**, have been isolated[21] and theoretical calculations have shown that the I_h-C_{80}:**7** structure is the least stable isomer overall.[22] In contrast, in the TNT endohedral metallofullerenes, only the cages with I_h and D_{5h} symmetry have been found. $Ti_2@C_{80}$ has also been shown to have D_{5h} symmetry through electron energy loss and ^{13}C NMR spectroscopic studies.[23] In very recent theoretical work, Kobayashi et al. have shown that the I_h isomer is strongly stabilized by the presence of the TNT unit inside the cage and that in the series of $Sc_{3-n}La_nN@C_{80}$ (n = 0-3) this stabilization decreases as the number of La atoms increases. The La_3N unit in these TNT endohedral metallofullerenes retains its pyramidal structure unlike Sc_3N in $Sc_3N@C_k$ (k = 68, 78, 80). Surprisingly, $La_3N@C_{80}$ has an electronic structure which is formally described as $La_3N^{8+}@C_{80}^{8-}$ according to Kobayashi et al..[24] For $La_2@C_{80}$,

calculations revealed that the I_h structure is favored with a formal $(La^{3+})_2@C_{80}^{6-}$ electron distribution within the molecule.[25]

There are five IPR isomers for the empty C_{78} cage with the following symmetries and numbering: D_3-C_{78}:**1**, C_{2v}-C_{78}:**2**, $C_{2v'}$-C_{78}:**3**, D_{3h}-C_{78}:**4** and $D_{3h'}$-C_{78}:**5**.[20] Calculations carried out at different levels of theory for these empty cages suggest the following relative stability order: $C_{2v'}$-C_{78}:**3** >C_{2v}-C_{78}:**2** > D_3-C_{78}:**1** >$D_{3h'}$-C_{78}:**5** > D_{3h}-C_{78}:**4**.[26] Three stable isomers of C_{78} have been separated and their symmetries identified as $C_{2v'}$-C_{78}:**3**, C_{2v}-C_{78}:**2**, and D_3-C_{78}:**1** through their ^{13}C NMR spectrum.[27] The X-ray structure of $Sc_3N@C_{78}$ corresponds to the encapsulation of the nitride moiety by the $D_{3h'}$-C_{78}:**5** cage, which is the second least stable empty cage isomer.

In conclusion, the wide range of novel TNT endohedral metallofullerenes, which can be prepared in reasonably high yields and purity, provide host-guest chemistry with new possibilities because of their unique structural, chemical and reactivity features. Experimental and theoretical studies of these new endohedral species are summarized in a very recent book by Nagase and Akasaka.[28]

4.2 IONIC BOND BETWEEN THE FULLERENE AND THE TRIMETALLIC NITRIDE TEMPLATE (TNT)

4.2.1 Structures of $Sc_3N@C_k$ (k = 68, 78, 80)

Greater effort on resolving the geometric structure has been done on the $Sc_3N@C_{78}$ cluster. The $D_{3h'}$-C_{78}:**5** isomer is one of the five IPR isomers of C_{78} and therefore all C–C bonds involve 6:6 or 6:5 ring junctions. There are several kinds of 6:6 C–C bonds in $D_{3h'}$-C_{78}:**5**, which range in distances from 1.372 to 1.470 Å. The shortest ones appear in the pyracylene C–C bonds (***A*** type in Appendix A.1). On the other hand, the corannulene 6:5 C–C bonds (***D*** type) have an average bond length of 1.44 Å. These values fall within the range of C–C distances reported in earlier theoretical studies.[26] A complete description of the different C–C bonds of $D_{3h'}$-C_{78}:**5** can be found in the Appendix A.5. There is no X-ray determinations for free C_{78} cages to check the computed geometries, but the present level of computation has demonstrated that is capable of reproducing the geometry of C_{60} very well. The computed distances for the two different C–C bonds in C_{60} are 1.397

and 1.452 Å (Appendix A.2), values that almost coincide with the experimental parameters of 1.391 and 1.455 Å from neutron powder diffraction[29] and of 1.401 and 1.458 Å from electron diffraction.[30]

Although the free Sc_3N molecule is pyramidal with an optimized Sc–N bond length of 1.957 Å and a Sc–N–Sc angle of 99.1º, this fragment has a planar structure inside the cage of C_{68}, C_{78} and C_{80} fullerenes.[1,2,4] A priori, several orientations of the Sc_3N unit inside the $D_{3h'}$-C_{78}:**5** fullerene are possible. However, the X-ray determination of $Sc_3N@C_{78}$ shows that the Sc_3N unit lies close to the original σ_h plane of the $D_{3h'}$-C_{78}:**5** cage. This most stable structure corresponds to the case in which the scandiums are over the set of C27–C28 bonds (pyracylene 6:6 C–C bond types) hereafter called as isomer **1**, $Sc_3N@C_{78}$:**1**. Such sites are completely analogous to the sites where metal units coordinate on the outside of fullerene surface in C_{60}, C_{70} and C_{84} (see Chapter 6). When a Sc_3N unit is encapsulated, there is a significant local distortion in the fullerene cage. This distortion results in the outward movement of the carbons closest to the scandium ions away from these ions. Thus this distortion resembles the distortions seen in the exohedral metallofullerene complexes, where binding to a metal center also results in an outward displacement of the fullerene carbons and an increase of the pyramidalization of the carbons bound to the external metal centers, see Chapter 6.[31] A similar, but smaller, distortion has also been seen in the chemically modified endohedral, $Sc_3N@C_{80}$-$C_8H_6(OCH_3)_2$,[13] see section 4.7. The Sc–N bond lengths were found to be 1.997 Å, a close value to the experimental one originally reported for $Sc_3N@C_{78}$, 1.983-2.125 Å. Nevertheless, a major discrepancy appears in the Sc–C bond lengths: hence, whereas the computed value of 2.255 Å is a common distance for Sc–C bonds, the experimental distances, which range between 2.024 and 2.107 Å in the original refinement with a fixed cage geometry, may be considered very short bond lengths for Sc–C bonds. Experimental and theoretical Sc–N and Sc–C distances are tabulated for the most stable TNT endohedral metallofullerenes in Table 4.1. The earlier X-ray crystallographic investigation of the structure of $Sc_3N@C_{78}\cdot Co(OEP)\cdot 1.5(C_6H_6)\cdot 0.3(CHCl_3)$ used rigid models for the fullerene cages to distinguish between the five possible IPR isomers for the C_{78} cage and concluded that the $D_{3h'}$-C_{78}:**5** cage was present. The resulting model identified three different orientations of the $D_{3h'}$-C_{78}:5 cage and three corresponding orientations of the Sc_3N unit.

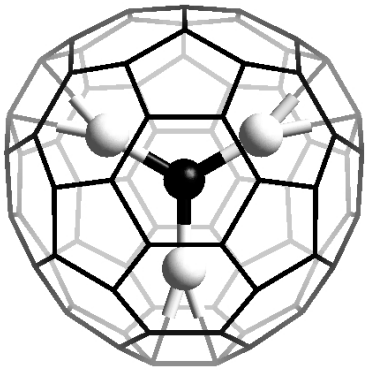

(a) D_{3h}-$Sc_3N@C_{78}$:**1**

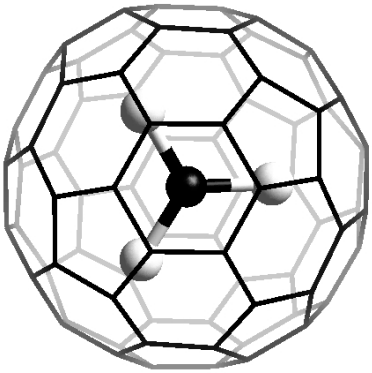

(b) C_s-$Sc_3N@C_{80}$:**11**

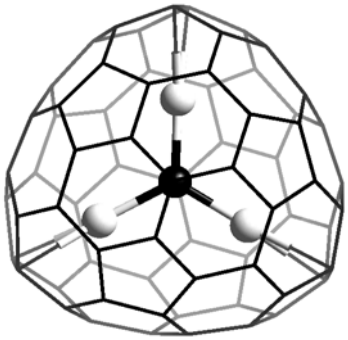

(c) D_3-$Sc_3N@C_{68}$

Figure 4.1 Optimized structures for $Sc_3N@C_{78}$:**1** (a), $Sc_3N@C_{80}$:**11** (b) and $Sc_3N@C_{68}$(c). For more details see Figures 4.5 and 4.7.

With that model, the closest Sc–C contacts inside the cage were short (2.024 Å) and also quite far from the mean (2.430 Å) and shortest (2.204 Å) Sc–C distances obtained in an exploration of 73 examples in the Cambridge Structural Database.[11] Because of the orientational disorder, free refinement of the cage parameters that might have revealed any structural distortion of the cage by the Sc_3N unit could not be done as part of the original refinement. However, knowing that the Sc_3N unit produced a significant change in the dimensions of the C_{78} cage, it was appropriate to re-examine the crystallographic data. Consequently, the crystallographic data for $Sc_3N@C_{78}$·Co(OEP)·1.5(C_6H_6)·0.3($CHCl_3$) were re-refined by Balch and

co-workers using the optimized and computed structure of the C_{78} cage as a new model for the fullerene portion of the structure.[32] Incorporation of this model in the structure into the three locations identified previously and further refinement, in which the orientations of these three groups were allowed to vary, produced a final structure in which the R factor decreased from 0.1107 to 0.0977. We consider this reduction in R to be significant and conclude that the computed structure is in better agreement with the experimental crystallographic data than was the formerly used rigid cage model. With this model, the Sc–C distances in the major site are Sc1–C34, 2.230(3); Sc1–C35, 2.281(3); Sc2–C27, 2.235(15); Sc2–C28, 2.206(15); Sc3–C41, 2.273(4); Sc3–C42, 2.239(4) Å. These values are within the range of Sc–C bond lengths found in the Cambridge Structural Database and are consistent with the calculated results reported. At the major site, the Sc–N distances are Sc1–N, 1.981(6); Sc2–N, 1.967(15); Sc3–N, 2.127(4). These values are similar to those obtained in the original refinement (Sc1–N, 1.988(7); Sc2–N, 1.983(15); Sc3–N, 2.125(5)).[4] The Sc_3N unit is planar. The sum of the Sc–N–Sc angle is 360º. The individual Sc–N–Sc angles are Sc1–N–Sc2 130.1(5), Sc1–N–Sc3 114.0(2), and Sc2–N–Sc3, 115.9(6) (See Appendix A.5 for the carbon numbering system of the cage). The optimized structure of the most stable isomer of Sc_3NC_{78} is shown in Figure 4.1a. It is special to realize that the 6:6 C–C bonds linked to the three Sc atoms (C27–C28, C34–C35, C41–C42) increase their distances in 0.069 Å giving some clues about the kind of Sc–C_2 bond established in the $Sc_3N@C_{78}$ cluster.

The Sc_3N unit strongly stabilizes the icosahedral isomer of C_{80}, which is the most unstable of the seven structures that satisfy the IPR for the C_{80} stoichiometry. I_h-C_{80}:**7** fullerene is spherical with almost non-differentiate C–C bonds, since this fullerene does not contain any pyracylene 6:6 C–C bond (***A*** type), only corannulene 6:5 C–C bonds (***D*** type) and ***B*** C–C bond types (Appendix A.1 and A.6). This geometry provokes that I_h-C_{80}:**7** fullerene contains no high electron density π-bonds in contrast to the common fullerenes: C_{60} and C_{70} (compare bond orders in Appendix A.6, A.2 and A.3). In the case of $Sc_3N@C_{80}$ there is evidence from the ^{13}C NMR spectrum that the TNT may freely rotate inside the cage.[1] Thus, several different orientations of the TNT have been found for the slightly different TNT endohedral metallofullerenes of C_{80}:

Table 4.1 Comparison of some computed and experimental bond lengths for the most stable isomers of $Sc_3N@C_{68}$, $Sc_3N@C_{78}$ and $Sc_3N@C_{80}$ endohedral metallofullerenes [a]

Complex	*Method*	*Sc–N* [b]	*Sc–C* [c]	*Source* [e]
$Sc_3N@C_{68}$	X-Ray	1.961-2.022	2.225	2
	DFT-BP	1.982	2.324	*
*$Sc_3N@C_{78}$:**1***	X-Ray	1.983-2.125	2.024	4
	X-Ray [d]	1.981-2.127	2.206	32
	DFT-BP	1.997	2.255	*
*$Sc_3N@C_{80}$:**11***	X-Ray	1.966-2.011	2.170	1
	DFT-BP	2.011-2.021	2.276	*

[a] Distances in Å. [b] Range of Sc–N bond lengths. [c] Contact distances between Sc and the nearest neighbour carbon. [d] Re-examination. [e] * means data from this work.

$ErSc_2N@C_{80}$,[11] $Sc_3N@C_{80}$[1] and $Sc_3N@C_{80}$-$C_8H_6(OCH_3)_2$.[13] However, we have chosen the most stable structure according to the calculations in order to study the bond between the nitride and the C_{80} cage. The differences among the most stable isomer are rather small, 0.00-0.10 eV, see subsection 4.3.2. In the theoretically most stable structure of $Sc_3N@C_{80}$ the three metal ions are oriented toward 6:5 C–C ring junctions, which indeed coincides with the X-ray structure observed for $Sc_3N@C_{80}\cdot Co^{II}(OEP)\cdot 1.5CHCl_3\cdot 0.5C_6H_6$.[1] This isomer will be named as $Sc_3N@C_{80}$:**11**. The mean Sc–C distances were found, again, higher than the experimental one, 2.276 Å versus 2.170 Å, but very close to the mean Sc–C distance in $Sc_3N@C_{78}$ (Table 4.1). It should be noted that the Sc–C distance of $Sc_3N@C_{80}$ is slightly shorter than those reported for other non-TNT endohedral metallofullerenes: mono- and dimetallofullerenes. For example, the shortest Sc–C distance has been estimated as 2.53 Å for $Sc@C_{82}$ [33] and 2.4 Å for $Sc_2@C_{84}$.[34] This agrees well with the calculated distances of 2.50 Å and 2.36 Å, respectively.[35] The cage radius is also slightly enlarged during the encapsulation process from 4.103 to 4.118 Å. Cage radius is defined as the average distance of all carbons to the center of the fullerene. The optimized structure of $Sc_3N@C_{80}$ is displayed in Figure 4.1b.

The third fullerene cage, which was capable of incarcerating four atoms, was the non-IPR D_3-C_{68}:**6140**.[2,36] The $Sc_3N@C_{68}$ complex is not the only non-IPR fullerene cage that has been seen to encapsulate metal units. Possible non-IPR structures have also been investigated for $Ca@C_{72}$, $La_2@C_{74}$,[37] $Ca@C_{74}$,[38] $Sc_2@C_{74}$[38,39] and $Sc_2@C_{66}$.[40] C_{74} and C_{82} cages seem to contain heptagon rings. IPR fullerene cages cannot exist in the range from C_{60} to C_{70}.[20] It is interesting to notice that the only known violations of the IPR rule are in endohedral metallofullerenes. Subsequent studies by Aihara confirmed that the IPR could not be applied to charged fullerenes.[41] For a C_{68} cage whose carbon surface consists solely of pentagons and hexagons, there are 6332 possible isomers, but the 12 ^{13}C NMR signals and a single ^{45}Sc NMR signal in the spectrum of $Sc_3N@C_{68}$ restricts these possibilities to only 11 isomers with either D_3 or S_6 symmetry.[2] On the basis of DFT calculations, isomers **6140** and **6275** emerged as the likely cage structure present in the TNT endohedral metallofullerene with D_3 symmetry.[2] Isomers **6140** and **6275** have only three fused pentagon pairs, which means that these are much more stable than other isomers that have more units like this.[42] Finally, the detailed structural characterization of $Sc_3N@C_{68}$ showed that the carbon cage is the **6140** isomer.[36] This fullerene is significantly different from the other mentioned fullerenes. Unlike other cages, the D_3-C_{68}:**6140** cage in $Sc_3N@C_{68}$ has a 5:5 ring junctions (***E*** type in appendix A.1). The distance of this kind of C–C bond is computed to be 1.436 Å. As in the D_{3h}-C_{78}:**5** cage, pyracylene C–C bonds are found in this isomer of C_{68}. The average computed distance for this type of C–C bond is 1.396 Å, similar to the 6:6 C–C bond lengths in C_{60} and C_{78}. C_{78} and C_{80} are spherical, so all carbons are approximately at the same distance from the center: the cage radius is 4.052 Å and 4.103 Å, respectively. Nevertheless, the cage radius of C_{68} is not only considerably shorter (3.783 Å) but also distorted, with only one plane which can encapsulate the TNT unit guest (Figure 4.1c). In this plane, the scandiums are directly connected to 5:5 ring junctions and the N–carbon cage distances are similar to those found in C_{78} and C_{80} cages. So, the internal structure of the nitride is planar, although only one position is possible inside the C_{68} cage. Consequently, only one isomer will be possible. Although the cavity of the C_{68} is smaller, it encapsulates the Sc_3N unit very efficiently and even has a Sc–C distances of 2.324 Å, which is longer than its $Sc_3N@C_{78}$ and $Sc_3N@C_{80}$ analogues. The experimental

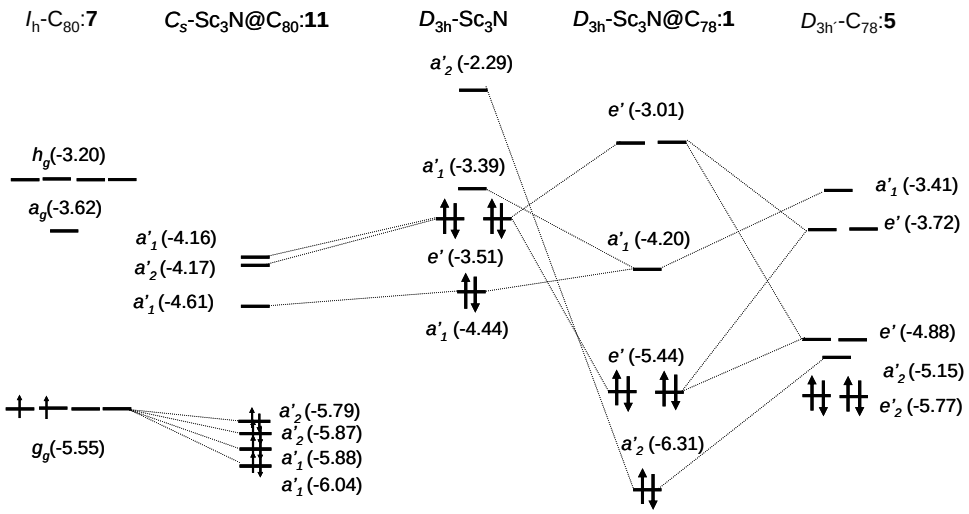

Figure 4.2 Orbital interaction diagram for $Sc_3N@C_{78}$:**1** and $Sc_3N@C_{80}$:**11**. Only the most important orbitals that participate in the bond have been drawn. The I_h-C_{80}:**7** fullerene has the open shell configuration ...$(t_{1g}+h_u)^{16}$ $(g_g)^2$ $(h_g+a_g)^0$… meanwhile the $D_{3h'}$-C_{78}:**5** fullerene has the closed shell configuration ...$(e_2)^4(a'_2)^0$...

distance (2.225 Å) also confirms this trend (Table 4.1).[36] The mean Sc–N distance is found to be 1.982 Å, slightly shorter than the distance found in $Sc_3N@C_{78}$ (1.997 Å) and $Sc_3N@C_{80}$ (2.014 Å). The TNT encapsulation causes a similar geometrical deformation of the cage for $Sc_3N@C_{68}$: the 5:5 C–C bond lengths linked to Sc atoms increase by 0.009 Å and the aforementioned C–C bond displaces outward from the fullerene surface.

4.2.2 Ionic model

The bond between the nitride and the cage is markedly defined by the ionic model $Sc_3N^{6+}@C_k^{6-}$. A total of six electrons formally go from the highest occupied nitride orbitals to the lowest unoccupied cage orbitals. $Sc_3N@C_{78}$ is the most symmetric endohedral complex (D_{3h}) and thus it will be a suitable model to explain the bond between both units. The $D_{3h'}$-C_{78}:**5** isomer has a closed–shell ground state with three low unoccupied orbitals of symmetries a'_2 (–5.15 eV) and e' (–4.88 eV) that are π antibonding orbitals basically centered in the set of C27–C28 bonds, a pyracylene C–C bond

type (see Appendix A.5). These unoccupied orbitals can receive six electrons from the three highest occupied orbitals of the TNT unit as the orbital interaction diagram of Figure 4.2 of $Sc_3N@C_{78}$ shows. The Sc_3N degenerate orbital of symmetry *e'* mixes with the lowest unoccupied fullerene orbitals of the same symmetry. The lowest one is the HOMO and is essentially a fullerene orbital. The most important orbitals involved in the charge transfer are drawn in Figure 4.4. The mixing of orbitals of *e'* symmetry leads to a formal transfer of four electrons from the Sc_3N unit to the carbon cage. Orbital a'_1 can also interact with C_{78} orbitals but the lowest a'_1 orbital in the empty fullerene is ~1.7 eV higher than the LUMO that is of a'_2 symmetry. Consequently, there is a transfer of two additional electrons from the metal orbital of symmetry a_1' to the cage orbital of symmetry a'_2. The a'_1 orbital of the Sc_3N fragment becomes the LUMO in the endohedral cluster. In summary, we concluded that formally six electrons are transferred from the nitride unit to the fullerene.

Like in C_{78}, the encapsulation of Sc_3N into the I_h-C_{80}:**7** results in a formal transfer of six electrons from the scandiums to the fullerene orbitals. Previous theoretical calculations have shown that the I_h-C_{80}:**7** isomer has the open shell configuration: $...(t_{1g} + h_u)^{16}\ (g_g)^2\ (h_g + a_g)^0$…. Moreover, I_h-C_{80}:**7** may deform to lower symmetries by Jahn-Teller effect.[43] It represents an electronic configuration with only 2 electrons in a four low-lying degenerate orbitals, –5.55 eV, which can easily accept 6 electrons. So, as a consequence of this electron charge transfer, the resulting endohedral has a closed shell configuration, Figure 4.2. From an electronic point of view, D_3-C_{68}:**6140** has got a closed-shell ground state with HOMO-LUMO gap of 0.5 eV and with three low unoccupied orbitals of symmetries *e'* (–5.38 eV) and a_1 (–4.79 eV) which can easily accept six electrons as the other two fullerenes do. Indeed, a high stabilization appears due to electron charge transfer from the three HOMOs of Sc_3N to D_3-C_{68}:**6140** cage, which is hugely stabilized since the final endohedral complex has a higher HOMO-LUMO gap of 1.27 eV. A similar gap was found for endohedral complexes of C_{78} and C_{80}: 1.24 and 1.18 eV, respectively. These electronic considerations seem to have the key to rationalize why only some cages can encapsulate metal units (in section 4.6 these ideas will be developed further).

Table 4.2 Mulliken populations for the Sc_3N unit in several TNT endohedral metallofullerenes

Molecule/Symmetry.		*Sc*				*N*	*Electron charge transfer* [c]
		Net charge	*s*	*p*	*d*	*Net charge*	
Sc_3N [a]	C_{3v}	+0.38	1.00	6.23	1.39	–1.14	--
Sc_3N [b]	D_{3h}	+0.46	1.20	6.21	1.13	–1.38	--
Sc_3N^{6+} [b]	D_{3h}	+2.59	0.00	5.93	0.48	–1.77	--
$Sc_3N@C_{68}$ [a]	D_3	+0.75	0.12	6.46	1.67	–1.36	0.89
$Sc_3N@C_{78}$:**1** [a]	D_{3h}	+0.88	0.12	6.39	1.61	–1.41	1.23
$Sc_3N@C_{80}$:**11** [a]	C_s	+0.86	0.15	6.43	1.56	–1.44	1.14

[a] Optimized structure. [b] Planar structures with Sc–N distance from distance found in $Sc_3N@C_{78}$:**1**. [c] Electron charge transfer from the Sc_3N unit to the fullerene cage (calculated from Mulliken net charges).

4.2.3 Electron charge transfer

In spite of the formal transfer, the Mulliken populations given in Table 4.2 suggest that the electron charge transfer is not so important. The atomic populations for the neutral nitride indicate that this molecule is a polar molecule with a strong negative charge localized on N (–1.14 *e*) and a positive charge on each Sc of +0.38 *e*. Taking as reference the planar form of Sc_3N, the encapsulation by C_{78} induces a lowering of 1.08 electrons in the *s* orbitals in each Sc. However, the populations of *p* and *d* orbitals increase by 0.18 and in 0.48 *e*, respectively, and the total charge of each Sc atom in the C_{78} endohedral is +0.88 *e*. The charge on the Sc atom in the endohedral is positive, but far from +2.59 *e*, the positive charge of the metal ion in a free Sc_3N^{6+} unit. Notice in values of Table 4.2, that in spite of the electron charge transfer between the neutral nitride and the fullerene, the nitrogen atom increases its negative charge up to –1.41 *e*. Globally, there is a electron charge transfer between the two units of 1.23 *e*. Mulliken population analysis given in Table 4.2 shows that the electronic population on the nitride unit and the electron charge transfer between the two moieties for the analogous $Sc_3N@C_k$ (k = 68, 80) clusters are almost identical to those found

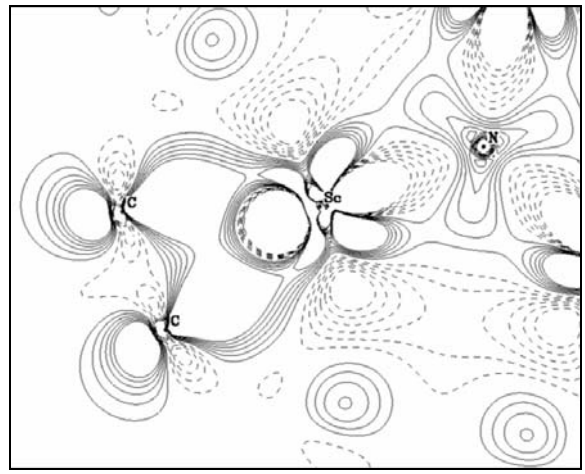

(a) $Sc_3N@C_{78}$:**1**

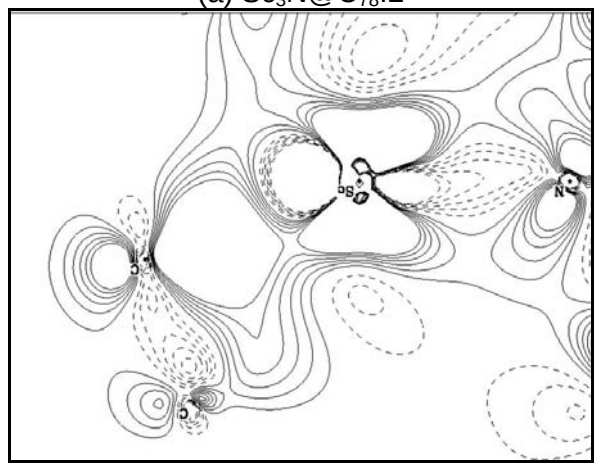

(b) $Sc_3N@C_{80}$:**11**

Figure 4.3 Electron density deformation map (EDDM) for $Sc_3N@C_{78}$:**1** (a) and $Sc_3N@C_{80}$:**11** (b)**.** The electron density that has been computed as the difference ρ(complex) – [ρ (nitride) + ρ(cage)] is represented in a plane containing Sc_3N and two carbons.

for $Sc_3N@C_{78}$. The mulliken population indicates that *s* orbitals of Sc loss this electronic density which is spread equally for all carbons in the carbon cage.

The analysis of the electron density deformation maps (EDDM) is a useful tool to characterize chemical bonds in large molecules.[44] An

Table 4.3 Decomposition of the encapsulation binding energy (EBE) for the most stable $Sc_3N@C_k$ (k = 68, 78, 80) isomers [a]

Complex	*Isom.*	ΔE_{ST}	ΔE_{ORB}	ΔE_{INT}	ΔE_{DE} [b]		*EBE* [c]
					Sc_3N	*Cage*	
$Sc_3N@C_{68}$	--	29.04	–42.04	–13.00	0.65	0.54	–11.81
$Sc_3N@C_{78}$	**1**	23.43	–35.34	–11.91	0.72	1.49	–9.70
	1 [d]	–81.62	–54.98	–136.60	--	0.72	--
$Sc_3N@C_{80}$	**11**	20.07	–33.04	–12.97	0.79	0.58	–11.60

[a] Energies are in eV. [b] Deformation energy (ΔE_{DE}) is the energy necessary to modify the fragments from its optimal geometry to the structure that have in the complex. [c] EBE = ΔE_{DE} + ΔE_{INT}. [d] Decomposition of the EBE with respect to the ionic fragments Sc_3N^{6+} and C_{78}^{6-}. The deformation energy for the Sc_3N unit was not determined since we were unable to find a minimum for the cation.

important property of the EDDMs is that they are less dependent on the basis set than the Mulliken populations. Figure 4.3 contains contour lines in the σ_h plane associated to accumulations and depletions of charge density when the electron density of $ScN_3@C_k$ (k = 78, 80) is calculated with respect its subunits Sc_3N and C_k (k = 78, 80). The electronic density exhibits accumulations close to carbons directly bonded to Sc atoms that may be associated to electronic transfers from Sc_3N to the π_{C-C}* orbitals. The accumulations near the Sc atoms show that there is a reorganization in the Sc orbitals that shows that 3*d* orbitals take an active part in the formation of the cluster. This reorganization is fully consistent with the Mulliken populations. Roszak and Balasubramanian investigated the metal–ligand bond in the simple molecule ScC_2 and concluded that the interaction between Sc and the C_2 unit is highly ionic with a strong transference to the σ C–C bond that does not occur in the present case.[45]

4.2.4 Decomposition of the encapsulation binding energy (EBE)

The bond between the C_k (k = 68, 78, 80) cage and the Sc_3N unit is also analyzed using the extended transition method developed by Ziegler and Rouk[46] and that is an extension of the well-known decomposition scheme of Morokuma.[47] According to this method, the binding energy (BE) between two fragments can be decomposed into several contributions. If BE

is related to an encapsulation process we will use the term encapsulation binding energy (EBE):

$$\text{EBE} = \Delta E_{DE} + \Delta E_{ST} + \Delta E_{ORB} \quad (4.1)$$

The first term, ΔE_{DE}, the deformation energy, is the energy necessary to convert the fragments from their equilibrium geometries to the conformation they assume in the optimized structure of the overall complex. Since the fragments have been considered in the same closed shell state both in the complex and as free molecules, this term corresponds simply to the sum of the fragment relaxation energies. ΔE_{ST} represents the steric repulsion between the two deformed fragments with the electron densities that each fragment would have in the absence of the other fragment. This term consists of two components; the first is the electrostatic interaction (ΔE_{elstat}) of the nuclear charges and the unmodified electronic charge density of one fragment with those of the other fragment and the second component is the so-called Pauli repulsion (ΔE_{Pauli}), which is essentially due to the antisymmetry requirement on the total wave function. ΔE_{ORB} known as the orbital interaction term represents the attracting orbital interactions that give rise to the energy lowering upon coordination. This term may be broken up into contributions from the orbital interactions within the various irreducible representations of the overall symmetry group of the system, according to the decomposition scheme proposed by Ziegler. The sum $\Delta E_{ST} + \Delta E_{ORB}$ is known as the fragment interaction energy and represented by ΔE_{INT}. Recently, Sgamellotti and co-workers have used this method to rationalize the C_{60}–metal bond in organometallic derivatives of C_{60}.[48]

The encapsulation process of the TNT unit into a C_{78} cage is a strongly exothermic process that yields a EBE of –9.70 eV for $Sc_3N@C_{78}$:**1**. Decomposition of the EBE with respect its components are given in Table 4.3. A free Sc_3N unit has a pyramidal geometry in which the Sc–N bond distance is computed to be 1.957 Å at the present level of theory. The ΔE_{DE} necessary for Sc_3N to achieve the planar structure with a Sc–N distance of 1.997Å, the optimal distance in $Sc_3N@C_{78}$:**1**, is 0.72 eV whereas 1.49 eV is the ΔE_{DE} that the fullerene cage requires to accommodate the Sc_3N unit in its interior. The interaction between the two fragments amounts –11.91 eV, term that is dominated by the orbital contribution (ΔE_{ORB} = –35.3 eV). The

other component to ΔE_{INT} is the steric repulsion that was found to be very positive, ΔE_{ST} = +23.4 eV. The large computed value for the orbital term corroborates that when two neutral fragments are put together there is an important electronic reorganization as we have seen through the orbital diagram in Figure 4.2 and the EDDM in Figure 4.3.

The formal transfer of six electrons between the two moieties makes also convenient the analysis of the EBE with respect to the ionic fragments Sc_3N^{6+} and C_{78}^{6-} (Table 4.3). The interaction energy between these two fragments to give $Sc_3N@C_{78}$:**1** is −136.6 eV, a large energy difference which is dominated by the classical electrostatic interaction between the two highly charged ions. The electrostatic interaction is much larger than the Pauli repulsion. Consequently the steric term, that is the sum of these two terms, is very negative; ΔE_{ST} = −81.6 eV. These two large energies are totally consistent with the high charge located on each fragment. Nevertheless, the very large contribution to the stabilizing energy associated with the orbital term is unexpected. The ΔE_{ORB} term was found to be −54.9 eV, value that is even larger than the corresponding term when the fragments are neutral. After the encapsulation of Sc_3N^{6+} by C_{78}^{6-} there is an important *orbital mixing* and consequently an important electronic reorganization that induces a transfer of charge (in this case from the anionic cage to the cationic nitride) and a polarization of each unit. Both fragment polarization and charge transfer occur simultaneously, and unfortunately they are not easy to separate. In the ionic decomposition, the ΔE_{DE} term is almost negligible in comparison to ΔE_{INT}.

The incorporation of Sc_3N into the I_h-C_{80}:**7** is somewhat more exothermic than in the case of formation of $Sc_3N@C_{78}$:**1**, since the EBE was found approximately 1.9 eV more stabilizing. The energetic difference between these two encapsulation processes essentially arises from the larger Sc–C bond distances in the larger fullerene (Table 4.1). Two factors contribute to the lengthening of Sc–C bond when going from C_{78} to C_{80}: a moderate increase of the cage radius from 4.052 Å to 4.103 Å and the different framework of these two cages. The direct consequence is that the steric repulsion (ΔE_{ST}) is less destabilizing in $Sc_3N@C_{80}$:**11**, and this lower steric repulsion is accompanied by a minor deformation energy on going from the empty cage to the endohedral geometry (Table 4.3). The orbital interaction term (ΔE_{ORB}) is also very important but somewhat minor in the

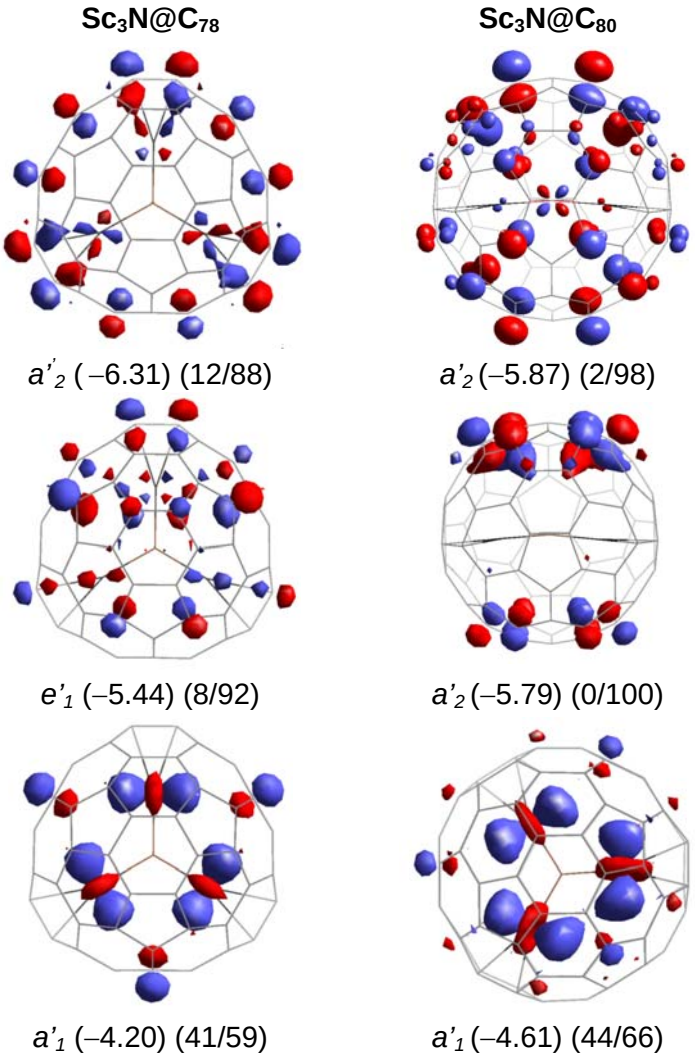

Figure 4.4 3D representations, symmetries, energies (in eV) and composition (% Sc_3N / % cage) of the most important molecular orbitals (MOs) involved in the electron charge transfer and the ionic metal bond for the $Sc_3N@C_{78}$:**1** and $Sc_3N@C_{80}$:**11** optimized complexes.

C_{80} cluster when it is compared with the most stable endohedral of C_{78}. Notice from the orbital interaction diagram in Figure 4.2 and orbital composition in Figure 4.4 that the quadruply degenerate g_g orbitals of I_h-

C_{80}:**7** are less stable than the corresponding frontier orbitals in C_{78} due to *lower mixing* with the Sc orbitals. The higher EBE for the larger cluster may be associated to the smaller steric repulsion between the two fragments and to the lower energy necessary to deform the larger fullerene (Table 4.3). The EBE for $Sc_3N@C_{80}$ is computed to be −11.6 eV, a value that is quite similar to the energy reported (−10.73 eV) very recently by Kobayashi and co-workers who studied the energetics of several isomers of $Sc_3N@C_{80}$.[24]

The EBE has also been decomposed for $Sc_3N@C_{68}$. The decomposition is quite similar to that of $Sc_3N@C_{80}$. The EBE, −11.81 eV, is even higher than for $Sc_3N@C_{80}$:**11**, −11.60. The slight advantage comes from the ΔE_{ORB} and ΔE_{DE} terms. Although the steric repulsion term of C_{68} is higher (29.04 eV) because of its smaller size, the higher stabilization in the orbital interaction (−42.04 eV) largely compensates for this destabilization. The low deformation energy (1.19 eV) also shows that this non-IPR fullerene encapsulate efficiently. The ΔE_{DE} is a little smaller than in $Sc_3N@C_{80}$:**11** (1.37 eV) and much smaller than in $Sc_3N@C_{78}$:**1** (2.21 eV). So, the final order of the EBE is: $C_{68} \approx C_{80} > C_{78}$.

4.3 ISOMERISM

4.3.1 $Sc_3N@C_{78}$

A priori, several orientations of the Sc_3N unit inside the fullerene are possible. Since the X-ray determination of $Sc_3N@C_{78}$ shows that the Sc_3N unit lies close to the original σ_h plane of the $D_{3h'}$-C_{78}:**5** cage, only isomers that retain this symmetry plane were studied. In the following discussion and in Figure 4.5 and 4.6 we consider that the Sc_3N unit is within the *xy* plane. The σ_h (or *xy*) plane crosses three pyracylene C–C bonds that are linked by hexagons as Figure 4.5 shows. By considering four additional orientations of the Sc_3N unit within the C_{78} cage, the five isomers shown in Figure 4.5 were studied. The most stable isomer, $Sc_3N@C_{80}$:**1**, which has been fully described in the first section, corresponds to the case in which the scandiums are over the pyracylene 6:6 C–C bonds, whereas in isomer **4**, the metals are over 6:5 C–C bonds. In isomer **2** the metal ions are directly connected to individual carbons. In the other two isomers, each metal is placed at the center of a pentagon (isomer **3**) or a hexagon (isomer **5**).

2D Scheme	Sym.	Isom.	RE
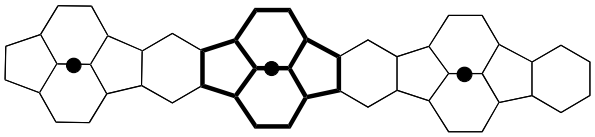	D_{3h}	1	0.00
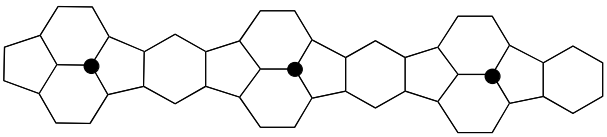	C_{3h}	**2**	+0.10
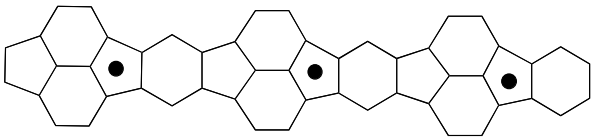	C_{3h}	**3**	+1.12
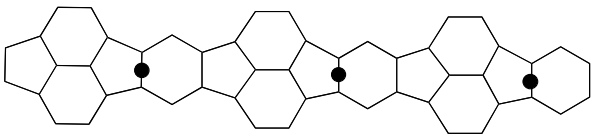	C_{3h}	**4**	+0.79
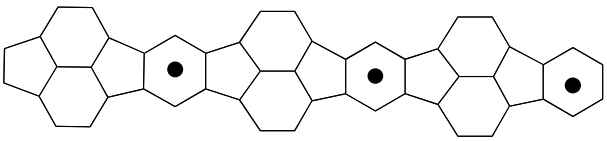	D_{3h}	**5**	+0.97

Figure 4.5 Carbon chains, symmetries, isomer number and relative energies (RE, in eV) with schematic positions of the scandiums with respect to the pyracylene C–C bond types for the $Sc_3N@C_{78}$ optimized isomers. Bold lines show the pyracylene patch in one of the 2D drawings. In the $Sc_3N@C_{78}$:**1** isomer the Sc_3N unit lies on the σ_h symmetry plane and the scandiums (represented by black dots) are over the set of pyracylene C27–C28 bonds (Fig. 4.14b and App. A.5). The rest of isomers correspond to rotations of the Sc_3N unit keeping the symmetry plane.

The fully optimization of these five isomers yields five structures with different stability. The relative energies (REs) for isomers **1**-**5** are collected in Figure 4.5. Isomer **1**, with the three scandiums bonded to the pyracylene 6:6 C–C bonds, gives the best orientation for the trimetallic unit inside the cage, an orientation that is 0.79 eV more stable than when the

Table 4.4 Decomposition of the encapsulation binding energy (EBE) for the $Sc_3N@C_{78}$ optimized isomers [a]

Isomer	ΔE_{ST}	ΔE_{ORB}	ΔE_{INT}	ΔE_{DE} [b]		*EBE* [c]
				Sc_3N	*Cage*	
1	23.43	–35.34	–11.91	0.72	1.49	–9.70
2	22.88	–34.54	–11.66	0.67	1.37	–9.62
3	21.60	–31.86	–10.26	0.62	1.05	–8.59
4	21.76	–32.69	–10.93	0.62	1.38	–8.93
5	21.47	–32.15	–10.68	0.65	1.29	–8.74

[a] Energies are in eV. [b] Deformation energy (ΔE_{DE}) is the energy necessary to modify the fragments from its optimal geometry to the structures that have in the endohedral cluster. [c] EBE = ΔE_{DE} + ΔE_{INT}.

three metals are over the 6:5 ring junctions (isomer **4**). The RE of isomers **3** and **5** with respect to **1** are +1.12 and +0.97 eV, respectively. These values clearly indicate that the nitride unit *can not freely rotate* inside the fullerene cage. However, a rotation of the Sc_3N unit by only 10 degrees in isomer **1** yields structure **2** in which the metals are linked to a unique carbon atom. Since the energy difference between these two isomers is only 0.1 eV, the conversion of **1** to **2** is nearly barrierless. This fact suggests that, although the rotation of the Sc_3N unit is hindered, the structure of the complex may fluctuate dynamically between these two forms. Several attempts have been made to obtain a C_{3v} complex with a pyramidal Sc_3N unit inside the fullerene. However, the optimization process always yielded a geometry with a planar Sc_3N unit.

Table 4.4 contains the decomposition energy terms of the EBE for isomers **1-5**. The values for isomer **2** are very similar to those of isomer **1** since both structures are very close. For the other three isomers **3-5** the repulsive steric term and the stabilizing orbital term are smaller in magnitude than in **1** but the decrease is larger in the orbital term. Consequently, ΔE_{INT} is less stabilizing when the scandium ions are focusing other sites than those close to carbons that form 6:6 ring junctions. In other words, when the Sc ions are over 6:6 C–C bonds the mixing of orbitals between the two fragments is maximized. Nevertheless, the *intrinsic* electronic and steric properties of the different fullerene sites are better

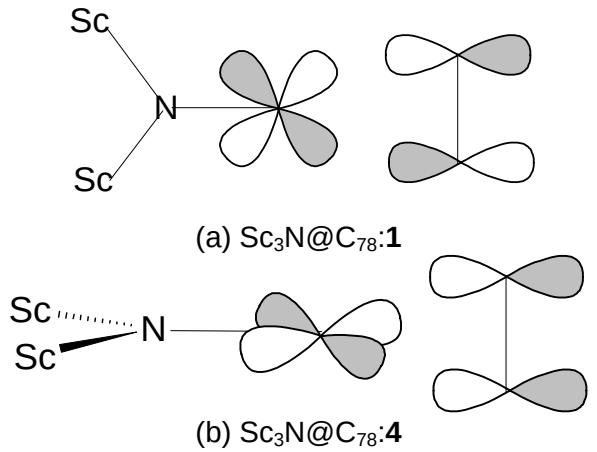

Figure 4.6 In-plane bonding interaction between a Sc metal and a 6:6 C–C bond in $Sc_3N@C_{78}$:**1** isomer (a) and non-bonding interaction between a Sc metal and a 6:5 C–C bond in $Sc_3N@C_{78}$:**4** isomer (b).

understood if fixed fragment geometries are used in the energy decomposition analysis. This process allows us isolate the changes in ΔE_{INT} from the effects due to changes in the geometry of the fragments. This procedure has been effective in identifying ligand donor and acceptor properties in organometallic complexes.[49] We have studied the interaction between a planar Sc_3N unit with the Sc–N distance equal to 1.975 Å —an intermediate value between 1.966 and 1.983 Å, the most frequent observed Sc–N bond lengths in these endohedral clusters— and a carbon cage with the geometry of the free fullerene.

Using these unrelaxed fragments we have searched the best orientation of a fixed planar Sc_3N unit in a rigid C_{78} cage for the five orientations described in Figure 4.5. Roughly, the REs obtained with the unrelaxed structures (Table 4.5) are quite similar to those found for the optimized clusters (Figures 4.5). Notice that in these model structures the deformation energy is only due to the Sc_3N fragment and has the same value for all orientations. This contribution has not been included in Table 4.5. Because of the similar environment that scandium ion has in **1** and **4**, the steric term is not very different in these two isomers. Therefore, the higher stabilization when Sc ions reside over a 6:6 C–C bond arises from the

Table 4.5 Decomposition of the interaction energy (ΔE_{INT}) for the $Sc_3N@C_{78}$ model complexes [a]

Isomer	ΔE_{ST} [b]	ΔE_{ORB} [c]	ΔE_{INT} [d]
1	26.76	–34.91	–8.15
2	26.58	–34.69	–8.11
3	26.42	–33.82	–7.40
4	26.85	–34.02	–7.17
5	25.69	–33.18	–7.49

[a] Energies are in eV. [b] Steric energy (ΔE_{ST}) includes Pauli repulsion + classical electrostatic interaction. [c] The orbital interaction term (ΔE_{ORB}) accounts for the stabilization produced when fragment orbitals of each subunit Sc_3N and C_{78} mix for giving the endohedral cluster. [d] Fragment interaction energy ($\Delta E_{INT} = \Delta E_{ST} + \Delta E_{ORB}$) is the resulting stabilizing energy associated to the interaction between the planar Sc_3N (d_{Sc-N} = 1.975Å) and D_{3h}-C_{78}:**5** at its optimal free geometry.

orbital contribution. The larger contribution of the ΔE_{ORB} term to ΔE_{INT} in **1** may be attributed to the effective overlap between the cage orbitals of symmetries *e'* and a_2*'* and the Sc d_{xy} type orbitals (Figure 4.6). This overlap does not occur when Sc atoms reside over 6:5 C–C bonds, as in isomer **4**, since the *e'* and a_2*'* cage orbitals in the 6:5 ring junctions regions are perpendicular to the Sc_3N plane (Figure 4.6). When the Sc ions are placed at the center of a pentagon (isomer **3**) or a hexagon (isomer **5**), the ΔE_{ST} and ΔE_{ORB} terms are smaller in absolute values than in **1**, because the Sc–C distances are larger. The longer Sc–C distances create less effective fragment orbital overlap but smaller steric repulsions. The loss of overlap effectiveness is higher than the diminution of the steric repulsion. Consequently, ΔE_{INT} in **3** and **4** are smaller than in **1**. In other words, when the scandium orbitals, localized in the symmetry plane, interact with the cage orbitals there is a gradual stabilization of the interacting cage orbitals. This effect reaches a maximum in isomer **1**. In summary, the analysis on the model structures clearly shows that Sc_3N is trapped in specific position due to an *orbital* effect.

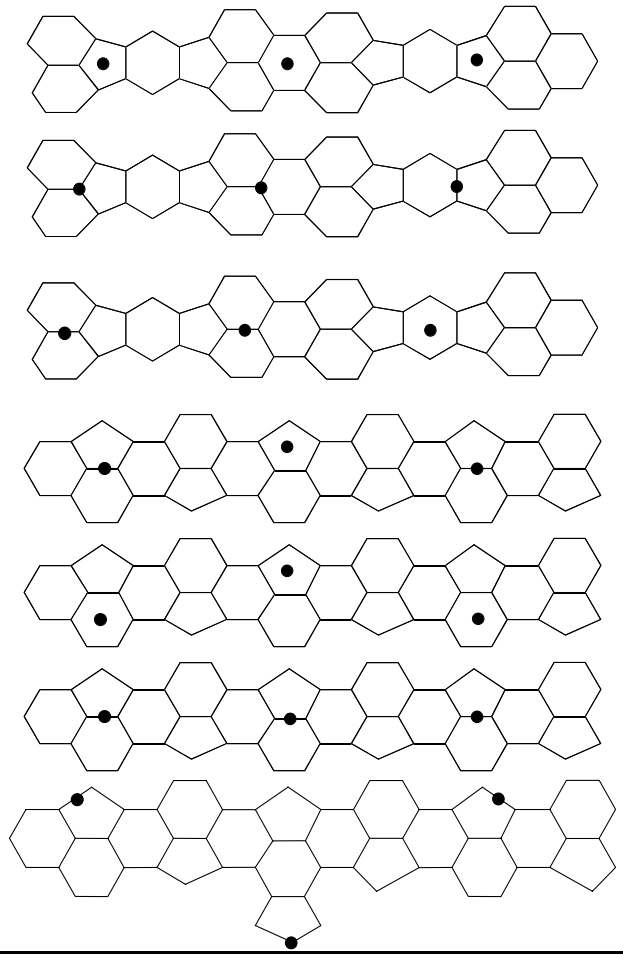

2D Scheme	Sym.	Isom.	RE
	C_{2v}	**6**	+0.23
	C_s	**7**	+0.06
	C_s	**8**	+0.08
	C_s	**9**	+0.07
	C_s	**10**	+0.04
	C_s	**11**	0.00
	C_s	**12**	+0.01

Figure 4.7 Carbon chains, symmetries, isomer number and relative energies (REs, in eV) with schematic position of scandiums in a 2D representation for the $Sc_3N@C_{80}$ optimized isomers. In isomer **6** the Sc_3N unit lies on one of the symmetry planes that retains the endohedral. Isomers **7** and **8** are simply rotations of the Sc_3N unit with respect **6**. Isomers **9**, **10, 11** and **12** have also C_s symmetry but in these isomers the symmetry plane contains the nitrogen atom and only one of the metals. Like in Figure 4.5 the relative position of scandiums with respect to the cage is represented by black dots in the 2D scheme. Isomer **11** is the most stable overall, the scandiums are facing the corannulene 6:5 C–C bonds: C24–C25, C31–C32 and C67–C68 (see Figure 4.12c and Appendix A.6).

4.3.2 $Sc_3N@C_{80}$

Following the same strategy used for C_{78}, we have studied several orientations of the TNT unit inside the fullerene. The orientations considered have always maintained one plane of symmetry in the endohedral. Figure 4.7 shows the seven structures we have considered. In three of them (**6**-**8**), the molecular plane of the Sc_3N unit coincides with the symmetry plane of the endohedral cluster. In the other four orientations (**9**-**12**) the plane of symmetry contains the N atom and one of the Sc atoms, the symmetry plane relates the other two Sc's.[50] With these seven isomers we have tried to cover a large number of the alternatives where the metals can found inside the icosahedral isomer of C_{80}. In structure **6**, the three metals are directed toward the center of two pentagons and one hexagon. Isomers **7** and **8** represent slight rotations of the trimetallic unit in relation to **6**, whereas in **11** the three metal ions are oriented toward 6:5 ring junctions and finally structures **9**, **10** and **12** correspond to a slight change in relation to **11**. Indeed, this later structure is computed to be the most stable and coincides with the X-ray structure observed for $Sc_3N@C_{80}{\cdot}Co^{II}(OEP){\cdot}1.5CHCl_3{\cdot}0.5C_6H_6$.[1] The geometry found for $ErSc_2N@C_{80}$ [11] is better represented by isomer **7** whereas the orientation of Sc_3N inside the functionalized $Sc_3N@C_{80}$-$C_8H_6(OCH_3)_2$[13] adjusts to isomer **12**. Like in the endohedral of C_{78} the theoretical Sc–C distances for $Sc_3N@C_{80}$ are longer than the experimental ones but the differences are smaller. On the other hand, our structures for isomers **8** and **9** almost coincide with those found by Kobayashi and co-workers using the B3LYP functional.[24] The geometries of the distinct isomers are in Table 4.6.

The energy difference between the distinct isomers is rather small, < 0.08 eV for the majority of the Sc_3N orientations (Figure 4.7) corroborating the variety of Sc_3N orientations found in the experimental complexes. Only in isomer **6**, in which the three ions are oriented toward the center of three polygons, is the RE of the cluster is somewhat higher, 0.23 eV with respect to **11**. These REs for the $Sc_3N@C_{80}$ isomers yield the conclusion that the Sc_3N unit may easily rotate inside the fullerene cage and there is not any preferred position for TNT unit inside the cage unlike the cases of $Sc_3N@C_k$ (k = 68, 78). The fast rotary motion of Sc_3N^{6+} is consistent with the observed ^{13}C NMR spectrum consisting of only two resolved lines with an

Table 4.6 Comparison of some computed and experimental bond lengths for several $Sc_3N@C_{80}$ isomers [a]

Isomer	*Method*	*Sc–N* [b]	*Sc–C* [c]	*Source* [d]
7	X-Ray [d]	1.97-2.06	2.03	4
	DFT-BP	2.004-2.018	2.272	*
8	DFT-B3LYP	2.020-2.029	2.329	24
	DFT-BP	2.008-2.034	2.259	*
9	DFT-B3LYP	2.014-2.029	2.320	24
	DFT-BP	2.010-2.021	2.284	*
11	X-Ray	1.966-2.011	2.170	1
	DFT-BP	2.011-2.021	2.276	*
12	X-Ray [e]	2.021-2.032	2.244	13
	DFT-BP	2.008-2.019	2.258	*

[a] Distances in Å. [b] Range of Sc–N bond lengths. [c] Contact distances between Sc and the nearest neighbour carbons. [d] Average values obtained for $ErSc_2N@C_{80}$. [e] Values obtained for $Sc_3N@C_{80}$-$C_8H_6(OCH_3)_2$. [d] * means data from this present work.

intensity ratio of 3/1, which preserves overall I_h symmetry for the carbon on the NMR time scale.[1]

4.4 PHYSICAL PROPERTIES

Calculations were also carried out to calculate the vertical electron affinity (EA) and ionization potential (IP) of these TNT endohedral metallofullerenes (Table 4.7). In general, fullerenes, exhibit relatively large EAs, and this is related to the presence of low-lying unoccupied orbitals. Smalley and co-workers used photoelectron spectra to estimate an EA of *ca.* 2.60-2.80 eV for C_{60}.[51] In the gas phase, C_{60} can accept two electrons, which gives rise to the C_{60}^{2-} ion. In solution electrochemical studies have shown that C_{60} can be easily reduced to form the ions C_{60}^{n-} (n = 1-6). At the present level of theory, the adiabatic and vertical EAs for C_{60} are computed to be 2.88 and 2.85 eV, respectively. These values are in excellent agreement with

Table 4.7 Vertical ionization potentials (IPs) and electron affinities (EAs) for several optimized molecules [a]

Molecule	*Sym.*	*IP*	*EA*	*E(HOMO)*	*E(LUMO)*	*HOMO-LUMO gap*
Sc_3N	C_{3v}	5.05	1.27	–3.21	–2.92	0.29
C_{60}	I_h	7.57	2.85	–6.25	–4.59	1.66
C_{68}	D_3	7.11	3.71	–5.90	–5.39	0.51
C_{78}**:5**	D_{3h}	6.88	3.49	–5.77	–5.15	0.62
C_{80}**:7**	I_h	6.92	3.75	–5.55	–5.55	0.00
$Sc_3N@C_{68}$	D_3	6.63	2.47	–5.48	–4.21	1.27
$Sc_3N@C_{78}$**:1**	D_{3h}	6.53	2.55	–5.44	–4.20	1.24
$Sc_3N@C_{80}$**:11**	C_s	6.88	2.99	–5.79	–4.61	1.18

[a] Energies in eV.

the experimental data.[52] The isolated D_3-C_{68}:**6140**, $D_{3h'}$-C_{78}:**5** and I_h-C_{80}:**7** clusters have larger vertical EAs: 3.71, 3.49 and 3.75 eV, respectively. The formal transfer of six electrons from the Sc_3N unit to the cage reduces the EA of these three TNT endohedral metallofullerenes with respect to that of the free fullerenes. This can be seen in Figure 4.8. The computed EA for $Sc_3N@C_{80}$ (2.99 eV) completely agrees with the experimental value of 2.81 ± 0.05 eV estimated by Ioffe et al.[53] To our knowledge, no EA has been determined for $Sc_3N@C_{68}$ and $Sc_3N@C_{78}$. These electronic behavior differs from the behavior of the classical endohedral metallofullerenes such as $M_n@C_k$ (M = Sc, Y, La, Gd; n = 1, 2). The EAs of the mono- and dimetallofullerenes are higher than those of the corresponding free fullerenes (between 3.2-3.4 eV). Nevertheless, the relatively large EAs calculated for $Sc_3N@C_k$ (k = 68, 78, 80) suggest that these complexes, like C_{60}, should still be easily reducible. It is important to notice from the values in Table 4.7 that the EAs of the endohedral metallofullerenes are not compared to the EA of the most stable empty isomer.

The HOMOs in $Sc_3N@C_k$ (k = 68, 78, 80) are somewhat less stable than are the HOMOs in C_{60} and C_k (k = 68, 78, 80). Therefore, the IPs of these endohedrals are slightly smaller than those of free fullerenes. Another interesting feature is that these three TNT endohedral metallofullerenes have

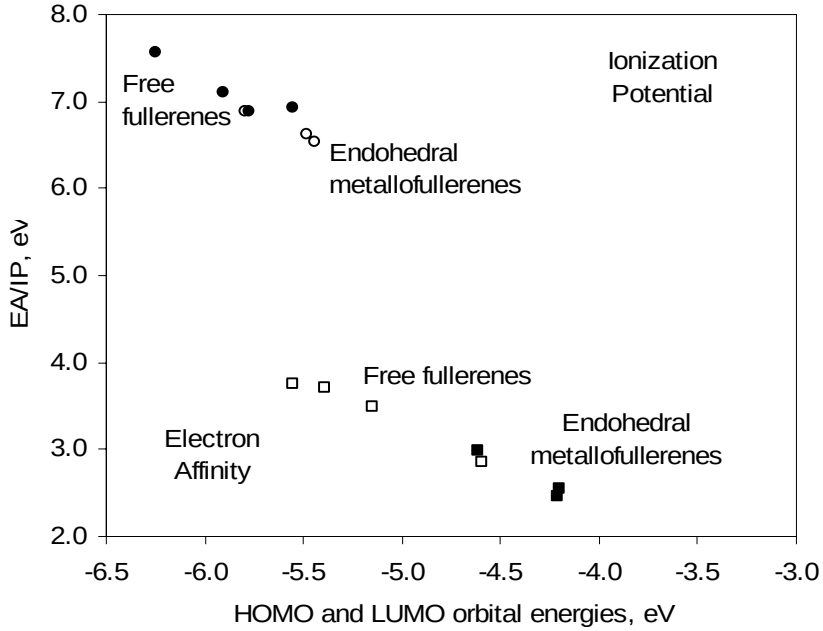

Figure 4.8 Vertical ionizaton potentials (IPs) and vertical electron affinities (EAs) versus HOMO and LUMO energies, respectively, for the free C_{60}, D_3-C_{68}:**6140**, $D_{3h'}$-C_{78}:**5**, I_h-C_{80}:**7** and their TNT endohedral metallofullerenes: $Sc_3N@C_{68}$, $Sc_3N@C_{78}$:**1** and $Sc_3N@C_{80}$:**11**.

moderately large HOMO-LUMO gaps, which explains their relative stability and abundance. In conclusion, TNT endohedral metallofullerenes are better electron donors and worse electron acceptors than the corresponding free fullerenes.

4.5 EXTENDED FAMILY: $M_3N@C_k$ (M = La, Y; k = 78, 80)

4.5.1 Experimental considerations

The Krätschmer-Huffman electric-arc generator has not only produced the previously studied TNT endohedral metallofullerenes ($Sc_3N@C_k$, k = 68, 78, 80) in relatively high yield but also a complete

Table 4.8 Geometric properties for several $M_3N@C_k$ (M = Sc, Y, La; k = 68, 78, 80) endohedral metallofullerenes [a]

Complex	*M*	*M–N* [b]	*M–C* [c]	*Pyram-idalization* [d]	*Cage radius*	*Electron charge transfer* [e]
$M_3N@C_{68}$	Sc	1.982	2.324	0.000	3.805	0.89
$M_3N@C_{78}$:**1**	Sc	1.997	2.255	0.000	4.069	1.23
	Y	2.056	2.350	0.502	4.087	2.14
	La	2.176	2.474	1.130	4.094	2.62
$M_3N@C_{80}$:**11**	Sc	2.014	2.282	0.122	4.118	1.14
	Y	2.076	2.380	0.337	4.129	1.72
	La	2.168	2.487	0.995	4.140	2.41

[a] Distances in Å. [b] Mean distance. Free values for C_{3v}-Sc_3N: Sc–N 1.957 Å and pyr. 0.934 Å. C_{3v}-Y_3N: Y–N 2.097 Å and pyr. 0.596 Å. C_{3v}-La_3N: La–N 2.218 Å and pyr. 1.126 Å. [c] Contact distances between M and the nearest neighbour carbon. [d] Separation between the nitrogen atom at the center of the cage and the final optimal position in the TNT endohedral metallofullerene, see also note b. [e] Electron transfer from the TNT unit to the cage calculated from the Mulliken net charges.

family of endohedral mixed-metallofullerenes: $A_nB_{3-n}N@C_k$ (n = 0-3, k = 68, 78, 80) where A and B are Sc, Y, La and rare-earth metals. These family members are prepared using graphite rods filled with A_2O_3, B_2O_3, powdered graphite and cobalt oxide under N_2 atmosphere. Some of these endohedral metallofullerenes with rare-earth metals have already been characterized spectroscopically[8,12] and, the mixed $Sc_{3-n}La_nN@C_{80}$ (n = 0-3) clusters have also been fully described theoretically by Kobashi et al.[24] To complete our study about TNT endohedral metallofullerenes, we shall discuss the encapsulation of the Y_3N and La_3N TNT units inside the $D_{3h'}$-C_{78}:**5** and I_h-C_{80}:**7** cages. Our primary concern is to reveal how the geometry and electronic structure differs from that of the previous analogous complexes and discuss some theoretical disagreements on the electronic structure of these non-scandium TNT endohedral metallofullerenes.

4.5.2 Geometry considerations

The most stable isomers for $M_3N@C_k$ (k = 78, 80; M = Y, La) complexes are found to be the same as those for $Sc_3N@C_{78}$ (isomer **1**) and $Sc_3N@C_{80}$ (isomer **11**). In the C_{78} cage, the M_3N (M = Y, La) TNT unit is also set in one position. In C_{80}, the encapsulation of Y_3N and La_3N units destabilises isomer **6** by 0.18 eV and 0.04 eV, respectively, with regard to the most stable isomer **11**. So, the nitride is allowed to rotate as the previous $Sc_3N@C_{80}$ complex does. The discussion will focus on the C_{80} because the C_{78} is not significant different with respect to the higher fullerene. Unlike Sc_3N, both M_3N (M = Y, La) TNT units retain their original pyramidal structure inside the cages. The pyramidalization of M_3N unit increases in the order Sc < Y < La, as can be seen in the optimal structures in Figure 4.9. The pyramidalization of M_3N unit is calculated as the distance between the center of the cage and the final optimal position of the nitrogen atom. For example, the pyramidalization was calculated to be 0.122 Å, 0.337 Å and 0.995 Å for Sc, Y and La in $M_3N@C_{80}$:**11**. The behavior of the Y atom will always be between that of the Sc atom and the La atom because of the intermediate atomic radii and electronegative character. The non-planarization of the M_3N unit is due to the lack of space since the M–N and M–C (M = Y, La) distances are longer than the Sc–N and Sc–C distances. For example, the mean M–N distance increases from 2.014 Å (M = Sc) to 2.168 Å (M = La) and the mean M–C distance increases from 2.282 Å (M = Sc) to 2.487 Å (M = La) for $M_3N@C_{80}$:**11** (Table 4.8). Furthermore, the cage radius increases in the same order as pyramidalization does. The cage radius for the free C_{80} is computed to be 4.103 Å whereas $La_3N@C_{80}$:**11** has the highest value in these TNT endohedral metallofullerenes (4.140 Å). The lack of space causes the nitride to pyramidalize and the fullerene cages to undergo major deformation.

4.5.3 Electronic structure

The electronic structure can also be presented by the ionic model proposed for the Sc analogous complexes: $M_3N^{6+}@C_k^{6-}$ (k = 68, 78, 80; M = Y, La). In detail, the scandium-based TNT units in the endohedral complexes can even be explained as $(Sc^{3+})_3(N^{3-})$. Instead of this formal

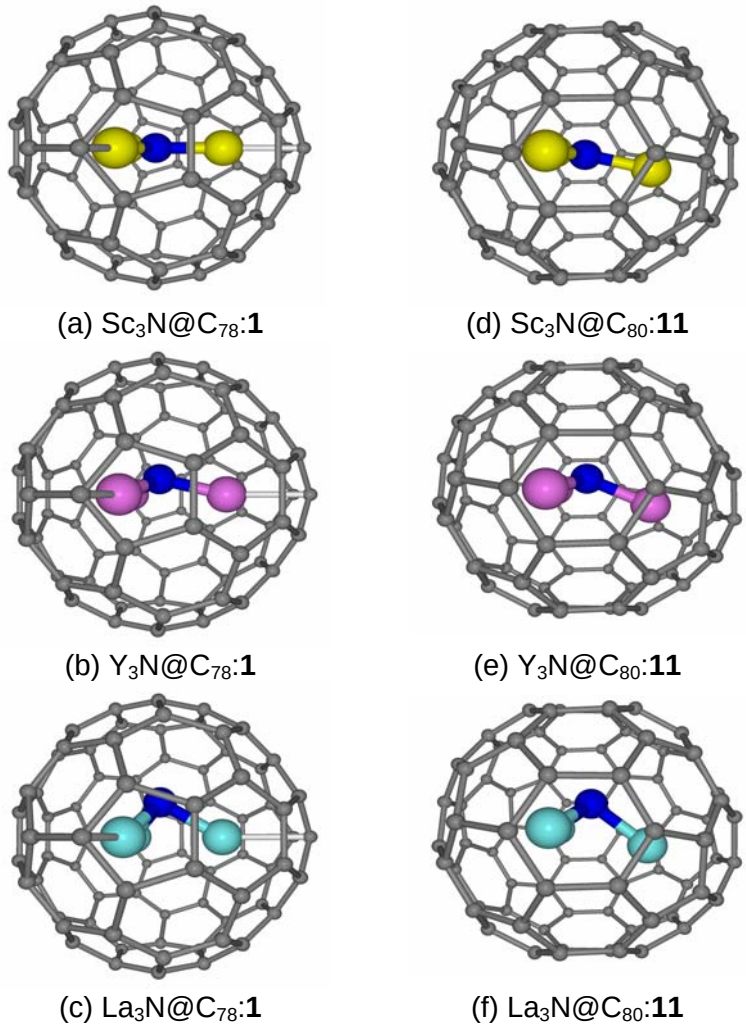

Figure 4.9 Optimized structures for $M_3N@C_{78}$:**1** (M = Sc (a), Y (b) and La (c)) and $M_3N@C_{80}$:**11** (M = Sc (d), Y (e) and La (f)).

charge of +3 on scandiums there is a more reliable Mulliken net charge of +0.86 *e* for $Sc_3N@C_{80}$:**11.** Electrons should be easier to remove from M_3N (M = Y, La) units than from Sc_3N. Indeed, the positive charges of +1.22 *e*

on Y and +1.12 *e* on La atoms are much larger than those of Sc atoms in $Sc_3N@C_{80}$:**11**. It is important to point out that the effect of these larger positive charges on the metals (Y and La) is that the electrostatic repulsion between metals is higher. This repulsion should be reduced by planarising the M_3N (M = Y, La) unit, as happened for Sc_3N. However, planarization is not permitted for M_3N (M = Y, La) units because of restrictions in cage size and the increase in M–N and M–C distances. For this reason, the M_3N (M = La, Y) unit is forced to maintain a pyramidal structure, which is as big as the M–N and M–C distances. The total Mulliken electron charge transfer from TNT unit to the cage is calculated in Table 4.8. This gradually increases from Sc to La TNT units. Despite these increases in the electron charge transfer, the description of $La_3N^{8+}@C_{80}^{8-}$ proposed by Kobayashi et al.[24] is not justified. This ionic model involves removing electrons from the highly stabilized nitrogen 2*p* shell, which (in the case of La) is 2.58 eV below the three donation occupied orbitals of La_3N. The $M_3N^{6+}@C_k^{6-}$ model only proposes the formal transfer of three electrons from the highest occupied orbitals of each metal: $3d^14s^2$ for Sc, $4d^15s^2$ for Y and $5d^16s^2$ for La, which are very predisposed since they are very destabilized (Figure 4.2). Furthermore, the $La_3N^{8+}@C_{80}^{8-}$ model would involve an open-shell electronic state that would lead to a higher reactivity than $Sc_3N@C_{80}$:**11**. Actually, the $La_3N@C_{80}$:**11** complex has a relatively big HOMO-LUMO gap of 1.422 eV, which confers the same stabilization as scandium-based TNT endohedral metallofullerenes.

4.5.4 Decomposition of EBE

The lack of space for the TNT units to expand freely makes $M_3N@C_k$ (M = Y, La; k = 78, 80) complexes less stable than the Sc analogous complexes. The decomposition of EBE for all non-scandium based TNT endohedral metallofullerenes is collated in Table 4.9. The decrease of the EBE follows the order of the group Sc < Y < La. The reduction for C_{78} is *ca.* 37 %, from –9.70 eV for Sc to –6.10 eV for La. In the case of C_{80}, the reduction is of 19 %. This reduction in the stability is consistent with the observation that the yield of $La_3N@C_{80}$ is one-fifth that of $Sc_3N@C_{80}$.[54] Actually, the lower yields for the $Sc_{3-n}La_n@C_{80}$ (n = 0-3) complexes are also consistent with the significantly higher increase in the

Table 4.9 Decomposition of the encapsulation binding energy (EBE) for $M_3N@C_k$ (M = Sc, Y, La; k = 68, 78, 80) [a]

Complex	*M*	ΔE_{ST}	ΔE_{ORB}	ΔE_{INT}	ΔE_{DE} [b]		*EBE* [c]
					Sc_3N	*Cage*	
$M_3N@C_{68}$	Sc	29.04	–42.04	–13.00	0.65	0.54	–11.81
$M_3N@C_{78}$:**1**	Sc	23.43	–35.34	–11.91	0.72	1.49	–9.70
	Y	30.57	–40.78	–10.21	0.04	2.70	–7.47
	La	35.57	–44.36	–8.79	0.06	2.63	–6.10
$M_3N@C_{80}$:**11**	Sc	20.07	–33.04	–12.97	0.79	0.58	–11.60
	Y	27.11	–38.57	–11.46	0.01	1.17	–10.28
	La	28.76	–39.80	–11.04	0.11	1.53	–9.40

[a] Energies are in eV. [b] Deformation energy (ΔE_{DE}) is the energy necessary to modify the fragments from its optimal geometry to the structures that have in the endohedral cluster. [c] EBE = ΔE_{DE} + ΔE_{INT}.

ionic radii of La (1.045 Å) than in those of Y (0.900 Å) and Sc (0.745 Å). The increment in the deformation energy (ΔE_{DE}) of the cage and also of the steric term (ΔE_{ST}) reduces the EBE. The La_3N TNT unit has the highest effects (just observe the ΔE_{DE} values for $M_3N@C_{80}$:**11** are 0.58 eV (Sc), 1.17 eV (Y) and 1.53 eV (La); and the corresponding ΔE_{ST} values are 20.07 eV, 27.11 eV and 28.76 eV). The deformation energy of the cage can be attributed to the increment in the cage radius. As expected, the energy involved in the deformation of the TNT unit is almost unappreciable: 0.01 eV for Y_3N and 0.11 for La_3N. On the other hand, the ΔE_{ST} increases because the electron transfer from the Y and La TNT units to the cage is higher, which in turn increases the repulsion between the charged fragments. In general, however, it is expected that the encapsulation of new TNT units containing a variety of metals will extend and enrich the research area of endohedral metallofullerenes.

4.6 GENERAL RULE FOR THE STABILIZATION OF CAGES ENCAPSULATING TNT UNITS

4.6.1 The stability can be predicted

The incorporation of a TNT unit into the fullerene results in an electron transfer from the metals to the carbon cage, in other words, the formation of a stable ion pair. Up to now, only four carbon cages have been capable of encapsulating TNT units: D_3-C_{68}:**6140**, $D_{3h'}$-C_{78}:**5**, D_{5h}-C_{80}:**6** and I_h-C_{80}:**7**. All these cages, except C_{68}, satisfy IPR. However, these fullerene isomers do not coincide with the most stable isomers for these stoichiometries: C_k (k = 78, 80). It is interesting to see that the empty fullerene isomers isolated so far are different from the carbon cages found in isolable endohedral metallofullerenes.[55] It should be noted that these fullerene cages are produced only when they are negatively charged by the encapsulated species. If a Sc_3N moiety is not encapsulated in these cages, they will possibly be very reactive in arc-discharge conditions. None of fullerene isomers that encapsulate TNT units have been isolated from fullerene soot as free fullerenes. Obviously, this is because the electron charge transfers from the metal units to the fullerene cages drastically change the relative stability of the fullerene isomers. Theoretical calculations indicated that the thermodynamic stability of a fullerene molecule depends heavily on the negative charge that resides on it.[19] So, TNT units can stabilize unconventional cage structures. Consequently, the stability of TNT endohedral metallofullerenes cannot be predicted from the theoretical methods used for the empty fullerene molecules, such as the IPR. Which fullerene cages will be capable of encapsulating TNT units? How can the stability of the TNT endohedral metallofullerenes be predicted? Some answers to these questions are now available and have almost been accepted by the scientific community. Firstly, Aihara et al. proposed a method related to the kinetic stabilization of the empty cages: the bond resonance method (BRE). Secondly, the observation of the electronic structure of the precursor fullerene cage gives us new ideas on how to rationalize the stabilization of these TNT endohedral metallofullerenes.

4.6.2 Bond resonance energy (BRE) method

The bond resonance energy method has been applied satisfactorily not only to TNT endohedral metallofullerenees but also to classical endohedral metallofullerenes that generally contain one, two or three metals: $M_n@C_k$ (n = 0-3). The non-TNT endohedral metallofullerenres were first synthesized, studied and characterized. The increase in the stability of the fullerene that contains positive charged units can be attributed to two main factors: first, the π-electronic systems of the fullerene shell are stabilized, and, second, there are an electrostatic interaction between the anionic shell and the cation metal inside it. Aihara studied the kinetic stability of free fullerenes and endohedral metallofullerenes using the BRE model.[56] Kinetic stability means stability against any chemical reaction or decomposition.[57,58] The BRE, defined in Hückel theory, represents the contribution of a given π bond to the topological resonance energy (TRE) of the molecule.[59] If the minimum BRE of a given molecule or its molecular ion has a large negative value, it will be kinetically very unstable with chemically reactive sites. Isolable fullerene cages and endohedral metallofullerenes were found to be devoid of reactive C–C bonds with large negative BREs. Aihara demonstrated that kinetically unstable fullerenes tend to form kinetically stable endohedral metallofullerenes. In this way Aihara detected the 15 kinetically unstable fullerene isomers between C_{60} and C_{84}.[60] Subsequently, they successfully investigated how many electrons must be added to unstable structures if they are to become kinetically stable and correlated this data with the accepted ionic model for endohedral metallofullerenes $M_n@C_k$.[60] As far as TNT endohedral metallofullerenes were concerned, Aihara concluded that D_3-C_{68}:**6140**, $D_{3h'}$-C_{78}:**5**, D_{5h}-C_{80}:**6** and I_h-C_{80}:**7** had a minimum BRE, like free fullerenes, but had the impressive capacity to accept six electrons and become extremely kinetically stable.[60,41] Aihara also corroborated that the complex with a formal charge distribution of $La_3N^{8+}@C_{80}^{8-}$ must be kinetically unstable because it contains the octaanion with minimum BRE. This electronic distribution, therefore, does not explain its relative stabilization. In conclusion, Aihara et al. provided a general explanation for the particular stabilization of some empty fullerene cages encapsulating TNT and other metal units.

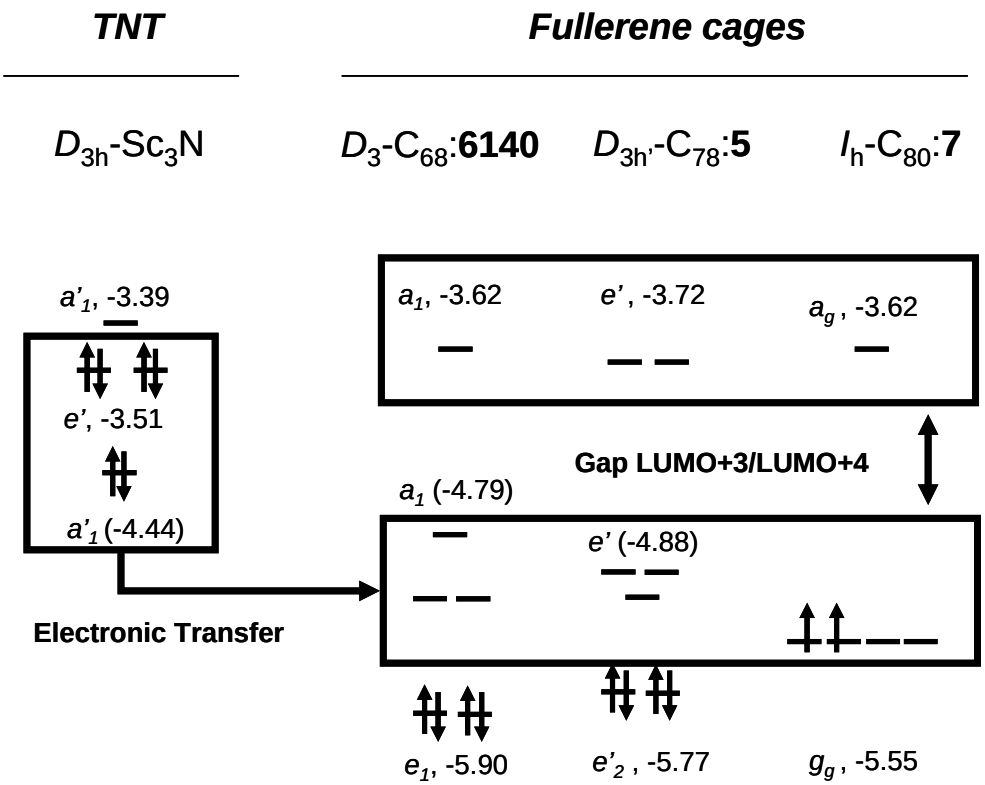

Figure 4.10 The ionic bond between the trimetallic nitride template (TNT) and the fullerene cages: D_3-C_{68}:**6140**, $D_{3h'}$-C_{78}:**5** and I_h-C_{80}:**7**. There is a formal transfer of six electrons of the three highest occupied orbitals of the TNT unit to the three low unoccupied orbitals of the fullerene cages. Consequently, the $M_3N@C_k$ (k = 68, 78, 80) complexes are described as $Sc_3N^{6+}@C_k^{6-}$ with a relatively big HOMO–LUMO gap nearly equal to the LUMO+3–LUMO+4 found in the free cages.

4.6.3 LUMO+3–LUMO+4 gap method

We have observed that the three cages studied here —D_3-C_{68}:**6140**, $D_{3h'}$-C_{78}:**5** and I_h-C_{80}:**7**— have three very low-lying LUMOs accompanied with non- or very small HOMO-LUMO gaps. These cage orbitals can easily accommodate the six electrons that come from the three destabilized TNT HOMOs. Note also that these cages have a large energy separation between the LUMO+3 and LUMO+4 as a consequence of the stabilization of the

three LUMOs mentioned above (see the electronic structure described in Figure 4.10). The electronic structure of the empty fullerenes means that it acquires a considerable HOMO–LUMO gap after a six electron transfer. It confers stability. Indeed, the final HOMO–LUMO gap of the TNT endohedral metallofullerenes can be estimated from the gap between LUMO+3 and LUMO+4 in the free cages. The calculated and estimated values are for $Sc_3N@C_{68}$: 1.27 / 1.17 eV; for $Sc_3N@C_{78}$:**1**: 1.24 / 1.16 eV and for $Sc_3N@C_{80}$:**11**: 1.18 / 1.93 eV. The main conclusion that can be drawn from this observation is that we can predict which isomers will be capable of encapsulating TNT simply by checking the molecular orbitals (MO) energies. Only the free isomers with a large LUMO+3–LUMO+4 gap will be predisposed to encapsulate TNT units. In order to check if this affirmation can be generalized, we calculated all LUMO+3–LUMO+4 gaps for all the IPR isomers between C_{60} and C_{84} stoichiometries.

There are 51 IPR isomers: 1 of C_{60}, C_{70}, C_{72} and C_{74}; 2 of C_{76}; 5 of C_{78}; 7 of C_{80}; 9 of C_{82} and 24 of C_{84}.[20] The LUMO+3–LUMO+4 gaps were calculated using DFT single point calculations on geometries from the Fullerene Structure Library constructed by Mitsuho Yoshida (Figure 4.11).[61] The result is quite surprising and conclusive: the LUMO+3–LUMO+4 gap for all IPR isomers is lower than 1 eV, except for $D_{3h'}$-C_{78}:**5**, D_{5h}-C_{80}:**6** and I_h-C_{80}:**7** isomers which range between 1.16 eV for $D_{3h'}$-C_{78}:**5** and almost 1.93 eV for I_h-C_{80}:**7**. In conclusion, only these isomers can stabilize such highly charged cations as Sc_3N^{6+}. The endohedral metallofullerenes constructed from these empty cages have already been isolated, and according to the present calculations, no more IPR fullerenes that have between 60 and 84 carbons will encapsulate TNT units in the future. The TNT endohedral metallofullerenes of the $D_{3h'}$-C_{78}:**5**[4] and I_h-C_{80}:**7**[1] cages were synthesized first, but the minor TNT endohedral metallofullerene of D_{5h}-C_{80}:**6** [9] cage came later. It was discovered during the purification and isolation process of $Sc_3N@C_{80}$ (cage I_h-C_{80}:**7**)**.** However, we do not exclude that other non-IPR fullerenes such as C_{66}, C_{68} and C_{72} can encapsulate TNT units. In fact, these cages have been isolated as endohedral metallofullerenes. So, non-IPR cages, such as the carbon cage in $Sc_3N@C_{68}$, also follow this rule (Figure 4.11).

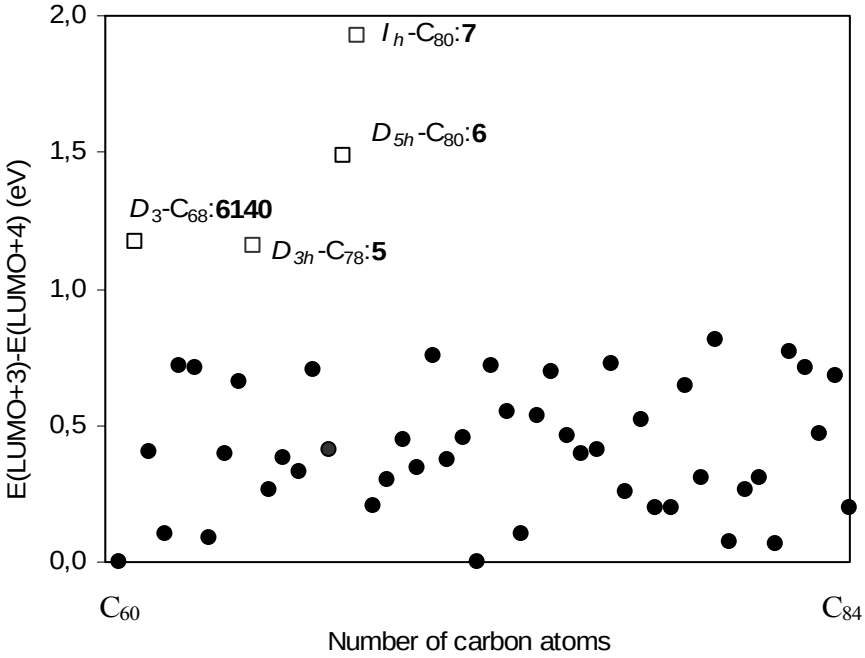

Figure 4.11 Why only D_3-C_{68},:**6140**, D_{3h}-C_{78}:**5**, I_h-C_{80}:**7** and D_{5h}-C_{80}:**6** encapsulate TNT units. The LUMO+3–LUMO+4 gap for all IPR isomers from C_{60} and C_{84} and also the non-IPR D_3-C_{68}:**6140** fullerene. Only isomers with the gap higher than 1 eV have been capable of encapsulating TNT units.

4.7 EXOHEDRAL REACTIVITY (I): [4 + 2] CYCLOADDITION

TNT endohedral metallofullerenes have attracted special attention because they engender new spherical molecules with unique electronic properties and structures that are unexpected for empty fullerenes. The successful isolation and purification of these metallofullerenes has encouraged into their physical and chemical properties. It would be of interest to understand how the chemical reactivity is affected by endohedral metal doping and how the electronic properties of TNT endohedral metallofullerenes are affected by reduction, oxidation and chemical functionalization processes.

The remarkable regioselectivity of the addition reactions (including [4 + 2] cycloadditions) to C_{60} and C_{70}, which occur to the 6:6 C–C bonds in C_{60} and to the 6:6 Ca–Cb / Cc–Cc in the C_{70},[62] encouraged us to find out how much the regioselectivity of the C_{68}, C_{78} and C_{80} cages have changed after the TNT encapsulation process. The effect of reduction and oxidation reactions on TNT endohedral metallofullerenes has already been dealt with in section 4.4, so here we will focus on the chemical functionalization of these endohedral complexes in comparison to that of their corresponding empty cages. Dorn and co-workers reported the first organic functionalization product of the endohedral metallofullerene $Sc_3N@C_{80}$ via a Diels-Alder reaction (see below) and recently Taylor obtained the $Sc_3N@C_{80}F_{52}$ compound as a prevalent product via a fluorination reaction (next section 4.8).

4.7.1 Experimental and theoretical considerations

The organic functionalization chemistry of the free C_{60} fullerene has grown exponentially since the molecule was produced in bulky quantities thanks to the Krätschmer-Huffman generator. Although the classical endohedral metallofullerenes were synthesized in low relative yields, this did not prevent these metallofullerenes from being the first to be exohedrally functionalized. The $La_2@C_{80}$ and $Sc_2@C_{84}$ dimetallofullerenes were functionalized by a thermal and photochemical reaction with an excess of 1,1,2,2-tetramesityl-1,2-disilirane to give the $La_2@C_{80}(Mes_2Si)_2CH_2$ and $Sc_2@C_{84}(Mes_2Si)_2CH_2$ adducts, respectively.[63] The analogous exohedral derivative of $La@C_{82}$, $La@C_{82}(Mes_2Si)_2CH_2$, was also synthesized. Unlike the first two exohedral compounds, this compound provided the additional valuable information that no multipleaddition occurred.[64] A carbene derivative of this monometallofullerene, $La@C_{82}$, has also been reported recently.[65] Kobayashi et al. carried out density functional calculations for two $La_2@C_{80}$ derivatives, $La_2@C_{80}(C_8H_6(OCH_3)_2)$ and $La_2@C_{80}(Si_2H_4CH_2)$. They concluded the attachment of the electron-accepting molecule $C_8H_6(OCH_3)_2$ has no significant effect on the internal rotation in $La_2@C_{80}$, but the random circular motion of two La atoms in $La_2@C_{80}$ can be highly controlled by attaching exohedrally electron-donating molecules such as disilirane (c-$Si_2R_4CH_2$). [66]

Dorn and co-workers have proposed a structure for the first symmetric derivative of the $Sc_3N@C_{80}$ TNT endohedral metallofullerene formed when it reacts with the 6,7-dimetoxyisochroman-3-one diene precursor.[13] The final structure is a Diels-Alder cycloadduct, $Sc_3N@C_{80}$-$C_8H_6(OCH_3)_2$, which is produced via a [4 + 2] cycloaddition mechanistic pathway.[67] The $Sc_3N@C_{80}$ acts as electron-deficient dienophile and the 6,7-dimetoxyisochroman-3-one as an diene precursor. The product has been crystallographically characterized and the ^{13}C NMR suggested that the molecule possesses a plane of symmetry.[14] Unlike C_{60}, the I_h-C_{80}:**7** cage does not have any of the reactive pyracylene C–C bonds (***A*** type in Appendix A.1). Instead, the I_h-C_{80}:**7** cage contains only corannulene 6:5 C–C bonds (***D*** type) and C–C bonds at 6:6 ring junctions abutted by a hexagon and a pentagon (***B*** type). The cycloaddition occurs to the 6:5 C1–C2 bond which is elongated and pulled away from the center of the carbon cage toward the addend. Moreover, a detailed inspection of the geometry shows that the Sc_3N unit is positioned well away from the site of external modification, in a relative position corresponding to that of the $Sc_3N@C_{80}$:**12** isomer (section 4.3). It is not surprising to find another isomer of $Sc_3N@C_{80}$ instead of the most stable one $Sc_3N@C_{80}$:**11** because the free motion of Sc_3N was predicted inside the fullerene cage. Even the high degree of disorder in the crystal structures indicates that the encapsulated entities are highly mobile.

4.7.2 Effects of TNT encapsulation on exohedral reactivity

It is well known that fullerenes can accept electrons and, thus, that they prefer to react with electron-rich reagents. This has been widely confirmed by the electronic nature of the organic and organometallic C_{60} adducts reported so far. And the Diels-Alder reaction is no exception. One of the characteristics of C_{60} is that dienes prefer to attack the shorter 6:6 C–C bonds rather than the longer 6:5 C–C bonds. Thus, as far as chemical reactivity is concerned, two characteristics appear to be determinant. First, regardless of the bond type, short bond lengths (which mean larger π-bond orders and higher π-density) are preferred; and second, additions to 6:6 C–C bond types are favoured by larger pyramidalization of the carbons. In the first step, we analyze how the TNT unit encapsulation affects the electron-

attracting character of the cage, the pyramidalization and the π-bond orders of the C–C bonds. The study is not restricted only to the most stable isomer, $Sc_3N@C_{80}$:**11**, but also includes the $Sc_3N@C_{80}$:**6** and $Sc_3N@C_{80}$:**12** isomers.

Electron–attracting character of the $Sc_3N@C_{80}$ dienophile. This character can be evaluated from the EAs. The electronic structure of C_{80} was characterized by the presence of energetically low-lying 4-fold degenerate LUMOs, which enables this fullerene to accept six electrons. This is corroborated by a high EA of 3.75 eV (section 4.4). After the TNT endohedral doping the EA of the new molecule decreases to 2.99 eV for the $Sc_3N@C_{80}$:**11** isomer, which indicates that the dienophile is less reactive. Although data are only available for the $Sc_3N@C_{80}$:**11** isomer, it is expected that the encapsulation process will modify the EA in the same way for all isomers.

Pyramidalization of carbons. The relationship between the local atomic structure and the chemical reactivity of fullerenes was characterized by Haddon using the pyramidalization angle of carbons (θ_p).[68] The pyramidalization angle is a simple quantitative measure of the local curvature and strain in carbon systems. The pyramidalization angle is obtained as $\theta_p = \theta_{\sigma\pi} - 90$. In POAV1[69] theory, the $\theta_{\sigma\pi}$ (π-orbital axis vector) is introduced and defined as that vector which makes equal angles to the three σ-bonds at a conjugated carbon atom. For planar sp^2 carbons the $\theta_{\sigma\pi}$ is 90° while for tetrahedral sp^3 carbons this angles is 109.47°. Consequently, the pyramidalization angle is 0 ° for sp^2 centers, 19.47° for sp^3 centers and 11.67° for C_{60}. There are other methods of calculating the pyramidalization but POAV1 is conceptually simple and widely used.[70] For purposes of comparison, we describe the different C–C bond types for each complex in several tables: $Sc_3N@C_{80}$:**6** in Table 4.10, $Sc_3N@C_{80}$:**11** in Table 4.11 and $Sc_3N@C_{80}$:**12** in Table 4.12. The description includes the C–C bond types, bond lengths, pyramidalization angles and bond orders. The equivalent data for the free I_h-C_{80}:**7** can be found in Appendix A.6. The I_h-C_{80}:**7** contains only two types of C–C bonds. The corannulene 6:5 C–C bonds (***D*** type) are more highly pyramidalized (θ_p = 10.58º) than the 6:6 C–C bonds (θ_p = 9.62º). Three important conclusions can be drawn from the pyramidalization

angle analysis after the TNT encapsulation: (1) the increases are not severe except in the C–C bonds closest to the Sc atoms; (2) the most pyramidalized C–C bonds are still the corannulene 6:5 C–C bonds; and (3) the highest pyramidalization angle is found in the $Sc_3N@C_{80}$:**11** and **12** complexes (13.15º in the set of C67–C68 bonds and 13.09º in the set of C7–C23 bonds, respectively). Unlike the two above mentioned complexes, in the $Sc_3N@C_{80}$:**6** complex the Sc atoms face one C_6 ring and two C_5 rings, so none of the C–C bonds are pyramidalized in a particular way. To sum up, in principle the exohedral reactivity is enhanced in the cage regions which face Sc atoms, especially for the $Sc_3N@C_{80}$:**11** and **12** isomers. However, this analysis by itself is not conclusive because it also requires bond order considerations.

Mayer bond order (MBO) and bond lengths. The MBO[71] is a measure of the electron density of C–C bonds as a generalization of the Wiberg bond index.[72] The MBO is related to the number of shared electron pairs between the atoms and is calculated using the density and overlap matrices. The MBO has proved to be an extremely useful, transparent, analytical and interpretative tool for measuring the strength of a chemical bond.[73] Bond lengths follow the same trend as MBO. The higher MBO, the shorter bond length. Dienes for [4 + 2] cycloadditions such as 6,7-dimethoxyisochroman-3-one (or 1,3-butadiene) require a C–C bond with high π-density. The MBO analysis finds no significant difference between two different C–C bonds in the free I_h-C_{80}:**7** cage: 1.209 for the 6:6 C–C bonds and 1.194 for the 6:5 C–C bonds. So no conclusive prediction can be made if only this factor is taken into account. To get some idea as to whether the relative differences are significant or not, the MBO can be compared with the C_{60} values. In all cases, the reactivity of these free C–C bonds in I_h-C_{80}:**7** is expected to be lower than that of C_{60} and C_{70} because the MBO are significantly lower than those for C_{60} and C_{70}. The MBO of the 6:6 C–C bond of C_{60} is computed to be 1.342 whereas the 6:6 Ca–Cb bond of C_{70} is computed to be 1.334. A complete description of the C–C bonds of I_h-C_{60}:**1**, D_{5h}-C_{70}:**1** and I_h-C_{80}:**7** is listed in Appendix A.1, A.4 and A.6, respectively.

However, the lack of regioselectivity in the I_h-C_{80}:**7** cage as a consequence of the numerous C–C bonds with similar reactivities deserves more attention. Because the MBOs are equal, the pyramidalization angles will become the most important factor in determining the most reactive site. The highest pyramidalization angle (and the most reactive) is found in the 6:5 C–C bonds, 10.58º, a long way from the value of 9.62º in the 6:6 C–C bonds. On the other hand, the encapsulation of the TNT unit inside the I_h-C_{80}:**7** cage changes the MBOs considerably and, more importantly, this change is extremely sensitive to the relative position of the Sc_3N unit within the cage. Consequently, the most reactive C–C bonds in all the isoenergetic isomers do not coincide with each other. However, one main rule emerges from the MBO analysis: the highest MBOs are never found in the C–C bonds of the cage interacting region which directly faces the Sc atoms. These C–C bonds, which are the most pyramidalized overall, have very low MBO. This makes them not suitable for addition reactions. The MBO for the C67–C68 bond in $Sc_3N@C_{80}$:**11** isomer is 1.125 and 1.122 for the C7–C23 in the $Sc_3N@C_{80}$:**12** isomer. The range of MBO for $Sc_3N@C_{80}$:**6** isomer is 1.226-1.109, for $Sc_3N@C_{80}$:**11** it is 1.247-1.095 and for $Sc_3N@C_{80}$:**12** it is 1.246-1.089.

We have marked the three most reactive sites according to the highest MBO and pyramidalization angle of the C–C bonds in a Schlegel diagram for the free I_h-C_{80}:**7**, $Sc_3N@C_{80}$:**6**, **11** and **12** isomers in Figure 4.12. The most important result is that the *regioselectivity* is considerably better in the TNT endohedral complexes than in the free cage. Each isomer has its own pattern of most reactive sites. These differences between isomers meant that extra computational effort had to be made in an attempt to obtain conclusive results about the most reactive site overall $Sc_3N@C_{80}$ isomers. On the other hand, it is not possible to predict whether $Sc_3N@C_{80}$ complexes will be more reactive than the free C_{80} toward the [4 + 2] cycloadditions just taking into account MBO and pyramidalization angle considerations. The simplicity of C_{80} is transformed: there is a huge variety of C–C bonds with a wide range of MBOs, pyramidalization angles and C–C bond lengths in the TNT endohedral metallofullerenes. But the electron–attracting character of the TNT endohedral metallofullerene compared with that of the free fullerene suggests that the reactivity will decrease.

Table 4.10 Description of the thirty-four distinct set of C–C bonds of the C_{2v}-$Sc_3N@C_{80}$:**6** isomer [a]

C–C Bond [b]	*Type* [c]	*Bond lengths*	θ_p [d]	*MBO* [e]
36,47	***B***	1.424	9.89	1.226
37,38	***B***	1.426	9.88	1.224
44,64	corann., ***D***	1.434	10.55	1.223
17,18	***B***	1.428	9.80	1.213
3,4	corann., ***D***	1.438	10.46	1.209
46,47	***B***	1.423	9.82	1.207
4,18	***B***	1.429	9.64	1.207
16,17	corann., ***D***	1.438	10.59	1.206
17,37	corann., ***D***	1.438	10.71	1.205
36,37	corann., ***D***	1.439	10.68	1.201
1,9	***B***	1.427	9.37	1.200
6,20	***B***	1.427	9.37	1.198
48,49	corann., ***D***	1.434	9.47	1.197
21,22	***B***	1.428	9.10	1.197
21,40	corann., ***D***	1.439	10.38	1.195
3,15	***B***	1.429	9.40	1.195
1,2	corann., ***D***	1.439	10.43	1.192
38,49	***B***	1.434	9.31	1.190
65,66	***B***	1.435	9.65	1.184
22,53	***B***	1.432	9.34	1.176
1,5	corann., ***D***	1.441	10.42	1.171
47,48	***B***	1.434	9.25	1.168
46,65	corann., ***D***	1.447	9.73	1.159
16,35	corann., ***D***	1.442	10.18	1.157
44,45	corann., ***D***	1.444	10.48	1.156
48,67	corann., ***D***	1.452	10.43	1.155
7,23	corann., ***D***	1.452	11.47	1.140
7,8	corann., ***D***	1.453	11.01	1.129
23,24	corann., ***D***	1.461	11.79	1.120
8,9	***B***	1.448	9.60	1.119
6,7	***B***	1.451	9.76	1.114
66,67	***B***	1.447	10.91	1.113
67,68	corann., ***D***	1.459	11.37	1.111
22,23	***B***	1.450	10.00	1.109

[a] Bond lengths in Å and pyramidalization angle in º. The Bond lengths, pyramidalization angle and Mayer bond order (MBO) of the two distinct set of C–C bonds of the free I_h-C_{80}:**7** are 1.428 Å, 9.62º and 1.209 for the ***B*** 6:6 C–C bond type and 1.438 Å, 10.58º, 1.194 for the corannulene 6:5 C–C bond type (***D*** type). [b] See Appendix A.6 for the systematic numeric system. [c] See Appendix A.1 for a graphical representation of the different C–C bond types. [d] Average pyramidalization angle (θ_p) of each carbon atom in the carbon bond. [e] Mayer bond order (MBO).

Table 4.11 Description of the sixty-four distinct set of C–C bonds of the C_s-$Sc_3N@C_{80}$:**11** isomer [a]

C–C Bond [b]	*Type* [c]	*Bond lengths*	θ_p [d]	*MBO* [e]
36,47	***B***	1.422	9.68	1.247
21,22	***B***	1.423	9.60	1.244
1,9	***B***	1.423	9.61	1.243
45,46	corann., ***D***	1.432	10.90	1.228
37,38	***B***	1.424	9.85	1.226
6,20	***B***	1.424	9.81	1.225
10,11	corann., ***D***	1.433	10.81	1.224
3,15	***B***	1.424	9.81	1.223
28,59	***B***	1.425	9.60	1.213
63,64	***B***	1.424	9.61	1.213
17,18	***B***	1.430	9.62	1.212
58,59	***B***	1.430	9.70	1.212
4,18	***B***	1.430	9.61	1.212
76,77	corann., ***D***	1.437	10.50	1.211
60,61	corann., ***D***	1.437	10.57	1.209
61,62	corann., ***D***	1.438	10.54	1.209
75,76	***B***	1.431	9.67	1.208
61,75	***B***	1.427	9.95	1.207
62,63	***B***	1.426	9.95	1.207
3,4	corann., ***D***	1.437	10.69	1.207
17,37	corann., ***D***	1.437	10.71	1.206
16,17	corann., ***D***	1.438	10.70	1.205
63,77	***B***	1.427	9.91	1.204
42,62	corann., ***D***	1.440	10.18	1.202
41,60	corann., ***D***	1.440	10.17	1.201
44,64	corann., ***D***	1.440	9.85	1.199
77,78	corann., ***D***	1.441	10.14	1.198
27,28	corann., ***D***	1.441	9.85	1.197
64,65	corann., ***D***	1.441	9.76	1.193
46,47	***B***	1.426	9.86	1.189
22,53	***B***	1.427	9.81	1.187
9,10	***B***	1.427	9.77	1.185
36,37	corann., ***D***	1.441	10.60	1.183

Table 4.11 Continue

16,35	corann., ***D***	1.441	10.57	1.182
1,5	corann., ***D***	1.441	10.57	1.182
65,66	***B***	1.434	9.40	1.181
43,44	***B***	1.433	9.32	1.181
26,27	***B***	1.434	9.38	1.179
21,40	corann., ***D***	1.444	10.52	1.178
1,2	corann., ***D***	1.444	10.49	1.177
38,49	***B***	1.440	8.87	1.166
6,7	***B***	1.441	8.92	1.159
44,45	corann., ***D***	1.444	10.27	1.155
10,27	corann., ***D***	1.444	10.23	1.154
46,65	corann., ***D***	1.445	10.17	1.152
48,49	corann., ***D***	1.437	9.07	1.150
26,57	***B***	1.432	9.35	1.149
42,43	***B***	1.432	9.30	1.148
7,23	corann., ***D***	1.439	9.29	1.146
7,8	corann., ***D***	1.439	9.33	1.146
66,78	***B***	1.434	9.49	1.140
48,67	corann., ***D***	1.457	11.29	1.130
8,25	corann., ***D***	1.458	11.45	1.129
23,24	corann., ***D***	1.457	11.40	1.129
24,25	corann., ***D***	1.468	13.08	1.128
67,68	corann., ***D***	1.469	13.15	1.125
47,48	***B***	1.446	9.12	1.125
22,23	***B***	1.446	9.22	1.124
8,9	***B***	1.447	9.27	1.123
41,42	corann., ***D***	1.446	9.60	1.114
78,79	corann., ***D***	1.448	9.60	1.109
66,67	***B***	1.456	11.27	1.095
25,26	***B***	1.456	11.10	1.095
24,55	***B***	1.455	11.04	1.095

[a] Bond lengths in Å and pyramidalization angle in degrees. The Bond lengths, pyramidalization angle and Mayer Bond Order (MBO) of the two distinct set of C–C bonds of the free I_h-C_{80}:7 are 1.428 Å, 9.62º and 1.209 for the ***B*** type and 1.438 Å, 10.58º, 1.194 for the ***D*** type. [b] See Appendix A.6 for the systematic numeric system. [c] See Appendix A.1 for a graphical representation of the different C–C bond types. [d] Average pyramidalization angle (θ_p) of each carbon atom in the carbon bond. [e] Mayer bond order (MBO).

Table 4.12 Description of the sixty-four distinct set of C–C bonds of the C_s-$Sc_3N@C_{80}$:**12** isomer [a]

C–C Bond [b]	*Type* [c]	*Bond lengths*	θ_p [d]	*MBO* [e]
9,10	***B***	1.422	9.72	1.246
66,67	***B***	1.421	9.67	1.242
26,27	***B***	1.422	9.84	1.236
1,2	corann., ***D***	1.430	11.02	1.233
38,49	***B***	1.426	9.69	1.229
47,48	***B***	1.425	9.88	1.227
46,65	corann., ***D***	1.433	10.70	1.226
28,59	***B***	1.425	9.89	1.226
21,22	***B***	1.425	9.93	1.222
36,37	corann., ***D***	1.434	10.41	1.220
41,60	corann., ***D***	1.435	10.68	1.220
17,18	***B***	1.426	9.91	1.207
17,37	corann., ***D***	1.438	10.52	1.207
43,44	***B***	1.422	9.54	1.205
46,47	***B***	1.428	9.72	1.205
63,64	***B***	1.430	9.57	1.205
37,38	***B***	1.432	9.71	1.204
4,18	***B***	1.427	9.58	1.204
44,64	corann., ***D***	1.437	10.42	1.203
65,66	***B***	1.428	9.88	1.203
42,62	corann., ***D***	1.438	10.41	1.202
61,75	***B***	1.430	9.65	1.200
48,49	corann., ***D***	1.440	10.60	1.199
1,9	***B***	1.426	9.94	1.198
3,4	corann., ***D***	1.440	9.73	1.197
27,28	corann., ***D***	1.440	10.79	1.197
60,61	corann., ***D***	1.441	9.96	1.197
48,67	corann., ***D***	1.439	10.65	1.197
16,17	corann., ***D***	1.441	10.15	1.195
36,47	***B***	1.430	9.66	1.194
21,40	corann., ***D***	1.443	10.03	1.193
41,42	corann., ***D***	1.442	10.66	1.191
22,53	***B***	1.433	9.46	1.185
10,27	corann., ***D***	1.441	10.58	1.185
3,15	***B***	1.434	9.37	1.184

Table 4.12 Continue

45,46	corann., ***D***	1.445	9.93	1.183
10,11	corann., ***D***	1.444	10.58	1.183
64,65	corann., ***D***	1.443	10.75	1.177
67,68	corann., ***D***	1.443	10.45	1.171
62,63	***B***	1.427	9.17	1.171
26,57	***B***	1.426	9.97	1.169
25,26	***B***	1.440	8.90	1.169
8,25	corann., ***D***	1.436	8.95	1.160
58,59	***B***	1.433	9.32	1.158
1,5	corann., ***D***	1.448	10.26	1.150
24,25	corann., ***D***	1.439	9.16	1.149
78,79	corann., ***D***	1.437	9.18	1.149
44,45	corann., ***D***	1.445	9.78	1.145
66,78	***B***	1.445	9.04	1.144
77,78	corann., ***D***	1.448	10.27	1.136
23,24	corann., ***D***	1.456	11.36	1.136
42,43	***B***	1.445	9.03	1.135
6,20	***B***	1.435	9.45	1.134
7,8	corann., ***D***	1.456	11.15	1.133
8,9	***B***	1.422	9.03	1.130
24,55	***B***	1.444	9.25	1.129
61,62	corann., ***D***	1.446	9.61	1.126
76,77	corann., ***D***	1.465	12.58	1.125
7,23	corann., ***D***	1.470	13.09	1.122
16,35	corann., ***D***	1.448	9.65	1.106
63,77	***B***	1.450	9.94	1.104
6,7	***B***	1.453	11.17	1.100
22,23	***B***	1.456	11.33	1.092
75,76	***B***	1.460	11.53	1.089

[a] Bond lengths in Å and pyramidalization angle in degrees. The Bond lengths, pyramidalization angle and Mayer Bond Order (MBO) of the two distinct set of C–C bonds of the free I_h-C_{80}:7 are 1.428 Å, 9.62º and 1.209 for the ***B*** type and 1.438 Å, 10.58º, 1.194 for the ***D*** type. [b] See Appendix A.6 for the systematic numeric system. [c] See Appendix A.1 for a graphical representation of the different C–C bond types. [d] Average pyramidalization angle (θ_p) of each carbon atom in the carbon bond. [e] Mayer bond order (MBO).

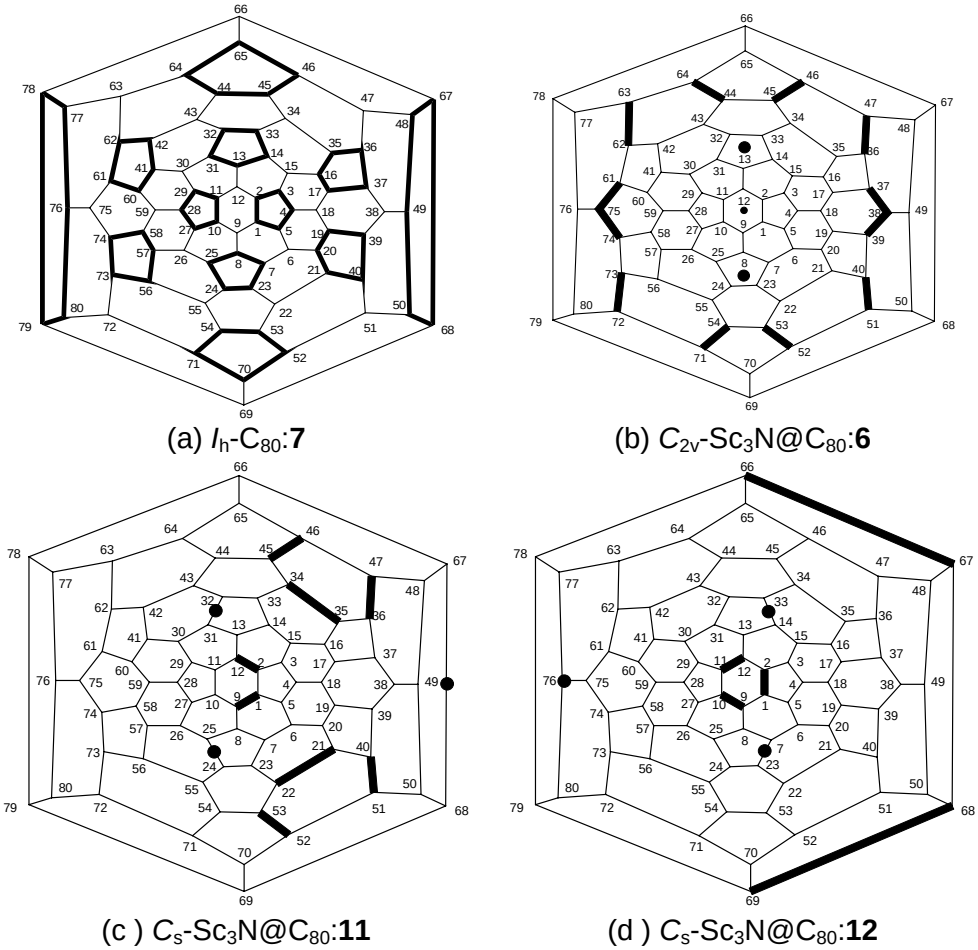

(a) I_h-C_{80}:**7** (b) C_{2v}-$Sc_3N@C_{80}$:**6**

(c) C_s-$Sc_3N@C_{80}$:**11** (d) C_s-$Sc_3N@C_{80}$:**12**

Figure 4.12 Evolution of the three most reactive exohedral sites (bold lines) for I_h-C_{80}:**7** and $Sc_3N@C_{80}$ isomers according to pyramidalization angle (θ_p) and Mayer bond order (MBO) analysis drawn in the Schlegel diagram of I_h-C_{80}:**7**. The Sc atoms of the TNT unit are facing endohedrally the fullerene surface in the circle positions. The ***B*** 6:5 C–C bond types have been marked for free I_h-C_{80}:**7** in (a), the set of the C36–C47, C37–C38 and C44–C64 bonds for C_{2v}-$Sc_3N@C_{80}$:**6** in (b), the set of the C36–C47, C21–C22, C1–C9 and C45–C46 bonds for C_s-$Sc_3N@C_{80}$:**11** in (c) and finally the set of the C9–C10, C66–C67 and C1–C2 bonds for C_s-$Sc_3N@C_{80}$:**12** in (d). The C–C bonds equivalents to C36–C47 in (b) are: C72–C73, C62–C63 and C40–C51; equivalents to C37–C38 in (b) are: C38–C39, C61–C75 and C74–C75; equivalents to C44–C64 are: C54–C71, C45–C46 and C52–C53;

Figure 4.12 Continue
equivalent to C36–C47 in (c) is: C40–C51; equivalent to C21–C22 in (c) is C34-C35; equivalent to C1–C9 in (c) is C2–C12; equivalent to C45–C46 in (c) is C52–C53; equivalent to C9–C10 in (d) is C11–C12; equivalent to C66–C67 in (d) is C68–C69; C1–C2 in (d) is unique. Also the equivalent C–C bonds are marked in the Schlegel diagrams. The experimental structure for $Sc_3N@C_{80}$-$C_8H_6(OCH_3)_2$ corresponds to adduct formation to the C1–C2 bond in the $Sc_3N@C_{80}$:**12** isomer (Schlegel diagram d). The characterization of the marked C–C bond types are (MBO, θ_p): I_h-C_{80}:**7** 6:5 (1.194, 10.58°); $Sc_3N@C_{80}$:**6** C36–C47 (1.226, 9.89°), C37–C38 (1.224, 9.88°), C44–C64 (1.223, 10.55 °); $Sc_3N@C_{80}$:**11** C36–C47 (1.247, 9.68 °), C21–C22 (1.244, 9.60 °), C1–C9 (1.243, 9.61 °); C45–C46 (1.228, 10.90º); $Sc_3N@C_{80}$:**12** C9–C10 (1.246, 9.72 °), C66–C67 (1.242, 9.67 °), C1–C2 (1.233, 11.02 °).

4.7.3 [4 + 2] cycloaddition on $Sc_3N@C_{80}$

Once the various factors affecting the exhohedral reactivity had been analyzed, we chose the most reactive sites that had been predicted to perform a cycloaddition reaction of 1,3-butadiene on the free I_h-C_{80}:**7** fullerene and also on the above mentioned isomers of $Sc_3N@C_{80}$. The experimental stoichiometry of the Diels-Alder cycloadduct $Sc_3N@C_{80}$-$C_8H_6(OCH_3)_2$ was modelled as $Sc_3N@C_{80}$-C_4H_{10}. The isomers that are to be calculated must be selected: otherwise it would be impossible to compute the 32 different C–C bonds for $Sc_3N@C_{80}$:**6** and the 64 for isomers **11** and **12** of $Sc_3N@C_{80}$. Moreover, most of them have no symmetry. As found experimentally, adducts adopt a boat conformation facing to the side where Sc atoms are connected to the carbon cage.

First we analyze the reactivity of the $Sc_3N@C_{80}$:**12** isomer because experimentalists have proposed that it is the $Sc_3N@C_{80}$ isomer found in the $Sc_3N@C_{80}$-$C_8H_6(OCH_3)_2$ functionalized complex. According to the MBO analysis, four C–C bonds are the most reactive: the C66–C67, C9–C10 and C26–C27 bonds have the highest overall MBO but a low pyramidalization angle (*ca.* 9.7°), while the C1–C2 bond has the fourth highest MBO but the highest pyramidalization angle (11.0º). Calculations corroborate that the most reactive site coincides with the sites found experimentally: the formation of the adduct in the corannulene 6:5 C1–C2 bond is approximately 0.5 eV more stable than the formation in the 6:6 C66–C67,

Table 4.13 Geometric properties and relative energies (REs) for $Sc_3N@C_{80}$-C_4H_6 and C_{80}-C_4H_6 isomers

	Reac. C–C bond [b]	*Sym.*	*$Sc_3N@C_{80}$ / C_{80}*			*$Sc_3N@C_{80}$-C_4H_6 / C_{80}-C_4H_6*	
			Bond lenghts	*Initial θ_p* [c]	*MBO*	*Final θ_p* [c]	*RE*
*$Sc_3N@C_{80}$:**12***	1,2*	C_s	1.430	11.02	1.233	20.68	0.00 [d]
	9,10	C_1	1.422	9.72	1.246	18.97	0.48
	66,67	C_1	1.421	9.67	1.242	18.85	0.52
	26,27	C_1	1.422	9.84	1.236	18.80	0.61
*$Sc_3N@C_{80}$:**11***	45,46*	C_1	1.432	10.90	1.228	20.70	0.02
	36,47	C_1	1.422	9.68	1.247	19.03	0.46
	21,22	C_1	1.423	9.60	1.244	19.09	0.48
	1,9	C_1	1.423	9.61	1.243	19.02	0.48
	1,2*	C_s	1.444	10.49	1.177	20.03	0.58
*$Sc_3N@C_{80}$:**6***	1,2*	C_s	1.439	10.43	1.192	20.86	0.16
*$Sc_3N@C_{80}$:**7***	1,2*	C_1	1.441	10.09	1.188	20.59	0.28
*$Sc_3N@C_{80}$:**8***	1,2*	C_1	1.448	9.76	1.162	20.34	0.51
*$Sc_3N@C_{80}$:**10***	1,2*	C_s	1.440	10.62	1.193	19.87	0.52
*$Sc_3N@C_{80}$:**9***	1,2*	C_s	1.444	10.49	1.177	19.88	0.71
*I_h-C_{80}:**7***	1,2*	C_s	1.438	10.58	1.194	19.91	0.00 [e]
	1,9	C_s	1.428	9.62	1.209	18.74	0.70

[a] Bond lengths in Å, angles in º and energies in eV. [b] Reactive C–C bond. All are ***B*** 6:6 C–C bond types except those with *, which indicate that the considered C–C bonds is a 6:5 corannulene type (***D*** type). See Figure A.1 for a graphical representation of the different C–C bond types. [c] Pyramidalization angle (θ_p) for the carbons attached to the diene. [d] Energy reaction of $Sc_3N@C_{80}$:**12** + 1,3-butadiene → $Sc_3N@C_{80}$-C_4H_6 is computed to be –0.54 eV. [e] Energy reaction of I_h-C_{80}:**7** + 1,3-butadiene → C_{80}-C_4H_6 is computed to be –1.04 eV.

C9–C10 and C26–C27 bonds (Table 4.13). We have also calculated the four most predicted reactive sites of the $Sc_3N@C_{80}$:**11** isomer which is slightly more stabilized than the $Sc_3N@C_{80}$:**12** isomer (0.01 eV, see section 4.3). Any functionalized compound from isomer **11** gives a more stable isomer although the reaction through the C45–C46 bond would be a serious

Table 4.14 Crucial geometric parameters which change during the derivatitzation via a [4 + 2] cycloaddition reaction on $Sc_3N@C_{80}$:**12** isomer [a]

	*$Sc_3N@C_{80}$:**12*** [b]	*$Sc_3N@C_{80}$-C_4H_6* [b]	*$Sc_3N@C_{80}$-$C_8H_6(OCH_3)_2$* [c]
Sc–N bond lengths [d]	2.008-2.019	2.010-2.019	2.021-2.032
Sc–C bond lengths [e]	2.258	2.268	2.244
Cage radius	4.118	4.122	4.098
C1–C2 θ_p	11.02	20.68	21
C1–C2 bond lengths	1.430	1.632	1.626

[a] Distances in Å and angles in °. [b] DFT calculations. [c] X-ray data from reference 13. [d] Range of Sc–N bond lengths. [e] Contact distances between Sc and the nearest neighbour carbons.

competitive site. The C45–C46 bond is also a corannulene 6:5 C–C bond type with the highest pyramidalization angle. The results are quite significant: the reaction through the corannulene 6:5 C1–C2 bond of the $Sc_3N@C_{80}$:**12** isomer appears to be the most favorable of all the calculated cycloaddition adducts because this site is the most pyramidalized of the C–C bonds with high MBO. In conclusion, the reaction through the C1–C2 bond of the $Sc_3N@C_{80}$:**12** isomer is a compromise between a high MBO and a high pyramidalization angle. The REs, MBOs and some geometrical parameters (bond lengths, initial θ_p, final θ_p) of the cycloaddition adducts are listed in Table 4.13. The correlation between the final pyramidalization angle (final θ_p) in the cycloaddition adducts and the RE indicates that if both fragments are to be bound efficiently, pyramidalization angle must be high. So, the isomers that most facilitate the pyramidalization of carbons will tend to be more stable.

For the most stable cycloaddition adduct, the C1–C2 distance (1.632 Å) is considerably longer than the average C1–C2 distance at the unaltered site (1.430 Å). The experimental value was 1.626 Å. The carbons C1 and C2 are pulled away from the center up to a maximum pyramidalization angle of 20.7° (experimental value of 21°). The average of the five Sc–C contacts is computed to be 2.283 Å, quite close to the experimental value of 2.272 Å and longer than the computed value for the free Sc_3NC_{80}:**12** (2.276 Å). The Sc_3N unit is planar and positioned well away from the site of external modification. The mean Sc–N distances (2.016 Å calculated and 2.027

measured) are slightly longer than those in the free Sc_3NC_{80}:**12** (2.012 Å). Finally, it should be noted that the cycloaddition increases the cage radius again, from 4.118 Å for $Sc_3N@C_{80}$:**12** to 4.122 Å for $Sc_3N@C_{80}$-C_4H_6. In conclusion, the computed geometry for the functionalized structure of Sc_3NC_{80} matches perfectly the experimental geometry proposed by Balch and co-workers. For purposes of comparison the above mentioned structures are drawn in Figure 4.13 and some geometrical parameters are listed in Table 4.14.

Finally, we computed the cycloaddition of 1,3-butadiene to the C1–C2 bond of all the $Sc_3N@C_{80}$ isomers to investigate whether Sc_3N can rotate inside the carbon cage after the cycloaddition reaction or whether, on the other hand, it is set in one specific position. Except for $Sc_3N@C_{80}$:**12**, for the other isomers the C1–C2 bonds are not very reactive because the MBO has intermediate values of 1.177-1.192 (Table 4.13). The main conclusion is that movement is more hindered after the cycloaddition of the diene. The REs of the Sc_3N motion within C_{80}-C_4H_6 increase significantly more than those found for the Sc_3N motion within C_{80}. Only isomer **6** decreases the RE from 0.23 eV to 0.16 eV. The other isomers increase the REs: 0.06 to 0.28 eV for isomer **7**, 0.08 to 0.51 eV for isomer **8**, 0.07 to 0.71 eV for isomer **9**, 0.04 to 0.52 eV for isomer **10** and 0.00 to 0.58 eV for isomer **11** (Figure 4.7 and Table 4.13). Thus, the exohedral derivatization helps to fix the endohedral position of the TNT unit.

To demonstrate the decrease in the exohedral reactivity of TNT endohedral metallofullerenes, we performed a series of calculations of 1,3-butadiene cycloaddition to the free C_{80}. These results are listed at the bottom of Table 4.13. As expected, the most stable isomer comes from the addition to the 6:5 C1–C2 bond. The energy involved in the addition reaction to the free C_{80} is almost twice that of the addition reactions to $Sc_3N@C_{80}$:**12** (–1.04 eV and –0.54 eV, respectively). We calculated the addition reaction as the energy reaction of $Sc_3N@C_{80}$:**12** + 1,3-butadiene → $Sc_3N@C_{80}$-C_4H_6 which was –0.54 eV and the energy reaction of I_h-C_{80}:**7** + 1,3-butadiene → C_{80}-C_4H_6 which was –1.04 eV. The numerical results also confirm that the TNT encapsulation improves the exohedral regioselectivity of the I_h-C_{80}:**7** fullerene surface: in I_h-C_{80}:**7** there are 60 C–C bonds with equal reactivity whereas in the TNT $Sc_3N@C_{80}$:**12** complex just 7 C–C bonds are the most reactive sites (Figure 4.12).

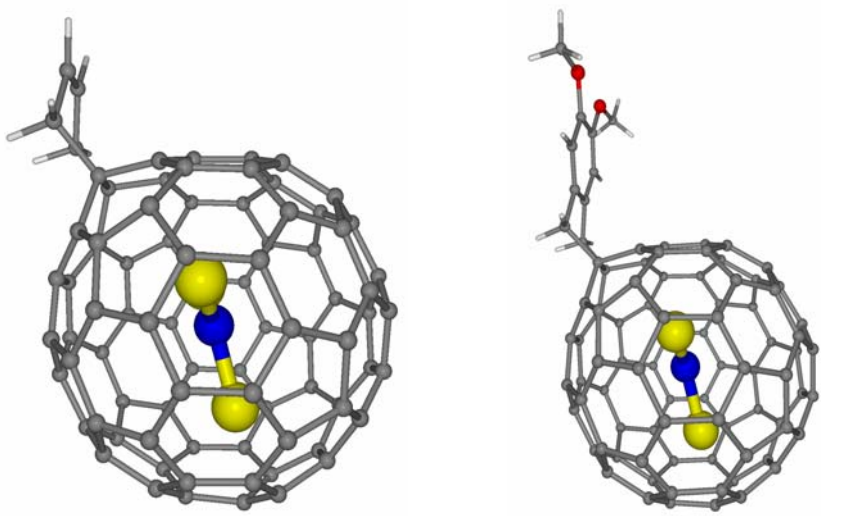

(a) $Sc_3N@C_{80}$-C_4H_6 (b) $Sc_3N@C_{80}$-$C_8H_6(OCH_3)_2$

Figure 4.13 Structures for the most stable $Sc_3N@C_{80}$-C_4H_6 isomer (a) and for the X-ray of $Sc_3N@C_{80}$-$C_8H_6(OCH_3)_2$ (b).

4.7.4 Clues about [4 + 2] cycloaddition on $Sc_3N@C_k$ (k = 68, 78)

The significant results obtained above in predicting the most reactive exohedral sites of $Sc_3N@C_{80}$ prompted us to investigate the [4 + 2] cycloaddition to other known TNT endohedral metallofullerenes: $Sc_3N@C_{68}$ and $Sc_3N@C_{78}$. The task seemed easier because there is only one possible isomer for these TNT endohedral complexes. We used the same strategy: we localized the most pyramidalized C–C bonds with the highest MBO in the TNT endohedral metallofullerenes of C_{68} and C_{78}. Table 4.15 lists the bond lengths, the pyramidalization angles and the MBOs of the different sets of C–C bonds of the free $D_{3h'}$-C_{78}:**5** and $Sc_3N@C_{78}$ while Table 4.16 lists the values for the free C_{68} and $Sc_3N@C_{68}$. Here, the MBO analysis suggests that the C–C bonds of the TNT endohedral metallofullerenes are less reactive than the corresponding C–C bonds of the free fullerenes. As was expected the MBO of the C–C bonds near the scandiums decreases and the pyramidalization angle increases significantly.

Table 4.15 Change of the characteristics of the thirteen different set of C–C bonds from free $D_{3h'}$-C_{78}:**5** (initial) to Sc_3N@C_{78}:**1** (final) [a]

C–C Bond [b]	*Type* [c]	*Initial Bond lengths*	*Final bond lengths*	*Initial* θ_p [d]	*Final* θ_p [d]	*Initial MBO* [e]	*Final MBO* [e]
8,24	***B***	1.424	1.403	9.48	10.05	1.214	1.280
7,21	***B***	1.419	1.429	9.63	9.51	1.283	1.271
1,2	***A***	1.392	1.403	11.67	11.28	1.392	1.267
23,44	***D***	1.470	1.427	10.31	9.20	1.090	1.208
1,6	***D***	1.443	1.441	11.67	11.28	1.158	1.176
1,9	***D***	1.446	1.437	11.15	10.95	1.129	1.173
23,24	***B***	1.423	1.434	9.56	8.98	1.221	1.165
7,8	***D***	1.443	1.453	10.39	10.98	1.195	1.163
22,23	***D***	1.414	1.447	10.49	9.68	1.293	1.150
22,42	***D***	1.451	1.455	10.57	12.02	1.111	1.137
10,11	***C***	1.470	1.469	8.63	8.36	1.163	1.118
10,26	***B***	1.436	1.454	9.65	9.26	1.205	1.097
27,28	***A***	1.372	1.441	10.47	13.88	1.373	1.086

[a] Bond lengths in Å and pyramidalization angle in º. [b] See Appendix A.5 for the systematic numeric system extracted from reference: Taylor, R. *J. Chem. Soc., Perkin Trans. 2* **1993**, 813. [c] See Appendix A.1 for a graphical representation of the different C–C bond types (***A***-*D*). [d] Average pyramidalization angle (θ_p) of each carbon atom in the C–C bond. [e] Mayer bond order (MBO).

The free $D_{3h'}$-C_{78}:**5** isomer has 13 distinct set of C–C bonds and is one of the fullerenes in which the four possible C–C bond types for IPR fullerenes are present: pyracylene (***A*** type), ***B*** type, pyrene (***C*** type) and corannulene (***D*** type) (Appendix A.1). The two distinct set of pyracylene C–C bonds are expected to be the most reactive sites for the free C_{78}: C1–C2 and C27–C28. Both C–C bonds have a commonly high MBO (1.392 and 1.373, respectively) which predict a high reactivity and regioselectivity across cycloadditions reactions. Even, these C–C bonds have higher MBOs than those of the 6:6 C–C bonds in C_{60} and the Ca–Cb in C_{70}. After Sc_3N encapsulation (scandiums are facing the set of C27–C28 bonds), only three distinct C–C bonds (C1–C2, C7–C21 and C8–C24) appear as the most reactive sites, the others being completely discarded because of their lower

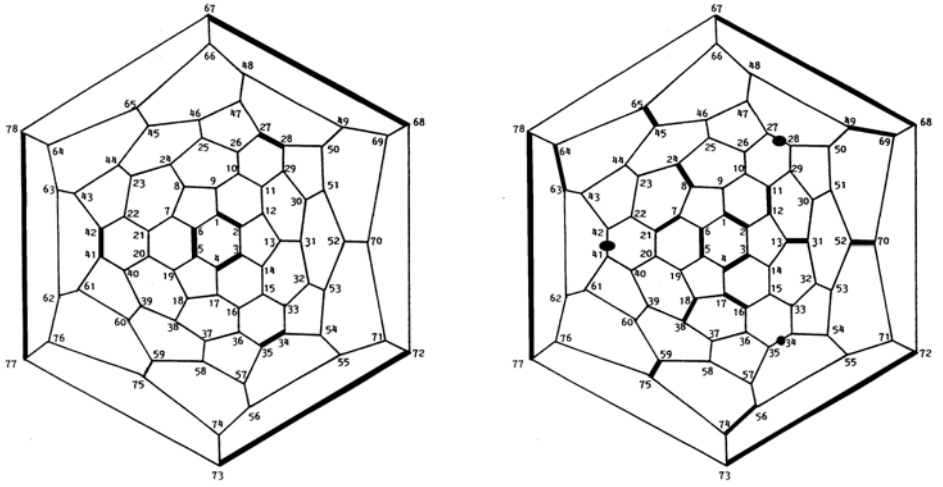

(a) $D_{3h'}$-C_{78}:**5** (b) D_{3h}-$Sc_3N@C_{78}$:**1**

Figure 4.14 The three most reactive exohedral sites for $D_{3h'}$-C_{78}:**5** (a) and $Sc_3N@C_{78}$:**1** (b) drawn in the Schlegel diagram. Sc atoms are facing the fullerene surface in the circle positions. The set of C1–C2 and C27–C28 bonds have been marked (bold lines) for the free $D_{3h'}$-C_{78}:**5** in (a), the set of C8–C24, C7–C21 and C1–C2 bonds for D_{3h}-$Sc_3N@C_{78}$ in (b). The C–C bonds equivalents to C1–C2 are: C3–C4, C5–C6, C67–C68, C72–C73; equiv. to C27–C28 are: C34–C35, C41–C42, C77–C78: equiv. to C7–C21: C11–C12, C16–C17, C49–C69, C63–C64, C56–C74; equiv. to C8–C24: C13–C31, C18–C38, C45–C65, C52–C70, C59–C75. Description of the marked C–C bonds (MBO, θ_p): (1) $D_{3h'}$-C_{78}:**5** C1–C2 (1.392, 11.67°), C27–C28 (1.373, 10.47°) and (2) D_{3h}-$Sc_3N@C_{78}$ C8–C24 (1.280, 10.05°), C7–C21 (1.271, 9.51°), C1–C2 (1.267, 11.28°).

MBOs. Special calculations would be necessary to determine the most reactive site because the ***B*** type 6:6 C7–C21 and C8–C24 have the highest MBO of 1.271 and 1.280, respectively, but a low pyramidalization angle of *ca.* 10° while the set of C1–C2 bonds also has a high MBO with a considerable pyramidalization angle of 11.28°.

Dorn and co-workers derivatized the $Sc_3N@C_{78}$ with a ^{13}C-labeled reagent and obtained mono-, di- and triadducts.[17] The ^{13}C and ^{1}H NMR data of the monoadduct support the idea that addend addition takes place at an asymmetric site (C7–C21 bond) on the C_{78} cage and so we discard the reaction in the C1–C2 and C8–C24 bonds because these would give symmetric structures. It is important to remark that $Sc_3N@C_{78}$ is predicted

Table 4.16 Change of the characteristics of the eighteen different set of C–C bonds from free D_3-C_{68}:**6140** (initial) to $Sc_3N@C_{68}$ (final) [a]

C–C bond [b]	*Patch type* [c]	*Initial bond lengths*	*Final bond lengths*	*Initial* θ_p [d]	*Final* θ_p [d]	*Initial MBO* [e]	*Final MBO* [e]
14,24	***B***	1.429	1.437	9.71	9.97	1.252	1.219
2,13	***D***	1.449	1.439	10.14	10.35	1.159	1.218
1,2	***B***	1.431	1.432	9.58	9.55	1.215	1.201
2,3	***D***	1.433	1.439	10.90	10.69	1.210	1.199
24,25	***C***	1.488	1.462	8.58	9.01	1.118	1.196
13,14	***D***	1.443	1.449	10.54	10.58	1.194	1.182
12,13	***B***	1.413	1.43	9.72	9.43	1.247	1.178
14,15	***D***	1.438	1.436	10.80	10.67	1.133	1.167
11,12	***B***	1.433	1.443	10.48	9.76	1.235	1.164
15,27	***A***	1.396	1.416	11.52	11.56	1.266	1.152
3,15	***D***	1.447	1.448	11.27	10.65	1.165	1.146
21,42	***E***	1.436	1.445	16.20	16.69	1.156	1.144
26,27	***D***	1.458	1.451	11.78	11.44	1.136	1.143
21,22	***F***	1.421	1.456	13.77	14.66	1.224	1.138
22,23	***D***	1.45	1.467	11.31	11.40	1.199	1.131
12,22	***B***	1.446	1.445	10.27	10.63	1.151	1.129
23,24	***B***	1.418	1.454	9.93	9.60	1.257	1.123
20,21	***F***	1.424	1.446	14.49	14.70	1.185	1.123

[a] Bond lengths in Å and pyramidalization angle in °. [b] See Appendix A.3 for the systematic numeric system. [c] See Appendix A.1 for a graphical representation of the different C–C bond types (***A***-***F***). [d] Average pyramidalization angle (θ_p)of each carbon atom in the carbon bond. [e] Mayer bond order (MBO).

to be the most reactive molecule in the cycloaddition reactions: it has the highest MBO of all the TNT endohedral metallofullerenes studied although several positions are possible for the cycloaddition.

According to MBO analysis the most reactive sites in the non-IPR D_3-C_{68}:**6140** fullerene are the ***B*** type 6:6 C–C bonds: C19–C31, C29–C30 and C18–C28 (Table 4.16 and Figure 4.15). When the Sc_3N is encapsulated, the most reactive sites move to the C5–C6, C6–C7, C18–C19 and C6–C17 bond types but in general the reactivity is substantially reduced. It would be

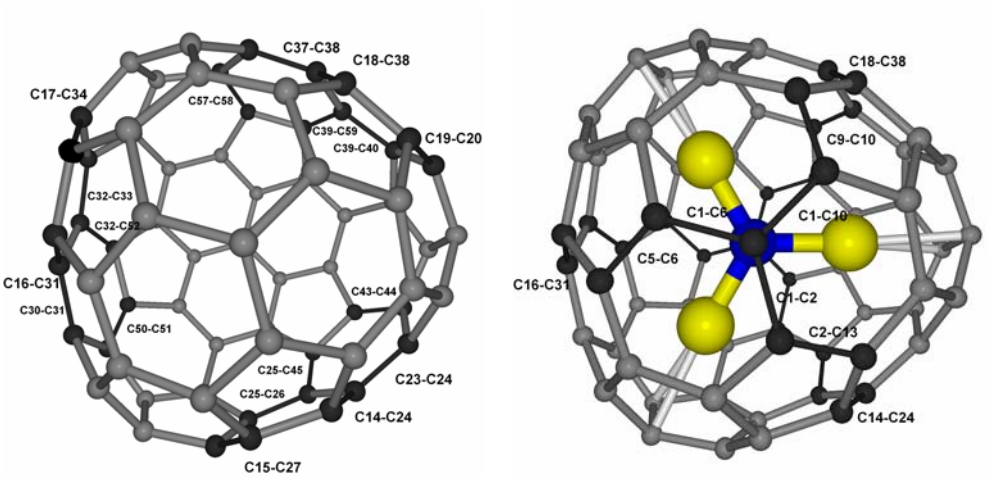

(a) D_3-C_{68}:**6140** (b) D_3-$Sc_3N@C_{68}$

Figure 4.15 The three most reactive exohedral sites for D_3-C_{68}:**6140** (a) and $Sc_3N@C_{68}$ (b). The set of C15–C27, C23–C24 and C14–C24 bonds have been marked (bold lines) for the free D_3-C_{68}:**6140** in (a), the set C14–C24, C2–C13 and C1–C2 bonds for D_3-$Sc_3N@C_{68}$ in (b). The C–C bonds equivalents to C15–C27 are: C43–C44, C19–C20, C57–C58, C17–C34, C50–C51; equivalents to C23–C24 are: C25–C26, C37–C38, C39–C40, C32–C33, C30–C31; equivalents to C14–C24: C25–C45, C18–C38, C39–C59, C16–C31, C32–C52; equivalents to C2–C13: C9–C10, C5–C6, C46–C63, C60–C67, C53–C65; equivalents to C1–C2: C1–C6, C1–C10, C67–C68, C65–C68 and C63–C68. Description of the marked C–C bonds (MBO, θ_p): (1) D_3-C_{68}:**6140**; C15–C27 (1.266, 11.52 °), C23–C24 (1.257, 9.93 °), C14–C24 (1.252, 9.71 °) and (2) D_3-$Sc_3N@C_{68}$; C14–C24 (1.219, 9.97 °), C2–C13 (1.218, 10.35 °), C1–C2 (1.201, 9.55°).

interesting to know the reactivity of the 5:5 C15–C46, 6:5 C25–C26 and C24–C25 bond types, which have the highest final pyramidalization angles of 16.69°, 14.66° and 14.70°, respectively.

In conclusion, the study of the electron-attracting character and the analysis of the pyramidalization angle and MBO have shown that the endohedral doping of free fullerenes changes the exohedral reactivity of the fullerene surface in two ways: (1) it reduces and changes the reactivity of the most reactive sites, principally those around the carbon region that the scandiums are facing and (2) it improves the regioselectivity for C_{80}, which showed a very poor character, but does not improve it for C_{78} and C_{68}. In

general, however, TNT encapsulation is a new tool for controlling the regioselectivity of additions to the fullerene surface.

4.8 EXOHEDRAL REACTIVITY (II): FLUORINATION OF $Sc_3N@C_{80}$

4.8.1. Experimental

Preliminary data for hydrogenation of a very small quantity (*ca*. 1 mg) of $Sc_3N@C_{80}$ (mainly I_h but containing *ca*. 10% of the D_{5h} isomer) showed in two separate samples, the addition of 60 H and 68 H.[16] Subsequent investigation of fluorination of $Sc_3N@C_{80}$ using a larger sample gave a number of products that contained, in varying relative concentrations, between 42 and 64 fluorines. Because of the larger sample used, we consider that the fluorination results are the more reliable, and in all the fluorinated fractions $Sc_3N@C_{80}F_{52}$ was present, being the dominant species in a number of them.[74] Because of the presence of the minor isomer (which is less soluble in toluene than the main one) and possibly others, we believe that further and meaningful experimental investigations of polyaddition can only be undertaken with larger quantities of the pure isomers, should these become available. We have therefore carried out theoretical calculations to predict stabilities of derivatives of various addition levels, and to consider the stabilities in particular of various isomers at the X_{52} (X = H, F) addition level, both with and without incarcerated Sc_3N. Because of the difficulty accompanying calculations for large highly polyfluorinated fullerenes, for the incarcerated Sc_3N derivatives we have used the isostructural hydrogenated species as models *cf*. reference 75.

4.8.2 Hydrogenation binding energies (HBE) for I_h-C_{80}:7

As a first step we determined the most stable structures for compounds $C_{80}H_x$ (x = 2, 4, 16, 36, 44, 48, 52, 72, 76, 78, 80), thereby covering low (x = 2, 4), intermediate (x = 16, 36, 44, 48, 52) and high (x = 72, 76, 78, 80) addition levels. Each group has a particular rule for their stabilization. Previously, a large number of isomers, including non-symmetric structures, have been examined with the AIMPRO program to

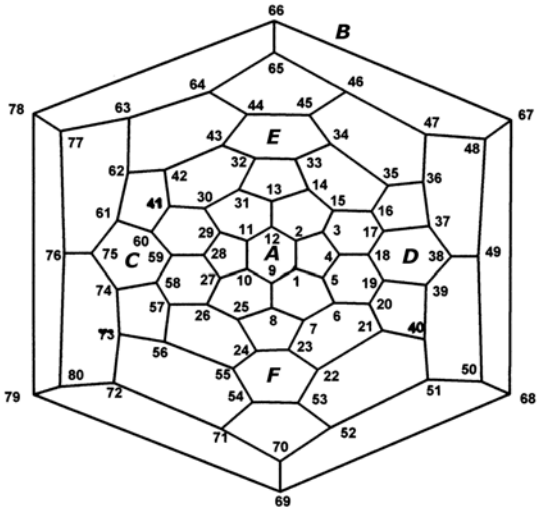

Figure 4.16 Schlegel diagram for the I_h-C_{80}:**7** fullerene showing numbering. The capital letters represent the position of the benzenoid rings.

obtain indications as to the most stable of them. The AIMPRO self-consistent density functional code running at the local spin density approximation (LSDA) level, allows an economic calculation as a first step.[76] With AIMPRO we found that non-symmetric structures for some stoichiometries are almost isoenergetic compared with the analogous symmetric structures presented in Table 4.17.[77] The description of the most stable isomers of each stoichiometry is given in Table 4.17, which shows the aromatic benzenoid rings, C=C bonds, symmetry, and the hydrogenation binding energies (HBE) for the process $C_{80} + nH_2 \rightarrow C_{80}H_{2n}$. Specifically, we computed the HBE per added H_2 (referred to as HBE/n) above the C_{80} surface because this BE allows us to compare all stoichiometries with each other. There are only two possibilities for the first addition to the C_{80} surface, either 6:5 C1–C2 or 6:6 C1–C9 bonds (see Figure 4.16 for numbering and position of the benzenoid rings) but we expect the most pyramidalized with a high MBO 6:5 C1–C2 bond ($\theta_p = 10.58^o$ and MBO = 1.194) to be the most reactive site (HBE = –1.25 eV). The product of H_2 addition across the 6:6 C1–C9 bond is 0.61 eV less stable.

Table 4.17 Hydrogenation binding energies (HBE/*n*, eV) per added H_2 of the most stable $C_{80}H_x$ and $Sc_3N@C_{80}H_x$ isomers [a]

x	*H atom locations* [a]	*Benzenoid rings* [b]	*C=C bonds* [b]	*Sym.* [c]	*HBE/n for* $C_{80}H_x$ [d]	*HBE/n for* $Sc_3N@C_{80}H_x$ [e]
2	1,2	0	--	C_s	–1.25	--
4	1,2,7,23	0	--	C_{2v}	–1.24	--
16	3-8, 25-31,13-15	A	--	C_{2v}	–1.04	--
36	[f]	A, C, D	--	C_2	–1.05	--
44	--	A, B, C, D, E, F	--	T_h	–1.08	–0.64
48	--	A, B, C, D	18,19; 37,38, 58,59; 61,75	C_s	–0.92	–0.53
*52:**1***	--	A, B, C, D	23,24; 32,33	C_{2v}	–0.83	–0.47
*52:**5***	--	A, B, C, D	22,23; 33,34	C_s	–0.82	–0.49
72	--	0	1,2; 39,40; 41,60; 78,79	C_s	–0.35	–0.10
76	--	0	1,2; 78,79	C_s	–0.20	--
78	--	0	1,2	C_s	–0.13	--
80	--	0	--	I_h	–0.06	--

[a] Up to the 36 H level the description is with respect to the hydrogenated carbons. Above the 16 H level it is with respect to benzenoid rings and the hydrogen-free C_2 bond atoms. [b] See Figure 4.16 for numbering. [c] Symmetry of $C_{80}H_x$ molecule. [d] HBE per H_2 added to C_{80}, HBE/n = ΔE/n, $n = x/2$, where ΔE = reaction energy for $C_{80} + nH_2 \rightarrow C_{80}H_{2n}$. [e] HBE per H_2 added to $Sc_3N@C_{80}$, HBE/n = ΔE/n, $n = x/2$, where ΔE = reaction energy for $Sc_3N@C_{80} + nH_2 \rightarrow Sc_3N@C_{80}H_{2n}$. [f] 3-8, 13-16, 20, 21, 25-31, 35, 36, 40-42, 48, 49, 56, 57, 62, 73,76, 80.

Formation of $C_{80}H_4$ is predicted to involve addition of H_2 to C_1–C_2 bond followed by addition to the 6:5 C7–C23 bond. By contrast, addition to the opposed remote C78–C79 or neighbouring 6:5 C4–C5 bonds gives isomers that are less stable by 0.38 and 1.20 eV, respectively. This suggests

that it is profitable to investigate additions fairly near to C–C bonds that have already undergone addition. The most stable isomers of $C_{80}H_x$ (x = 16, 36, 44, 48, 52) involve hydrogen addition so as to produce aromatic (benzenoid) rings, as is the case in the formation of $C_{60}Y_x$ (Y = H, F; x = 18, 36).[78, 79] $C_{80}H_{16}$ has only one benzenoid ring (A), whereas $C_{80}H_{44}$ has the maximum number of six (A-F). The latter structure adopts a 'cubic' shape due to the six planar aromatic faces together connected with twenty-two hydrogenated C–C bonds (Figure 4.17). $C_{80}H_{48}$ and $C_{80}H_{52}$ add the additional H_2 units to the E and F rings of $C_{80}H_{44}$ and consequently retain four benzenoid rings. In the higher stoichiometries, (x = 72, 76, 78) there are no benzenoid rings, and the remaining free 6:5 bonds are separated as far possible from each other. Thus the two unhydrogenated C=C bonds in $C_{80}H_{76}$ are located in the opposite hemispheres at C1–C2 and C78–C79. Location of the sole unhydrogenated bond in $C_{80}H_{78}$ across a 6:5 C1–C2 bond is marginally (0.11 eV) favoured over a 6:6 C1–C9 bond. Full sphericity is restored in $C_{80}H_{80}$, the cage radius being 4.502 Å compared with 4.103 Å for C_{80}, due to C–C bond lengthening arising from strong H–H steric repulsions rather than to rehybridization effects.[80]

We have also analyzed the bond between the C_{80} cage and the H_2 units using the extended transition method developed by Ziegler and Rouk (an extension of the decomposition scheme of Morokuma). According to this method, the BE between two fragments can be dissected into two main contributions: $BE = \Delta E_{DE} + \Delta E_{INT}$. In our specific case, ΔE_{DE} comprises only the deformation energy of C_{80}, *i.e.* the energy difference between the free C_{80} and C_{80} with the geometry of the particular $C_{80}H_x$ compound. ΔE_{INT}, the interaction energy, represents the energy involved in the interaction between the deformed C_{80} fullerene and the nH_2 units. ΔE_{DE} is always > 0 *i.e.* destabilising, whereas ΔE_{INT} can be > or < 0. An exothermic reaction requires $\Delta E_{INT} < 0$ and $|\Delta E_{INT}| > |\Delta E_{DE}|$. More details about this decomposition can be found in subsection 4.2.4. Recently this method has been used very satisfactorily, to rationalise the metal-C_{60} bonding in organometallic derivatives of C_{60}.[48] The components of the HBE are collated in Table 4.18.

There is a relatively small variation in the HBE/n between $C_{80}H_2$ and $C_{80}H_{44}$, (−1.25 and −1.08 eV per added H_2, respectively), but at higher hydrogenation levels the stabilities rapidly decrease, and $C_{80}H_{80}$ is only

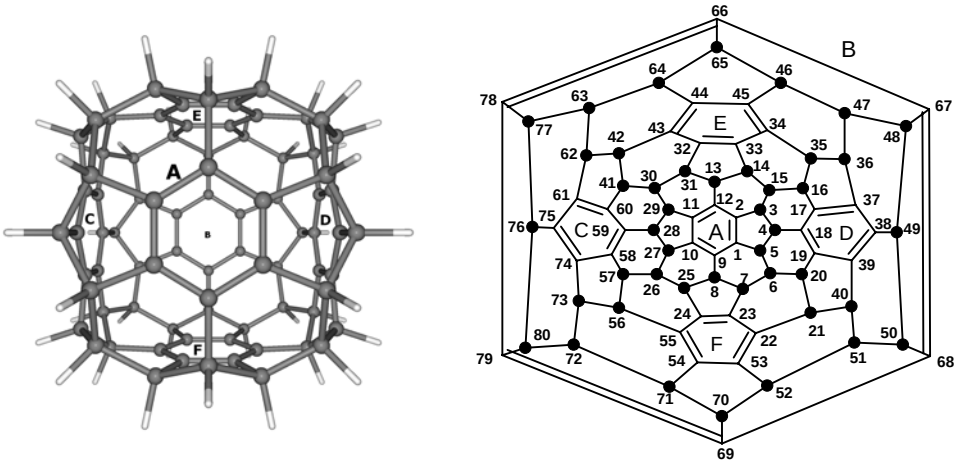

(a) $C_{80}H_{44}$ (b) $C_{80}H_{44}$

Figure 4.17 Optimized structure (a) and Schlegel diagram (b, ● = H) for $C_{80}H_{44}$. The benzenoid rings are located in both for comparison.

marginally stabilized (–0.06 eV per added H_2). This trend can be clearly seen in Figure 4.18 (circles). A parallel observation was found for C_{60} and C_{70} in that hydrogenation and fluorination led to maximum addend levels only of *ca*. 52 and 56 respectively.[81] A significant feature is that $C_{80}H_{44}$ possesses six benzenoid rings, the aromaticity of the latter arising from the presence of three sp^3 hybridised carbons in the two pentagons adjacent to each, thereby allowing delocalization without strain.[82] From $C_{80}H_2$ to $C_{80}H_{52}$ the ΔE_{DE} values increase gradually from 1.40 to 1.62 eV but thereafter reduce substantially to 1.01 eV for $C_{80}H_{80}$. This trend is closely related to the deformation of the cage; at hydrogenation levels above $C_{80}H_{52}$ the C_{80} geometry becomes increasingly spherical again up to $C_{80}H_{80}$. The ΔE_{INT} values also increase slightly up to $C_{80}H_{44}$ but thereafter decrease even more rapidly than the ΔE_{DE} values due to the lack of reactivity of the remaining C=C bonds towards H_2. The C–C bonds at high $C_{80}H_x$ stoichiometries are long and have low π-bond character. This seems to be the important factor in determining the notable change in HBE/*n* at around $C_{80}H_{44}/C_{80}H_{52}$ stoichiometry (Figure 4.18). For this reason, the $C_{80}H_{52}$ stoichiometry is particularly important, and in the next section we focus on the encapsulation of Sc_3N nitride in several isomers of $C_{80}H_{52}$ in order to find the most stable

Table 4.18 Deformation (ΔE_{DE}) and interaction energy (ΔE_{INT}) components of the hydrogenation binding energies per added H_2 (HBE/*n*) for the most stable isomers of $C_{80}H_x$ [a]

x	$\Delta E_{DE}/n$ [b]	$\Delta E_{INT}/n$ [c]	*HBE/n* [d]
2	1.40	–2.65	–1.25
4	1.42	–2.66	–1.24
16	1.67	–2.71	–1.04
36	1.59	–2.64	–1.05
44	1.60	–2.68	–1.08
48	1.62	–2.54	–0.92
*52:**1***	1.62	–2.45	–0.83
*52:**5***	1.59	–2.41	–0.82
72	1.31	–1.66	–0.35
76	1.16	–1.36	–0.20
78	1.08	–1.21	–0.13
80	1.01	–1.07	–0.06

[a] Energies in eV. [b] $\Delta E_{DE}/n$ = [E(C_{80}* geometry fixed at $C_{80}H_x$) - E(C_{80} optimized)]/*n*. [c] $\Delta E_{INT}/n$ = [E(C_{80}* + *n* $H_2 \rightarrow C_{80}H_{2n}$)]/*n*. [d] HBE/*n* = $\Delta E_{DE}/n + \Delta E_{INT}/n$.

one. Tables 4.17 and 4.18 present only a brief summary of the $C_{80}H_{52}$ study: the values for the most stable empty cage $C_{80}H_{52}$:**1**, and for the empty $C_{80}H_{52}$:**5** cage that produces the most stable $Sc_3N@C_{80}H_{52}$:**5** complex.

4.8.3 HBE for $Sc_3N@C_{80}$

Cages $C_{80}H_x$ (x = 44, 48, 52, 72) selected for encapsulation with Sc_3N are completely deformed, consequently there is only one possible position where the nitride can be stabilized (see below). The nitride is planar in $Sc_3N@C_k$ (k = 68, 78, 80), but is pyramidal in most $Sc_3N@C_{80}H_{52}$ studied isomers and $Sc_3N@C_{80}H_{72}$ as it is a free molecule. We compare HBE/*n* for $C_{80}H_{2n}$ and $Sc_3N@C_{80}H_{2n}$ to determine the difference in the values arising from adding H_2 units to the corresponding parents (last two columns of Table 4.16). The data for the endohedral complexes parallel those for the empty cages, except that the BE disadvantage on going to higher addition levels is even larger (see squares compared with circles in Figure 4.18). For

Table 4.19 Decomposition of the hydrogenation (HBE) and encapsulation (EBE) binding energies for $Sc_3N@C_k$ (k = 78, 80) and $Sc_3N@C_{80}H_x$ (x = 44, 48, 52, 72) [a]

Compound	ΔE_{DE}	ΔE_{INT}	*HBE* [b]	ΔE_{DE}		ΔE_{INT}	*EBE* [c]
				Sc_3N	*Cage*		
$Sc_3N@C_{78}$:**1**	--	--	--	0.72	1.49	–11.91	–9.70
$Sc_3N@C_{80}$:**11**	--	--	--	0.79	0.58	–12.97	–11.60
$Sc_3N@C_{80}H_{44}$	35.20	–58.96	–23.76	0.53	1.47	–5.69	–3.69
$Sc_3N@C_{80}H_{48}$	38.95	–60.98	–22.03	0.57	1.84	–6.34	–3.93
$Sc_3N@C_{80}H_{52}$:**5**	41.29	–62.56	–21.27	0.28	2.62	–7.83	–4.93
$Sc_3N@C_{80}H_{72}$	47.09	–59.65	–12.56	0.34	2.55	–7.09	–4.20

[a] Energies in eV. [b] Hydrogenation binding energies (HBE) for the reaction $C_{80} + nH_2 \rightarrow C_{80}H_{2n}$; HBE = $\Delta E_{DE} + \Delta E_{INT}$. [c] Encapsulation binding energies (EBE) for the reactions $C_k + Sc_3N \rightarrow Sc_3N@C_k$ (k = 78, 80) and $C_{80}H_x + Sc_3N \rightarrow Sc_3N@C_{80}H_x$ (x = 44, 48, 52, 72); EBE = $\Delta E_{DE} + \Delta E_{INT}$.

example, the addition of 22 H_2 to empty C_{80} produces an energy of *ca.* 1.08 per added H_2, whereas the same addition to $Sc_3N@C_{80}$ gives an energy of only 0.64 eV per added H_2. Encapsulation of Sc_3N is a strongly exothermic process that is accompanied by a formal transfer of six electrons from the scandiums to the fullerene cage, thereby making hydrogen addition less favourable. In large stoichiometries such as $Sc_3N@C_{80}H_{72}$ the lack of reactivity of the remaining C–C bonds also disfavours addition, and the HBE/n is reduced to only –0.10 eV.

4.8.4 Sc_3N encapsulation in free cages vs. hydrogenated fullerenes cages

The comparison (Table 4.19) between $Sc_3N@C_k$ (k = 78, 80) and $Sc_3N@C_{80}H_x$ (x = 44, 48, 52, 72) provides a measure of the energy involved in the encapsulation and hydrogenation processes. The EBE for $C_k + Sc_3N \rightarrow Sc_3N@C_k$ accounts –11.60 and –9.70 eV for k = 80 and 78, respectively. The deformation energy component (ΔE_{DE}) of EBE comprises the deformation produced in the Sc_3N nitride and the cage, both of which are small components, *e.g.* 1.37 eV in total for k = 80. The much more significant contributor to the EBE is the favourable interaction energy (ΔE_{INT}) arising from the electron transfer from nitride to fullerene cage, and which for x = 80 is –12.97 eV. Whereas for $Sc_3N@C_k$ complexes, only

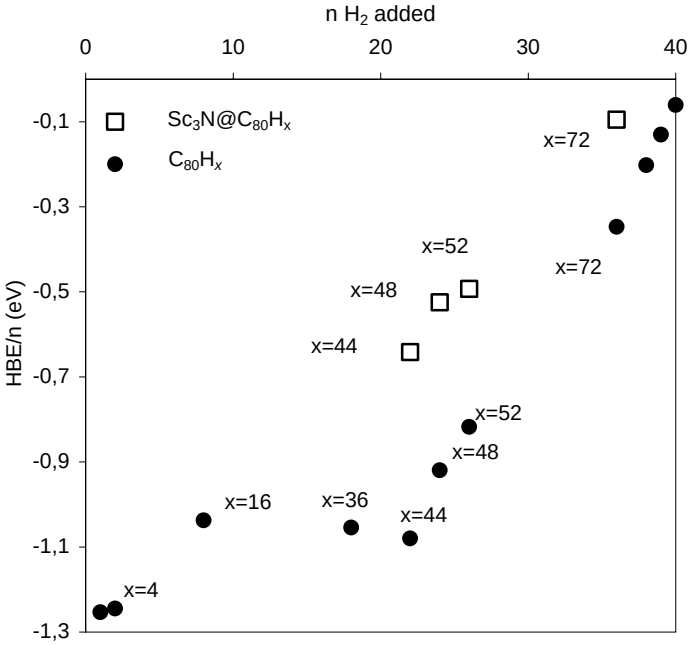

Figure 4.18 Hydrogenation binding energy per added H_2 (HBE/*n*) for series $C_{80}H_x$ (*x* = 2, 4, 16, 36, 44, 48, 52, 72, 76, 78 and 80), circles, and $Sc_3N@C_{80}H_x$ (*x* = 44, 48, 52, 72), squares.

computation of encapsulation is required, $Sc_3N@C_{80}H_x$ requires computation of both encapsulation and hydrogenation, for which two sequences exist. To simplify the calculations involved in finding the most stable structures of $Sc_3N@C_{80}H_x$ we first narrow down the hydrogenated possibilities (in order to make the computations manageable) and then determine energies for placing Sc_3N inside them. Note that this simplification is based on the difference of the absolute EBE and HBE. HBE for $C_{80}H_x$ (*x* = 44, 48, 52) are *ca*. –22 eV, almost double the EBE involved in formation of $Sc_3N@C_{80}$ (–11.6 eV). Consequently, hydrogenation rather than encapsulation will determine the selection of the most stable isomers, so that this energy difference validates our procedure. The HBE for $C_{80}H_x$ are dominated by the favourable ΔE_{INT} between the cages and the H_2 units, and decrease in the order $C_{80}H_{44} > C_{80}H_{48} > C_{80}H_{52} > C_{80}H_{72}$. The EBE in these hydrogenated cages decrease drastically from –

11.6 for $Sc_3N@C_{80}$ to *ca*. –4 for $Sc_3N@C_{80}H_x$ (x = 44, 48, 52, 72) complexes due to an increase of ΔE_{DE} of the fullerene cage, but above all due to a decrease of the ΔE_{INT} between the hydrogenated cage and the nitride *i.e.* –12.97 eV for $Sc_3N@C_{80}$ compared to *ca*. –7 for $Sc_3N@C_{80}H_x$ (x = 44, 48, 52, 72) complexes. This less effective interaction may reflect electron transfer from the nitride to the hydrogenated cage being less facilitated due to the lower acceptor character of the unoccupied orbitals of the hydrogenated cage compared to those of C_{80}. The decrease in the in-cage space and consequent increase in steric repulsion between the nitride and cage is involved in the ΔE_{INT} diminution.

The highest HBE is found for $C_{80}H_{44}$ and the highest EBE for $Sc_3N@C_{80}H_{52}$:**5**. The EBE is favoured by having a suitable in-cage space to incarcerate Sc_3N, the largest space being found in $Sc_3N@C_{80}H_{52}$ among $Sc_3N@C_{80}H_x$ (x = 44, 48, 52, 72). Note that the only marginally stabilized H_2 addition to $Sc_3N@C_{80}$ at higher addition levels is caused by HBE rather than EBE, as exemplified by $Sc_3N@C_{80}H_{72}$ (–0.10 eV). Compared to $Sc_3N@C_{80}H_{44}$ the HBE decreases from –23.76 to –12.56 eV, whereas the EBE are closely similar (–3.69 and –4.20 eV respectively).

4.8.5 Stabilities of $C_{80}H_{52}$ and $C_{80}F_{52}$ isomers

A common experimental occurrence of a 52-addend level for hydrogenation and fluorination of $Sc_3N@C_{80}$, prompted a deeper investigation to find the most stable isomers of $C_{80}H_{52}$, $C_{80}F_{52}$, and $Sc_3N@C_{80}H_{52}$ and the stabilising factors affecting their REs. Following the procedure in subsection 4.8.4, the most stable structures obtained from hydrogenation were determined and then Sc_3N was encapsulated. Fourteen isomers of $C_{80}H_{52}$ are collated in Table 4.20 showing the number of benzenoid rings, C=C bonds and REs. Isomers **1-8** are the most stable, the stabilities differing by only 0.35 eV overall, with **1** being the most stable. These isomers uniquely each possess four benzenoid rings (A, B, C, D) and two C=C bonds in hexagons E and F *i.e.* on opposite sides of the cage (Figure 4.16 and Table 4.20). Isomers **9** and **10** also have four benzenoid rings but here the C=C bonds are not located in hexagons **E** and **F** and this is seen to have a marked difference on the calculated stabilities. The calculated energies for isomers **9-14** are also high due evidently to the lower

Table 4.20 Description and relative energies (RE) of $C_{80}H_{52}$, $C_{80}F_{52}$ and $Sc_3N@C_{80}H_{52}$ isomers [a]

Iso.	*Benzenoid rings* [b]	*C=C bond* [c]	*Sym.* [d]	$C_{80}H_{52}$	$C_{80}F_{52}$	$Sc_3N@C_{80}H_{52}$
1	A, B, C, D	23,24; 32,33	C_{2v}	0.00	0.00	0.00
2	A, B, C, D	23,24; 44,45	C_{2h}	0.03	0.05	–0.39
3	A, B, C, D	22,53; 32,33	C_1	0.18	--	--
4	A, B, C, D	22,23; 32,33	C_2	0.32	0.51	0.43
5	A, B, C, D	22,23; 33,34	C_s	0.31	0.50	–0.55
6	A, B, C, D	22,23; 32,43	C_2	0.35	0.55	–0.25
7	A, B, C, D	22,23; 34,45	C_2	0.32	0.51	0.44
8	A, B, C, D	22,23; 44,45	C_i	0.35	0.58	--
9	A, B, C, D	7,23; 14,33	C_s	1.73	2.21	1.77
10	A, B, C, D	21,22; 42,43	C_2	2.26	3.07	--
11	A, B	17,37; 19,39; 22,23; 24,55; 32,43; 33,34; 58,74; 60,61	C_s	1.39	0.19	--
12	A, B	17,18; 22,23; 24,55; 32,43; 33,34; 38,39; 58,59; 61,75	C_2	1.44	0.79	0.49
13	--	[e]	C_s	5.24	5.22	--
14	--	[f]	C_{2v}	3.58	4.04	2.90

[a] Energies in eV. Description with respect to hydrogen-free carbons, benzenoid rings, and C_2 free bonds. [b] See Figure 4.16. [c] Double bond locations, either 6:6 or 6:5 bonds. [d] Symmetry of $C_{80}H_{52}$ and $C_{80}F_{52}$ isomers. [e] 1,5; 7,23; 10,27; 14,33; 17,37; 19,39; 31,32; 44,64; 45,46; 50,68; 52,53; 58,74; 60,61; 79,80. [f] 4,18; 8,9; 12,13; 22,23; 24,55; 28,59; 32,43; 33,34; 36,47; 40,51; 62,63; 65,66; 69,70; 72,73.

number of benzenoid rings in the structures, and thus the least stable isomers **13** and **14** have no benzenoid rings, the fourteen C=C bonds being spread around the cage.

The Schlegel diagram and optimized structure of $C_{80}H_{52}$:**1** are shown in Figure 4.19. The lengths of the C–C bond in the aromatic benzenoid rings are calculated to vary only from 1.377 to 1.386 Å, the aromaticity being

confirmed also by the calculated planarity. This parallels the structural situation found experimentally for $C_{60}H_{36}$ isomers.[79] The lengths of the isolated C=C bonds are calculated as 1.335 Å. The resultant structure resembles a cube with four planar faces and two wrinkled ones which contain the C=C bonds, and notably, the hydrogenation of 26 C–C bonds in C_{80} produces a major distortion of the original shape. The C–C bond lengths for the other isomers differ little from the above values. Results for fluorination are similar, except that isomer **11** is relatively more stable than the hydrogenated counterpart. The C–F distances for the most stable isomer **1** are calculated to range from 1.367-1.396 Å which parallels the values found for $C_{60}F_{48}$ (1.362-1.395 Å)[83] and $C_{60}F_{18}$ (1.361-1.396 Å).[84] This indicates that the present level of computing is very satisfactory. The similar results for H and F atoms allow us to use with some confidence, hydrogen as a model for calculating the energies of the *incar* Sc_3N derivatives.

4.8.6 Stabilities of $Sc_3N@C_{80}H_{52}$ isomers

To construct the $Sc_3N@C_{80}H_{52}$ isomers we encapsulated the Sc_3N unit retaining some symmetry properties such as symmetry plane or C_2 axis and also orientating the Sc atoms over the C=C bonds and the benzenoid rings. These requirements and the space limitation of the fullerene restrict the stabilising orientation of the nitride in each $C_{80}H_{52}$ isomer to one possibility only. By contrast, in $Sc_3N@C_{80}$ the Sc_3N unit is not trapped in a specific position and free rotation is expected. The preference for Sc atoms to be close to the free C atoms is expected because the latter can use their p_z orbitals to make Sc–C bonds. Moreover, to accomplish these requirements, Sc_3N adopts a pyramidal structure in most of the isomers. Isomers of $Sc_3N@C_{80}H_{52}$ were optimized from $C_{80}H_{52}$ isomers **1, 2, 4-7, 9** that have four benzenoid rings, and also isomers **12** and **14** that have two and no benzenoid rings, respectively; lack of symmetry precluded calculations on isomers **3, 8, 10** and **11**. The REs show significant differences from those of their empty-cage counterparts (see last column of Table 4.20), but the most stable $Sc_3N@C_{80}H_{52}$ isomers come from the first eight most stable $C_{80}H_{52}$ isomers. Isomers $Sc_3N@C_{80}H_{52}$:**2, 5,** and **6** are predicted to be more stable than isomer $Sc_3N@C_{80}H_{52}$:**1** (derived from the most stable $C_{80}H_{52}$ isomer)

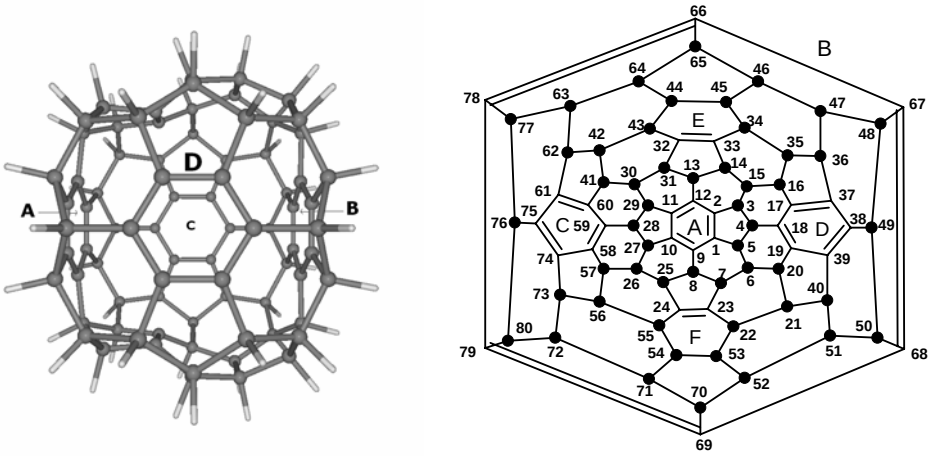

(a) $C_{80}H_{52}$:**1** (b) $C_{80}H_{52}$:**1**

Figures 4.19 Optimized structure (a) and the Schlegel diagram (b, ● = H) for $C_{80}H_{52}$:**1**. Structure (a) is rotated relative to the Schlegel diagram. The benzenoid rings are located in both for comparison.

with $Sc_3N@C_{80}H_{52}$:**5** the most stable overall; both isomers are displayed in Figures 4.20 and 4.21.

The substantial alteration of the REs as a result of encapsulation of Sc_3N arises from different interaction between the nitride and the relevant hydrogenated cage, together with the different number and strength of the Sc–C bonds. This argument is developed further in section 4.3. The geometric and electronic structure of the most stable isomer $Sc_3N@C_{80}H_{52}$:**5** is considered first, followed by determination of the factors that affect the stabilization of the $Sc_3N@C_{80}H_{52}$ isomers.

4.8.7 Geometric and electronic structure of $Sc_3N@C_{80}H_{52}$:5

Some values of the HOMO-LUMO gap in eV (a measure of stability) are: I_h-C_{80}, 1.93; $C_{80}H_{52}$:**5**, 3.96; $Sc_3N@C_{80}$:**11**, 1.18; $Sc_3N@C_{80}H_{52}$:**5**, 0.23. The latter thus appears to be the least stable amongst this family of complexes. When Sc_3N is encapsulated by $C_{80}H_{52}$:**5**, there is significant local distortion in the hydrogenated cage. In this isomer, two Sc atoms face the two isolated C=C bonds (C22–C23 and C33–C34) and the other faces benzenoid ring D and two atoms of B (Figure 4.20b). This

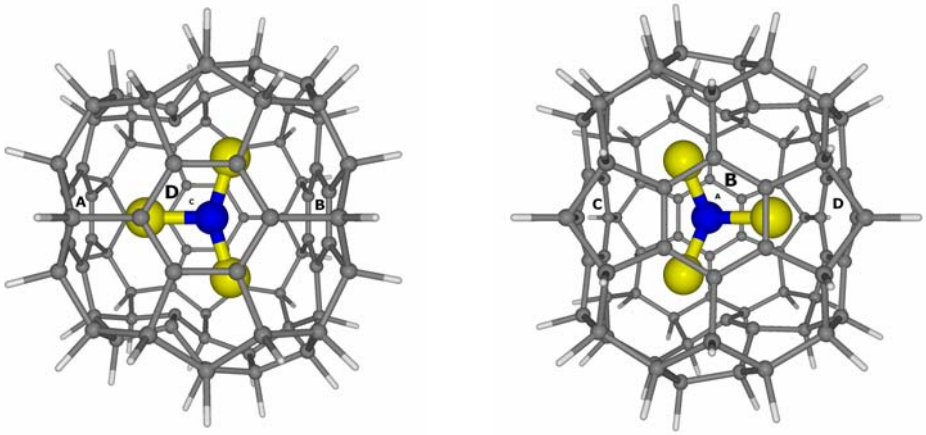

(a) $Sc_3N@C_{80}H_{52}$:**1** (b) $Sc_3N@C_{80}H_{52}$:**5**

Figure 4.20 Optimized structures for $Sc_3N@C_{80}H_{52}$:**1** (a) and $Sc_3N@C_{80}H_{52}$:**5** (b). For comparison, the benzenoid rings are located in each picture.

distortion results in inward movement of the non-hydrogenated carbons until they attain bonding Sc–C distances. The benzenoid ring B is moved substantially inward. The pyramidal Sc_3N unit (Sc–N distance of 1.921 Å, *cf.* 1.957 Å in the free molecule, Table 4.21) is unable to either rotate or fluctuate *i.e*. it is completely fixed in this orientation. The cage otherwise retains the overall structure of the $C_{80}H_{52}$:**5** precursor (Figure 4.21). Hence hydrogenation determines the main geometric features of the cage, whilst encapsulation produces modification. During the geometrical optimization process, the contacts between Sc and free C atoms become favoured and maximized. The average distance between Sc and the eight carbons of benzenoid ring D and two of ring B decrease to a bonding distance of 2.391 Å. The aromaticity of these two rings is broken and the range of C–C distances within them is increased (1.384–1.446 Å). The other non-bonded benzenoid rings (A and C) retain their aromaticity. The shortest Sc–C distances (2.293 Å) are found between the other two Sc atoms and one of the carbons of the two C=C bonds. Due to these Sc–C_2 bonds the C=C bond lengths of the cage are increased by 0.085 Å.

These Sc–C distances fall within the range of values obtained in an exploration of 73 examples in the Cambridge Structural Database, where the mean is 2.430 Å and the shortest 2.204 Å. Both experimental (2.170 Å) and

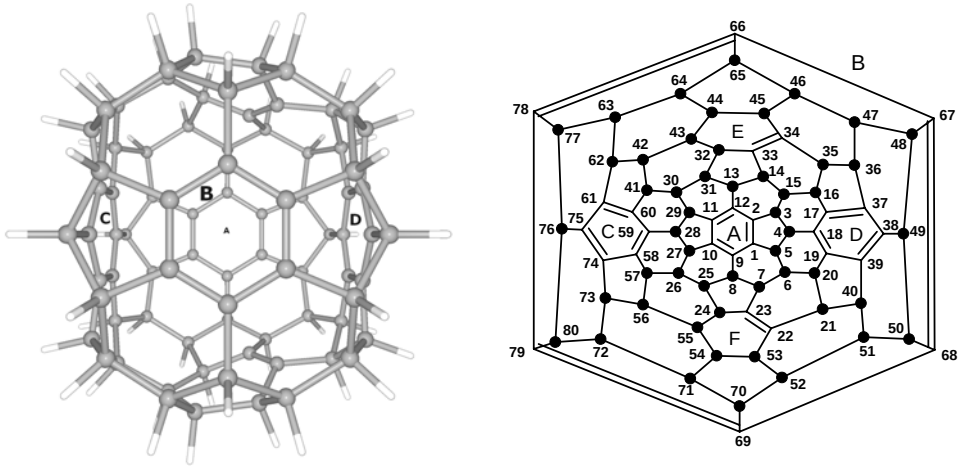

(a) $C_{80}H_{52}$:**5** (b) $C_{80}H_{52}$:**5**

Figure 4.21 Optimised molecular structure (a) and Schlegel diagram (b, ● = H) for $C_{80}H_{52}$:**5**. The benzenoid rings are located in both for comparison.

theoretical (2.276 Å) distances for $Sc_3N@C_{80}$ were shorter than the calculated Sc–C distances in $Sc_3N@C_{80}H_{52}$:**5**. The presence of bonding Sc–C distances and the potential for trapping of Sc_3N in a specific position, prompted us to investigate the possibility of strong Sc–C bonds between the Sc_3N unit and the hydrogenated cage. However, $Sc_3N@C_{80}$ may be *formally* described by the $Sc_3N^{6+}@C_{80}^{6-}$ ionic model involving the transfer of six electrons from the three nitride highest occupied orbitals to the three lowest unoccupied orbitals of C_{80}, and free rotation of Sc_3N unit. The electronic structure of $Sc_3N@C_{80}H_{52}$:**5** is characterized not only by the ionic interaction but also by orbital interactions of both fragments which incarcerate the Sc_3N in a specific position. Likewise, there is formal transfer of six electrons from the three highest occupied orbitals of Sc_3N unit to the three lowest unoccupied orbitals of $C_{80}H_{52}$ molecule, which become the three HOMOs of the new $Sc_3N@C_{80}H_{52}$:**5** complex. These cage orbitals, which represent π^* C–C orbitals of $C_{80}H_{52}$:**5** also become highly stabilized due to bonding interactions with empty *d* metal orbitals, so explaining the strong link between Sc atoms and the free C atoms of the cage. The three bonding orbitals are displayed in Figure 4.22.

Table 4.21 Optimized distances for $Sc_3N@C_{80}H_{52}$ isomers [a]

Iso.	*Mean Sc–N distance* [a]	*No. of Sc–C_2 connections*	*Mean Sc–C distance* [b]	*No. of Sc–C_6 connections*	*Mean Sc–C distances*
1	1.879	4	2.224	6	2.361
2	1.895	4	2.326	6	2.387
4	1.884	4	2.391	6	2.366
5	1.921	4	2.423	8	2.391
6	1.897	4	2.313	6	2.437
7	1.891	4	2.363	6	2.371
9	1.903	2	2.269	8	2.388
12	1.877	6	2.318	--	--
14	1.920	4	2.364	--	--

[a] Distances in Å. [b] Calculated as 1.957 Å in Sc_3N. [c] Calculated as 2.276 Å in $Sc_3N@C_{80}$.

4.8.8 Factors affecting the stabilization energies

The REs were analyzed in terms of their components in order to determine the origin of the differences amongst the $Sc_3N@C_{80}$ isomers (Table 4.22). To aid this analysis, the Sc–N bond lengths and the different type of Sc-cage connections with their respective lengths are collated in Table 4.21. The main contributions to the RE (HBE and EBE), can each be dissected into the deformation energy (ΔE_{DE}) and the interaction energy (ΔE_{INT}). As seen from Table 4.22, EBE but not HBE is the crucial component of the RE and determines the stability order of the $Sc_3N@C_{80}H_{52}$ isomers. Thus whilst $Sc_3N@C_{80}H_{52}$:**5**, the most stable isomer, does not have the highest HBE, it has the highest EBE of –4.93 eV. For the first eight most stable $C_{80}H_{52}$ isomers the relative HBE ranges between 0.00 and 0.35 eV whereas the relative EBE between 0.44 and –0.55 eV. So the differences in the interaction between Sc_3N and the different $C_{80}H_{52}$ cages determine the final RE of $Sc_3N@C_{80}H_{52}$ isomers. This isomer is therefore the most favourable because Sc_3N unit is encapsulated favouring Sc–C contacts,

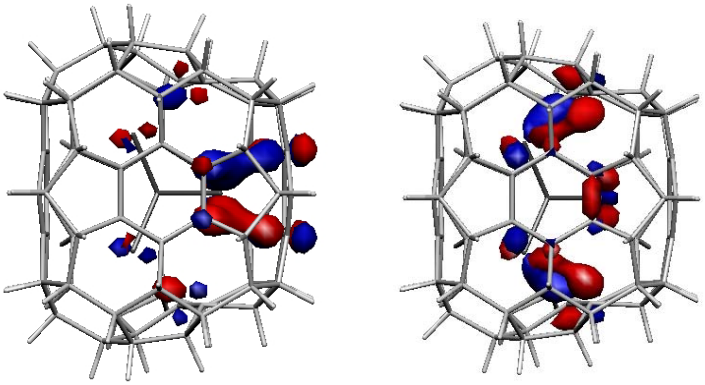

(a) HOMO-2 (b) HOMO-1

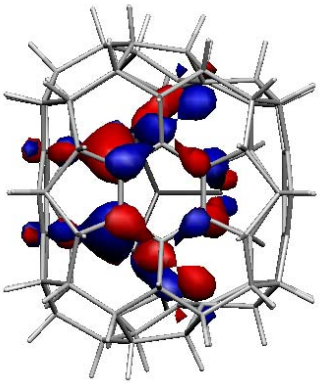

(c) HOMO

Figure 4.22 The three highest occupied molecular orbitals (MO) of $Sc_3N@C_{80}H_{52}$:**5**. The orbitals represent the bonding between (a) Sc atom and the 6 carbons of D benzenoid ring, (b) two Sc atoms and the two C=C bonds (C22–C23, C33–C34) and (c) Sc atom and the B benzenoid. ring. All orbitals comprise the empty Sc *d*-orbitals and π^* C–C orbitals of $C_{80}H_{52}$:**5**.

shown by the maximum interaction term (ΔE_{INT} = –7.83 eV) and minimum deformation of Sc_3N (ΔE_{DE} = 0.28 eV) compared to the other isomers.

Unlike isomers $Sc_3N@C_{80}H_{52}$:**1**, **2**, **4**, **6** and **7**, which have at least four Sc–C_2 type and six Sc–C_6 type interactions, the most stable isomer $Sc_3N@C_{80}H_{52}$:**5** has the advantage of two additional Sc–C_6 type interactions. Moreover these two additional bonding interactions are

Table 4.22 Relative binding energies (RE[HBE] and RE[EBE]) for the most stable $Sc_3N@C_{80}H_{52}$ isomers [a]

Iso.[b]	ΔE_{DE}	ΔE_{INT}	*HBE* [c]	*RE [HBE]*	ΔE_{DE}	ΔE_{INT}	*EBE* [d]	*RE [EBE]*	*Total RE* [e]
1*	42.02	–63.58	–21.56	0.00	2.87	–6.94	–4.07	0.00	0.00
2°	42.04	–63.57	–21.53	0.03	3.13	–7.62	–4.49	–0.42	–0.39
4°	41.41	–62.64	–21.23	0.33	3.15	–7.12	–3.97	0.10	0.43
5*	41.30	–62.55	–21.25	0.31	2.90	–7.83	–4.93	–0.86	–0.55
6°	41.12	–62.33	–21.21	0.35	3.10	–7.77	–4.67	–0.60	–0.25
7°	41.41	–62.65	–21.24	0.32	3.03	–6.98	–3.95	0.12	0.44
9*	--	--	–19.83	1.73	--	--	–4.03	0.04	1.77
12°	--	--	–20.12	1.44	--	--	–5.02	–0.95	0.49
14ª	--	--	–17.98	3.58	--	--	–4.75	–0.68	2.90

[a] Energies in eV. The binding energy of $Sc_3N@C_{80}H_{52}$ isomers comprise the energy required to hydrogenate C_{80} to the $C_{80}H_x$ isomers (HBE) and the energy of incarcerating Sc_3N (EBE). This necessarily differs from the experimental sequence involving encapsulation followed by hydrogenation. [b] * = C_s; ° = C_2 and ª = C_{2v}. Symmetry of $Sc_3N@C_{80}H_{52}$ which in some cases is reduced from corresponding symmetry of $C_{80}H_{52}$ isomers. [c] Hydrogenation binding energy (HBE), ΔE for $C_{80} + 26\ H_2 \rightarrow C_{80}H_{52}$. HBE = $\Delta E_{DE} + \Delta E_{INT}$. [d] Encapsulation binding energy (EBE), ΔE for $C_{80}H_{52} + Sc_3N \rightarrow Sc_3N@C_{80}H_{52}$. EBE = $\Delta E_{DE} + \Delta E_{INT}$. $\Delta E_{DE} = \Delta E_{DE}(Sc_3N) + \Delta E_{DE}$ (cage). [e] Total RE = RE[HBE] + RE[EBE].

obtained with only minor distortion of the Sc_3N unit. Finally, it is noteworthy that for encapsulation of Sc_3N unit inside isomers $C_{80}H_{52}$:**12** and **14** the EBE is not enough to counteract the destabilization produced by the HBE. This is important because it deters searching for $Sc_3N@C_{80}H_{52}$ with a HBE for C_{80} destabilized more than 1 eV (the highest relative EBE found has been –0.95 eV for $Sc_3N@C_{80}H_{52}$:**12**).

In conclusion, the most stable $Sc_3N@C_{80}H_{52}$ isomer is that in which the Sc_3N unit can be hosted to allow the highest number of bonding interactions between the Sc atoms and the 28 free carbons, provided the destabilization produced by the HBE is not too high. This has allowed us to predict the most stable isomers for $Sc_3N@C_{80}H_x$ (x = 44, 48, 72) complexes.

4.9 CONCLUDING REMARKS

The experimental results illustrate that a wide range of new endohedral metallofullerenes that contain four atoms can be prepared in reasonably high yields and purity. The unique structure, chemistry and reactivity of these new encapsulated molecules will clearly provide new directions in host-guest chemistry. The fact that the internal atomic or molecular species (*e.g.* Er, Sc, Gd, etc. as well as mixed metals), the number of caged atoms and the fullerene cage size (*e.g.* C_{68}, C_{78}, C_{80}) can be controlled separately in TNT endohedral metallofullerenes means that considerably more variations may be found in the near future. The TNT process for the production of endohedral metallofullerenes opens up new vistas for developing and understanding how the properties are determined by metal encapsulation and for exploiting these unique materials in a wide range of electronic, optoelectronic, magnetic, catalytic, nanomechanical and medical applications.

Experimental advances. A new family of trimetallic nitride template (TNT) endohedral metallofullerenes have been synthesized and fully characterized recently in yields that are relatively higher than the classical endohedral metallofullerenes with a formula of $A_{3-n}B_nN@C_k$ (n = 0-3; A and B = group III, IV and rare-earth metals, k = 68, 78, 80). The archetypal examples are: $Sc_3N@C_{80}$, $Sc_3N@C_{78}$ and $Sc_3N@C_{68}$. The high yields produced by the modified Krätschmer-Huffman method have enabled these new endohedral metallofullerenes to be fully characterized by X-ray and spectroscopic techniques. It is interesting to see that the IPR fullerene cages encapsulating the TNT units (D_{3h}-C_{78}:**5**, I_h-C_{80}:**7**) are not the most stable IPR isomers for each stoichiometry. The theoretically most stable and experimentally isolable isomers are the C_{2v}-C_{78}:**3** and D_{5d}-C_{80}:**1** fullerene isomers. Even the TNT encapsulation can stabilize non-IPR cages such as D_3-C_{68}:**6140**. Finally, the exohedral functionalization via cycloaddition and fluorination addition reactions has been carried out successfully, mostly in the $Sc_3N@C_{80}$ complex.

Ionic bond. $Sc_3N@C_k$ (k = 68, 78, 80) complexes may be *formally* described by the ionic model $Sc_3N^{6+}@C_k^{6-}$. A total of six electrons formally

go from the three highest occupied orbitals to three low-lying unoccupied cage orbitals. The resulting endohedral complex has a relatively high HOMO-LUMO gap, which confers stability. We have shown that the final HOMO-LUMO gap of these TNT endohedral metallofullerenes can be estimated from the LUMO+3-LUMO+4 gap found in the free cages, which corresponds to the hypothetical anion when six additional electrons are added to the free cage, C_k^{6-}. The search for high LUMO+3-LUMO+4 gaps in the 51 IPR isomers of the cages between C_{60} and C_{84} revealed that only D_{3h}-C_{78}:**5**, D_{5h}-C_{80}:**6** and I_h-C_{80}:**7** provide an electronic structure that is suitable for encapsulating the TNT units. Moreover, the non-IPR D_3-C_{68}:**6140** cage was similarly stabilized by the formal six electron charge transfer. Indeed, only these cages have been detected experimentally to encapsulate TNT units. Two conclusions can be drawn the electronic structure of TNT endohedral metallofullerenes: (1) the IPR cannot be applied to charged fullerenes, and (2) so far only endohedral metallofullerenes have been capable of producing non-IPR fullerenes and non-stabilized IPR fullerene cages.

$Sc_3N@C_{78}$. In the endohedral $Sc_3N@C_{78}$ the Sc_3N unit lies planar unlike the free Sc_3N and the scandium ions are strongly linked to pyracylene 6:6 C–C bonds. This bond does not allow the Sc_3N unit to rotate freely inside the fullerene. Steric repulsion forces the C_2 units closest to the Sc ions to be pushed away from the fullerene surface, a feature that the original X-ray characterization of $Sc_3N@C_{78}$ did not show. The consequence is an increment in the cage radius and an elongation of the pyracylene 6:6 C–C bonds. However, re-examination of the crystallographic data using the computed structure for $Sc_3N@C_{78}$ shows that this model provides a better fit to the data than the rigid C_{78} cage used previously. The EBE for this TNT endohedral metallofullerene is computed to be –9.70 eV, rather large stabilization energy. Although $Sc_3N@C_{78}$ may also be *formally* described by the $Sc_3N^{6+}@C_{78}^{6-}$ ionic model, the difference of 1.11 eV between the most and least stable isomers ($Sc_3N@C_{78}$:**1** and $Sc_3N@C_{78}$:**3**, respectively), constructed by the hypothetical Sc_3N rotation, is basically due to an *orbital* effect.

$Sc_3N@C_{80}$. In essence, the bond between the Sc_3N unit and the icosahedral isomer of C_{80} is comparable to the analogous bond in C_{78}, but the lack of any pyracylene C–C bond in I_h-C_{80}:**7** makes the two endohedrals ($Sc_3N@C_{78}$ and $Sc_3N@C_{80}$) different. In the latter, the scandium ions are not trapped in a specific position in the fullerene. This was confirmed experimentally by (1) the numerous Sc_3N orientations in complexes with the $Sc_3N@C_{80}$ unit; and (2) the ^{13}C NMR spectrum which preserves the I_h symmetry of the cage. The majority of the isomers are less stable than the most stable isomer —where the Sc atoms are facing three corannulene 6:5 C–C bonds— by only 0.01-0.08 eV. The EBE is somewhat higher for the larger cluster, a fact that may be attributed to the smaller steric repulsion.

$Sc_3N@C_{68}$. All isomers of C_{68} are non-IPR fullerenes but isomer D_3-C_{68}:**6140** has the minimum number of destabilising fused pentagon pairs, which means that it has an advantage over the other isomers with a higher number of this kind of C–C bonds. The nitride donates six electrons to the C_{68} cage, so the resulting closed-shell electronic structure with a high HOMO-LUMO gap is formally described as the $Sc_3N^{6+}@C_{68}^{6-}$ ionic model. It is noteworthy that only endohedral encapsulation is capable of producing non-IPR fullerene cages since these cages would be very unstable as free fullerenes. This fullerene is significantly different from the other fullerenes whose endohedral complexes are detected. $D_{3h'}$-C_{78}:**5** and I_h-C_{80}:**7** are spherical with a cage radius of 4.052 Å and 4.103 Å, respectively, but C_{68} not only has a smaller cage radius (3.783 Å) but also a distorted cage with only one plane which can accommodate the host. In this plane, where the planar Sc_3N is directly connected to 5:5 ring junctions, there is enough space to encapsulate the TNT unit because the distances between the fullerene surface and the cage-center are similar to those found in C_{78} and C_{80} fullerene cages. Only one Sc_3N orientation is possible for the $Sc_3N@C_{68}$ complex. The EBE and its decomposition is similar to those found in C_{80}. Although C_{68} has a higher steric repulsion term because it is smaller, the highest stabilization in the orbital interaction compensates for this destabilization.

Extended family. The geometry and electronic structure of the encapsulation of the Y_3N and La_3N TNT units inside the $D_{3h'}$-C_{78}:**5** and I_h-C_{80}:**7** cages were studied. The TNT unit maintains a pyramidal shape because the ionic radius of the Y and La atoms increases. This prevents the unit from being planarized. Although the electron charge transfer to the cage in these new members of the TNT endohedral metallofullerenes is expected to be higher, the formal electronic structure can also be described as $M_3N^{6+}@C_k^{6-}$ (M = Y and La, k = 78, 80). This observation disagrees with the electronic structure for $La_3N@C_{80}$ proposed by Kobayashi, who theorizes about an eight electron charge transfer from the TNT unit to the cage. In our studies, this electron charge transfer is not observed because it involves the removal of highly stabilized electrons from the *p* nitrogen orbitals. It is expected that encapsulation of TNT units containing a variety of metals will extend and enrich the research area of TNT endohedral metallofullerenes.

Physical properties. The formal transfer of six electrons from the TNT unit to the cage reduces the electron affinity (EA) of the TNT endohedral metallofullerenes with respect to the analogous free cages. This behavior differs from that of the classical endohedral metallofullerenes, the EA of which increases after the metal unit is encapsulated. However, these TNT endohedrals still retain relatively large EAs, which suggests that their redox properties are similar to those of C_{60}. The ionization potentials (IPs) are calculated to be slightly smaller. This is because the HOMOs in the TNT endohedral metallofullerenes are less stable than in the empty cages. In conclusion, TNT endohedral metallofullerenes are better electron donors and worse electron acceptors than the corresponding free fullerenes.

Exohedral reactivity: [4 + 2] cycloaddition. $Sc_3N@C_{80}$ and $Sc_3N@C_{78}$ complexes have already been exohedrally functionalized via cycloaddition reactions. The TNT endohedral metallofullerenes of C_{80}, C_{78} and C_{68} have demonstrated that endohedral doping of the free fullerenes changes the exohedral reactivity of the fullerene surface in two ways: (1) it reduces and changes the reactivity of all C–C bonds, principally those around the carbon region that scandiums are facing; and (2) it improves the regioselectivity in the case of C_{80}, the character of which was very poor but

does not improve it in the cases of C_{68} and C_{78}. In general, TNT encapsulation is a new tool for the regioselectivity in the addition reactions to fullerenes. The combination of the analysis of the MBO and the pyramidalization angle of the C–C bonds is a general tool for predicting the most reactive site. The most pyramidalized C–C bonds with the highest MBO appear to be the most reactive in the [4 + 2] cycloaddition of 1,3-butadiene.

Exohedral reactivity: hydrogenation and fluorination of $Sc_3N@C_{80}$. We calculated the stabilities of the highly hydrogenated and fluorinated I_h-C_{80}:**7** fullerene cages, both of which are empty and contain the Sc_3N molecule. We also confirmed that the hydrogenation of the free fullerene is more favourable than the hydrogenation of the $Sc_3N@C_{80}$ metallofullerene. The addition of 44 hydrogen atoms to C_{80} and $Sc_3N@C_{80}$ is predicted to be the most favourable addition pattern because of the formation of six octahedrally-located aromatic benzenoid rings, whilst the addition of up to 52 atoms (consistent with preliminary fluorination data) gives a structure that is stabilized by four aromatic benzenoid rings. The hydrogenation binding energy per added hydrogen (HBE/*n*) remains constant for the addition of up to 52 atoms but at higher hydrogenation levels the HBE/*n* reduces drastically because of the unreactivity of the remaining C–C bonds, which increase in length and have a low π bond order. The most stable isomers at this addition level were determined, and the relative stabilities of a number of $C_{80}H_{52}$, $C_{80}F_{52}$, and $Sc_3N@C_{80}H_{52}$ species were calculated. From the geometrical point of view, the Sc_3N molecule is planar in the parent C_{80} but is calculated to be pyramidal in some of the hydrogenated/fluorinated derivatives, where it also has fixed locations due to orbital interactions caused by the deformation of the cage and the presence of localized double bonds.

REFERENCES AND NOTES

[1] Stevenson, S.; Rice, G.; Glass, T.; Harich, K.; Cromer, F.; Jordan, M.R.; Craft, J.; Hadju, E.; Bible, R.; Olmstead, M. M.; Maltra, K.; Fisher, A. J.; Balch, A. L.; Dorn, H. C. *Nature*, **1999**, 401, 55.

[2] Stevenson, S.; Fowler, P. W.; Heine, T.; Duchamps, J. C.; Rice, G.; Glass, T.; Harich, K.; Hajdu, E.; Bible, R.; Dorn, H. C. *Nature* **2000**, *408*, 428.

[3] Jacobs, H. O.; Tao, A. R.; Schwartz, A.; Gracias, D. H.; Whitesides, G. M. *Science* **2002**, *296*, 323.

[4] Olmstead, M. M.; Bettencourt-Dias, A.; Duchamp J. C.; Stevenson, S.; Marciu, D.; Dorn, H. C.; Balch, A. L. *Angew. Chem., Int. Ed. Engl.* **2001**, *40*, 1223.

[5] Stevenson, S.; Dorn, H. C.; Burbank, P.; Harich, K. *Anal. Chem.* **1994**, *66*, 2675.

[6] (a) Olmstead, M. M.; Costa, D. A.; Maitra, K.; Noll, B. C.; Philips, S. L.; Van Calcar, P. M.; Balch, A. L. *J. Am. Chem. Soc.* **1999**, *121*, 7090. (b) Boyld, P. D. W.; Hodgson, M. C.; Rickard, C. E. F.; Oliver, A. G.; Chaker, L.; Brothers, P. J.; Bolskar, R. D.; Tham, F. S.; Reed, C. A. *J. Am. Chem. Soc.* **1999**, *121*, 10487. (c) Dunsch, L.; Bartl, A.; Georgi, P.; Kuran, P. *Synth. Met.* **2001**, *121*, 1113.

[7] Krause, M.; Kuzmany, H.; Georgi, P.; Dunsch, L.; Vietze, K.; Seifert, G. *J. Chem. Phys.* **2001**, *115*, 6596.

[8] Dunsch, L.; Krause, M.; Noack, J.; Georgi, P. *J. Phys. Chem. Sol.* **2004**, *65*, 309.

[9] Duchamp, J. C.; Demortier, A.; Fletcher, K. R.; Dorn, D.; Iezzi, E. B.; Glass, T.; Dorn, H. C. *Chem. Phys. Lett.* **2003**, *375*, 655.

[10] Kroto, H. *Nature* **1987**, *329*, 529. (b) Scmalz, T. G.; Seitz, W. A.; Klein, D. J.; Hite, G. E. *J. Am. Chem. Soc.* **1988**, *110*, 1113.

[11] Olmstead, M. M.; Bettencourt-Dias, A.; Duchamp, J. C.; Stevenson, S.; Dorn, H. C.; Balch, A. L. *J. Am. Chem. Soc.* **2000**, *122*, 12220.

[12] Iezzi, E. B.; Ducamp, J. C.; Fletcher, K. R.; Glass, T. E.; Dorn, H. C. *Nano Lett*. **2002**, *2*, 1187.

[13] Iezzi, E. B.; Ducamp, J. C.; Harich, K.; Glass, T. E.; Lee, H. M.; Olmstead, M. M.; Balch, A. L.; Dorn, H. C. *J. Am. Chem. Soc.* **2002**, *124*, 524.

[14] Lee, H. M., Olmstead, M. M., Iezzi, E., Duchamp, J. C., Dorn, H. C.; Balch, A. L. *J. Am. Chem. Soc.* **2002**, *124*, 3494.

[15] Iezzi, E. B.; Cromer, F.; Stevenson P.; Dorn, H. C. *Synth. Metals* **2002**, *128*, 289.

[16] Darwish, A. D.; Dorn, H. C.; Taylor, R. unpublished work.

[17] Iezzi, E. B. Ph. D. Dissertation *Exohedral Functionalization and Applications of the Trimetallic Nitride Endohedral Metallofullerenes,* Virgina Tech, 2003.

[18] Gillan, E. G.; Yeretzian, C.; Min, K. S.; Alvarez, M. M.; Whetten, R. L.; Kaner, R. B. *J. Phys. Chem.* **1992**, *96*, 6869.

[19] Fowler, P. W.; Zerbetto, F. *Chem. Phys. Lett.* **1995**, *243*, 36.
[20] Fowler, P. W.; Manoloupoulus, D. E. *An Atlas of Fullerenes*, Oxford University Press, Oxford, **1995**.
[21] (a) Hennrich, F. H.; Michel, R. H.; Fischer, A.; Richard-Schneider, S.; Gilb, S.; Kappes, M. M.; Fuchs, D.; Bürk, M.; Kobayashi, K.; Nagase, S. *Angew. Chem. Int. Ed.* **1996**, *35*, 1732. (b) Wang, C. R.; Sugai, T.; Kai, T.; Tomiyama, T.; Shinohara, H. *Chem. Commun.* **2000**, 557.
[22] Kobayashi, K.; Nagase, S.; Akasaka, T. *Chem. Phys. Lett.* **1995**, *245*, 230.
[23] Cao, B.; Hasegawa, M.; Okada, K.; Tomiyama, T.; Okazaki, T.; Kazutomo, S.; Shinohara, H. *J. Am. Chem. Soc.* **2001**, *123*, 9674.
[24] Kobayashi, K.; Sano, Y.; Nagase, S.; *J. Comput. Chem.* **2001**, *22*, 1353.
[25] Akasaka, T.; Nagase, S.; Kobayashi, K.; Wälchli, M.; Yamamoto, K.; Funasaka, H.; Kako, M.; Hoshino, T.; Erata, T. *Angew. Chem., Int. Ed. Engl.* **1997**, *36*, 1643.
[26] (a) Zhang, B. L.; Wang, C. Z.; Ho, K. M. *Chem. Phys. Lett.* **1992**, *193*, 225. (b) Slanina, Z.; Francois, J. P.; Bakowies, D.; Thiel, W. *J. Mol. Struct. (THEOCHEM)* **1993**, *279*, 213. (c) Bühl, M.; van Wüllen, C. *Chem. Phys. Lett.* **1995**, 247, 63. (d) Osawa, E.; Ueno, H.; Yoshida, M.; Slanina, Z.; Zhao, X; Nishiyama M.; Saito, H. *J. Chem. Soc. Perkin Trans 2* **1998**, 943. (e) Sun, G.; Kertesz, M. *J. Phys. Chem. A* **2000**, *104*, 7398. (f) Heine, T.; Seifert, G.; Fowler, P. W.; Zerbetto, F. *J. Phys. Chem.* **1999**, *103*, 8738.
[27] (a) Diederich, F.; Whetten, R. L.; Thielgen, C.; Ettl, R.; Chao, I.; Alvarez, M. M. *Science* **1991**, *254*, 1768. (b) Kikuchi, K; Nakahara, N.; Wakabayashi, T.; Suzuki, S.; Shiromaru, H.; Miyake, Y.; Saito, K.; Ikemoto, I.; Kainosho, M.; Achiba, Y. *Nature*, **1992**, *357*, 142. (c) Taylor, R.; Langley, J. G.; Dennis, T.J.S.; Kroto, H. W.; Walton, D. R. M. *J. Chem. Soc. Chem. Commun.* **1992**, 1043.
[28] Akasaka, T.; Nagase, S. *Endofullerenes: a new family of carbon clusters, Developments in fullerene science*, Kluwer Academic Publishers, Dordrecht, 2002, chapter 4 and 5.
[29] David, W. I. F.; Ibberson, R. M.; Mattewman, J. C.; Prassides, K.; Dennis, T. J. S.; Hare, P. J.; Kroto, H. W.; Taylor, R.; Walton, D. R. M. *Nature* **1991**, *252*, 1160.
[30] Hedberg, K.; Hedberg, L.; Bethune, D.S.; Brown, C.A.; Dorn, H.C.; Johnson, R. D.; de Vries, M. *Science* **1991**, *254*, 410.
[31] Balch, A.; Olmstead, M. M. *Chem. Rev.* **1998**, *98*, 2123.
[32] Campanera, J. M.; Bo, C.; Olmstead, M. M.; Balch, A. L.; Poblet, J. M. *J. Phys. Chem. A* **2002**, *106*, 12356.

[33] Nishibori, E.; Takata, M.; Sakata, M.; Inakuma, M.; Shinohara, H. *Chem. Phys. Lett.* **1998**, *298*, 79.
[34] Takata, M.; Nishibori, E.; Umeda, B.; Sakata, M.; Yamamoto, E.; Shinohara, H. *Phys. Rev. Lett.* **1997**, *78*, 3330.
[35] Kobayashi, K.; Nagase, S. *Chem. Phys. Lett.* **1998**, *282*, 325.
[36] Olmstead, M. M.; Lee, H. M.; Duchamp, J. C.; Stevenson, S.; Marciu, D.; Dorn, H. C.; Balch, A. L. *Angew. Chem. Int. Ed.* **2003**, *42*, 900.
[37] Kobayashi, K.; Nagase, S.; Yoshida, M.; Osawa, E. *J. Am. Chem. Soc.* **1997**, *119*, 12693.
[38] Nagase, S.; Kobayashi, K.; Akasaka, T. *J. Mol. Struct. (Theochem)* **1999**, *97*, 161.
[39] Dorn, H. C.; Stevenson, S.; Burbank, P.; Harich, K.; Sun, T.; Glass, T.; Anderson, A.; Bethume, D. S.; Sherwood, M. *Recent Advances in the Chemistry and Physics of Fullerenes and Related Materials* Kadish, K. M. and Ruoff, R. S., Eds., Pennington, The Electrodhemical Society, Inc., 1998, p. 990.
[40] Wang, C.; Kai, T.; Tomiyama, T.; Yoshida, T.; Kobayashi, Y.; Nishibori, E.; Takata, M.; Sakata, M.; Shinohara, H. *Nature* **2000**, *408*, 426.
[41] Aihara, A. *Chem. Phys. Lett.* **2001**, *343*, 465.
[42] (a) Fowler, P. W.; Heine, T.; Manolopoulos, D. E.; Mitchell, D.; Orlandi, G.; Schmidt, R.; Seifert, G.; Zerbetto, F. *J. Phys. Chem.* **1996**, *100*, 6984. (b) Fowler, P. W.; Manolopoulos, D. E.; Orlandi, G.; Zerbetto, F. *J. Chem. Soc., Faraday Trans.* **1995**, *91*, 1421. (c) Fowler, P. W.; Heine, T.; Manolopoulos, D. E.; Mitchell, D.; Orlandi, G.; Schmidt, R.; Seifert, G.; Zerbetto, F. *J. Chem. Soc., Faraday Trans.* **1996**, *92*, 2203.
[43] Lee, S. L.; Sun, M. L.; Slanina, Z. *Int. J. Quantum Chem.* **1996**, *60*, 355.
[44] Coppens, P.; Hall, M. B *Electron Distributions and the Chemical Bond* Eds. Plenum Press, New York, **1981**.
[45] (a) Roszak, S.; Balasubramanian, K. *J. Phys. Chem. A* **1997**, *101*, 2666. (b) Benard, M.; Rohmer, M. M.; Poblet, J. M. *Chem. Rev.* **2000**, *100*, 495. (c) Li, X.; Wang, L. S. *J. Chem. Phys.* **1999**, *111*, 8389.
[46] (a) Ziegler, T.; Rauk, A. *Teor. Chim. Acta* **1977**, *46*, 1. (b) Ziegler, T.; Rauk, A. *Inorg. Chem.* **1979**, *18*, 1558.
[47] (a) Morokuma, K. *J. Chem. Phys.* **1971**, *55*, 1236. (b) Kitaura, K.; Morokuma, K. *Int. J. Quantum. Chem.* **1976**, *10*, 325.
[48] Nunzi, F; Sgamelloti, A.; Re, N.; Floriani, C. Organometallics **2000**, *19*, 1628.
[49] Gonzalez-Blanco, O.; Branchadell, V. Organometallics, **1997**, *16*, 5556.
[50] In structures **6-12** the four atoms of the Sc_3N fragment are not strictly coplanar but the deviation from the planarity is very small.

[51] Yang, S. H.; Pettiette, C. L.; Conceicao, J.; Cheshnowsky, O.; Smalley, R. E. *Chem. Phys. Lett.* **1987**, *139*, 233.
[52] Brink, C.; Andersen, L. H.; Hvelplund, P.; Mathur, D.; Voldstad, J. D. *Chem. Phys. Lett.* **1995**, *233*, 52.
[53] Ioffe, I. N.; Boltalina, O. V.; Sidorov, L. N.; Dorn, H. C.; Stevenson, S.; Rice, G. *Fullerenes: Recent Advances in the Chemistry and Physics of Fullerenes and Related Materials*; Kadish, K. M.; Ruoff, R. S., Eds., Electrochmical Society, Pennington, **2000**; p. 166.
[54] Dorn, H. C.; Stevenson, S.; Craft, J.; Cromer, F.; Duchamp, J.; Rice, G.; Glass, T.; Harich, K.; Fowler, P. W.; Heine, T.; hajdu, E.; Bible, R.; Olmstead, M.M.; Maitra, K.; Fisher, A. J.; Balch, A. L. Proc IWEPNM2000 Conf 2000, 135.
[55] Shinohara, H. *Rep. Prog, Phys.* **2000**, *63*, 843.
[56] (a) Aihara, J. *J. Am. Chem. Soc.* **1995**, *117*, 4130. (b) Aihara, J. *J. Phys. Chem.* **1995**, 99, 12739. (c) Aihara, J.; Oe, S.; Yoshida, M.; Osawa, E. *J. Comput. Chem.* **1996**, *17*, 1387. (d) Aihara, J. *Bull. Chem. Soc. Jpn.* **1999**, *72*, 7 (e) Aihara, J. *Phys. Chem.* **2001**, *3*, 1427. (f) Aihara, J. *Chem. Phys. Lett.* **2001**, *343*, 465.
[57] Manolopoulos, D. E.; May, J. C.; Down, S. E. *Chem. Phys. Lett.* **1991**, *181*, 105.
[58] Minkin, V. I. *Pure Appl. Chem.* **1999**, *71*, 1919
[59] (a) Aihara, J. *J. Am. Chem. Soc.* **1976**, *98*, 2750. (b) Gutman, I.; Milun, M.; Trinajstic, N. *J. Am. Chem. Soc.* **1977**, *99*, 1692.
[60] Aihara, J. *J. Phys. Chem. A* **2002**, *106*, 11371.
[61] http://www.cochem2.tutkie.tut.ac.jp/Fuller/Fuller.html
[62] (a) Solà, M.; Duran, M.; Mestres, J. *J. Am. Chem. Soc.* **1996**, *118*, 8920. (b) Mestres, J.; Duran, M.; Solà, M. *J. Phys. Chem.* **1996**, *100*, 7449.
[63] Akasaka, T.; Nagase, S.; Kobayashi, K.; Suzuki, T.; Kato, T.; Kikuchi, K.; Achiba, Y.; Yamamoto, K.; Funasaka, H.; Takahashi, T. *Angew. Chem., Int. Ed. Engl.* **1995**, *34*, 19.
[64] Takeshi, A.; Kato, T.; Kobayashi, K.; Nagase, S.; Yamamoto, K.; Funasaka, H.; Takahashi, T. *Nature* **1995**, *374*, 600.
[65] Maeda, Y.; Matsunaga, Y.; Wakahara, T.; Takahashi, S.; Tsuchiya, T.; Ishitsuka, O.; Hasegawa, T.; Akasaka, T.; Liu, M. T. H.; Kokura, K.; Horn, E.; Yoza, K.; Kato, T.; Okubo, S.; Kobayashi, K.; Nagase, S.; Yamamoto, K. *J. Am. Chem. Soc.* **2004**, *126*, 6858.
[66] Kobayashi, K.; Nagase, S.; Maeda, Y.; Wakahara, T.; Akasaka, T. *Chem. Phys. Lett.* **2003**, *374*, 562.
[67] (a) Belik, P.; Gügel, A.; Kraus, A.; Spickermann, J.; Enkelmann, V.; Frank, G.; Müllen, K. *Adv. Mater.* **1993**, *5*, 854. (b) Belik, P.; Gügel, A.; Kraus, A.;

Spickermann, J.; Enkelmann, V.; Frank, G.; Müllen, K. *Angew. Chem., Int. Ed. Engl.* **1993**, *32*, 78.

[68] (a) Haddon, R. C. ; Scott, L. T. *Pure Appl. Chem.* **1986**, *58*, 137. (b) Haddon, R. C. *J. Am. Chem. Soc.* **1986**, *108*, 2837. (c) Haddon, R. C. ; Chow, S. Y. *J. Am. Chem. Soc.* **1998**, *120*, 10494.

[69] Haddon, R. C. *Acc. Chem. Res.* **1988**, *21*, 243.

[70] (a) Rabideau, P. W.; Sygula, A. *Acc. Chem. Res.* **1996**, *29*, 235. (b) Abdourazak, A. H.; Marcinow, Z.; Sygula, A.; Sygula, R.; Rabideau, P. W. *J. Am. Chem. Soc.* **1995**, *117*, 6410.

[71] (a) Mayer, I. *Chem. Phys. Lett.* **1983**, *97*, 270. (b) Mayer, I. *J. Quantum Chem.* **1984**, *26*, 151.

[72] Wiberg, K. A. *Tetrahedron* **1968**, *24*, 1083.

[73] Bridgeman, A. J.; Cavigliasso, G. *Faraday Discussions* **2003**, *124*, 239.

[74] Darwish, A. D.; Avent, A. G.; Boltalina, O. V.; Stevenson S.; Taylor, R. unpublished work.

[75] Fowler, P. W.; Sandall, J. P. B.; Taylor, R. *J. Chem. Soc., Perkin Trans. 2* **1997**, 419.

[76] Jones, R.; Briddon, P. R. *Semicond. Semimet.* **1998**, *51A*, 287.

[77] Some of the structures reported here could eventually be saddle points corresponding to hydrogen transfer between two minima. The characterization would require the calculation of the vibrational frequencies but this still requires a huge computational effort.

[78] (a) Darwish, A. D.; Avent, A. G.; Taylor, R.; Walton, D. *J. Chem. Soc., Perkin Trans. 2*, **1996**, 2051. (b) Boltalina, O. V.; Markov, V. Yu.; Taylor, R.; Waugh, M. P. *Chem. Commun*. **1996**, 2549. (c) Boltalina, O. V.; Street, J. M.; Taylor, R. *J. Chem. Soc., Perkin Trans. 2* **1998**, 649. (d) Nossal, J.; Saini, R. K.; Sadana, A. K.; Bettinger, H. F.; Alemany, L. B.; Scuseria, G. E.; Billups, W. E.; Saunders, M.; Khong, A.; Weisemann, R. *J. Am. Chem. Soc.* **2001**, *123*, 8482.

[79] (a) Hitchcock, P. B.; Taylor, R**.** *Chem. Commun*. **2002**, 2078. (b) Avent, A. G.; Clare, B. W.; Hitchcock, P. B.; Kepert, D. L.; Taylor, R. *Chem. Commun*. **2002**, 2370.

[80] Cioslowski, J. *Chem. Phys. Lett*. **1991**, *181*, 68.

[81] For collation of data and leading references see (a) Taylor, R.; Langley, G. J.; Holloway, J. H.; Hope, E. G.; Brisdon, A. K.; Kroto, H. K.; Walton, D. R. M. *J. Chem. Soc., Perkin Trans. 2* **1995**, 181. (b) Darwish, A. D.; Abdul-Sada, A. K.; Langley, G. J.; Kroto, H. W.; Taylor, R.; Walton, D. R. M. *J. Chem. Soc., Perkin Trans. 2* **1995**, 2359.

[82] (a) Taylor, R. *Philos. Trans. R. Soc. London, A* **1993**, *343*, 87. (b) Austin, S. J.; Batten, R. C.; Fowler, P. W.; Redmond, D. B.; Taylor, R. *J. Chem. Soc., Perkin Trans. 2* **1993**, 1383.

[83] Troyanov, S. I.; Troshin, P. A.; Boltalina, O. V.; Ioffe, I. N.; Sidorov, L. N.; Kemnitz, E. *Angew. Chem., Int. Ed. Engl.* **2001**, *40*, 2285.

[84] Neretin, I. S.; Lyssenko, K. A.; Antipin, M. Yu.; Slovokhotov, Yu. L.; Boltalina, O. V.; Troshin, P. A.; Lukonin, A. Yu.; Sidorov, L. N.; Taylor, R. *Angew. Chem., Int. Ed. Engl.* **2000**, *39*, 3273.

CHAPTER 5

HETEROHEDRAL METALLOFULLERENES

Heterohedral metallofullerenes, fullerenes with metals in the carbon network, are less common and have been studied less than the other members of the metallofullerene family: the endohedral (Chapter 4) and the exohedral (Chapter 6). The term heterofullerenes will be used as an abbreviation of heterohedral metallofullerenes. Also, the mono- and di- prefixes before heterofullerenes will indicate the number of metals incorporated into the fullerene carbon framework.

Although nitrogen and boron atoms are common as doped atoms in C_{60} and C_{70} fullerenes and give a formidable range of stoichiometries, the chemical art of incorporating metals by replacing one or two carbons is still in its infancy. Branz's and Balch's groups were the first experimentalists to detect this kind of metallofullerenes. Heterohedral metallofullerenes are detected by mass spectra studies, but the synthesis of bulky quantities and the use of spectrometric techniques have yet to be reported. The new heterohedral metallofullerenes have the following four stoichiometries: (1) monoheterofullerenes in which one carbon is replaced by one metal: $C_{59-2x}M$ and $C_{69-2x}M$ (x = 0, 1, 2; M = Si, Fe, Co, Ni, Rh, Pt, Ir, Sm, Ni, La, Y, Rh) — x = 1 and 2 are obtained from x = 0 stoichiometry by successive losses of C_2 units — (2) monoheterofullerenes in which a C_2 unit is replaced by single metal: $C_{58}M$ (M = Pt, Ir); (3) diheterofullerenes in which one C atom and a C_2 unit are replaced by two metals: $C_{57}Pt_2$ and finally (4) diheterofullerenes in which two C_2 units are replaced, $C_{56}Pt_2$.

The present chapter starts by presenting the limited experimental studies and some theoretical advances made in the comprehension of the electronic structure of these new metallofullerenes (section 5.1). The encapsulation of Sc_3N inside the C_{68}, C_{78} and C_{80} provided us with a good clear example of an ionic bond between two units. However, in heterohedral fullerenes the metal bond in the fullerene carbon framework does not seem as easy to rationalize as in the TNT endohedral metallofullerenes. The metal is incorporated in the carbon network of the fullerene as another atom and does not disrupt the rest. To date no studies have dealt with how the metals are bonded to the other carbons. Bora- and azafullerenes can not be taken as suitable models because they have only slight electronic variations from the original carbon. The metal bond will be exemplified by the simplest monoheterofullerene: $C_{58}Pt$ (section 5.2). In order to understand how the metal is incorporated into the fullerene carbon framework two tools are mainly used: (1) the decomposition of the substitution energy, and (2) the fragment molecular orbital method applied to the analogous $C_{24}H_{12}Pt$ compound. Then the isomerism, and the geometric and electronic structures of the monoheterofullerenes: $C_{58}M$ and $C_{59}M$ (M = Pt, Ir, Os, Ti) are systematically studied in section 5.3. The experimental evidence for the ability of $C_{59}M$ and $C_{58}M$ (M = Pt, Ir) to bind to olefins is studied in the next section 5.4. In section 5.5, we present the huge theoretical study on the $C_{56}Pt_2$ and $C_{57}Pt_2$ diheterofullerenes. The substitution of two C_2 units or one C_2 unit and one C atom in C_{60} yields a very high number of regioisomers, which makes the theoretical analysis of the dimetallic species much more complicated. We report a detailed DFT study on the factors that govern the relative stability of the regioisomers of $C_{56}Pt_2$ and $C_{57}Pt_2$. Because of the numerous factors affecting the stability, we were forced to use chemometric techniques. Finally in section 5.6, these heterofullerenes are characterized by the calculation of the ionization potentials and the electron affinities.

5.1 INTRODUCTION

5.1.1 Experimental part

The macroscopic synthetic methods that have been developed for azafullerenes and borafullerenes of C_{60} and C_{70} since 1995 have led to a whole new rich area in the science of fullerenes: cage modification chemistry. Heterohedral non-metallofullerenes have been synthesized using a modified Krätschmer-Huffman process.[1] Moreover, the fact that these compounds are numerous has also led to a wide variety of studies on the characterization and determination of their physicochemical properties. Heterohedral metallofullerenes, on the other side, have appeared very recently in fullerene chemistry. Without a doubt, this area is in its infancy because only mass spectrometric studies have been made up to now, not characterization or spectrometric studies. However, these new heterohedral fullerenes are expected to increase rapidly when ways of producing them in significant quantities are discovered.

Mass spectrometric studies have identified a number of fullerene-like clusters with heteroatoms incorporated into the fullerene carbon framework. First, Jarrold and coworkers demonstrated that NbC_x^+ clusters could be generated by pulsed laser vaporization of graphite/NbC composites and that the mobilities of the NbC_x^+ clusters indicated that those with odd values of x contained Nb atoms that resided on the surface.[2] Related clusters could also be formed by substitution-like processes that use preformed fullerene cages. For example, Branz and co-workers prepared the gas phase clusters $C_{60}M_x$ and $C_{70}M_x$ by evaporating of the metal (M) into the fullerene vapor.[3,4] Subsequent photo fragmentation of $C_{60}M_x$ and $C_{70}M_x$ produces new clusters with the compositions $C_{59-2x}M$ and $C_{69-x}M$ with M = Si, Fe, Co, Ni, Rh, Ir and x = 0, 1, 2. As demonstrated in Balch's laboratories, an alternative route to the formation of the clusters $C_{59-2x}M^+$ and $C_{69-x}M^+$ involves laser ablation of electrochemically deposited films (C_{60}/Pt or C_{60}/$Ir(CO)_2$) that contain polymeric, covalently bound chains: ...$C_{60}ML_xC_{60}ML_xC_{60}ML_x$..., where ML_x = $Ir(CO)_2$ or Pt.[5,6,7] This process extended to form related clusters involving Sm, Ni, La, Y, and Rh.[8] In the negative ion mode, the C_{60}/Pt film produces, among other species, the ion $C_{58}Pt^-$ —the result of the substitution of two C atoms for a Pt atom — and

the ions $C_{57}Pt_2^-$ and $C_{56}Pt_2^-$, which incorporate two Pt atoms into the cage. The $C_{60}/Ir(CO)_2$ film produces a different series of products: $C_{59}Ir^-$, $C_{58}Ir^-$, $C_{57}Ir^-$ and $C_{56}Ir^-$, in which an iridium atom can also replace one or two carbons within the fullerene cage. On the other hand, evidence for the ability of the metals in some of these fullerenes to bind additional ligands was obtained by conducting the laser ablation studies in the presence of 2-butene where adducts such as $[C_{59}Ir(2\text{-butene})]^-$, $[C_{58}Ir(2\text{-butene})]^-$, $[C_{57}Ir(2\text{-butene})]^-$ and $[C_{56}Ir(2\text{-butene})]^-$ were observed.[9] The results of laser ablation studies of the electrochemically deposited $C_{60}\{Ir(CO)_2\}_n$ film in positive ion mode revealed the presence of $C_{59}Ir^+$ and $C_{57}Ir^+$. The spectral features of the formation of $C_{69}Ir^+$ were obtained by desorption from a film prepared by electrochemical reduction of a solution of C_{70} and $Ir(CO)_2Cl(NH_2C_6H_4Me\text{-}p)$. Finally, $C_{59}Pt^+$ was obtained by desorption from a film of $C_{60}Pt_n$ prepared by electrochemical reduction of a solution of C_{60} and $PtCl_2(pyridine)_2$.

5.1.2 Theoretical part

As far as theory is concerned, semiempirical methods have been used to study regioisomerism for nitrogen and boron doped fullerenes[10,11,12] and other atoms such as oxygen, sulfur[13] and aluminum.[14] The development of the heterofullerene isomerism can be seen in a recent paper by Jiao et al., which contains the latest literature on semiempirical methods.[15] Density functional theory (DFT) based calculations have been performed to study the structure and the electronic properties of the $C_{59}M$ (M = Si,[16] Pt, Ir, Fe, Co, Ni, Rh[17]) and $C_{69}M$ (M = Co, Rh, Ir)[18] monoheterofullerenes. Although Si is not a transition-metal atom, it is interesting how this atom replaces carbons because it is a larger dopant than nitrogen and boron. Its effect, then, can be easily compared to that of a transition-metal atom. The replacement of two single carbons by two Si atoms in C_{60} led to $C_{58}Si_2$. The structure of this fullerene turns out to be modified only in the vicinity of the dopant atoms, and the Si–C distances are as much as 30% longer that the C–C distances. The $C_{58}Si_2$ compound is more stable when the Si atoms are rather close, 3.47 Å. DFT studies of $C_{59}Pt$ and $C_{59}Ir$ showed that the metals are found in three coordinated sites on the fullerene surface. Because the Ir–C or Pt–C bond lengths are longer than the C–C bond lengths, the Ir or Pt

atoms protrude from the fullerene surface. The theoretical work has also indicated that the addition of a ligand to the exposed metal would be energetically favorable. Studies of $C_{59}Fe$ revealed a similar structure.[19] The electronic structure of $C_{59}M$ varies with the M and can be described in terms of defect levels in the free fullerene host, C_{60}. Computational studies of $C_{69}M$ structures, where M = Co, Rh, and Ir, demonstrated that substitution at the more highly pyramidalized poles of the fullerene was energetically favored. Recently DFT calculations have been performed to determine the structure of the heterohedral metallofullerenes: $C_{53}Rh$ and $C_{54}M$ (M = Rh, Y). They belong to the group of $C_{2x+1}M$ and $C_{2x}M$ (M = Rh, Y) heterohedral and endohedral metallofullerenes obtained from a laser ablation of $C_{60}M_n$ (M = Rh, Y) metal fullerides.[20]

5.2 COVALENT METAL BOND IN THE FULLERENE CARBON FRAMEWORK

5.2.1 Geometric and electronic structure of $C_{58}Pt$

Substitution of a C_2 unit for a metal in C_{60} results in the formation of two different isomers, because the C_2 unit can be removed from a 6:6 or a 6:5 ring junction. Hereafter, the resulting structures will be referred to as C_{2v}-$C_{58}Pt$ and C_s-$C_{58}Pt$, respectively, according to their symmetry. Figure 5.1 shows drawings of the optimal structures of $C_{58}M$ isomers. They are compared to the $C_{59}M$ structure, in which only one carbon is replaced by a metal. Table 5.1 collates the geometric properties and Mulliken net charges for the monoheterofullerenes $C_{58}Pt$ and $C_{59}Pt$. C_{2v}-$C_{58}Pt$ possesses four equivalent Pt–C distances equal to 2.034 Å but C_s-$C_{58}Pt$ possesses two lower distances of 2.013 Å between Pt and the hexagonal C atoms and two higher distances of 2.049 Å between Pt and the pentagonal C atoms. As can be seen in Figure 5.1, the four-coordinated metals in both isomers of $C_{58}Pt$ do not protrude from the fullerene surface but stay within the fullerene carbon framework. In contrast, the three-coordinated metal in $C_{59}M$ bulges out from the fullerene surface.

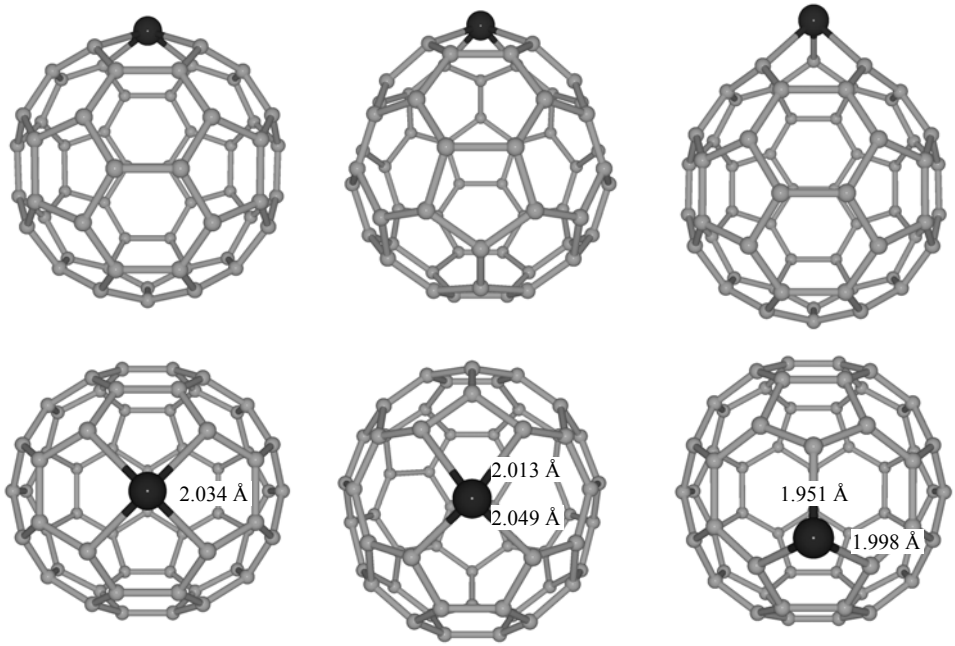

Figure 5.1 Two perspective visions of the C_{2v}-C_{58}Pt (a) (substitution at 6:6 C–C bond) and C_s-C_{58}Pt (b) (substitution at 6:5 C–C bond) isomers. For comparison the figure also includes the structure of C_{59}M (c). All Pt–C distances are shown for each heterofullerene.

C_{2v}-C_{58}Pt is the most stable isomer, 0.63 eV lower in energy than the C_s-C_{58}Pt isomer. Mulliken population analysis of the most stable isomer indicates that the electron charge transfer takes place from the metal to the carbon cage in C_{58}Pt. The net charge on the metal center is +0.82 *e*, and the negative charge on the carbons bonded to Pt is –0.37 *e*. The other carbons have smaller charges. The electronic populations of the *s*, *p* and *d* Pt orbitals are 2.590, 6.385 and 8.201 *e*, respectively. These values are quite similar to the electronic populations of the corresponding orbitals in C_{59}Pt: 2.547, 6.313 and 8.385 *e*. The Voronoi partition scheme of the electron density suggests that the electron charge transfer is higher, since it gives a net charge of +1.46 *e* for the metal center and of –0.39 *e* for the carbons connected to Pt.

Table 5.1 Geometric and electronic properties for $C_{59}Pt$, C_{2v}-$C_{58}Pt$, C_s-$C_{58}Pt$ and $C_{24}H_{12}Pt$. The $C_{24}H_{12}Pt$ doped molecule will be used as a metal-carbon bond model for heterofullerenes [a]

Molecule	*Symmetry*	*Cage radius* [b]	*Pt–C Bond lengths* [c]	*Mulliken Net Charge*	
				M	C [c]
$C_{59}Pt$	C_s	3.580	1.998/1.951	0.755	–0.344
$C_{58}Pt$	C_{2v}	3.562	2.034	0.824	–0.367
$C_{58}Pt$	C_s	3.569	2.049/2.013	0.843	–0.361
$C_{24}H_{12}Pt$	D_{4h}	--	1.929	1.312	–0.228

[a] Distances in Å. [b] Cage radius is defined as the average distance of all surface atoms to the center of the fullerene. Cage radius for C_{60} is 3.551 Å. [c] Average values for the carbons bonded to the metal.

5.2.2 Substitution energy (SE) and their decomposition

The relative stability of the various monoheterofullerenes is evaluated through the substitution energy (SE). This energy corresponds to the energy process of the substitution of carbon units by metals. The processes are $C_{60} + M \rightarrow C_{59}M + C$ for $C_{59}M$ and $C_{60} + M \rightarrow C_{58}M + C_2$ for $C_{58}M$. Substitution of a 6:6 C_2 unit in C_{60} by a Pt atom requires a considerable amount of energy, 7.35 eV, and even slightly more when the Pt heteroatom replaces a 6:5 C_2 unit, 7.98 eV. Hence, the C_{2v} isomer is more stable than the C_s isomer by 0.63 eV. SE can be decomposed into several energies, each one of which provides clues about how metal is incorporated into the fullerene carbon framework. This decomposition also makes it possible to rationalize the different isomer stabilities of $C_{58}Pt$ and the insertion of different metals into the $C_{58}M$ structure. First we divide SE into two main parts:

(5.1) $$SE = \Delta E_{HOLE} + IBE$$

Table 5.2 Decomposition of the substitution energy (SE) for C_{2v}-$C_{58}Pt$ and C_s-$C_{58}Pt$ and D_{4h}-$C_{24}H_{12}Pt$ [a]

Carbon structure			C_{60}	C_{60}	$C_{26}H_{12}$
Doped structure			$C_{58}Pt$	$C_{58}Pt$	$C_{24}H_{12}Pt$
Symmetry			C_{2v}	C_s	D_{4h}
ΔE_{HOLE} [b]			17.90	19.31	16.92
IBE [c]	ΔE_{DE} [d]	$C_{58}/C_{24}H_{12}$	1.80	1.63	2.94
		C_2	–0.57	–0.98	–0.12
		M	0.49	0.49	0.49
		Total	1.72	1.14	3.31
	ΔE_{INT} [e]	ΔE_{ST}	18.11	16.15	28.49
		ΔE_{ORB}	–30.38	–28.62	–37.00
		Total	–12.27	–12.47	–8.51
	Total		–10.55	–11.33	–5.20
SE			7.35	7.98	11.72

[a] Energies in eV. The Substitution Energy (SE) is defined as the energy reaction of the process C_{60} + M → $C_{58}M$ + C_2 for $C_{58}M$ -and $C_{26}H_{12}$ + M→ $C_{24}H_{12}M$ + C_2 for $C_{24}H_{12}M$. This energy can be diveded into several contributions SE = ΔE_{HOLE} + IBE. [b] ΔE_{HOLE}, hole energy, accounts for the energy reaction of the process $C_{60} \rightarrow C_{58}^* + C_2^*$ and $C_{26}H_{12} \rightarrow C_{24}H_{12}^* + C_2^*$. C_{58}^* is calculated at the most stable electronic state (singlet) with the fixed geometry of free C_{60}. For the model, $C_{24}H_{12}^*$ is calculated as a triplet with the fixed geometry of $C_{26}H_{12}$. C_2* keeps the electronic configuration as its free C_2 analogue but the C–C distance from their precursor (C_{60} or $C_{26}H_{12}$). [c] IBE (insertion binding energy) account for the energy reaction of the process $C_{58}^* + C_2^* + M \rightarrow C_{58}M + C_2$ and $C_{24}H_{12}^* + C_2^* + M \rightarrow C_{24}H_{12}M + C_2$. IBE = ΔE_{DE} + ΔE_{INT}. [d] ΔE_{DE} accounts for the deformation energy for the fragments: $C_{58}^* \rightarrow C_{58}$, $C_{24}H_{12}^* \rightarrow C_{24}H_{12}$, $C_2^* \rightarrow C_2$ and M → M*. Where C_{58} with the fixed geometry found in $C_{58}Pt$, also $C_{24}H_{12}$ with the fixed geometry found in $C_{24}H_{12}Pt$ and C_2 optimised. The most stable electronic state for that holed carbon systems are triplet for both C_{58} and $C_{24}H_{12}$. M is calculated at the most stable electronic state (unrestricted). [e] Finally ΔE_{INT} accounts for the interaction energy between the fragments C_{58} and M* at the fixed $C_{58}M$ geometry or $C_{24}H_{12}$ and M* at the $C_{24}H_{12}M$ geometry. M* is calculated as a restricted electronic state while C_{58} and $C_{24}H_{12}$ are triplet according to previous comments.

The hole energy, ΔE_{HOLE}, is the energy necessary to make a hole in the free C_{60} fullerene. The binding energy (BE) between the hole and the metal for constructing the final structure of $C_{58}Pt$ is included in the insertion bonding energy (IBE). More details about the intricacies of these energies are given in the footnote of Table 5.2. The bond between the holed C_{58} fullerene and the M atom unit is also analyzed using the extended transition method

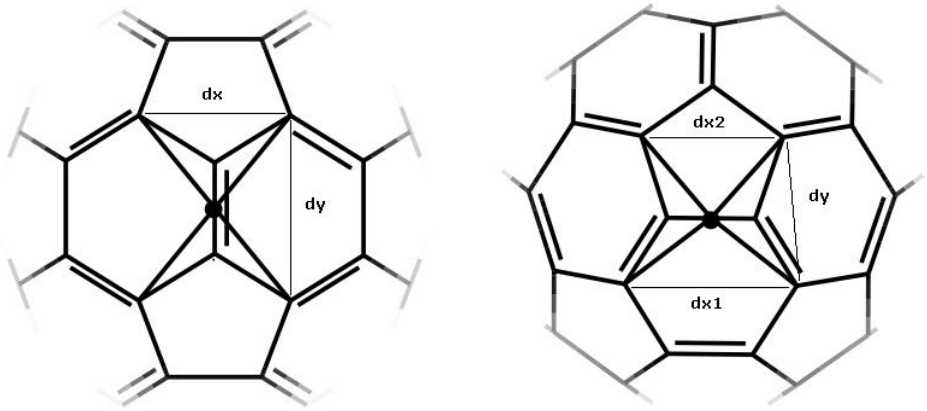

(a) substituted 6:6 C–C in C_{2v}-C_{58}M (b) Substituted 6:5 C–C in C_s-C_{58}M

Figure 5.2 Differences between the substitution of a pyracylene 6:6 C–C bond (a) and a corannulene 6:5 C–C bond (b) for a Pt atom in C_{60}. The formation of C_{2v}-C_{58}M requires the lost of 4 σ C–C bonds whereas the formation of C_s-C_{58}M a bit more: the lost of 4 σ and 2 π C–C bonds. Examples for d_x and d_y distances: d_x = 2.349 Å and d_y = 2.848 Å (in C_{2v}-C_{58} with C_{60} geometry), d_x = 2.657 Å and d_y = 2.665 Å (in C_{2v}-C_{58} with C_{2v}-C_{58}Pt geometry), d_{x2}/d_{x1} = 2.350/2.850 Å and d_y = 2.468 Å (C_s-C_{58} with C_{60} geometry) and d_{x2}/d_{x1} = 2.246/2.668 Å and d_y = 2.938 Å (in C_s-C_{58} with C_s-C_{58}Pt geometry).

developed by Ziegler and Rouk,[21] which is an extension of the well-known decomposition scheme of Morokuma.[22] According to this method, the IBE between two fragments can be decomposed into several contributions:

(5.2) $$IBE = \Delta E_{DE} + \Delta E_{ST} + \Delta E_{ORB}$$

More details about this decomposition can be found in subsection 4.2.4. The sum, $\Delta E_{ST} + \Delta E_{ORB}$, is known as the fragment interaction energy and represented by ΔE_{INT}. The values of this decomposition for both isomers of C_{58}Pt heterofullerene are shown in Table 5.2.

5.2.3 Hole energy, ΔE_{HOLE}

The process of making a hole is highly endothermic. The reaction $C_{60} \rightarrow C_{58} + C_2$ requires 17.90 eV when a 6:6 C_2 unit is removed and a little more is required, 19.31 eV, in the case of a 6:5 C_2 unit. In other words, the holed C_{58} fullerene is 1.41 eV more stable when the hole originates in a pyracylene C–C bond type than in a corannulene type. In the first step, C_{58} and C_2 keep the geometry which they had in the free C_{60} fullerene. The electronic state of a fullerene with a hole is not easy to determine because of the presence of dangling bonds. However, we found that the most stable electronic state of a holed C_{58} fullerene is a singlet independently of the type of hole. The triplet state is found to be 0.74 and 0.34 eV higher in energy for C_{2v}-C_{58} and C_s-C_{58}, respectively. The number of broken C–C bonds gives us some idea of the nature of the difference in the ΔE_{HOLE} between both holed C_{58} isomers. Unlike the most stable C_{2v}-C_{58} in which only four σ C–C bonds were broken, in the least stable C_s-C_{58} two additional π C–C bonds were also removed (see Figure 5.2 for clarification). ΔE_{HOLE} is the significant energy for determining the final value of SE, and hence for determining the most stable $C_{58}M$ isomer. In contrast, IBE is computed to be slightly more favorable in C_s-C_{58} by only 0.78 eV than in C_{2v}-C_{58}.

5.2.4 Insertion binding energy (IBE)

IBE is an exothermic process which helps monoheterofullerene formation. The first term of IBE, ΔE_{DE}, accounts for the energy necessary to convert C_2 and C_{58} fragments from their geometry and electronic state in the free C_{60} to their final forms: optimized C_2 and C_{58} with a $C_{58}M$ geometry, respectively. The electronic state of holed fullerenes is very sensitive to geometric changes. This is why the holed C_{58} fullerene with $C_{58}Pt$ geometry (either the C_{2v} or C_s isomer) has a triplet as the most stable electronic state, instead of the singlet shown in C_{58} with C_{60} geometry. The triplet is 0.35 eV and 0.26 eV stabilized above the singlet electronic state for holed C_{58} fullerenes with C_{2v}-$C_{58}Pt$ and C_s-$C_{58}Pt$ geometries, respectively. The dependence of the electronic state on the geometry deserves further discussion and will be dealt with in the next section.

In general, the deformation of the C_{58} core, $\Delta E_{DE}(C_{58})$, is very small and is restricted to the carbons directly linked to the metal. It is slightly higher for the C_{2v} isomer than for the C_s isomer, 1.80 and 1.63 eV, respectively. These differences in $\Delta E_{DE}(C_{58})$ between the C_s and C_{2v} isomers of $C_{58}Pt$ will also follow the same trend and magnitude for other analogue monoheterofullerenes: $C_{58}M$ (M = Ir, Os). The total ΔE_{DE} was computed to be 1.72 eV and 1.14 eV for C_{2v}-$C_{58}Pt$ and C_s-$C_{58}Pt$, respectively.

However, IBE is dominated by the ΔE_{INT}, and in particular by ΔE_{ORB}, because of favorable exothermic orbital interactions between both fragments and a lower repulsive ΔE_{ST} term. The ΔE_{ST} is related to the Pauli repulsion and the classical electrostatic interaction, but dominated by the former. So, the Pt–C distances and the space available in each hole to make the metal-carbon bond will be decisive in ΔE_{ST}. This space can be calculated as the delimited area by the four dangling C atoms: 6.690 $Å^2$ for the 6:6 hole and a little higher, 7.200 $Å^2$, for the 6:5 hole. These magnitudes confirm that the repulsion in the ΔE_{ST} term when the Pt metal is incorporated in the 6:6 hole, 18.11 eV, is higher than in the 6:5 hole, 16.15 eV. The computed exothermic values for the orbital term (ΔE_{ORB}) are high: –30.38 eV for C_{2v}-$C_{58}Pt$ and –28.81 eV for C_s-$C_{58}Pt$. They exemplify that when two neutral fragments are joined there is considerable electronic reorganization. The IBE, after ΔE_{DE}, ΔE_{ST} and ΔE_{ORB} are calculated, is clearly favorable to the C_s-$C_{58}Pt$ isomer by 0.78 eV. However, this is not enough to compensate for the more favorable stability (by 1.41 eV) of the ΔE_{HOLE} for the C_{2v}-$C_{58}Pt$ isomer. The IBE can be easily understood from the electronic structure of both isomers. Unlike C_{2v}-C_{58} which has only four dangling sp^2 electrons, the C_s-C_{58} isomer has two additional dangling p_z electrons, which means that the latter can interact more efficiently than the former.

5.2.5 Fragment molecular orbital analysis

In order to investigate how the metal is incorporated into the carbon framework, we analyzed the interaction orbital diagram between the two fragments: Pt and C_{58}. Albright made an in-depth study of orbitals in organometallic compounds.[23] The main idea is that the important valence orbitals of a molecule can be constructed from the valence orbitals of its

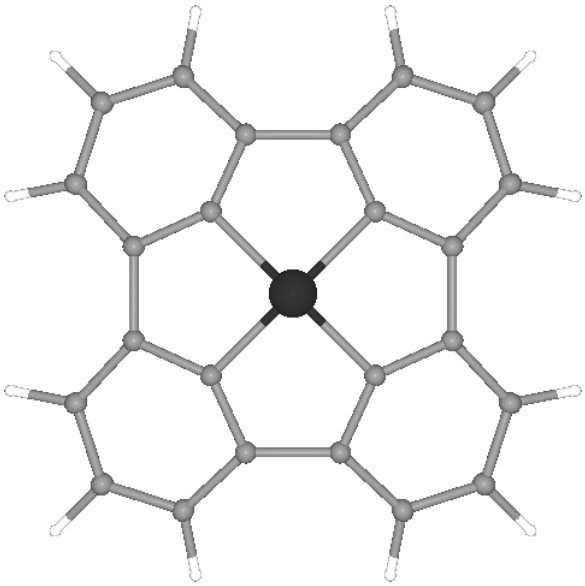

Figure 5.3 Optimized structure for D_{4h}-$C_{24}H_{12}Pt$, used as a bonding model for C_{2v}-$C_{58}Pt$.

constituent fragments. This method is another approach to, and a development of, the IBE described in above section.

The most stable diamagnetic organometallic compounds have a total of 18 electrons around the transition metal. In other words, there should be a total of 18 *d* metal electrons and electrons formally assigned to coordinate bonds from the surrounding ligands. In our specific case, the first fragment, the Pt atom, has 10 *d*-based valence electrons ($3d^9$ $4s^1$ $4p^0$) and the second fragment, the holed C_{2v}-C_{58} fullerene, has 4 σ-sp^2 electrons and 4 π-p_z electrons from the four dangling carbons. In conclusion, 18 electrons are involved in the metal-carbon bond. Therefore, Pt is formally in the 0 oxidation state.

Initially we used the planar D_{4h}-$C_{24}H_{12}Pt$ system in an attempt to explain the metal-carbon bond in the most symmetric C_{2v}-$C_{58}M$ isomer. Figure 5.3 shows the optimized structure of this compound. The substitution of the central 6:6 C–C bond in the polycyclic aromatic $C_{26}H_{12}$ compound leads to the planar D_{4h}-$C_{24}H_{12}Pt$ structure in which the Pt atom is tetra-tetracoordinated. This coordination can be taken as a model insertion because Pt incorporation into the fullerene carbon framework can be

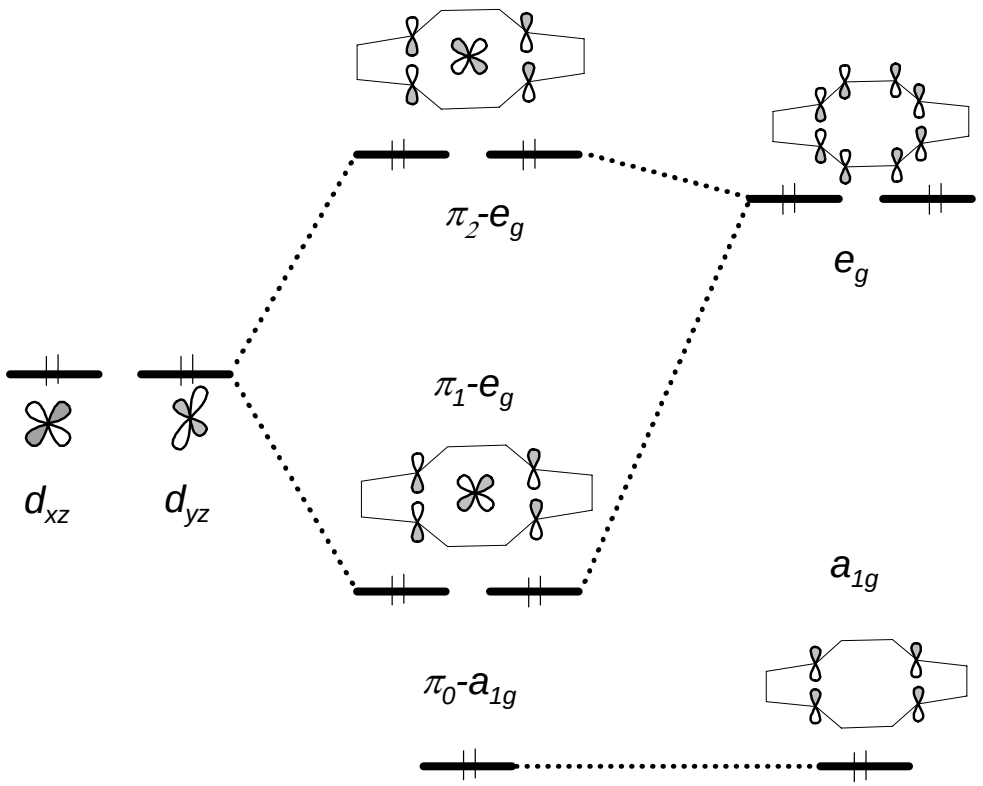

Figure 5.4 Molecular orbital (MO) correlation diagram for π interaction system between Pt (left, 4 *d* electrons in two metal orbitals) and $C_{24}H_{12}$ (right, 4 p_z electrons + 2 additional electrons in three carbon ligand orbitals) for the D_{4h}-$C_{26}H_{12}Pt$.

expected as a local interaction between the metal and the four dangling carbons. The most important distances and the decomposition of SE for this heterocompound have also been added to Table 5.1 and 5.2.

As is to be expected, the SE is clearly higher than the SE for heterofullerenes. When the C_2 unit is substituted by a Pt atom an energy of +11.72 eV is required. The $C_{26}H_{12}$ compound is highly aromatic and changes in the carbon skeleton will have a dramatic effect on their stability. So although it has fewer carbons the ΔE_{HOLE} is computed to be +16.92 eV. The insertion of Pt in this planar structure is also favorable but less than we expected (–5.20 eV for IBE). The expected high value for the ΔE_{ORB}

(–37.00 eV) is considerably compensated for by the ΔE_{DE} (3.31 eV) and the unexpected repulsive value of ΔE_{ST} (+28.49 eV). The repulsive value is probably due to the short Pt–C distance of 1.929 Å. The planar D_{4h}-$C_{24}H_{12}Pt$ heterocompound is a simplification of the C_{2v}-$C_{58}Pt$ metallofullerene but it is a suitable and powerful model for understanding the metal bond in the metallofullerene because: (1) all distances between close dangling carbons are equal and (2) the σ/π interactions are completely separable. The metal bond established in the D_{4h}-$C_{24}H_{12}Pt$ heterocompound will be explained through two independent molecular orbital correlation diagrams: one for the σ ligands (sp^2 carbon electrons) and the other for the π ligands (p_z carbon electrons). The knowledge acquired for the D_{4h}-$C_{24}H_{12}Pt$ heterocompound will be used to construct the metal bonds in C_{4v}-$C_{24}H_{12}Pt$ and C_{2v}-$C_{24}H_{12}Pt$, which are closer to those found in C_{2v}-$C_{58}Pt$.

Model MOs of D_{4h}-$C_{24}H_{12}Pt$. The π diagram is shown in Figure 5.4. The e_g and a_{1g} carbon ligand orbitals on the right hand side of the diagram represent the four π-p_z atomic orbitals of the four dangling carbons. It is important to notice that although the e_g orbital should be half filled, it is in fact completely filled because the four π-p_z electrons form π adjacent C–C bonds. The e_g ligand orbital matches the d_{xz} and d_{yz} metal orbitals and gives the bonding interaction π_1-e_g molecular orbital (MO) and the antibonding π_2-e_g MO. The a_{1g} ligand orbital, on the other hand, finds no ligand combination to interact with, π_0-a_{1g}. The σ diagram is shown in Figure 5.5. The four σ-sp^2 carbon electrons are located at two ligand orbitals: the a_{1g}, completely symmetric and filled, and the e_u, less stable and half filled. The latter ligand orbital makes the triplet the most stable electronic state for the holed D_{4h}-$C_{24}H_{12}$ system. As a result, the four σ-sp^2 electrons (e_u ligand orbital), and not the four π-p_z electrons, determine the electronic state for these holed carbon systems. The main factors affecting the e_u ligand orbital are the distances between the four dangling carbons, the d_x and d_y distances in Figure 5.2a. The triplet is maintained while the d_x and d_y distances are almost identical, but it breaks up to give the singlet when the distances are different. So, the most stable electronic state of D_{4h}-$C_{24}H_{12}$ is a triplet. However, the C_{2v}-C_{58} with the C_{60} geometry is a singlet, d_x = 2.349 Å and d_y = 2.848 Å rather different. In contrast, the C_{2v}-C_{58} with the C_{2v}-$C_{58}Pt$ geometry yields the triplet since d_x and d_y are almost equal: 2.657 Å and

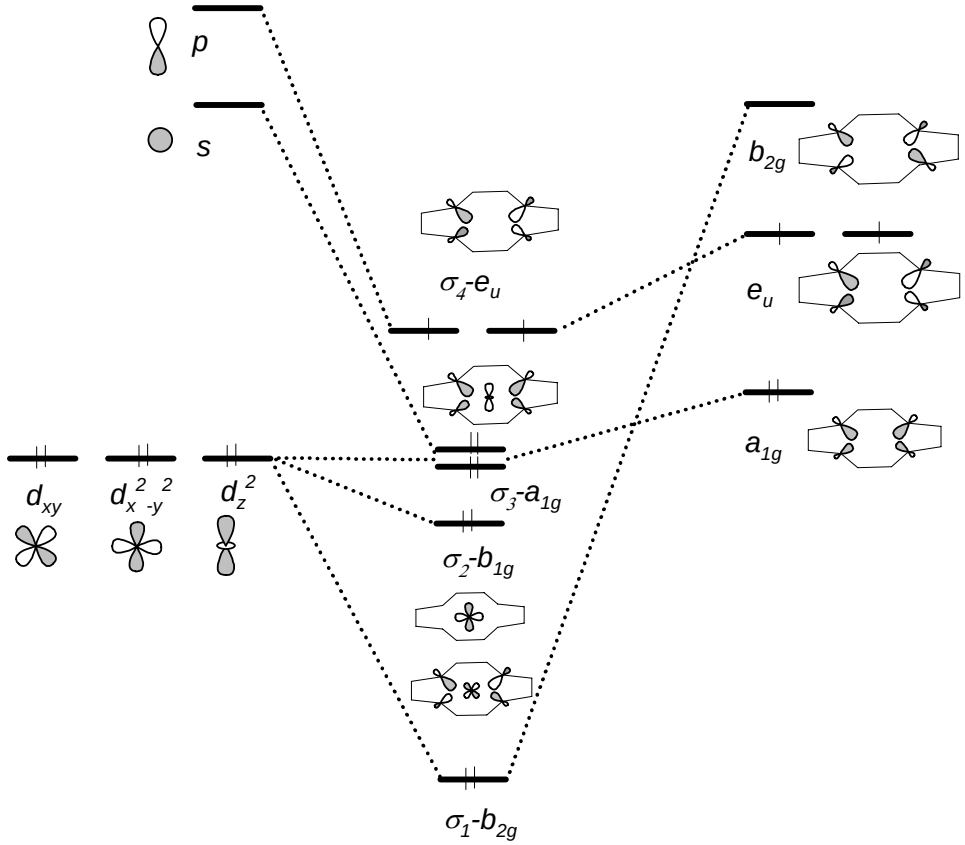

Figure 5.5 Molecular orbital (MO) correlation diagram for σ interaction system between Pt (left, 6 *d* electrons in three metal orbitals) and $C_{24}H_{12}$ (right, 4 sp^2 electrons in three carbon ligand orbitals) for D_{4h}-$C_{26}H_{12}Pt$.

2.665 Å, respectively. Also, the e_u ligand orbital is stabilized by interaction with the empty *p* metal orbitals but it also appears as HOMO (σ_4-e_u) in the MO diagram that gives the triplet as the most stable electronic state of D_{4h}-$C_{24}H_{12}Pt$. The a_{1g} ligand orbital matches the *s* and d_z^2 metal orbitals and gives one of the most bonding interactions: σ_3-a_{1g}. On the other hand, the $d_{x^2-y^2}$ metal orbital is also stabilized by the presence of carbon ligands but it finds no ligand combination to interact with (σ_2-b_{1g}). Finally, the σ_1-b_{2g} is the second most bonding σ MO. It represents the interaction between the d_{xy} metal orbital and the empty σ b_{2g} ligand. To sum up, the triplet is the most stable electronic state of the D_{4h}-$C_{24}H_{12}Pt$ system and the metal-carbon bond

is dominated by (1) two bonding σ MOs: σ_3-a_{1g}, whose carbons transfer a small amount of electron density to metals, and σ_1-b_{2g}, whose metals transfer a considerable amount of electron density to carbon ligands and; (2) two degenerate bonding π MOs included into π_1-e_g. This approximation agrees with the positive net charge on the Pt atom and the negatively charged neighboring carbons in D_{4h}-$C_{24}H_{12}Pt$ and C_{2v}-$C_{58}Pt$.

MOs of C_{2v}-$C_{58}Pt$. The MOs of D_{4h}-$C_{24}H_{12}Pt$ can be easily adapted to the MOs of $C_{58}Pt$ when we take into account two concepts: the curvature of the fullerene surface (C_{4v} symmetry) and the non-equivalency of the four carbons (C_{2v} symmetry). First, we constructed the hypothetical evolution of each MO from the D_{4h}-$C_{24}H_{12}Pt$ system to the C_{2v}-$C_{24}H_{12}Pt$ system, bearing in mind the intermediate curved C_{4v}-$C_{24}H_{12}Pt$ system (Figure 5.6). A posteriori, we demonstrated that the MOs involved in the Pt–C bond for the C_{2v}-$C_{24}H_{12}Pt$ system are a simplification of the MOs found in the C_{2v}-$C_{58}Pt$ heterofullerene. Nevertheless, they provide all the important information for describing the Pt–C bond. The σ and π MOs can mix together when their symmetry changes from D_{4h} to C_{4v}. Basically, this affects the e_u and e_g MOs of the D_{4h} system. After evolution, these MOs become *e* MOs of the C_{4v} system with a high σ-π electron mixing. It is important to remark that the antibonding π_2-e_g MO of the D_{4h} system is transformed to the bonding *6-e* MO of the C_{4v} system due to the considerable presence of σ-sp^2 ligand orbitals. Also, the *7-e* HOMO contains more π-p_z character than its antecessor σ_4-e_u. On the other hand, the σ a_{1g}, b_{1g}, and b_{2g} MOs incorporate p_z contributions to become now a_1, b_1 and b_2 MOs in the C_{4v} system, respectively. In conclusion, the hypothetical C_{4v}-$C_{24}H_{12}Pt$ system would also evolve a triplet as the most stable electronic state. Now, the evolution of the MOs from the C_{4v}-$C_{24}H_{12}Pt$ to the C_{2v}-$C_{24}H_{12}Pt$ will help us to understand the MOs of the $C_{58}Pt$ monoheterofullerene. In this evolution, the equivalency of each carbon is broken and consequently there is a preferred direction for metal-carbon interaction: perpendicular to the orientation of the substituted C_2 unit (d_x direction in Figure 5.2a). The *e* MOs divide into b_2 and b_1 MOs. The most stable MOs are the bonding b_1 MOs with the d_{xz} metal orbital contribution. The d_{xz} metal orbital is perpendicular to the previous C_2 unit. In this orientation, the overlap of the d_{xz} metal orbital with the carbon ligand orbitals is maximum and most effective because the

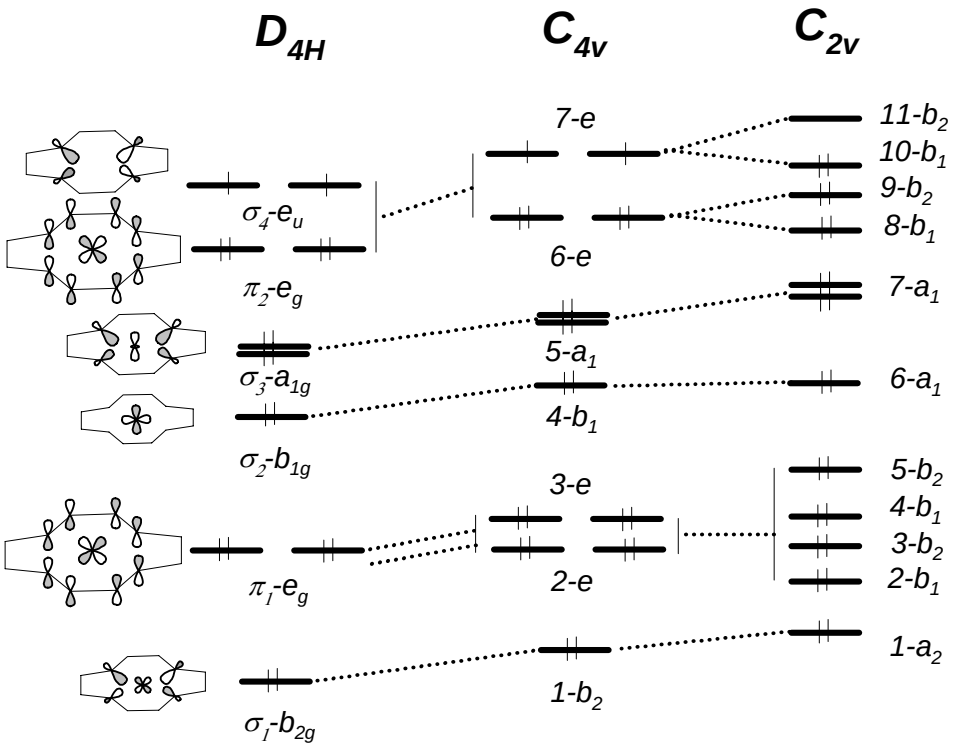

Figure 5.6 Evolution of the molecular orbitals (MOs) of the interaction between a tetracoordinated Pt atom and four carbons with 4 p_z electrons and 4 sp^2 electrons from D_{4h}-$C_{24}H_{12}Pt$ to C_{4v}-$C_{24}H_{12}Pt$ and C_{2v}-$C_{24}H_{12}Pt$. The MOs of the final C_{2v}-$C_{24}H_{12}Pt$ model can be taken as a good simplification of the C_{2v}-$C_{58}M$ MOs.

distances between them are shorter than in the other orientation (compare the d_x with d_y distances in Figure 5.2a for C_{2v} holed heterofullerenes). The analogous d_{yz} metal orbital is represented by the b_2 symmetry in the C_{2v} system. The fact that the stabilization of b_1 MOs is higher than that of b_2 MOs means that the C_{2v}-$C_{58}Pt$ heterofullerene becomes a singlet electronic state with a relatively large HOMO-LUMO gap of 0.59 eV. The triplet state is 0.50 eV above the ground state. Although the *d* metal orbitals are completely spread over several MOs, the contribution of the d_{xz} Pt orbital to *10*-b_1 HOMO is of 21 %, and the contribution of the d_{yz} Pt orbital to *11*-b_2 LUMO is of 13 %. On the other hand, the highly bonding *1*-b_2 MO of the

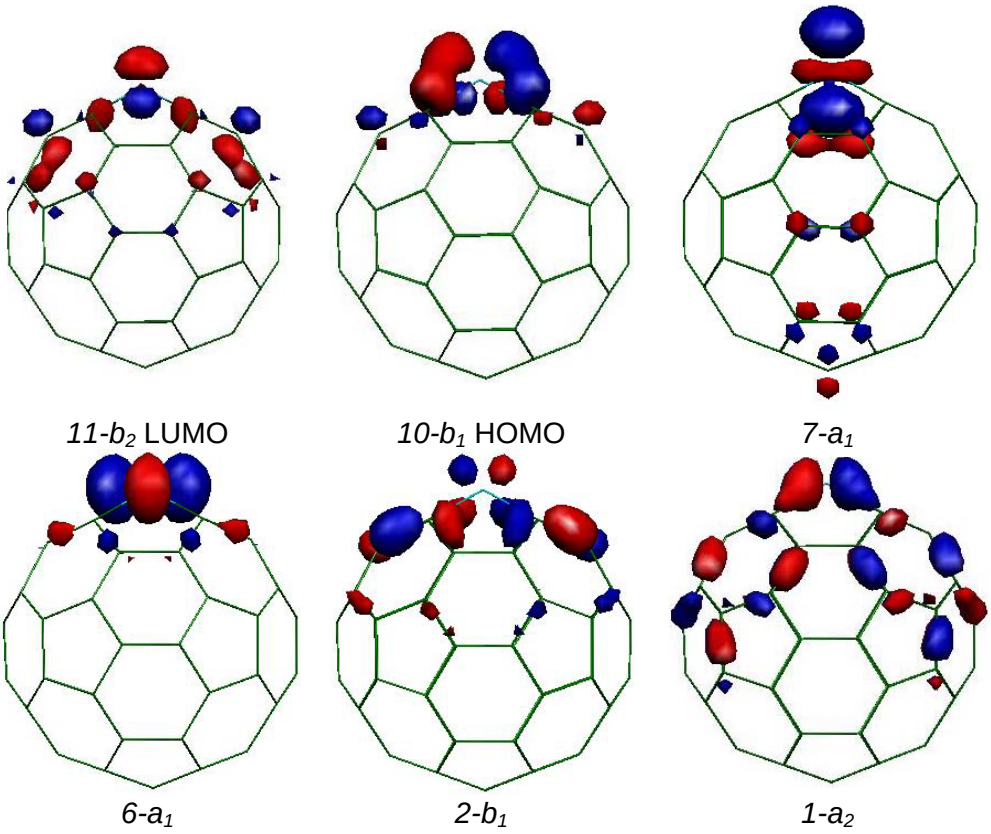

Figure 5.7 The most important molecular orbitals (MOs) of the C_{2v}-C_{58}Pt.

C_{4v} system now becomes the *1-a₂* MO in the C_{2v} system, which retains the σ bonding character of the antecessor. The bonding *5-a₁* MO of the C_{4v} system becomes the *7-a₁* in the C_{2v} system and the stability decreases considerably due to the curvature effect, but it still represents a bonding σ MO. To sum up, the metal-carbon bond in the C_{2v}-C_{58}Pt is basically suspended from: (1) two bonding σ MOs of *1-a₂* and *7-a₁* symmetry between the d_{xy} and d_{z2} metal orbitals and the sp^2 carbon ligand orbitals, respectively; and (2) two bonding π MOs of symmetry b_2 and b_1 between the d_{xz}/d_{yz} metal orbitals and the p_z/sp^2 carbon ligand orbitals spread over several MOs: *2-b₁*, *3-b₂*, *4-b₁*, *5-b₂*, *8-b₁*, *9-b₂* and *10-b₁*. The most important MOs involved in the Pt–C bonds of C_{2v}-C_{58}Pt are plotted in Figure 5.7.

Decomposition of the orbital interaction. The ΔE_{ORB} can be broken up into the contributions made by the orbital interactions within the various irreducible representations of the system's overall symmetry group, in accordance with the decomposition scheme proposed by Ziegler. This decomposition scheme is particularly useful in the complexes considered here because it makes it possible to separate the energy contributions corresponding to σ and π interactions and also to assign these contributions to the corresponding *d* metal orbitals. Table 5.3 shows the results of this energy decomposition for D_{4h}-$C_{24}H_{12}Pt$, C_{2v}-$C_{58}Pt$ and C_s-$C_{58}Pt$. Indeed, the most important contributions that the D_{4h}-$C_{24}H_{12}Pt$ system makes to ΔE_{ORB} are the two σ interactions and the two π interaction: the ligand to metal σ donation through the d_z^2 and the *s* metal orbitals makes a contribution of −19.14 eV (σ_3-a_{1g}), the metal to ligand σ donation through the d_{xy} metal orbital makes a contribution of −8.34 eV (σ_1-b_{2g}) and the two π interactions through d_{xz}/d_{yz} metal orbitals makes a contribution of −4.28 eV (π_1-e_g). As can be seen, σ interactions (−29.56 eV) dominate clearly over π interactions (−7.44 eV) in the insertion of the metal into the planar D_{4h}-$C_{24}H_{12}Pt$ structure. The decomposition of ΔE_{ORB} for C_{2v}-$C_{58}Pt$ shows that σ interactions are reduced dramatically, by almost 9 eV, when the structure is curved from D_{4h}-$C_{24}H_{12}Pt$ to C_{2v}-$C_{58}Pt$. On the other hand, the π interactions even increase by 2.23 eV. This can be attributed to the improvement in the orbital overlap between the d_{xz} metal orbital and the p_z/sp^2 carbon ligand orbitals. The decomposition also shows that the bonding character of d_{xz} (b_1) is stronger than that of d_{yz} (b_2). Subsection 5.2.3 shows that the difference between the C_{2v}-$C_{58}Pt$ and C_s-$C_{58}Pt$ isomers is caused by the energy required for making the hole (ΔE_{HOLE}), but, even so, it is interesting to understand the differences in how the metal is incorporated into both isomers of $C_{58}Pt$. The interaction between C_s-C_{58} and the metal is no different from the interaction of C_{2v}-C_{58} except that two of the four p_z electrons of the dangling bonds in the holed C_s-C_{58} cage are unpaired (Figure 5.2b). The consequence is that the π interactions between the metal and the carbons (*a''* symmetry) increases from −9.67 eV in the C_{2v}-$C_{58}Pt$ to −11.95 eV in the C_s-$C_{58}Pt$. On the other hand the σ interactions (d_{xy}, d_z^2 and *s* represented by *a'* symmetry) are reduced by almost 4 eV in C_s-$C_{58}Pt$, considerably more than in C_{2v}-$C_{58}Pt$. This decrease may be related to the fact that two of the four C−Pt bond lengths increase with respect to the most

Table 5.3 Decomposition of the orbital interaction term (ΔE_{ORB}) for D_{4h}-$C_{24}H_{12}Pt$, C_{2v}-$C_{58}Pt$ and C_s-$C_{58}Pt$ in the irreducible representation of each symmetry [a]

d and p metal orbitals	$C_{24}H_{12}Pt$		$C_{58}Pt$		$C_{58}Pt$	
	D_{4h}		C_{2v}		C_s	
d_z^2, *s*	a_{1g}	–19.14				
$d_{x^2-y^2}$	b_{1g}	–1.89				
--	a_{1u}	0.00				
p_z	a_{2u}	–0.19	a_1	-13.13		
d_{xy}	b_{2g}	–8.34				
--	a_{2g}	0.00	a_2	–7.58	*a'*	–16.87
σ interactions		*–29.56*		*–20.71*		*–16.87*
d_{xz}	e_g	–2.14				
p_x	e_u	–1.58				
--	b_{1u}	0.00	b_1	–6.83		
d_{yz}	e_g	–2.14				
p_y	e_u	–1.58				
--	b_{2u}	0.00	b_2	–2.84	*a''*	–11.75
π interactions		*–7.44*		*–9.67*		*–11.75*
total		*–37.00*		*–30.38*		*–28.62*

[a] Energies in eV.

symmetric isomer (Table 5.1). The sum of both terms accounts for the total ΔE_{ORB}, which is 1.76 eV favorable to the C_{2v}-$C_{58}Pt$ isomer.

5.3 MONOHETEROFULLERENES: $C_{58}M$, $C_{59}M$ (M = Pt, Ir, Os, Ti) and $C_{68}Pt$

5.3.1 $C_{58}M$ (M = Pt, Ir, Os, Ti)

Table 5.4 Geometric properties for C_{2v}-C_{58}M and C_s-C_{58}M (M = Pt, Ir, Os) [a]

$C_{58}M$	*Pt*		*Ir*		*Os*	
Isomer [b]	C_{2v}	C_s	C_{2v}	C_s	C_{2v}	C_s
C–M	2.034	2.049/ 2.013	2.045	2.065/ 1.996	2.058	2.082/ 1.990
Cage radius [c]	3.562	3.569	3.558	3.565	3.556	3.562
HOMA [d]	0.279	0.236	0.308	0.258	0.309	0.274
SE [e]	7.35	7.98	5.43	6.09	5.55	6.12
RE C_s/C_{2v} [f]	–0.63		–0.66		–0.57	

[a] Distances in Å and energy in eV. [b] When Pt replace a C_2 unit in C_{60} two isomer can appear: (1) Pt replaces a 6:6 C_2 bond in the C_{2v} isomer and (2) 6:5 C_2 bond is substituted in the C_s isomer. [c] 3.551 Å for free C_{60}. [d] Harmonic oscillator model of aromaticity (HOMA), 0.274 for free C_{60}. [e] The substitution energy (SE) is defined as the energy reaction of the process $C_{60} + M \rightarrow C_{58}M + C_2$. The true atomic groundstate for M atom is used according to reference: Baerends, E. J.; Branchadell, V.; Sodupe, M. *Chem. Phys. Lett.* **1997**, *265*, 481. [f] Relative energy (RE) between C_s and C_{2v} isomers.

The geometry of both isomers of $C_{58}M$ (M = Pt, Ir, Os, Ti) has been optimized so that effects of substituting different metals in the fullerene carbon framework can be compared. For this purpose, we use the M–C bond lengths, cage radius and also a structure-based measure of aromaticity called the *harmonic oscillator model of aromaticity* (HOMA).[24] HOMA index is probably the most effective index of this kind. The change in aromaticity can also be a measure of how the carbon skeleton of the fullerene is distorted by the irruption of the metal. This relationship is discussed in a recent review of the structural aspects of aromaticity.[25] HOMA varies from 0 for non-aromatic systems to 1 for fully aromatic systems. Table 5.4 shows all the data of the monoheterofullerenes mentioned. Changing the Pt metal for another metal varies the geometric properties only slightly and the structure is rather similar to the structure found for $C_{58}Pt$. The most stable isomer, independently of the metal substitution, is still C_{2v}-$C_{58}M$, which is more stable than the C_s-$C_{58}M$ by *ca.* 0.60 eV. The substitution energy (SE) increases in the order Ir < Os < Ti < Pt. Thus substituting a C_2 unit by M is slightly easier for Ir and Os, around 1.92 and 1.80 eV respectively, than for Pt in the C_{2v}-$C_{58}M$ monoheterofullerenes. The cage radius and the HOMA indexes provide some clues about SE on different metals (Figure 5.8).

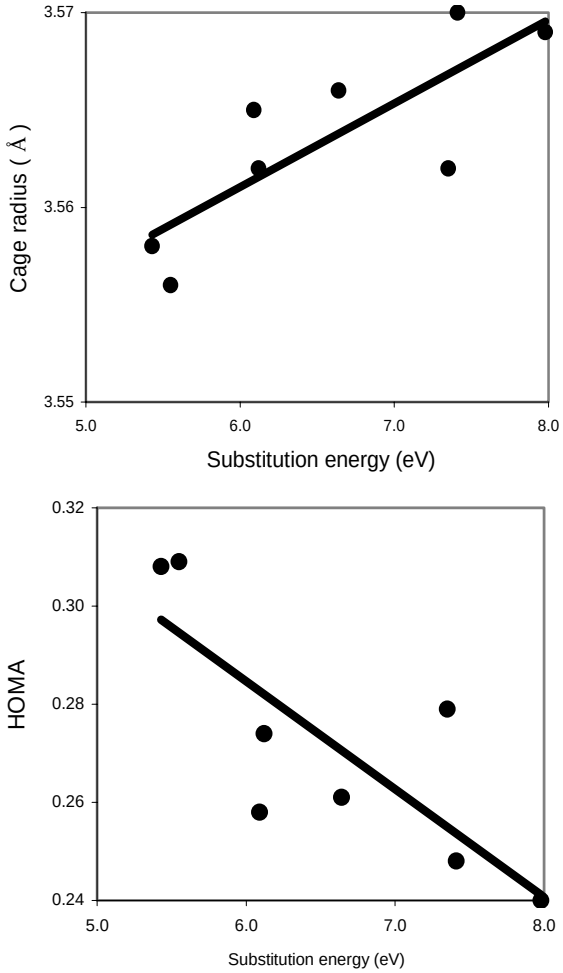

Figure 5.8 Correlation between cage radius and HOMA versus the substitution energy (SE) for C_{2v}-$C_{58}M$ and C_s-$C_{58}M$ (M = Pt, Ir, Os, Ti).

Both geometric parameters are a measure of the cage distortion and it is to be expected that cage distortion and non-aromatic values of HOMA are accompanied by a destabilization of the monoheterofullerenes. Indeed, as can be seen in Figure 5.8, there is a rough correlation between both parameters and SE. So, the most endothermic substitutions found for $C_{58}Pt$ and $C_{58}Ti$ lead to larger cage radius (3.562 and 3.566 Å) and low HOMA values (0.279 and 0.261) whereas $C_{58}Os$ and $C_{58}Ir$, for which the

endothermic substitutions were calculated to be lower, lead to higher HOMA values (0.301 and 0.303) and less cage distortion than C_{60} (lower cage radius: 3.558 and 3.555 Å, respectively). This relationship between geometric parameters and relative stability will be discussed in greater depth with reference to diheterofullerenes (section 5.5).

The SE for $C_{58}M$ (M = Pt, Ir, Os) monoheterofullerenes were decomposed in Table 5.5. This decomposition makes it possible to compare C_s and C_{2v} isomers and also the different metal insertions in the fullerene carbon framework of C_{60}. The energy necessary to make a hole (ΔE_{HOLE}) is the significant energy which determines the most stable isomer: 17.90 eV for C_{2v}-C_{58} and 19.31 eV for C_s-C_{58}. ΔE_{HOLE} is clearly endothermic and favorable to C_{2v}-$C_{58}M$ isomers whereas IBE is exothermic and slightly favorable to C_s-$C_{58}M$ isomers. The geometric parameters (cage radius and HOMA) always suggest that the C_{2v}-$C_{58}M$ isomers will be more stable. C_{2v}-$C_{58}M$ isomers have smaller cage radius and more aromatic HOMA values than C_s-$C_{58}M$ isomers. For instance, the cage radius and HOMA value for C_{2v}-$C_{58}Os$ are computed to be 3.556 Å and 0.309, respectively, and for C_s-$C_{58}Os$, they are 3.562 Å and 0.274. These results can be extrapolated to other pairs of monoheterofullerene isomers. As in $C_{58}Pt$ isomers, the stabilizing IBE values help to form the C_s-$C_{58}M$ isomers but the higher destabilizing ΔE_{HOLE} values help to form the C_{2v}-$C_{58}M$ isomers, which shifts the SE in favour to the latter. This decomposition will be particularly useful to rationalize the decrease in the SE for the series C_{2v}-$C_{58}M$ (M = Pt > Ir ≈ Os) (Pt, 7.35 eV; Os, 5.55 eV and Ir, 5.43 eV). The decrease may be explained by the increase in ΔE_{ORB} from −31.85 eV for Pt to −39.45 eV for Os, which compensates for the expected increase in ΔE_{ST} and ΔE_{DE} due to the larger atomic radii of Os and Ir atoms. It is important to point out that although Ir and Os have larger atomic radii and it could deform the fullerene cage to a much greater extent than Pt atom, they do not do so because these bigger metals protrude a little from the fullerene surface. These atoms still interact with the fullerene carbon framework but do not deform the cage structure. This is reflected by the decrease in the ΔE_{DE} both in the C_{2v}-$C_{58}M$ isomers (1.80 eV for Pt, 1.63 for Ir and 1.71 eV for Os) and the C_s-$C_{58}M$ isomers (1.63 for Pt, 1.53 for Ir and 1. 56 eV for Os) from Pt to Os.

Table 5.5 Decomposition of the substitution energy (SE) for C_{2v}-$C_{58}M$ and C_s-$C_{58}M$ (M = Pt, Ir, Os) [a]

	$C_{58}M$	*Pt*		*Ir*		*Os*	
	Isomer	C_{2v}	C_s	C_{2v}	C_s	C_{2v}	C_s
ΔE_{HOLE} [b]		17.90	19.31	17.90	19.31	17.90	19.31
ΔE_{DE} [c]	C_{58}	1.80	1.63	1.63	1.53	1.71	1.56
	C_2	–0.57	–0.98	–0.57	–0.98	–0.57	–0.98
	M	0.49	0.49	1.36	1.36	2.40	2.40
	Total	1.72	1.14	2.42	1.91	3.54	2.98
ΔE_{INT} [d]	ΔE_{ST}	18.11	16.15	21.99	20.48	22.31	23.13
	ΔE_{ORB}	–30.38	–28.62	–36.88	–35.61	–38.20	–39.30
	Total	–12.27	–12.47	–14.89	–15.13	–15.89	–16.17
IBE [e]		–10.55	–11.33	–12.47	–13.22	–12.35	–13.19
SE		7.35	7.98	5.43	6.09	5.55	6.12
RE C_s/C_{2v} isomers [f]		–0.63		–0.66		–0.57	

[a] Energy in eV. The Substitution Energy (SE) is defined as the energy reaction of the process $C_{60} + M \rightarrow C_{58}M + C_2$ .This energy can be dived into several contributions $SE = \Delta E_{HOLE} + IBE$. [b] ΔE_{HOLE} accounts for the energy reaction of the process $C_{60} \rightarrow C_{58}^* + C_2^*$. Both species C_{58}^* and C_2^* with the fixed geometry of free C_{60}. C_2* keeps the electronic configuration as its free C_2 analogue whereas C_{58}^* is calculated at the most stable electronic state in this geometry, a singlet. [c] ΔE_{DE} accounts for the deformation energy for the three fragments: $C_{58}^* \rightarrow C_{58}$, $C_2^* \rightarrow C_2$ and $M \rightarrow M^*$. C_{58} with the fixed geometry found in $C_{58}M$ and a triplet as the most stable electronic state. C_2 geometrical optimised. M is calculated at the most stable electronic state (unrestricted) and M* at restricted electronic state. [d] ΔE_{INT} accounts for the interaction energy between the C_{58} and M* fragments at the fixed $C_{58}M$ geometry. [e] IBE (insertion binding energy) accounts for the energy reaction of the process $C_{58}^* + C_2^* + M^* \rightarrow C_{58}M + C_2$. Also, $IBE = \Delta E_{DE} + \Delta E_{INT}$. [f] Relative energies (RE) between C_{2v} and C_s isomers.

5.3.2 $C_{68}Pt$, a doped fullerene from D_{5h}-C_{70}.

Finally, to find out more about the relationship between the substituted C–C bond and its stabilization, we constructed all possible hypothetical regioisomers by replacing a C_2 unit with a Pt atom in the C_{70}

Table 5.6 Characterization of the eight distinct regioisomers of $C_{68}Pt$, a doped fullerene from the free D_{5h}-C_{70}:**1** [a]

Isom.	*Sym.*	*C–C bond type* [b]	*C–C bond lenghts*	θ_p [c]	*MBO* [d]	*Cage Radius* [e]	*HOMA* [f]	*RE* [g]
d,e	C_1	***B***	1.421	9.43	1.246	3.855	0.337	0.00
c,c	C_s	pyracylene, ***A***	1.393	11.49	1.332	3.847	0.353	0.01
a,b	C_s	pyracylene, ***A***	1.399	11.92	1.334	3.842	0.350	0.06
c,d	C_1	corannulene, ***D***	1.446	10.88	1.138	3.855	0.318	0.63
b,c	C_1	corannulene, ***D***	1.448	11.73	1.140	3.851	0.323	0.69
a,a	C_s	corannulene, ***D***	1.451	11.85	1.138	3.848	0.321	0.83
e,e	C_{2v}	pyrene, ***C***	1.470	8.60	1.167	3.861	0.300	0.93
d,d	C_s	corannulene, ***D***	1.438	10.28	1.219	3.859	0.327	1.19

[a] Distances in Å, angles in º and energy in eV. [b] The different C–C bond types in the IPR fullerenes can be visualized in Appendix A.1 [c] Pyramidalization angle (θ_p). [d] Mayer bond order (MBO). [e] Cage Radius is defined as the average distance of all surface atoms to the center of the fullerene. Cage radius for D_{5h}-C_{70} is 3.837 Å. [f] The HOMA index for D_{5h}-C_{70}:1, 0.362. [g] Relative energies (RE).

fullerene. Basically, the C–C bonds are characterized by their different pyramidalization angles (θ_p), distances and topologies. The C_{70} fullerene is highly suitable because it contains eight different C–C bonds with different pyramidalization angles unlike the previous C_{60} studied. Only one isomer obeys the isolated pentagon rule (IPR) for the C_{70} stoichiometry.[26] This structure, which is of D_{5h} symmetry, has five types of carbons, which form nine layers. These carbons are connected by eight different C–C bond types, four of which occur at 6:6 ring junctions: Ca–Cb, Cc–Cc, Ce–Ce and Cd–Ce. The first two are pyracylene types while the third is a pyrene type (see Appendix A.4 for a full description of the distinct C–C bonds). The C_{70} is most curved at the poles and flatter at the equator. The flat area in the middle is the most aromatic and has a low Mayer bond order (MBO) whereas in the more curved area the C–C bonds have a greater double bond character and higher MBOs. Table 5.6 shows the characterization of all eight distinct C–C bonds and the relative energies (RE) of the eight $C_{68}Pt$ regioisomers.

Three regioisomers corresponding to the 6:6 Ca–Cb, Cc–Cc and Cd–Ce substitutions appear very close in energy (0.00-0.06 eV) and are the most stable regioisomers. The other regioisomers are much less stable (by 0.63-1.19 eV). The Ca–Cb and Cc–Cc structures represent doping at the poles whereas the Cd–Ce represents doping in the flat area. This last regioisomer was not expected to be as stable as it is found. Apart of this discrepancy, some conclusions can be drawn from the data in Table 5.6. First, the substitution of a 6:6 C–C bond seems to be particulary important, except when the pyramidalization angle and MBO of the bond are extremely low: for example the Ce–Ce bond. Second, the MBO is a good reference for the double bond localization and the substitution in these sites is favoured. The three most stable regioisomers are those in which the three C–C bonds with the highest MBOs have been substituted. Third, the pyramidalization angle seems not to have a crucial effect on the stabilization and shows unambiguous results. We would need more data on other heterofullerenes to draw any conclusions about the effect of the pyramidalization angle on the substitution patterns. Finally, the fourth conclusion is maybe the most important: the regioisomer constructed with the smallest change in the aromaticity will become the most stable regioisomer. The three most stable regioisomers have the three highest aromatic HOMA values: 0.337, 0.353 and 0.350. This was also observed in the section above for the $C_{58}M$ monoheterofullerenes constructed from the C_{60}. On the other hand, the SE was computed to be 7.50 eV for the most stable $C_{68}Pt$ isomer which is rather similar to the SE for C_{2v}-$C_{58}Pt$, 7.35 eV.

5.3.3 $C_{59}M$ (M = Pt, Ir, Os, Ti)

The substitution of one carbon by one metal results in the formation of the $C_{59}M$ heterofullerenes. This tricoordinated metal protrudes from the fullerene surface because there is no space for it to be included completely, unlike the $C_{58}M$ heterofullerenes. The geometrical parameters for $C_{59}M$ (M = Pt, Ir, Os, Ti) are listed in Table 5.7 and an optimized geometry of $C_{59}Pt$ is displayed in Figure 5.1. The Pt–C bond lengths in the $C_{59}M$ heterofullerene are somewhat shorter than in their homologous $C_{58}M$ heterofullerene. For example, the mean Pt–C bond length in $C_{59}Pt$ is 1.961 Å and in C_{2v}-$C_{58}Pt$ it is 2.016 Å. The electronic configuration of $C_{59}Pt$ is a singlet closed-shell in

Table 5.7 Geometric properties for $C_{59}M$ (M = Pt, Ir, Os, Ti) [a]

	$C_{59}Pt$	*$C_{59}Ir$*	*$C_{59}Os$*	*$C_{59}Ti$*
M–C [b]	1.998/ 1.951	1.962/ 1.921	1.951/ 1.892	2.020/ 1.939
Cage radius [c]	3.580	3.578	3.578	3.581
Substitution energy (SE) [d]	6.20	3.51	3.46	4.69

[a] Distances in Å and energy in eV. [b] The longest M–C bond lengths occur between the metal and the carbons which belong to a hexagon while the shortest ones occurs between the metal and the carbon atom which belong to the pentagon. [c] 3.551 Å for C_{60}, 3.562 Å, 3.558 Å and 3.556 Å for C_{2v}-$C_{58}M$ (M = Pt, Ir Os), respectively. [d] The Substitution energy (SE) is defined as the energy reaction of the process $C_{60} + M \rightarrow C_{59}M + C$. The true atomic groundstate for M and C atom is used according to reference: Baerends, E. J.; Branchadell, V.; Sodupe, M. *Chem. Phys. Lett.* **1997**, *265*, 481.

which the HOMO-LUMO gap was computed to be 0.70 eV. The triplet structure with one electron in the HOMO and another in the LUMO was also optimized but its relative energy with respect to the singlet structure was quite high (0.44 eV). Mulliken population analysis indicates that there is significant electron charge transfer from the metal to the carbon fragment. The net charge on platinum is +0.76 *e*. The electronic populations of the *s*, *p* and *d* Pt orbitals are 2.547, 6.313 and 8.385 *e*, respectively. The metal orbitals in $C_{59}Pt$ are spread over a wide range of MOs. Each of these MOs in the metallofullerene has a low metal contribution. Specifically, the participation of the metal orbitals is 17% in the HOMO and 20% in the LUMO. The ground state for the analogue iridium cluster is a doublet in which the spin density is quite delocalized with 0.21 *e* on the metal center, 0.29 *e* on the nearest carbon and the rest of the spin density delocalized through the carbon cage in smaller increments. Mulliken population analyses suggest that the electron charge transfer from the metal to the fullerene is somewhat lower than in the platinum analogue.

The substitution of one carbon by one metal does not lead to the same cage deformation as in $C_{58}M$ monoheterofullerenes. In consequence, the SE is reduced considerably more in $C_{59}M$ than in $C_{58}M$. Indeed, for Ir and Os, the SE was computed to be less endothermic when a C atom is substituted rather than a C_2 unit. In this stoichiometry no correlation between the SE, the cage radius and HOMA values is appreciated (compare values in Table 5.7). Table 5.8 shows the decomposition of SE for $C_{59}M$ heterofullerenes. The SE value in this stoichiometry is lower because: (1) the energy required to make the tricoordinated holed C_s-C_{59} fullerene is

Table 5.8 Decomposition of the substitution energy (SE) for $C_{59}M$ (M = Pt, Ir, Os) [a]

		$C_{59}M$ Isomer	Pt C_s	Ir C_s	Os C_s
ΔE_{HOLE} [b]			16.85	16.85	16.85
IBE [c]	ΔE_{DE} [d]	C_{59}	–0.47	–0.19	0.01
		C	–1.27	–1.27	–1.27
		M	0.49	1.36	2.40
		Total	–1.25	–0.10	1.14
	ΔE_{INT} [e]	ΔE_{ST}	14.78	20.30	24.22
		ΔE_{ORB}	–24.18	–33.54	–38.75
		Total	–9.40	–13.24	–14.53
	Total		–10.65	–13.34	–13.39
SE [a]			6.20	3.51	3.46

[a] Energy in eV. The SE is defined as the energy reaction of the process $C_{60} + M \rightarrow C_{59}M + C$. This energy can be dived into several contributions, $SE = \Delta E_{HOLE} + IBE$. [b] ΔE_{HOLE} accounts for the energy reaction of the process $C_{60} \rightarrow C_{59}^* + C^*$. C_{59}^* with the fixed geometry of free C_{60} and triplet as the most stable electronic state. [c] IBE (insertion binding energy) accounts for the energy reaction of the process $C_{59}^* + C^* + M^* \rightarrow C_{59}M + C$. $IBE = \Delta E_{DE} + \Delta E_{INT}$. [d] ΔE_{DE} accounts for the deformation energy for the three fragments: $C_{59}^* \rightarrow C_{58}$, $C^* \rightarrow C$ and $M \rightarrow M^*$. C_{59} with the fixed geometry found in $C_{59}M$ and a singlet as the most stable electronic state. C and M are calculated at the most stable electronic state (unrestricted) and C* and M* always at restricted electronic state. [e] Finally, ΔE_{INT} accounts for the interaction energy between the fragments C_{59} and M* at the fixed $C_{59}M$ geometry.

substantially lower (ΔE_{HOLE} = 16.85 eV, which is 1.05 eV lower than the energy required to create a holed C_{2v}-C_{58} fullerene) and (2) no deformation energy (ΔE_{DE}) is required to adapt the C_s-C_{59} geometry of C_{60} to the C_s-C_{59} geometry in $C_{59}M$. On the other hand, ΔE_{INT} is less favorable in the tricoordinated Pt than in the tetracoordinated Pt because the overlap between the metal orbitals and the carbon ligand orbitals is less effective. The SE for $C_{59}M$ also follows the same trend for the different metals as $C_{58}M$ does. $C_{59}M$ heterofullerenes (M = Os, Ir) are easier to construct than the $C_{59}Pt$ homologues: 6.20 eV for $C_{59}Pt$, 3.51 eV for $C_{59}Ir$ and 3.46 eV for $C_{59}Os$ are the values for the SE.

Table 5.9 Substitution energy (SE) for cation, neutral and anion C_xM (x = 58, 59; M = Pt, Ir, Os) clusters [a]

Heterofullerene	*M*	*cation*	*neutral*	*anion*
$C_{58}M$ [b]	*Pt*	7.16	7.35	6.57
	Ir	4.94	5.43	4.81
	Os	5.41	5.55	5.08
$C_{59}M$ [c]	*Pt*	5.32	6.20	6.03
	Ir	2.37	3.51	3.27
	Os	2.90	3.46	3.39

[a] Energies in eV. [b] The SE for $C_{58}M$ is defined as the energy reaction of the process $C_{60} + M \rightarrow C_{58}M + C_2$. [c] For $C_{59}M$ is defined as the energy reaction of the process $C_{60} + M \rightarrow C_{59}M + C$. The true atomic groundstate for M and C atoms is used according to reference: Baerends, E. J.; Branchadell, V.; Sodupe, M. *Chem. Phys. Lett.* **1997**, *265*, 481.

5.3.4 Stability of neutral monoheterofullerenes versus cation and anion analogues

At the present level of theory, the BE per atom for C_{60} is 7.36 eV. In general, the C substitution by a metal in the free C_{60} is a highly endothermic process. The SE of a C atom by a Pt atom in C_{60} is computed to be 6.20 eV and the BE per atom for $C_{59}Pt$ is reduced to 7.25 eV. When the metal replaces a 6:6 C_2 bond to give $C_{58}Pt + C_2$, the SE involved is 7.35 eV and the BE per atom is equal to that of the $C_{59}Pt$, 7.25 eV. However, we are also interested in the cation and anion because these monoheterofullerenes are detected via positive or negative ion mode in the mass spectrum studies. The oxidation or reduction of these neutral monoheterofullerenes may seriously affect their stability. The SEs for the cationic, neutral and anionic monoheterofullerenes of $C_{58}M$ and $C_{59}M$ (M = Pt, Ir, Os) are listed in Table 5.9. Independently of the metal, all cations and anions are easier to obtain than their respective neutral monoheterofullerene. The SE is reduced for all cases. Nevertheless, each monoheterofullerene has a different stabilization pattern: $C_{58}M$ follows the trend: anion > cation > neutral while $C_{59}M$ follows the trend: cation > anion > neutral. So the easiest way to obtain $C_{58}M$ and $C_{59}M$ monoheterofullerenes will be in the negative ion mode and the positive ion modes, respectively.

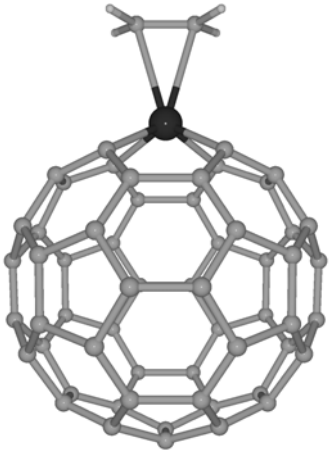

Figure 5.9 Optimized structure for $[C_{58}Ir(C_2H_4)]^-$.

5.4 ADDITION OF ETHYLENE TO MONOHETEROFULLERENES

5.4.1 Experimental evidence

In order to demonstrate that the metals in these newly formed clusters were indeed on the outside of the fullerene, they were exposed to added substrates. Experimentalists have investigated the reactions of these new cluster ions with a potential ligand, 2-butene. The high mass portion of the spectrum acquired upon laser ablation of a $C_{60}/Ir(CO)_2$ film in an atmosphere of 2-butene reveals several new species including: $[C_{59}Ir(2\text{-butene})]^-$, $[C_{58}Ir(2\text{-butene})]^-$, $[C_{57}Ir(2\text{-butene})]^-$ and $[C_{56}Ir(2\text{-butene})]^-$. Clearly, the metal ions in $C_{60-x}Ir^-$ with both x odd and x even can add an external ligand. Similar experiment were carried out with laser ablation of a C_{60}/Pt film in the presence of 2-butene. In this case only one new species, $[C_{57}Pt_2(2\text{-butene})]^-$, was revealed. The ions $C_{58}Pt^-$, $C_{56}Pt^-$, $C_{58}PtO^-$ and $C_{56}PtO^-$ appeared to be unreactive toward the bonding of 2-butene. It is particularly interesting to note that both $C_{58}Ir^-$ and $C_{56}Ir^-$ bind 2-butene while $C_{58}Pt^-$ and $C_{56}Pt^-$ are unreactive under similar conditions. In view of the low reactivity of $C_{58}Pt^-$ and $C_{56}Pt^-$ toward 2-butene, the reactivity of

Table 5.10 Geometric and electronic properties for cation, neutral and anion $C_{58}Ir(C_2H_4)$ and $C_{58}Pt(C_2H_4)$ complexes [a]

Mole.		$[C_{58}M(C_2H_4)]^+$	$C_{58}M(C_2H_4)$	$[C_{58}M(C_2H_4)]^-$
Ir	*M–C (fullerene)* [a]	2.036	2.039	2.038
	M–C	2.749	2.479	2.236
	C–C (ethylene) [b]	1.352	1.373	1.425
	Cage Radius [c]	3.556	3.556	3.559
	Transfer cage $\rightarrow C_2H_4$	–0.316	–0.196	0.138
Pt	*M–C (fullerene)* [d]	2.005	2.009	2.012
	M–C	2.447	2.447	2.435
	C–C (ethylene)	1.371	1.373	1.375
	Cage Radius [e]	3.556	3.557	3.560
	Transfer cage $\rightarrow C_2H_4$	–0.258	–0.166	–0.062

[a] Values in Å. [b] M–C bond lengths for $C_{58}Ir^+$, $C_{58}Ir$ and $C_{58}Ir^-$ are 2.037 Å, 2.033 Å and 2.039 Å, respectively. [b] The C–C distance in the free C_2H_4 molecule is 1.333 Å. [c] The cage radius for $C_{58}Ir^+$, $C_{58}Ir$ and $C_{58}Ir^-$ are 3.554 Å, 3.558 Å and 3.561 Å, respectively. [d] M–C bond lengths for $C_{58}Pt^+$, $C_{58}Pt$ and $C_{58}Pt^-$ are 2.025 Å, 2.016 Å and 2.018 Å, respectively. [e] The cage radius for $C_{58}Pt^+$, $C_{58}Pt$ and $C_{58}Pt^-$ are 3.558 Å, 3.561 Å and 3.564 Å, respectively.

$C_{59}Pt^+$ toward addition was also examined. $C_{59}Pt^+$ adds 2-butene to form $[C_{59}Pt(2\text{-butene})]^+$. Calculations were carried out to analyze the reactivity of cationic, neutral and anionic $C_{58}M$ (M = Pt, Ir) structures with ethylene as a model for 2-butene.

5.4.2 Interaction between ethylene and monoheterofullerenes

Calculations were also carried out to analyze the reactivity of $C_{58}M^-$, $C_{58}M$ and $C_{58}M^+$ (M = Pt, Ir) with 2-butene. To simplify the problem and to save computer time, the 2-butene ligand was modeled as an ethylene molecule. The computed structure of $[C_{58}Ir(C_2H_4)]^-$ is shown in Figure 5.9. The ethylene ligand coordinates to the metal in the C_{2v}-$C_{58}M$ clusters without altering the structure of the fullerene as the values in Table 5.10

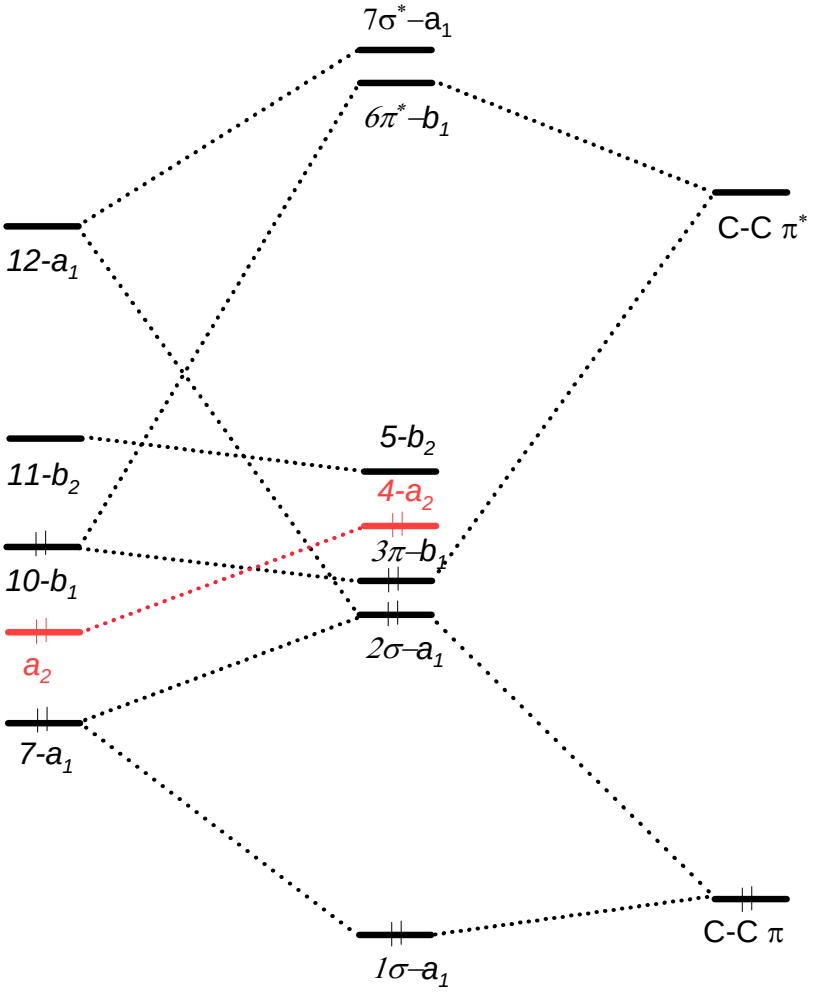

Figure 5.10 Molecular orbital (MO) correlation diagram for the interaction between C_2H_4 ligand (right) and $C_{58}Ir^-$ (left) in order to construct the $[C_{58}Ir(C_2H_4)]^-$ complex (only black lines). The addition of the red lines converts the draw to the MO correlation diagram of $C_{58}Pt(C_2H_4)$ cluster.

show. All the structures were optimized under the C_{2v} symmetry constraints. The process:

(5.3) $C_{58}M + C_2H_4 \rightarrow C_{58}M(C_2H_4)$ (M = Pt or Ir)

is exothermic for neutral, monoanionic and monocationic molecules. The formation energy of $[C_{58}Ir(C_2H_4)]^-$ from $C_{58}M^-$ and C_2H_4 units was computed to be 0.68 eV. This relatively large value is consistent with the experimental observation of a peak in the mass spectrum that may be associated to $[C_{58}Ir(2\text{-butene})]^-$. It is also consistent with a metal-ligand distance of 2.236 Å, which is only somewhat longer than in conventional organometallic iridium complexes, in which the Ir–C bond lengths range between 2.03 and 2.21Å.[27] The energy involved in the formation of the analogous complex of platinum, $[C_{58}Pt(C_2H_4)]^-$, is –0.54 eV. Although $[C_{58}Pt(2\text{-butene})]^-$ was not observed in the laser ablation experiment using a C_{60}/Pt film in the presence of 2-butene, current DFT calculations do not exclude that the $C_{58}Pt^-$ fullerene may coordinate the double C–C bonds through the platinum atom. We also included the neutral and monocationic species in our study because the comparison can be quite useful for understanding the bonding features between both fragments.

The correlation diagram of $[C_{58}Ir(C_2H_4)]^-$ in Figure 5.10 shows the origin of the σ donation and π back-donation interactions between the frontier MOs of C_{2v}-$C_{58}Ir^-$ and those of the C_2H_4 fragment. The MO of C_{2v}-$C_{58}Ir^-$ is a slight variation on the MO of C_{2v}-$C_{58}Pt$ in Figure 5.7 because both molecules are isoelectronic. The σ donation to the empty metal orbitals involves the occupied orbital in C_2H_4 with C–C π character and two metal orbitals of the monoheterofullerene with d_{z2} + *s* character: *7*-a_1 and *12*-a_1. The resulting MOs are two bonding occupied σ MOs (*1*σ-a_1 and *2*σ-a_1) and one highly destabilized unoccupied MO (*7*σ^*-*a1*). The π back-donation mainly involves the C_{2v}-$C_{58}Ir^-$ HOMO (*10*-b_1) and the π^*_{C-C} LUMO of the C_2H_4 ligand. Now, the resulting MOs are the HOMO of the interacted system (*3*π-b_1) and another highly destabilized orbital (*6*π^*-b_1). The LUMO of the final adduct (*5*-b_2) is almost the LUMO of the C_{2v}-$C_{58}Ir^-$ monoheterofullerene (*11*-b_2). The correlation diagram for isoelectronic $C_{58}Pt(C_2H_4)$ differs from this model only in the HOMO designation. The interaction destabilizes the a_2 orbitals and one of them becomes the HOMO of the final adduct (*4*-a_2), thus replacing the π back-donation (*3*π-b_1) in this function. The diagram for the analogue complexes $[C_{58}Ir(C_2H_4)]^+$, $C_{58}Ir(C_2H_4)$, $[C_{58}Pt(C_2H_4)]^+$ and $[C_{58}Pt(C_2H_4)]^-$ is easily constructed by

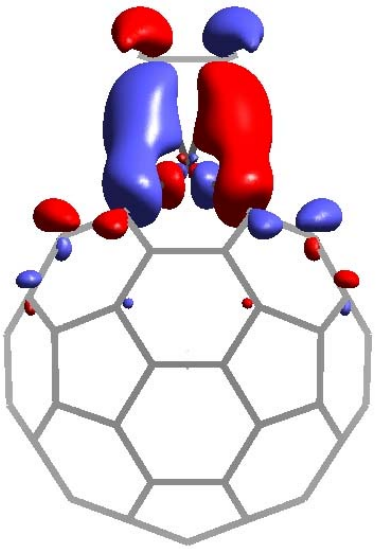

Figure 5.11 3D representation of the HOMO of $[C_{58}Ir(C_2H_4)]^-$, 3π-b_1 in Figure 5.10. The π back-donation orbital from *d* Ir filled orbitals to the empty π *C–C ethylene orbital.

removing or adding electrons from the above mentioned well-known diagrams of $C_{58}Pt(C_2H_4)$ and $[C_{58}Ir(C_2H_4)]^-$.

To characterize the heterofullerene-ethylene bond we used an extension of the Morokuma decomposition scheme developed by Ziegler and Rauk to decompose the BE. According to this scheme, the BE between the fullerene and the ethylene can be decomposed into three main contributions: ΔE_{DE}, ΔE_{ST} and ΔE_{ORB}. More details about this decomposition can be found in subsection 4.2.4. The various terms of the BE partition for the cationic, neutral and anionic complexes $C_{58}M(C_2H_4)$ (M = Ir, Pt) are given in Table 5.11 and Table 5.12. For $C_{58}Ir(C_2H_4)$, the deformation energy (ΔE_{DE}) is only 0.19 eV because the deformation of both cage and ethylene units with respect to the isolated molecules is very small. The Pauli repulsion, 4.76 eV, is larger than the electrostatic term, –3.20 eV, and, therefore, the steric term (ΔE_{ST}) that is the sum of these two contributions is repulsive: +1.56 eV. The orbital term (ΔE_{ORB}), which is –2.16 eV, overcomes the ΔE_{ST} and the ΔE_{DE} of the fragments and is responsible for the adduct formation. The examination of the ΔE_{ORB} values

Table 5.11 Decomposition of the binding energy (BE) for $C_{58}Ir(C_2H_4)$ [a]

		$[C_{58}Ir(C_2H_4)]^+$	$C_{58}Ir(C_2H_4)$	$[C_{58}Ir(C_2H_4)]^-$
ΔE_{DE}	*Cage*	0.04	0.12	0.25
	Ethylene	0.02	0.07	0.40
	Total	0.06	0.19	0.65
ΔE_{ST}	ΔE_{Pauli}	2.06	4.76	9.84
	ΔE_{elstat}	–1.45	–3.20	–6.66
	Total	0.61	1.56	3.18
ΔE_{ORB}	$\Delta E_{a1}(\sigma)$	–0.93	–1.32	–1.96
	ΔE_{a2}	–0.02	–0.03	–0.04
	$\Delta E_{b1}(\pi)$	–0.11	–0.71	–2.32
	ΔE_{b2}	–0.07	–0.10	–0.19
	Total	–1.13	–2.16	–4.51
ΔE_{INT}		–0.52	–0.60	–1.33
BE [b]		–0.46	–0.41	–0.68

[a] Values in eV. [b] The BE is the energy difference between the optimized $C_{58}Ir(C_2H_4)$ adduct and the two relaxed $C_{58}Ir$ and C_2H_4 fragments.

exemplify that the interactions of the a_1 symmetry, which give the σ donation from the π ethylene orbital to the metal orbitals, clearly make the largest contribution to ΔE_{ORB}, –1.32 eV. The contribution associated to the b_1 symmetry, which accounts for the π back-donation, is approximately half this value (–0.71 eV). The other symmetries are almost negligible. In contrast, when the fullerene acts as a ligand in complexes such as (η^2-C_{60})$M(PH_3)_2$ (M = Ni, Pd, Pt), Sgamelloti and co-workers have demonstrated that the π back-donation from the metal to the fullerene is more important than the corresponding ligand to metal σ donation.[28] This idea will be discussed at length in Chapter 6.

The addition of one electron to the single occupied bonding MO of 3π-b_1 symmetry in $C_{58}Ir(C_2H_4)$ shortens the M–ethylene bond lengths from 2.479 Å in the neutral complex to 2.236 Å in the reduced complex. This

shortening is accompanied by a larger deformation of the ethylene fragment, the ΔE_{DE} term increasing to 0.65 eV. The repulsive ΔE_{ST} and ΔE_{ORB} terms also increase after reduction and the total Ir–ethylene BE is greater by 0.27 eV when the π back-donation orbital represented in Figure 5.11 accommodates two electrons. The values in Table 5.11 show that in the anionic $[C_{58}Ir(C_2H_4)]^-$ complex the contribution of b_1 MOs to the ΔE_{ORB} term is larger that of the electron density rearrangement associated with the mixing between a_1 MOs, which suggests that in $[C_{58}Ir(C_2H_4)]^-$ the π back-donation is more important than the σ donation. In the other case, when the only electron of the bonding 3π-b_1 HOMO is removed, the M-ethylene distance lengthen considerably to 2.749 Å in the oxidized complex. However, the lower interaction of both fragments does not drastically reduce BE. This is because ΔE_{INT} is reduced drastically, as expected, from –2.16 eV in the neutral complex to –1.13 eV in the oxidized complex, but the ΔE_{DE} and ΔE_{ST} are also reduced. The final BE is 0.05 eV more stable than in the neutral complex. There is an association between the lower interaction between the two fragments and the shorter C–C distance in the ethylene of the oxidized complex. (1.352 Å, 1.373 Å and 1.425 Å in the $[C_{58}Ir(C_2H_4)]^+$, $[C_{58}Ir(C_2H_4)]$ and $[C_{58}Ir(C_2H_4)]^-$, respectively).

As expected from the isoelectronic nature of $C_{58}Pt(C_2H_4)$ and $[C_{58}Ir(C_2H_4)]^-$, these two complexes have similar BEs (Table 5.11 and Table 5.12). However, in the platinum complex the coordination distance between the ethylene and the transition metal is quite long (2.447 Å). This value is similar to the computed value for the neutral iridium complex. Usually, the Pt(0)–ethylene bond length is close to 2.10 Å,[29] and many theoretical studies have shown that the Pt(0)–ethylene bond in (η^2-CH_2=CH_2)$Pt(PH_3)_2$ is stronger, with dissociation energies (DEs) between 0.87 and 1.21 eV.[30] Therefore one can conclude from present studies that π ligands might coordinate to $C_{58}Pt$ but with an interaction that is weaker than that in the diphenylphosphine complexes. The partitioning energy values for $C_{58}Pt(C_2H_4)$ indicate that the orbital term is clearly dominated by the σ donation, as it is in the neutral Ir-complex. In other words, the ligand→metal σ donation is more effective than the metal→ligand π back-donation at long M–ethylene bond lengths. For an extensive discussion on

Table 5.12 Decomposition of the binding energy (BE) for $C_{58}Pt(C_2H_4)$ [a]

		$[C_{58}Pt(C_2H_4)]^+$	$C_{58}Pt(C_2H_4)$	$[C_{58}Pt(C_2H_4)]^-$
ΔE_{DE}	*Cage*	0.22	0.12	0.16
	Ethylene	0.07	0.07	0.08
	Total	0.29	0.19	0.24
ΔE_{ST}	ΔE_{Pauli}	4.63	4.72	5.17
	ΔE_{elstat}	–3.09	–3.20	–3.43
	Total	1.54	1.52	1.74
ΔE_{ORB}	$\Delta E_{a1}(\sigma)$	–1.73	–1.58	–1.50
	ΔE_{a2}	8.94	–0.02	–0.02
	$\Delta E_{b1}(\pi)$	–9.73	–0.73	–0.88
	ΔE_{b2}	–0.10	–0.09	–0.12
	Total	–2.62	–2.42	–2.52
ΔE_{INT}		–1.08	–0.90	–0.78
BE [b]		–0.79	–0.71	–0.54

[a] Values in eV. [b] The BE is the energy difference between the optimized $C_{58}Pt(C_2H_4)$ adduct and the two relaxed $C_{58}Pt$ and C_2H_4 fragments.

the nature of the bonding in transition metal complexes see the recent review by Frenking and Frölich.[31]

The reduction of the neutral platinum complex to give $[C_{58}Pt(C_2H_4)]^-$ differs from the iridium complex because the added electron goes to a non-bonding MO of b_2 symmetry (*5*-b_2) between the heterofullerene and the ethylene ligand. Consequently, the orbital interaction and the deformation energy of both fragments are not modified significantly. The C–C bond in ethylene remains almost invariant whereas the Pt–ethylene bond increases only slightly (0.012 Å). The smaller BE for the anionic $[C_{58}Pt(C_2H_4)]^-$ cluster can be attributed to an increase in the Pauli repulsion between the ethylene and the negatively charged heterofullerenes, from 4.72 eV in the neutral complex to 5.17 eV in the reduced system. In no way does the oxidation change the geometry of the

$C_{58}Pt(C_2H_4)$ cluster. However, the removal of one electron of *4-a_2* symmetry containing only cage electrons significantly changes the contribution of each irreducible representation of the ΔE_{ORB} term. In conclusion, the BE is favored a little in the oxidation process and the addition of ethylene to $C_{58}Pt^+$ has a value that is 0.08 eV more favorable than the neutral complex.

It is important to mention the inverse order of BE for the interaction of $C_{58}M$ and C_2H_4 fragments in the cationic, neutral and anionic mode of the monoheterofullerene species. For the iridium atom the most favorable interaction will appear between the anionic species whereas for the platinum atom it will appear between the cationic species.

5.5 DIHETEROFULLERENES: $C_{57}Pt_2$, $C_{56}Pt_2$ and $C_{81}Pt_2$

A systematic search of the regioisomers of the heterofullerenes, $C_{57}Pt_2$ and $C_{56}Pt_2$, was made through density functional calculations in order to find the most stable structures. Both heterofullerenes incorporate two metals into the fullerene surface. In the case of $C_{57}Pt_2$ one Pt replaces one C atom of C_{60} and the other Pt replaces a C–C bond, whereas in $C_{56}Pt_2$ each Pt atom replaces one C–C bond. Several geometric factors were studied, three of which have particularly important effects on the relative stability of regioisomers: the Pt–Pt separation, the number of C–C bonds remaining after the substitution and the substituted C–C bond type. All the factors point to the deformation of the fullerene carbon framework as being a general factor that governs the relative stability of the regioisomers. Because of the high number of factors affecting the stability, we used chemometric techniques. Partial Least Squares (PLS) regression was used to establish structure-energy relationships for $C_{57}Pt_2$ and $C_{56}Pt_2$ heterofullerenes. The resulting understanding of the factors that affect the relative isomer stabilities allowed us to predict the stability of larger disubstituted carbon cages, *e.g.* $C_{81}Pt_2$, heterofullerene.

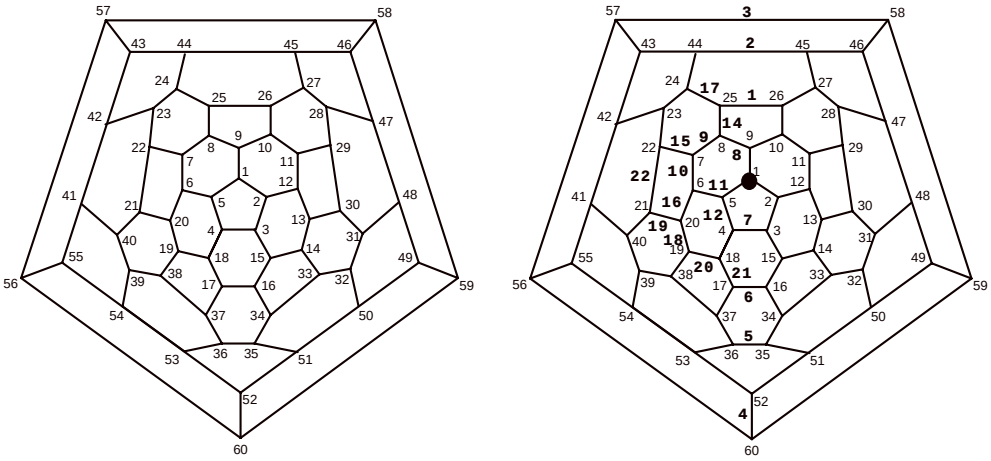

(a) Schlegel diagram of C_{60} (b) Regioisomers of $C_{57}Pt_2$

Figure 5.12 Schlegel diagram showing the numbering system for C_{60} (a) and regioisomers of $C_{57}Pt_2$ (b). The small numbers represent C_{60} numbering. The tricoordinated platinum atom is situated in the black dot. The bigger bold numbers represent the position of the tetracoordinated platinum atom and the regioisomer number. For instance, the regioisomer $C_{57}Pt_2$:**1** is constructed after the substitution of the C1 atom by the first metal and the substitution of C25–C26 bond by the second metal

5.5.1 Regioisomers of $C_{57}Pt_2$

All the carbons in C_{60} are equivalent. As a result, the $C_{59}Pt$ heterofullerene exists as a single isomer with a tricoordinated metal center. The $C_{57}Pt_2$ heterofullerene may be viewed as a derivative of $C_{59}Pt$ in which one of the C–C bonds has been substituted by a second Pt atom. There are 47 different regioisomers for $C_{57}Pt_2$. In these regioisomers one of the Pt atoms is tricoordinated while the other is tetracoordinated. The high number of regioisomers made it necessary to select the isomers to be computed. In the first step, we explored the dependence of the relative stability of the regioisomers on the separation between the two metals. Figure 5.12a shows the numbering system for the carbons in C_{60}. Initially, we consider the series of regioisomers with C_s symmetry [$C_{57}Pt_2$:**1-7**]. In these, one Pt atom replaces the C1 atom and the second Pt atom consecutively replaces the bonds: C25–C26, C44–C45, C57–C58, C52–C60, C35–C36, C16–C17 and

Table 5.13 Description and numbering scheme for regioisomers of $C_{57}Pt_2$

Isomer number	*Symmetry*	*Substituted C–C bonds* [a]	*C–C bond type*
1	*C*s	25,26	6:5
2	*C*s	44,45	6:6
3	*C*s	57,58	6:5
4	*C*s	52,60	6:6
5	*C*s	35,36	6:5
6	*C*s	16,17	6:6
7	*C*s	3,4	6:5
8	C_1	8,9	6:5
9	C_1	7,8	6:6
10	C_1	6,7	6:5
11	C_1	5,6	6:6
12	C_1	4,5	6:5
13	C_1	4,18	6:6
14	C_1	8,25	6:5
15	C_1	7,22	6:5
16	C_1	6,20	6:5
17	C_1	24,25	6:6
18	C_1	19,20	6:6
19	C_1	20,21	6:5
20	C_1	19,20	6:5
21	C_1	17,18	6:5
22	C_1	21,22	6:5

[a] This is the substituted C–C bond which gives a tetracoordinated space to the Pt atom. The tricoordinated Pt atom replaces the C1 atom in all regioisomers.

C3–C4. These regioisomers are represented schematically in the Schlegel diagram of Figure 5.12b as follows: the first Pt atom is represented by a black dot and the second by the position of the isomer number. All the

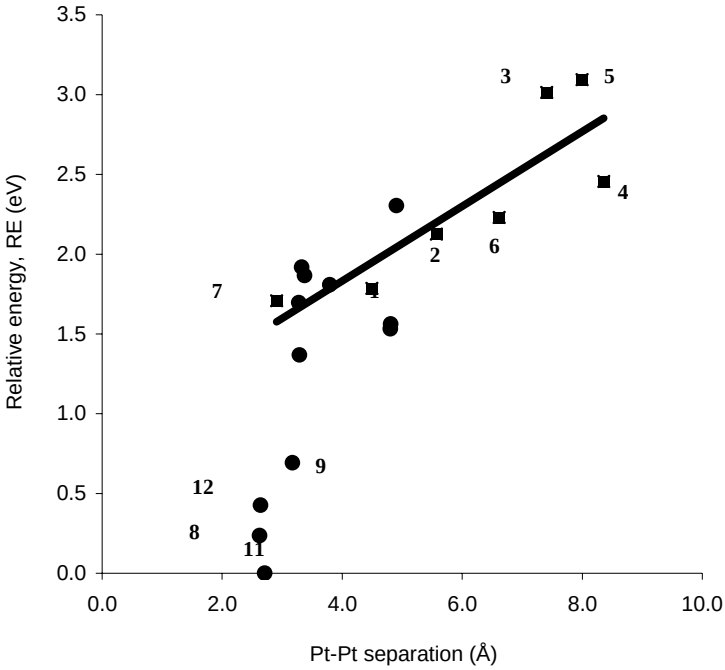

Figure 5.13 Relationship between Pt–Pt separation and stability of the different regioisomers of $C_{57}Pt_2$. The first series of regioisomers, [$C_{57}Pt_2$:**1-7**], are represented by squared dots whereas the rest of regioisomers, [$C_{57}Pt_2$:**8-22**], by circled dots. All regioisomers of the first series are situated in the plot to check the relationship between Pt–Pt separation and isomer stability. $C_{57}Pt_2$:**11** is the most stable regioisomer with Pt–Pt distance of 2.708 Å and the least stable is $C_{57}Pt_2$:**5** with 7.998 Å between both metals. The linear correlation is done with the values of regioisomers [$C_{57}Pt_2$:**1-7**]. Pt–Pt separation and relative energies (REs) for all regioisomers of $C_{57}Pt_2$ are listed in Table 5.17.

regioisomers of $C_{57}Pt_2$ are also tabulated with symmetry, the substituted C–C bond and the C–C bond type in Table 5.13.

Figure 5.13 shows the computed relative energies (RE) of these regioisomers plotted against the Pt–Pt separation in each isomer. The squared dots in Figure 5.13 represent the initial set of seven regioisomers with C_s symmetry. These data show that there is dependence between the

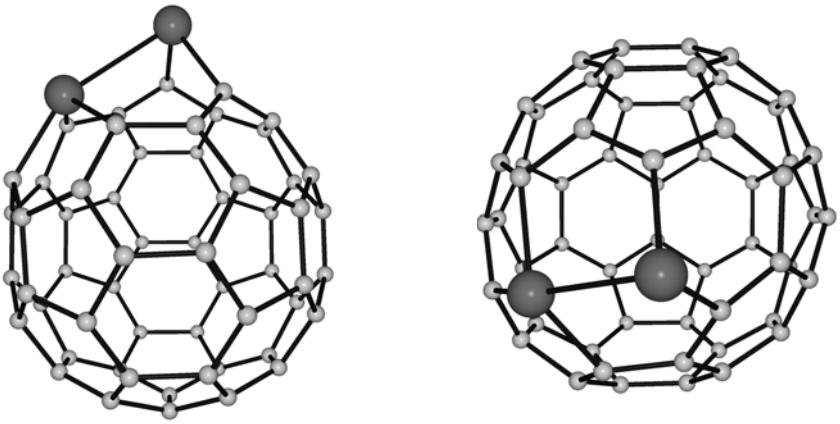

Figure 5.14 Different views of the optimized structure of the most stable $C_{57}Pt_2$:**11** regioisomer.

separation of the heteroatoms and the isomer stability. For example, [$C_{57}Pt_2$:**1** and **7**] regioisomers, which have the two Pt atoms in the same hemisphere, are ~0.8–1.4 eV more stable than the regioisomers in which metals are in different hemispheres of the fullerene: [$C_{57}Pt_2$:**3, 4** and **5**]. Semiempirical studies on heterofullerenes $C_{60-x}Y_x$ (Y = N and B, x = 2-8) and $C_{70-x}Y_x$ (Y = N and B, x = 2-10) also found that the stabilities of the regioisomers decrease as the distance between the heteroatoms increases. It is remarkable that this behavior of the heterofullerenes is clearly different from those found in the exohedral metallofullerenes such as $(\eta^2\text{–}C_{60})\{Pt(PH_3)_2\}_2$ where the double metal addition occurs on opposite ends of the fullerene.[32]

In the second step, each of the C–C bonds in the hemisphere where the first substitution occurs were replaced by a second Pt atom leading to [$C_{57}Pt_2$:**8-22**] regioisomers (Figure 5.12b). These regioisomers retain no symmetry elements. The assumption that substitution in neighbouring sites yields stable structures is fully confirmed. The new [$C_{57}Pt_2$:**8, 11** and **12**] regioisomers have the lowest REs. The most stable regioisomer correspond to the substitution of the 6:6 C–C bond nearest to the previously substituted C1 (C6–C5), $C_{57}Pt_2$:**11** regioisomer, whereas the two next regioisomers, [$C_{57}Pt_2$:**8** and **12**], are those corresponding to the substitution of the 6:5 C–C bond nearest to the previously substituted C1, C8–C9 and C4–C5

respectively. All the regioisomers of $C_{57}Pt_2$ are fully described in Table 5.13. In Figure 5.13, the correlation between Pt–Pt separation and the REs of the regioisomers indicates that this separation will be one of the main factors to govern the stability of the different regioisomers. However, there is no direct correlation between the two variables. The relatively short Pt–Pt distances in the three most stable regioisomers (2.708 Å for $C_{57}Pt_2$:**11**, 2.626 Å for $C_{57}Pt_2$:**8** and 2.643 Å for $C_{57}Pt_2$:**12**, Figure 5.13) suggest the presence of some metal-metal interaction (see below in subsection 5.5.4).

The most stable $C_{57}Pt_2$:**11** regioisomer retains the fullerene structure of C_{60} in the unperturbed hemisphere but some changes are necessary in the substituted hemisphere to accommodate the two Pt atoms. Figure 5.14 shows two views of the optimized structure for $C_{57}Pt_2$:**11** regioisomer. Like $C_{59}Pt$, the tricoordinated-type Pt atom with Pt–C bond lengths of 1.956 Å sticks out from the fullerene surface. The Pt–C distance, 2.025 Å, is somewhat longer for the tetracoordinated-type Pt atom which is located in the fullerene surface in the same way as in $C_{58}Pt$. Heteroatoms such as nitrogen or boron, which replace one single carbon, do not cause such important deformation since the B–C (1.54 Å in $C_{59}B$) and N–C (1.44 Å in $C_{59}N$) bond lengths are more similar to the C–C (1.398 Å for 6:6 and 1.453 Å for 6:5) bond lengths than the Pt–C bond lengths are. The position of the tricoordinated-type Pt atom in $C_{57}Pt_2$ heterofullerene is fully comparable to the situation in $C_{59}M$ (M = Fe, Co, Ni, Rh, Ir, Pt). For example, the computed M–C bond lengths are 1.80 Å in $C_{59}Fe$, 1.81 Å in $C_{59}Co$, in 1.83 Å $C_{59}Ni$, 1.93 Å in $C_{59}Rh$, 1.94 Å in $C_{59}Ir$ and 1.97 Å in $C_{59}Pt$. The significant degree of deformation of the carbon cage in $C_{57}Pt_2$: **11** regioisomer can be appreciated in Figure 5.14.

5.5.2 Regioisomers of $C_{56}Pt_2$

We followed a similar strategy to construct the regioisomers of $C_{56}Pt_2$. When two C_2 units are substituted by two metals the number of possible regioisomers is even larger than in the $C_{57}Pt_2$ heterofullerene. Consequently, we began by exploring the dependence of the isomer stability on the separation of the two tetracoordinated-type Pt atoms. The first nine regioisomers [$C_{56}Pt_2$:**1-9**] incorporate both Pt atoms into the main symmetry plane of C_{60}. These nine structures can be formally separated into two

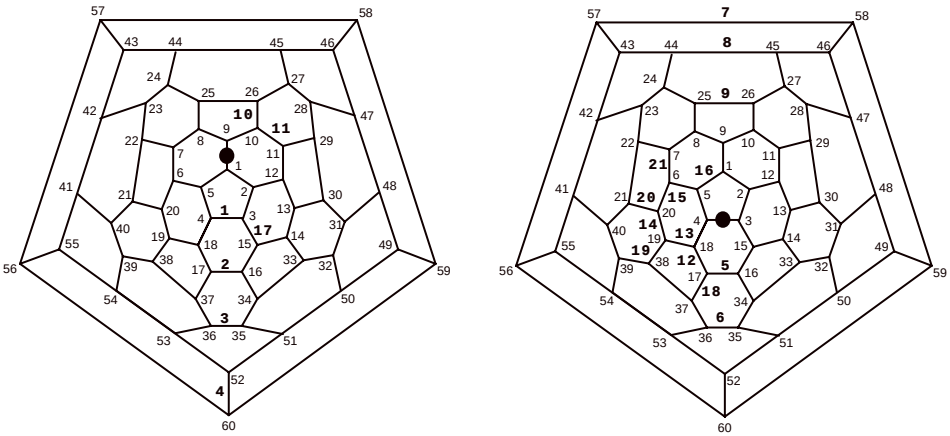

(a) regioisomers of $C_{56}Pt_2$ (b) regioisomers of $C_{56}Pt_2$

Figure 5.15 Schlegel diagram showing the numbering system for regioisomers of $C_{56}Pt_2$. The small numbers represents C_{60} numbering. The first platinum atom is situated in the black dot. In plot on the left (a) the first platinum atom replaces the 6:6 C1–C9 bond whereas in (b) the first platinum atom replaces the 6:5 C3–C4 bond. The bigger bold numbers represent the position of the second metal respect to the first one and also the regioisomer number. For instance, the regioisomer $C_{57}Pt_2$:**10** is constructed after the substitution of the C1–C9 and C10–C26 bonds by two platinum atoms.

subsets: in the first, one Pt replaces the 6:6 C1–C9 bond and a second platinum successively replaces the C_2 units at sites C3–C4, C16–C17, C35–C36 and C52–C60 to produce [$C_{56}Pt_2$:**1-4**] regioisomers. In the second subset, the first heteroatom replaces the 6:5 C3–C4 bond and the second metal successively substitutes the C–C bonds through the symmetry plane without repeating the previous ones to form [$C_{56}Pt_2$:**5-9**] regioisomers. A schematic representation of all these regioisomers is shown in Figure 5.15 and they are fully described in Table 5.14. As in $C_{57}Pt_2$, there is no strict relationship between the Pt–Pt separation and the isomer stability, although in general the destabilization of the cluster increases when the two metals occupy opposite sites in the fullerene. Since the stability of the regioisomers is higher when the two heteroatoms are in the same hemisphere of the fullerene, all the regioisomers of $C_{56}Pt_2$ with a Pt–Pt separation less than 5 Å were constructed and computed. Under this restriction, twelve new additional structures corresponding to substitutions of neighbouring C_2 units

Table 5.14 Description and numbering scheme for regioisomers of $C_{56}Pt_2$

Isomer number	*Symmetry*	*Substituted C–C bonds*	*C–C bond type*
1	C_s	1,9/3,4	6:6/6:5
2	C_s	1,9/16,17	6:6/6:6
3	C_s	1,9/35,36	6:6/6:5
4	D_{2h}	1,9/52,60	6:6/6:6
5	C_s	3,4/17,18	6:5/6:6
6	C_{2v}	3,4/35,36	6:5/6:5
7	C_{2h}	3,4/57,58	6:5/6:5
8	C_s	3,4/44,45	6:5/6:6
9	C_{2v}	3,4/25,26	6:5/6:5
10	C_1	1,9/10,26	6:6/6:5
11	C_s	1,9/10,11	6:6/6:6
12	C_1	3,4/17,18	6:5/6:5
13	C_1	3,4/18,19	6:5/6:5
14	C_1	3,4/19,20	6:5/6:6
15	C_1	3,4/6,20	6:5/6:5
16	C_1	3,4/1,5	6:5/6:5
17	C_s	1,9/3,15	6:6/6:6
18	C_1	3,4/17,37	6:5/6:5
19	C_1	3,4/19,36	6:5/6:5
20	C_s	3,4/20,21	6:5/6:5
21	C_1	3,4/6,7	6:5/6:5

appeared, [$C_{56}Pt_2$:**10-21]** regioisomers, nine of which were non-symmetric structures. The two most stable, [$C_{56}Pt_2$:**10** and **11],** are separated by only 0.037 eV.

Figure 5.16 shows the optimised structure of the most stable $C_{56}Pt_2$:**10** regioisomer. The average Pt–C bond length in $C_{56}Pt_2$:**10** was computed to be 2.042 Å, similar to the Pt–C distances found in the tetracoordinated-type Pt atom of $C_{57}Pt_2$:**11**, 2.025 Å, and $C_{58}Pt$, 2.034 Å. As

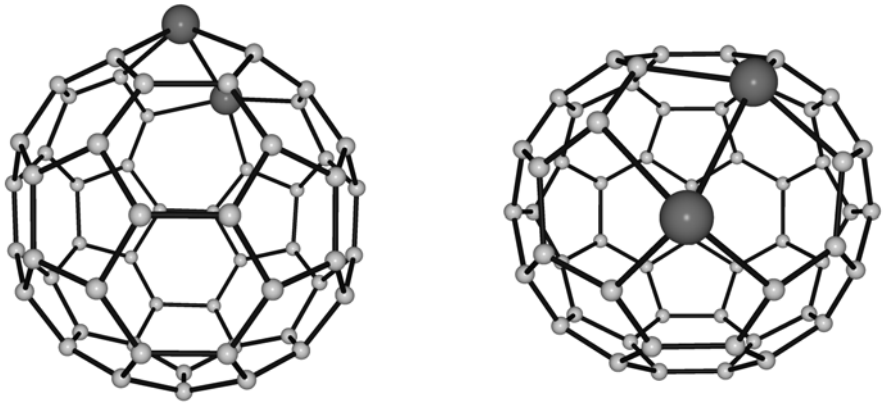

Figure 5.16 Different views of the optimized structure of the most stable $C_{56}Pt_2$:**10** regioisomer.

the views in Figure 5.16 show, the Pt atoms do not protrude far from the fullerene surface. This is also true for the other regioisomers of $C_{56}Pt_2$.

5.5.3 Electronic structure

The SE and BE for mono- and diheterofullerenes are listed in Table 5.15. The values for the monoheterofullerenes were commented in the subsection 5.3.4. When the metal replaces a 6:6 C_2 bond to give $C_{58}Pt + C_2$, the BE involved is 7.35 eV. A subsequent C_2 substitution in $C_{58}Pt$ to give the $C_{56}Pt_2$ diheterofullerene requires a similar amount of energy, more than 6 eV. The analogous process that converts $C_{59}Pt$ to $C_{57}Pt_2$ is less endothermic, 4.88 eV. Hence, in the disubstituted cluster the BE per atom is reduced to −7.16 and −7.19 eV for $C_{56}Pt_2$ and $C_{57}Pt_2$, respectively. Semiempirical studies on B and N heterofullerenes of C_{60} and C_{70}, and DFT calculations on $C_{59}M$ (M = Fe, Co, Ni, Rh) also confirm that when the number of heteroatoms increases the stability is seriously affected.

The ground states of the two most stable regioisomers, [$C_{56}Pt_2$:**10** and **11**], are both singlets with relatively large HOMO-LUMO gaps of *ca.* 0.5 eV. Mulliken charges distinguish the two kinds of metal coordination in $C_{57}Pt_2$:**11**. The net charge for the tricoordinated-type Pt atom is +0.55 *e* whereas for the tetracoordinated-type Pt atoms it is somewhat larger, +0.64 *e*. This trend had already been observed in the $C_{59}Pt$ and $C_{58}Pt$

Table 5.15 Substitution energy (SE) and bonding energy (BE) per atom for mono- and diheterofullerenes [a]

Heterofullerene	*BE* [b]	*Substitution reaction*	*SE* [c]
$C_{59}Pt$	–7.25	$C_{60} + Pt \rightarrow C_{59}Pt + C$	6.20
$C_{58}Pt$	–7.25	$C_{60} + Pt \rightarrow C_{58}Pt + C_2$	7.35
$C_{57}Pt_2$	–7.19	$C_{59}Pt + Pt \rightarrow C_{57}Pt_2 + C_2$	4.88
$C_{56}Pt_2$	–7.16	$C_{58}Pt + Pt \rightarrow C_{56}Pt_2 + C_2$	6.29

[a] Values in eV. [b] BE per atom of the heterofullerene. For C_{60}, the BE was computed to be –7.36 eV. [c] The SE is corrected using the energy of the true atomic groundstate for Pt and C atoms according to reference: Baerends, E. J.; Branchadell, V.; Sodupe, M. *Chem. Phys. Lett.* **1997**, *265*, 481.

monoheterofullerenes: the tetracoordinated Pt atom in $C_{58}Pt$ donates more charge, +0.82 *e*, to the neighbouring C atoms than the tricoordinated Pt atom of $C_{59}Pt$, + 0.76 *e*. The electronic populations of the *s*, *p* and *d* Pt orbitals for the tetracoordinated-type Pt atom of $C_{57}Pt_2$:**11** are 2.66, 6.30 and 8.40 *e*, respectively. These values are quite similar to the electronic populations of the *s*, *p* and *d* Pt orbitals in the tricoordinated-type Pt atoms, 2.65, 6.21, 8.58 *e*, respectively. These values show that Pt donates the electron density through its *d*-orbitals. The Voronoi partition scheme of the electron density suggests that the charge transfer is somewhat greater because this method gives a net charge of +0.95 *e* for the tricoordinated-type Pt atom and +1.10 *e* for the tetracoordinated-type. No significant differences can be seen for the two tetracoordinated-type Pt atoms in the $C_{56}Pt_2$:**10** regioisomer.

As in $C_{59}Pt$ and $C_{58}Pt$, the highest occupied orbitals of $C_{56}Pt_2$:**10** and $C_{57}Pt_2$:**11** regioisomers are formally *d*-metal orbitals. However, in the disubstituted heterofullerenes, the metal-fullerene compounds the *d*-metal orbitals are spread over several molecular orbitals. Specifically, the contribution of the platinum *d* orbitals in $C_{56}Pt_2$:**10** is 26 % in the HOMO and 13 % in the LUMO. For $C_{57}Pt_2$:**11**, the metal contributions to the HOMO and LUMO are 15% and 12%, respectively. Chen and co-workers described these metal-related orbitals for $C_{59}M$ heterofullerenes as defect levels in the C_{60}. This means that heterofullerene orbitals can be seen as the free C_{60} orbitals with a percentage contribution from the metals and, as a result, the electronic structure depends on the incorporated metal.

Nevertheless, it is interesting to note that the energy difference between C-HOMO (the highest carbon-derived occupied orbital) and C-LUMO (the lowest carbon-derived unoccupied orbital) changes very little from one cluster to another and is very close to 1.65 eV, the gap of pure C_{60}. Similar behavior was observed for all the regioisomers of these diheterofullerenes since the C-HOMO/C-LUMO gap appears constant ~1.6 eV.

5.5.4 Metal-metal coupling

The short metal-metal distances found in the most stable regioisomers of $C_{57}Pt_2$ and $C_{56}Pt_2$ heterofullerenes suggest that a significant metal-metal coupling is present. Usually, Pt–Pt bond lengths smaller than 2.6 Å appear in Pt complexes with the metal in low oxidation state. The stabilization produced by the interaction of the two Pt atoms in some heterofullerenes may significantly determine the relative energy of all the regioisomers of $C_{56}Pt_2$ and $C_{57}Pt_2$ heterofullerenes. The mean Pt–Pt distance in the Cambridge Structural Data Base (CSD)[33] for 53 examples, in which Pt atom is tetracoordinated or tricoordinated with a 0 oxidation state, is 2.643 ± 0.045 Å, and the shortest distance is 2.554 Å, which is found in the complex $[Pt_2(\mu\text{-}OPPh_2)(PMePh_2)_2]$ (Refcode JEMLOC [34]). We have regioisomers with a wide range of Pt–Pt distances, from 2.626 Å to 8.358 Å in $C_{57}Pt_2$ and from 2.683 Å to 7.750 Å in the $C_{56}Pt_2$ heterofullerene. The Pt–Pt coupling has been investigated only in the regioisomers with metal-metal distances shorter than 3 Å. The molecular orbital analysis does not make it possible to draw conclusions about the nature of the metal-metal interaction because the Pt *d* orbitals are spread into multiple molecular orbitals. The topological analysis of the total charge density function has proved to be a powerful tool in determining the bonding character in several kinds of bonds.[35] According to the theory of Atoms in Molecules, the presence of a (3,–1) bond critical point (bcp) linking two atoms is a *sufficient* condition for the presence of the bond. Our experience with transition-metal compounds shows that the lack of a bond critical point linking two transition metals does not exclude the existence of metal-metal interactions. For example, a critical point was not detected between the titanium atoms in Ti_8C_{12} but there is a clear metal-metal interaction.[36] On the other hand, the characterization of a bcp between two transition-metal

Table 5.16 Several parameters for determining the bonding character of the platinum-platinum bond

Isomer number	*Pt–Pt* [a]	*Critical point*	*Number of Pt–C bonds* [b]	*Sum of Mulliken net charges of both Pt*
$C_{57}Pt_2$				
8	2.626	(3, –1)	2,3	1.168
12	2.643	(3, –1)	2,3	1.132
11	2.708	(3, –1)	2,3	1.189
7	2.905	(3,1)	3,4	1.608
9	3.171	(3,1)	3,4	1.564
3	7.408	--	3,4	1.588
$C_{56}Pt_2$				
1	2.683	(3,1)	4,4	1.583
16	2.683	[c]	3,3	1.301
5	2.700	(3,1)	4,4	1.583
13	2.714	(3, –1)	3,3	1.240
10	2.739	(3, –1)	3,3	1.249
11	2.836	(3, –1)	3,3	1.162
12	2.847	(3, –1)	3,3	1.124
18	2.856	(3,1)	4,4	1.514
14	2.863	(3,1)	4,4	1.469
15	2.866	(3,1)	4,4	1.526
3	7.071	--	4,4	1.654

[a] Pt–Pt separation in Å. [b] Number of Pt–C bonds with a distance shorter than 2.212 Å. In the regioisomers of $C_{57}Pt_2$, the first number refers to the tricoordinated-type Pt atom and the second number to the tetracoordinated type. In the regioisomers of $C_{56}Pt_2$, both platinum atoms are tetracoordinated. [c] No critical point was localized in regioisomer $C_{56}Pt_2$:**16** but a (3, –1) bcp is expected.

atoms is strong evidence of the coupling. Bonding and charge properties for these regioisomers and some others are given in Table 5.16 for purposes of comparison.

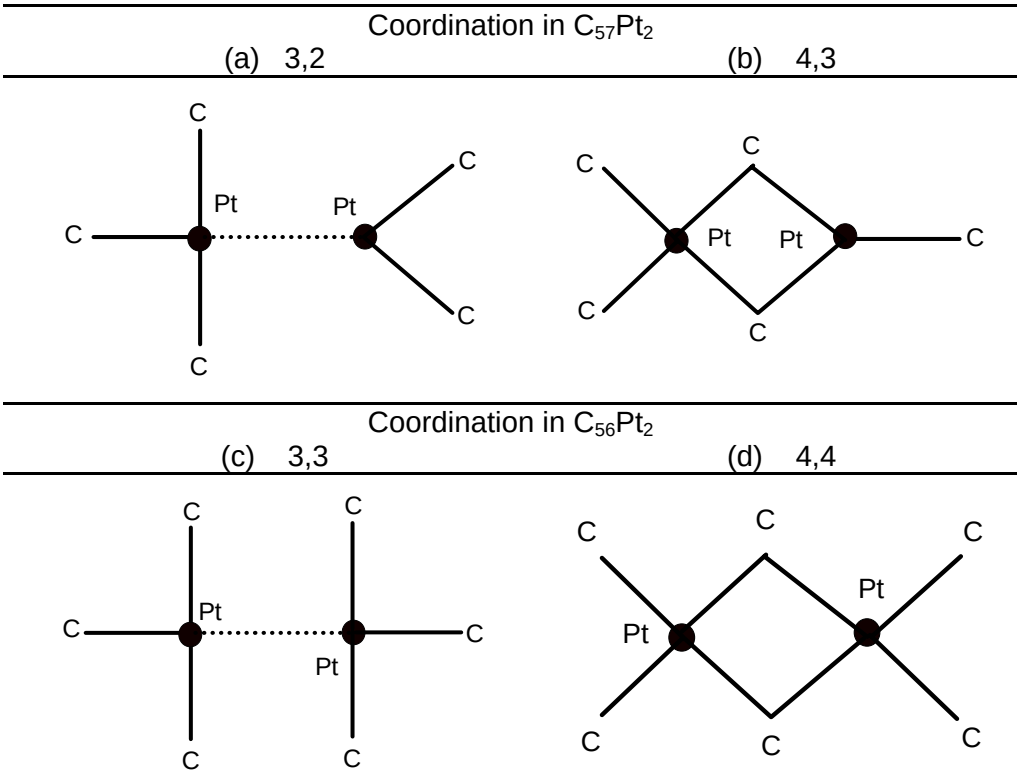

Figure 5.17 Schematic representation of the platinum atoms coordination in regioisomers of $C_{57}Pt_2$ and $C_{56}Pt_2$ that the platinum-platinum distance is lower than 3 Å. Scheme (a) with a platinum surrounded by three carbons and the other by two (3,2) corresponds to regioisomers [$C_{57}Pt_2$:**8**, **11** and **12**] and scheme (b) corresponds to regioisomers [$C_{57}Pt_2$:**7** and **9**]. Scheme (c) and (d) correspond to $C_{56}Pt_2$ heterofullerenes, regioisomers [$C_{56}Pt_2$:**10, 11**, **12** and **13**] and regioisomers [$C_{56}Pt_2$:**1**, **5**, **14**, **15** and **18**], respectively.

In $C_{57}Pt_2$, bonding critical points were found to link the Pt atoms for the three regioisomers with the shortest Pt–Pt separation, [$C_{57}Pt_2$:**8**, **11** and **12**] (Table 5.16). In these clusters, the presence of the bcp coincides with a low Pt coordination number. As seen in Figure 5.17, one of the metals is coordinated to three C atoms and the other to two C atoms (coordination 3,2 in Figure 5.17). In all other regioisomers, the Pt atoms are coordinated to four and three C atoms (coordination 4,3) and the result is the lack of any metal-metal interaction. In $C_{57}Pt_2$:**7** regioisomer, which has a relatively short

Pt–Pt distance of 2.905 Å, a (3,+1) critical point that denotes the absence of metal-metal interaction was found in the region between the two metals. Mulliken net charges can also provide some clues about the metal coupling. According to the sum of net charges of both metals, there are two groups of heteroatoms: one group with a positive charge of +1.2 *e* corresponds to the metals for which a bcp was characterized. In all other isomers the metals have somewhat larger net charges, between +1.5 and +1.6 *e*. The low depopulation of the platinum orbitals in [$C_{57}Pt_2$:**8**, **11** and **12**] regioisomers permits a concentration of the electronic density in the intermetallic region, and this is another indication of a metal-metal interaction in these clusters.

The situation in $C_{56}Pt_2$ is not so simple. There are 10 regioisomers with a Pt–Pt distance shorter than 3 Å. In five of them, [$C_{56}Pt_2$:**10**, **11**, **12**, **13** and **16**], both platinum atoms are surrounded by three C atoms (coordination 3,3 in Figure 5.17), whereas in the other structures the metal is coordinated to four C atoms (coordination 4,4). The presence of a direct Pt–Pt interaction is only expected for coordination 3,3. Indeed, the bcp linking the two Pt atoms is only characterized for isomers with this low coordination, [$C_{56}Pt_2$:**10, 11, 12** and **13**] (Table 5.16). It is worth mentioning that for isomer $C_{56}Pt_2$:**16**, which has a 3,3 coordination and a short Pt–Pt distance of 2.683 Å, it was not possible to characterize the expected bcp, even though an accurate search was made. In all these structures, the Mulliken charges follow the same tendency as that observed for $C_{57}Pt_2$: the group of Pt atoms characterized by a low coordination and by the presence of Pt–Pt interaction produces a smaller charge transfer to the fullerene carbon framework.

5.5.5 Topological and structural factors that govern isomer stability

The substitution of several C atoms in a fullerene produces a high number of possible regioisomers and computations on all of these become unrealistic as the size of the fullerene increases. Therefore, it is necessary to know which factors determine the isomer stability and to have some information about how to search for the most stable structures in any substituted fullerene. Kurita et al.[37] have already pointed out that the electronic properties of $C_{58}X_2$ (X = B, N) largely depend on the relative positions of the heteroatoms in the heterofullerenes. Furthermore, they

presented a systematic search which found the most stable isomer for $C_{58}X_2$ using semiempirical methods.[38] If we know a priori where to look for the most stable structures of heterofullerenes, we will be able to save a huge amount of the computational effort involved in predicting electronic properties.

The most important factors that have an effect on the stability of $C_{57}Pt_2$ and $C_{56}Pt_2$ are listed in Tables 5.17 and 5.18, respectively. We classified them into topological and structural factors. The topological factors are those which provide constitutive information about each regioisomer and can be determined or estimated a priori without any calculation. Topological factors are the Pt–Pt separation, the number of C–C bonds, the substituted C–C bond type and the number of heterorings. These factors are listed in the third to sixth columns in Table 5.17 and 5.18. The structural factors are determined once the geometry of the molecules is fully determined and characterize the geometry of each regioisomer in detail. The structural factors considered here are: cage radius, average bond lengths (Pt–C, 6:6 C–C and 6:5 C–C) and HOMA index (a geometric parameter of aromaticity). These factors are listed in the last five columns of Table 5.17 and 5.18. Below we discuss the topological factors first and then the structural factors.

Pt–Pt separation. The incorporation of one metal in the fullerene cage requires a hole to be made in the carbon cage. When two metals are close together, only one hole is necessary in the dimetallic heterofullerenes and this situation is energetically more favorable than the double perforation of the carbon skeleton that occurs when, for example, the two metals are in different hemispheres. The regioisomers of $C_{57}Pt_2$ with a bonding Pt–Pt distance, [$C_{57}Pt_2$:**8**, **11** and **12**], are the most stable structures whereas the regioisomers with a Pt–Pt separation longer than 5 Å are more than 2 eV less stable (Figure 5.13 and Table 5.17). The longest Pt–Pt separation is found in the $C_{57}Pt_2$:**4** regioisomer, 8.358 Å, which is 2.456 eV less stable than $C_{57}Pt_2$:**11**. For regioisomers of $C_{56}Pt_2$, the correlation is not so high but the Pt–Pt distances of the first seven most stable regioisomers are shorter than 3 Å. Although, a priori, we do not know the exact value of Pt–Pt separation, this factor has been classified as topological due to the fundamental information that it gives about the regioisomers and moreover it can be estimated approximately. In fact, Pt–Pt separation has been the

guide to construct all regioisomers of $C_{57}Pt_2$ and $C_{56}Pt_2$ in the previous sections and it is one of the most important factors affecting the relative stability.

Number of C–C bonds. Not all regioisomers have the same number of C–C and Pt–C bonds. Structures with metal-metal contacts have more C–C bonds, although are correspondingly fewer Pt–C bonds. We have checked that it is preferred to maintain the number of C–C before creating Pt–C bonds. So, all regioisomers of $C_{57}Pt_2$ have 82 C–C bonds and 7 Pt–C bonds except the three most stable ones, [$C_{57}Pt_2$:**8, 11** and **12**], which have 83 C–C bonds, 5 Pt–C bonds and one Pt–Pt bond. Regioisomers of $C_{56}Pt_2$ can be divided into two groups: the group, [$C_{56}Pt_2$:**10**, **11**, **12**, **13** and **16**], has one metal-metal bond, 81 C–C bonds and 6 Pt–C bonds and the rest of the regioisomers have just 80 C–C bonds and 8 Pt–C bonds.

Substituted C–C bonds. Previous calculations for the monosubstituted $C_{58}Pt$ and $C_{58}Ir$ heterofullerenes showed that the substitution of a 6:5 C–C bond by a metal instead of a 6:6 C–C bond is disfavoured by 0.58 eV for Pt and 0.61 eV for Ir. This trend is also found for $C_{57}Pt_2$ and $C_{56}Pt_2$ heterofullerenes. Of the three most stable structures of $C_{57}Pt_2$, [$C_{57}Pt_2$:**8, 11** and **12**] regioisomers, the most stable, $C_{57}Pt_2$:**11**, corresponds to a 6:6 C–C bond substitution. Again, the most stable regioisomers of the group with intermediate relative energy and medium Pt–Pt distance are those with a 6:6 C–C bond substitution, [$C_{57}Pt_2$:**9**, **13**, **17** and **18**] regioisomers. This trend is also observed for the regioisomers with the longest Pt–Pt distances. The most stable are [$C_{57}Pt_2$:**2** and **6**] regioisomers, which Pt atom substitutes a 6:6 C–C bond. $C_{57}Pt_2$:**4** regioisomer is a good example that isomer stability is a compromise of different factors. Following the observed trends, the 6:6 C–C bond substitution stabilizes the isomer, while the large Pt–Pt distance increases instability. As a whole, $C_{57}Pt_2$:**4** is less stable than $C_{57}Pt_2$:**19**, which has a substitution of a 6:5 C–C bond but the distance Pt–Pt is much shorter. In regioisomers of $C_{56}Pt_2$, both platinum atoms are tetracoordinated and come from a C_2 substitution. The second most stable $C_{56}Pt_2$:**11** regioisomer, which is only 0.037 eV higher in energy, has two 6:6 C–C bond type substitutions,

although the most stable regioisomer $C_{56}Pt_2$:**10** has just one 6:6 C–C bond type substitution. Of the group of regioisomers which have only 80 C–C bonds, the most stable are those that have 6:6 C–C bond type substitutions, [$C_{56}Pt_2$:**1, 2, 4, 5, 14** and **17**], and the least stable are those that have only 6:5 C–C bond type substitutions, such as [$C_{56}Pt_2$:**6, 7, 19, 20** and **21**].

Heterorings. The number of rings with a heteroatom incorporated — referred to *heterorings*— is also a topological factor. This parameter gives an indirect measure of the carbon skeleton change and it is closely related to the metal-metal distance. The regioisomers with the fewest heterorings (5 in $C_{57}Pt_2$ and 4 in $C_{56}Pt_2$) tend to have the shortest metal-metal distances and in consequence the lower REs. If both substitutions occur at opposite hemispheres of the fullerene the number of heterorings increases to 7 in $C_{57}Pt_2$ and 8 in $C_{56}Pt_2$ and the destabilization also increases.

Structural factors. The structural factors are obtained after the geometry optimization of each regioisomer. The cage radius characterizes the geometric structure of each regioisomer. At the present level of theory, the cage radius for C_{60}, $C_{59}Pt$, $C_{58}Pt$ and $C_{58}Pt$ is computed to be 3.551 Å, 3.580 Å, 3.562 Å and 3.569 Å, respectively. We obtained a cage radius of around 3.587 Å for $C_{57}Pt_2$:**11** and somewhat smaller for $C_{56}Pt_2$:**10**, 3.575 Å. For structural factors we also took into account the average bond lengths of all Pt–C distances, 6:6 C–C distances and 6:5 C–C distances, because short bond lengths could lead to special stabilization in regioisomers. Finally, our study also includes a structure-based measure of aromaticity: the HOMA index. The HOMA value calculated at the present level of computation for reference systems such as benzene, C_{60}, $C_{59}Pt$, $C_{58}Pt$ and $C_{58}Pt$ were computed to be 0.969, 0.274, 0.268, 0.279 and 0.240, respectively. For purposes of comparison, more HOMA values for polycyclic aromatic hydrocarbons can be found in ref. [39]. The values for the regioisomers of the disubstituted species of C_{60} range between 0.20 and 0.31. The second least stable regioisomer of $C_{56}Pt_2$, $C_{56}Pt_2$:**7**, has the less aromatic HOMA value (0.205) and the second most stable regioisomer, $C_{56}Pt_2$:**11**, has the most aromatic HOMA value (0.310).

Table 5.17 Geometric factors and relative energies (REs) for regioisomers of $C_{57}Pt_2$ [a]

Iso.	*RE*	*Topological factors*				*Structural factors*				
		Pt–Pt	*No. C–C bonds*	*C–C bond type*	*Hete-ro-rings*	*Cage radius*	*Pt–C*	*6:6 C–C*	*6:5 C–C*	*HOMA* [b]
C_{60}		--	90	--	--	3.551	--	1.398	1.453	0.274
$C_{59}Pt$		--	87	--	3	3.580	1.982	1.400	1.452	0.268
$C_{58}Pt$	0.000	--	85	6:6	4	3.562	2.034	1.403	1.451	0.279
	0.630	--	85	6:5	4	3.569	2.031	1.400	1.453	0.240
11	0.000	2.708	83	6:6	5	3.587	1.997	1.400	1.451	0.279
8	0.237	2.626	83	6:5	5	3.592	1.999	1.400	1.452	0.263
12	0.426	2.643	83	6:5	5	3.592	2.007	1.399	1.452	0.259
9	0.692	3.171	82	6:6	6	3.591	2.028	1.400	1.451	0.285
13	1.368	3.289	82	6:6	7	3.598	2.030	1.403	1.451	0.313
17	1.531	4.806	82	6:6	7	3.593	2.025	1.401	1.450	0.287
18	1.562	4.809	82	6:6	7	3.590	2.020	1.403	1.450	0.304
10	1.696	3.280	82	6:5	6	3.595	2.020	1.399	1.452	0.265
7	1.708	2.905	82	6:5	7	3.595	2.005	1.401	1.452	0.237
1	1.787	4.493	82	6:5	7	3.596	2.024	1.399	1.452	0.263
15	1.808	3.792	82	6:5	6	3.606	2.034	1.398	1.452	0.271
14	1.866	3.376	82	6:5	6	3.602	2.024	1.401	1.451	0.283
16	1.917	3.327	82	6:5	6	3.605	2.022	1.402	1.451	0.276
2	2.126	5.566	82	6:6	7	3.590	2.012	1.405	1.450	0.276
6	2.230	6.614	82	6:6	7	3.590	2.012	1.404	1.449	0.284
4	2.456	8.358	82	6:6	7	3.591	2.011	1.405	1.451	0.273
19	2.303	4.903	82	6:5	7	3.598	2.021	1.399	1.450	0.269
21	2.624	4.837	82	6:5	7	3.599	2.019	1.404	1.451	0.271
20	2.765	4.762	82	6:5	7	3.598	2.015	1.401	1.452	0.257
22	2.912	5.193	82	6:5	7	3.600	2.010	1.403	1.452	0.241
3	3.014	7.408	82	6:5	7	3.599	2.012	1.402	1.452	0.238
5	3.094	7.998	82	6:5	7	3.599	2.012	1.402	1.452	0.243

[a] Distances in Å. [b] Taking into account only C–C bonds. For these bonds, calculated with $\alpha = 257.7$ and $R_{opt} = 1.388$ according to reference 24.

Table 5.18 Geometric factors and relative energies (REs) for regioisomers of $C_{56}Pt_2$ [a]

Iso. Num.	*RE*	*Topological factors*				*Structural factors*				
		Pt–Pt	*No. C–C bonds*	*C–C bond type*	*Hetero-rings*	*Cage radius*	*Pt–C*	*6:6 C–C*	*6:5 C–C*	*HOMA* [b]
10	0.000	2.739	81	6:6/6:5	4	3.575	2.042	1.401	1.451	0.287
11	0.037	2.836	81	6:6/6:6	4	3.568	2.046	1.401	1.450	0.310
13	0.200	2.714	81	6:5/6:5	4	3.583	2.041	1.400	1.452	0.278
16	0.789	2.683	81	6:5/6:5	4	3.573	2.010	1.399	1.453	0.230
12	1.083	2.847	81	6:5/6:5	4	3.581	2.032	1.400	1.452	0.288
5	0.123	2.700	80	6:6/6:5	6	3.573	2.042	1.403	1.451	0.296
1	0.911	2.683	80	6:6/6:5	6	3.578	2.058	1.402	1.451	0.298
2	0.943	5.488	80	6:6/6:6	8	3.571	2.038	1.405	1.449	0.310
17	1.048	3.429	80	6:6/6:6	6	3.582	2.054	1.403	1.449	0.304
14	1.123	2.863	80	6:5/6:6	6	3.582	2.074	1.399	1.449	0.318
4	1.267	7.750	80	6:6/6:6	8	3.575	2.038	1.408	1.451	0.281
15	1.584	2.866	80	6:5/6:5	6	3.587	2.066	1.400	1.451	0.300
18	1.589	2.856	80	6:5/6:5	6	3.587	2.068	1.400	1.451	0.294
3	1.776	7.071	80	6:6/6:5	8	3.581	2.036	1.406	1.453	0.247
8	1.887	7.290	80	6:5/6:6	8	3.581	2.036	1.405	1.452	0.241
6	2.152	5.395	80	6:5/6:5	8	3.582	2.038	1.401	1.452	0.238
19	2.156	3.667	80	6:5/6:5	6	3.594	2.051	1.401	1.452	0.243
21	2.271	3.664	80	6:5/6:5	6	3.579	2.050	1.401	1.453	0.231
9	2.399	5.959	80	6:5/6:5	8	3.584	2.034	1.401	1.453	0.214
7	2.481	7.729	80	6:5/6:5	8	3.590	2.033	1.402	1.454	0.205
20	2.723	4.135	80	6:5/6:5	6	3.598	2.059	1.400	1.451	0.268

[a] Distances in Å. [b] Taking into account only C–C bonds. For these bonds, calculated with $\alpha = 257.7$ and $R_{opt} = 1.388$ according to reference 24.

5.5.6 Chemometric study of the structure-energy relationship

Although the analysis of each topological factor and the relative energy showed some relevant trends, the relationship between the structural factors and the stability is less clear. Actually, none of the nine factors by itself can satisfactorily explain the order of the relative energy or the groups of regioisomers observed according to their structure-energy relationship. Hence we decided to investigate the simultaneous (multivariate) relationship among the nine factors and the relative energy using Partial Least Squares (PLS) regression. This multivariate data analysis technique, which has become very popular in chemometrics in the past years,[40] will search for the combinations of the topological/structural factors (*x*-variables) that best explain the relative energy (*y*-variable). Each combination is called a latent variable (LV). The first latent variable (LV1) describes the largest part of the *x*-variables that has the highest correlation with the relative energy. The second latent variable (LV2) describes the largest part of the variability left over by LV1, and so on. The latest latent variables describe non-useful variation and can be discarded. Hence, by considering only the first few latent variables we can study trends between the nine original factors/*x*-variables and the relative energy without being blurred by the redundancy in the data.

The exploratory analysis using PLS regression was first applied to the data in Table 5.17. In order to prepare the data for the analysis, the variable C–C bond type was coded as 1 and 0, corresponding to 6:6 and 6:5 respectively. Then all the *x*-variables were autoscaled so that each variable had the same *a priori* importance in the calculation of the model.

Figure 5.18 shows the two-dimensional biplot (LV1 versus LV2) for regioisomers of $C_{57}Pt_2$. The plot shows 60 % of the original *x*-data, which are correlated to 95% of the *y*-data. This means that 40% of the *x*-data is not relevant for describing the relative energy. Each regioisomer is indicated by a dot. Its position depends on the values of the *x*-variables. Two regioisomers are close to each other when they have similar values of the original *x*-variables. Their separation is large when they have very different values of the *x*-variables. Each *x*-variable is indicated by an arrow, which points to the direction of increasing values of that variable.

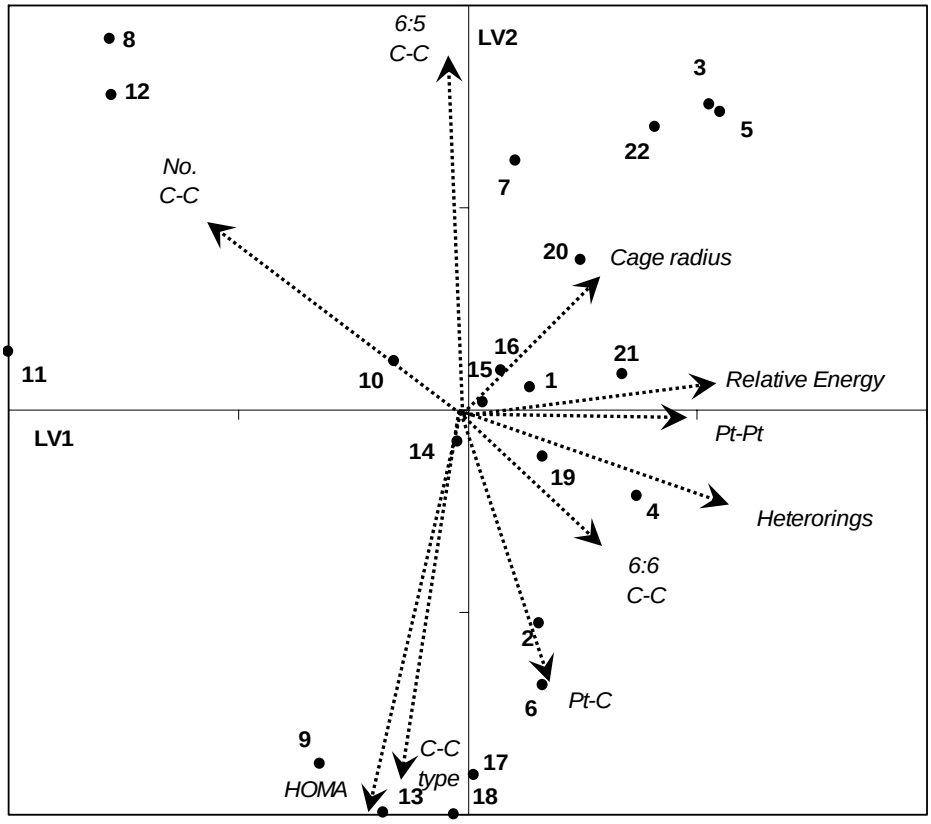

Figure 5.18 *Biplot* for regioisomers of $C_{57}Pt_2$ obtained after PLS regression on the nine factors of Table 5.17. Dots represent regioisomers and arrows represent factors. The plot shows 60 % of the *x*-data, which are correlated to 95 % of the *y*-data.

By considering regioisomers and original variables together, we can visually find similarities and differences among regioisomers and study what variables are responsible for such interdependencies, thus obtaining chemical/structural information. The arrow of the relative energy points in the direction of the positive values of LV1 (abscissa axis). Hence, LV1 discriminates the regioisomers in decreasing order of stability from left to right: [$C_{57}Pt_2$:**8**, **11** and **12**], on the far left, are the most stable and [$C_{57}Pt_2$:**3, 5** and **22**], on the far right, are the least stable. By considering the arrows of

the *x*-variables that are most parallel to LV1, we note that stability is mainly characterized by the combined effect of a short Pt–Pt separation, a small number of heterorings and a large number of retained C–C bonds. [$C_{57}Pt_2$:**8**, **11** and **12**] regioisomers have 83 C–C bonds, 5 heterorings and the shortest Pt–Pt separation. The regioisomers with less C–C bonds, a longer Pt–Pt separation and more heterorings are on the right. The other six variables contribute to the stability to a smaller extend. HOMA, C–C bond type and 6:5 C–C bond lengths are responsible for position of the regioisomers at the top and the bottom of the plot. As we move down-left, the regioisomers have higher aromatic HOMA values, 6:6 C–C substitution and a low 6:5 C–C distance. The combined effect of these three factors also makes the regioisomers more stable. For example, $C_{57}Pt_2$:**11** regioisomer is down-left compared to [$C_{57}Pt_2$:**8** and **12**] regioisomers, which have smaller HOMA values, 6:5 C–C bond substitution and larger 6:5 C–C distances. The same trend can be observed with [$C_{57}Pt_2$:**9**, **13**, **17** and **18**] regioisomers with respect to [$C_{57}Pt_2$:**1**, **7**, **10**, **14**, **15** and **16**], and [$C_{57}Pt_2$:**2**, **4** and **6**] regioisomers with respect to [$C_{57}Pt_2$:**3**, **5**, **19**, **20**, **21** and **22**]. It is a quite important conclusion that will be studied later: the removal of 6:6 C–C bonds affect less the aromaticity of the cage than the removal of 6:5 C–C bonds. As far the cage radius, Pt–C distance and 6:6 C–C bond lengths are concerned, a high value increases instability of the regioisomers. This is to be expected for cage radius since a high value of this parameter indicates more distortion.

The regression coefficients of the PLS model (Table 5.19) give a quantitative measure of the relative importance of each *x*-variable in defining the stability of the regioisomers. A positive sign indicates that an increase in the value of the *x*-variable increases the relative energy. A negative sign indicates the contrary effect. The sign agrees with the trends observed in the biplot. Based on the magnitude of these coefficients we can distinguish three groups.

The largest regression coefficients are those of the topological factors: Pt–Pt separation, the number of heterorings and number of retained C–C bonds. The Pt–C and the 6:5 C–C bond lengths are the two least important factors and the rest of the factors have an intermediate impact on the relative stability in the order: Cage radius > HOMA > 6:6 C–C bond lengths. This result is quite significative, since it suggests that the

Table 5.19 Regression coefficients of PLS model considering two latent variables

Factor		$C_{57}Pt_2$	$C_{56}Pt_2$
Topological	Pt–Pt	0.258	0.150
	No. C–C bonds	–0.218	–0.247
	C–C bond type	–0.134	–0.183
	No. Heterorings	0.258	0.201
Structural	Cage radius	0.179	0.307
	Pt–C	0.024	0.106
	6:6 C–C	0.152	–0.055
	6:5 C–C	0.023	0.104
	HOMA	–0.159	–0.200

topological factors by themselves can almost estimate the relative energy of regioisomers of $C_{57}Pt_2$. Actually we can compare the ability of the PLS model for predicting the relative energy in terms of the average error of the predictions. This value is given by the root mean squared error of prediction (RMSEP) calculated by cross-validation. The model calculated with the nine *x*-variables has a RMSEP of 0.233 eV while the model calculated considering only the four topological factors has a RMSEP of 0.288 eV. This result suggests that considering the remaining factors the prediction is only improved slightly. In both cases, average errors of 0.233 eV or 0.288 eV are low enough compared to the relative energy values range (from 0 to 3.094) to enable trends to be observed just from the predictions using the geometric parameters of the molecule. The accomplishment of the prediction is clearly shown in the plot of DFT calculated versus PLS predicted REs (Figure 5.19).

The PLS analysis was also applied to the $C_{56}Pt_2$ data in Table 5.18. Data were handled as in the PLS analysis of Table 5.17 except that, in this case, the variable C–C bond type was coded as 0, 1 and 2. The biplot is shown in Figure 5.20. The trends observed in the structure-energy relationship are similar to those seen for regioisomers of $C_{57}Pt_2$ although the difference between topological and structural factors is not so marked and the prediction of relative stability for $C_{56}Pt_2$ is less accurated (the PLS model of two latent variables yields a RMSEP of 0.379 eV). The number of C–C bonds, and the number of heterorings are still highly related to the relative energy but, in this case, Pt–Pt distance is not so related to a higher stability

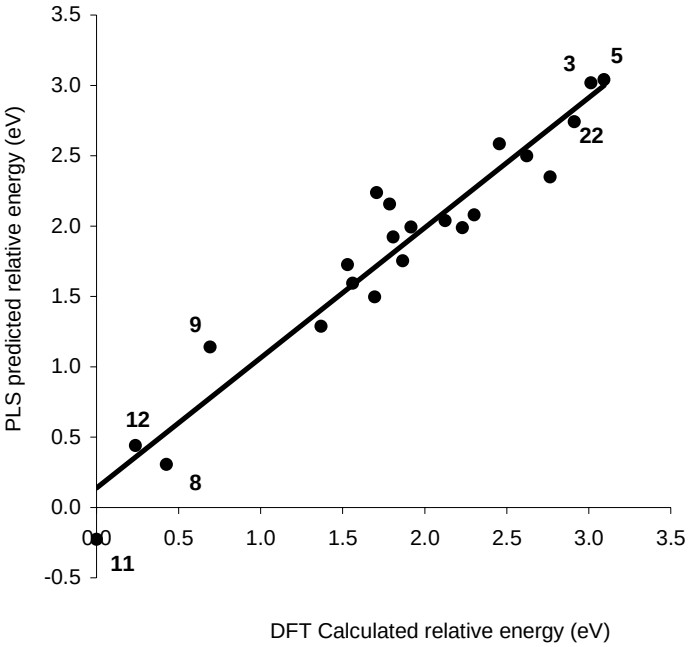

Figure 5.19 DFT calculated versus PLS predicted relative energy (RE) obtained from the PLS regression model on the nine studied factors of $C_{57}Pt_2$. Only the most stable and least stable regioisomers are labeled.

while the cage radius and HOMA confirm their correlation to the stability of heterofullerenes (Table 5.19). We also realise that the Pt–C, 6:6 C–C and 6:5 C–C bond lengths have an ambiguous and weak correlation to the stability of heterofullerenes and thus these factors are not important for describing stability of heterofullerenes. This trend was also found in $C_{57}Pt_2$ analysis.

5.5.7 Stability of the carbon skeleton is the principal factor that determines the isomer stability

Without a doubt, the PLS technique enables us to find structure-energy relationships and it has proved to be valid for analysing multivariate data. Apart from the stabilization produced by the weak metal coupling detected in some regioisomers, the factors that dominate the structure-

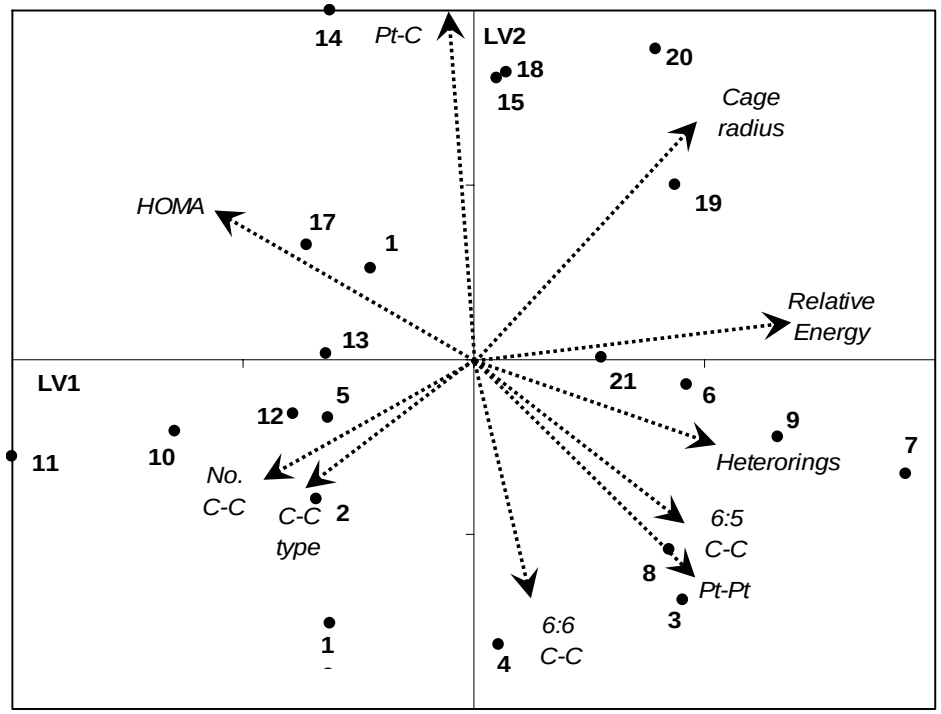

Figure 5.20 *Biplot* for regioisomers of $C_{56}Pt_2$ obtained after PLS regression on the nine factors of Table 5.18. Dots represent regioisomers and arrows represent factors. The plot shows 60 % of the x-data, which are correlated to 86 % of the y-data.

energy relationship are practically independent of the metal. In fact, the relative energy seems to be a measure of the distortion of the cage skeleton from the free equilibrium geometry produced by the inclusion of both metal atoms. So the Pt–Pt separation, the number of C–C bonds, the substituted C–C bond type, the number of heterorings, cage radius, the different bond lengths and the HOMA index are closely related and interdependent because they are all simply indirect measurements of this distortion. To confirm that the REs of the various regioisomers are independent of the metal incorporated, first we changed the number of electrons in several regioisomers of $C_{56}Pt_2$ calculating the cation, $C_{56}Pt_2^+$, and anion, $C_{56}Pt_2^-$ species (Table 5.20). The regioisomers selected for the test are some of the most symmetric regioisomers from the groups with high, [$C_{56}Pt_2$:**10** and **11**],

Table 5.20 Relative energies (REs) for different clusters: $C_{56}Pt_2$, $C_{56}Pt_2^+$, $C_{56}Pt_2^-$, $C_{56}Ti_2$ and C_{56} [a]

Isomer number	$C_{56}Pt_2$	$C_{56}Pt_2^+$	$C_{56}Pt_2^-$	$C_{56}Ti_2$	C_{56}
10	0.00	0.00	0.00	0.00	0.00
11	0.04	–0.09	0.15	0.57	–1.06
2	0.94	1.07	0.75	1.06	2.27
4	1.27	1.27	1.04	1.40	2.58
6	2.15	2.27	2.17	2.35	4.07
9	2.40	2.38	2.57	2.58	4.14
7	2.48	2.59	2.58	3.08	4.25

[a] Values in eV.

intermediate, [$C_{56}Pt_2$: **2** and **4**], and low, [$C_{56}Pt_2$:**6, 7** and **9**], stability. The positive charge is localized basically in both platinum atoms rather than in the fullerene carbon framework: for instance, the sum of the Mulliken net charge of both Pt atoms in $C_{56}Pt_2$:**10** was computed to be 1.249 *e* and in the analogue cation 1.333 *e*. Despite the repulsion between both charges, the relative stability of the various regioisomers does not change (Table 5.20). The anion spreads all the additional charge over the fullerene carbon framework and also retains the relative energy of the neutral platinum analog. Secondly, the incorporation of another metal such as titanium was also tested without changing the order of the relative energy but increasing the REs among regioisomers. A Ti atom behaves like a Pt atom in the $C_{56}Pt_2$ heterofullerene because the computed Ti–C bond length is very similar to Pt–C in $C_{56}M_2$ heterofullerenes, 2.098 Å versus 2.042 Å for $C_{56}M_2$:**10**.

Finally, single point calculations were carried out by extracting Pt atoms from the optimized $C_{56}Pt_2$ structures. In that case we analyse the effect of having a hole in the stabilization of the rest of carbon skeleton. Determining the electronic state of fullerenes with holes is not easy because of the presence of dangling bonds. The lowest electronic state of holed C_{58} fullerene formed from C_{60} by removal of 6:6 C–C bond type is a triplet but when two C_2 units are removed to form C_{56} the singlet competes with the triplet for the most stable electronic state, which is governed by the hole type produced in C_{60}. As can be seen in Table 5.20, the order of the REs of the regioisomers follows the trend of neutral platinum incorporation, which

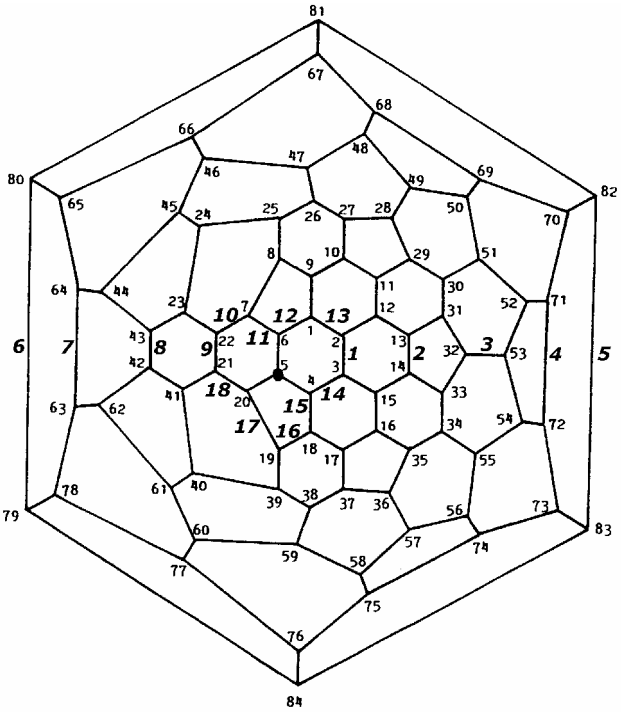

Figure 5.21 Schlegel Diagram showing the numbering system for D_{2d}-C_{84}:**23** fullerene and regioisomers of $C_{81}Pt_2$. See Appendix A.8 for more details in the numbering system of the free D_{2d}-C_{84}:**23**. The small numbers represents C_{84} numbering. At the black dot is situated the tricoordinated-type heteroatom, which substitute the C5 atom. The bigger bold numbers represent the position of the tetracoordinated heteroatom substituting the C–C bond and also the regioisomer number. For instance, the regioisomer $C_{81}Pt_2$:**1** is constructed after the substitution of the C5 atom and C2–C3 bond by two heteroatoms.

confirms the general idea that the most important factor is the destabilization of the carbon cage produced by the incorporation of a metal into the free carbon framework.

*5.5.8 Prediction of isomer stability of $C_{81}Pt_2$, a heterofullerene from D_{2d}-(C_{84}:**23**)*

In the previous sections, we have combined quantum chemistry (DFT) and chemometrics (PLS regression) to analyse and understand the

stabilities of the computed regioisomers of $C_{57}Pt_2$ and $C_{56}Pt_2$. The low prediction error of 0.288 eV for the PLS model of $C_{57}Pt_2$ calculated using only topological factors encouraged us to go further. Since the four topological factors can be estimated a priori, we used PLS regression to predict the stability trends for non-computed structures of the same heterofullerenes or of larger clusters.

In larger fullerenes the complexity may be enormous. Consider for example C_{84}. This fullerene has 24 IPR isomers of which isomer 23 of symmetry D_{2d} has one of the lowest energy similar to those of isomer 22 of symmetry D_2.[41] In this section, we will show that we can use data from heterofullerenes of C_{60} to find relative stabilities for other carbon cages. In particular, we have analysed the substitution of a C_2 unit and a C atom in the D_{2d}-C_{84}:**23** isomer. The resulting $C_{81}Pt_2$ heterofullerene contains a tetracoordinated-type and tricoordinated-type Pt atom which is similar to the situation in $C_{57}Pt_2$. The pyramidalization angle of carbons (θ_p),[42] which is a measure of fullerene sphericity, has not been taken into account in C_{60} because all carbons have the same value however it could be also important. According to Changgeng et al it has an important effect on the regioisomers of $C_{69}M$ –a doped fullerene from C_{70}–, which M replace the most pyramidalized carbon. Pyramidalization angles and bond lengths of all different C–C bonds of D_{2d}-C_{84}:**23** are tabulated in Table 5.21. 18 hypothetical regioisomers of $C_{81}Pt_2$ were built in which the tricoordinated-type heteroatom substitutes the most pyramidalized carbon (C5, θ_p = 10.98°). The second heteroatom substitutes all C–C bonds through the C5–C6 symmetry plane, regioisomers [$C_{81}Pt_2$:**1-9**], and all the C–C bonds which make the Pt–Pt separation less than 3 Å, [$C_{81}Pt_2$:**10-18**] regioisomers (Table 5.21 and Figure 5.21).

The values of the four factors considered for prediction are shown in Table 5.22. Since the geometries were not optimized for regioisomers of $C_{81}Pt_2$, the Pt–Pt separation was estimated from the free C_{60} and C_{84} structures: the tricoordinated heteroatom was placed 0.8 Å above the fullerene surface (like in $C_{59}Pt$) and the tetracoordinated in the middle of the substituted C–C bond. Also for C_{84}, the substituted C–C bond lengths were used instead of C–C bond type due to higher variability in bond lengths in this higher fullerene compared to C_{60}. Because of the different range values of the factors for $C_{57}Pt_2$ and $C_{81}Pt_2$, we could not use the previously

Table 5.21 PLS prediction of isomer stability of $C_{81}Pt_2$, a doped heterofullerene from the D_{2d}-C_{84}:**23** isomer [a]

Iso. Num.	*Subs. C–C bonds* [b]	*Set of C–C bond* [c]	*Pred. RE* [d]	*Calc. RE* [e]	*Pt–Pt* [f]	*No. C–C bonds*	*C–C bond lengths*	*No. Hetero-rings*
18	20,21	7,22	0.000	0.000	2.280	119	1.416	5
14	3,4	1,2	0.041		2.298	119	1.419	5
17	19,20	7,8	0.117		2.164	119	1.428	5
12	1,6	1,6	0.162		2.192	119	1.431	5
15	4,18	1,9	0.317		2.130	119	1.445	5
11	6,7	5,20	0.434		2.200	119	1.453	5
10	7,22	7,22	1.127	0.583	2.952	118	1.416	6
13	1,2	1,2	1.165		2.959	118	1.419	6
16	18,19	8,9	1.368		2.556	118	1.444	6
8	42,43	32,53	1.665		5.371	118	1.375	7
1	2,3	2,3	1.693		3.008	118	1.461	6
9	21,22	21,22	1.771	1.935	2.975	118	1.468	6
3	32,53	32,53	2.254		7.653	118	1.375	7
6	79,80	5,6	2.629		8.731	118	1.377	7
2	13,14	13,14	2.667	2.250	5.401	118	1.456	7
7	63,64	21,22	3.305		7.304	118	1.468	7
4	71,72	13,14	3.554	2.473	8.839	118	1.456	7
5	82,83	2,3	3.670		9.051	118	1.461	7

[a] Distances in Å and energy in eV. The first Pt atom replaces the most pyramidalized carbon (C5, θ_p = 10.98°) and thus it is tricoordinated. The second Pt atom substitutes a C_2 unit and is consequently the tetracoordinated one. So the $C_{81}Pt_2$ heterofullerene shares the same topology as $C_{57}Pt_2$. [b] The substituted C–C bond. See the Appendix A.8 for the numbering system of D_{2d}-C_{84}:**23**. [c] The C–C bond in the previous column belong to this set of C–C bond. The 18 different set of C–C bonds of D_{2d}-C_{84}:**23** are described in Appendix A.8. [d] Predicted from PLS regression model of the four topological factors of $C_{57}Pt_2$ data. [e] DFT calculated relative energy (cal. RE) [f] Non-optimized Pt–Pt separation. The tricoordinated Pt atom is 0.80 Å above the fullerene surface as Pt is in $C_{59}Pt$ whereas the tetracoordinated Pt atom is in the middle of the substituted C–C bond.

calculated regression model. Hence, a PLS model was calculated again from the $C_{57}Pt_2$ data using a different preprocessing. In this case, the four topological factors of $C_{57}Pt_2$ were range-scaled between 0 and 1. The data in Table 5.22 were scaled so that a variation in the scaled variables of $C_{57}Pt_2$ and Table 5.22 corresponded to the same variation in the original *x*-

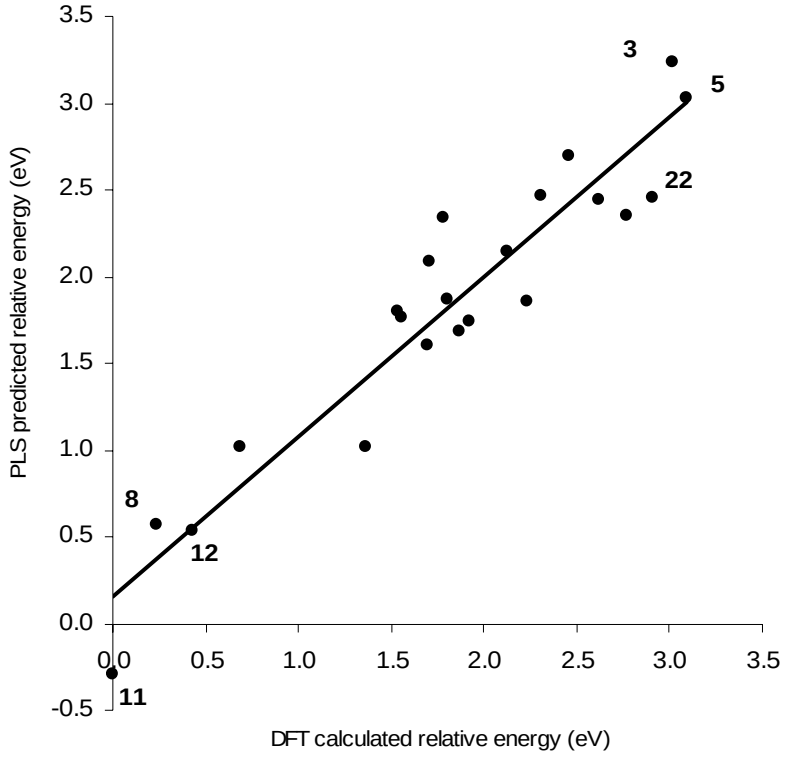

Figure 5.22 DFT calculated versus PLS predicted relative energy (RE) obtained from the PLS regression model on the four topological factors of $C_{57}Pt_2$. Only the most stable and least stable regioisomers are labeled.

variables. The RMSEP of the new PLS model was 0.283 eV, which is similar to the one obtained for autoscaled data hence the different scaling did not reduce the predictive performance of the model. In this case the PLS model represents an 84 % of the original four topological *x*-variables and a 90 % of the relative energy for $C_{57}Pt_2$. The plot of DFT calculated versus PLS predicted REs for this PLS model can be see in Figure 5.22.

The predicted REs are listed in the third column of Table 5.21. Their reliability was tested by comparing the predictions for the representative [$C_{81}Pt_2$:**2**, **4**, **9**, **10** and **18**] regioisomers with the calculated relative energy from the fully optimized DFT geometries. The PLS predicted reliable

relative energy except for $C_{81}Pt_2$:**4** which is the regioisomer with longer Pt–Pt separation and it is an extrapolation for the $C_{57}Pt_2$ PLS model. The mean difference between calculated and predicted for the first three calculated regioisomers was 0.38 eV which is close to the prediction error expected for this model (0.28 eV) so we can consider the PLS predictions as a good indication of the trends in the relative energy to be expected for regioisomers of $C_{81}Pt_2$. All the predictions are consistent with the knowledge acquired about the $C_{56}Pt_2$ and $C_{57}Pt_2$ heterofullerenes. [$C_{81}Pt_2$:**18, 14, 17, 12, 15** and **11**] regioisomers appear as the most stable regioisomers of $C_{81}Pt_2$ because of a short Pt–Pt distance, the high number of retained C–C bonds and fewer heterorings in their structure. Like in $C_{57}Pt_2$ the most stable substitutions are those that distort least the fullerene carbon framework of the D_{2d}-C_{84}:23 fullerene. It is quite probably that the isomer $C_{81}Pt_2$:**18** is not the most stable of all possible structures with formula $C_{81}Pt_2$ but this analysis shows that we have a powerful tool that may help in the study of multiple substitutions in a carbon cage.

5.6 PHYSICAL PROPERTIES

Table 5.23 lists the ionization potentials (IPs) and the electron affinities (EAs) of C_{60}, the monoheterofullerenes C_{2v}-C_{58}M (M = Pt, Ir, Os) and C_{59}M (M = Pt, Ir, Os) and the diheterofullerenes $C_{56}Pt_2$:**10** and $C_{57}Pt_2$:**11** with the corresponding HOMO and LUMO energies. The computed IP and EA of the free C_{60}, 7.56 eV and 2.89 eV, respectively, are in good agreement with the experimental values of 7.6 eV[43] and 2.7 eV[44] estimated from photoelectron spectra. In general, the incorporation of metals in the carbon cage reduces the IP and increases the EA of the cluster. The computed IPs for C_{2v}-C_{58}M were calculated to be 7.37 eV for Pt, 7.06 eV for Ir and 7.41 eV for Os. In the case of C_{59}M, these monoheterofullerenes lose electrons somewhat more readily to form positive ions than C_{2v}-C_{58}M. The EA of C_{60} is increased by doping *ca.* 0.48-0.78 eV for C_{58}M and a little less for C_{59}M (0.09-0.16 eV). Therefore, doping with metals enhanced the redox properties of C_{60}. The changes in the EAs and IPs are easily understood from the relative energies of the HOMO and LUMO. This trend of having somewhat smaller IPs and greater EAs than those of C_{60} has

Table 5.22 Ionization potentials (IPs) and electron affinities (EAs) for several mono- and diheterofullerenes [a]

Molecule	*Sym.*	*IP*	*EA*	*E(HOMO)*	*E(LUMO)*	*HOMO/LUMO gap*
C_{60}	I_h	7.56	2.89	–6.25	–4.59	1.66
$C_{58}Pt$	C_{2v}	7.37	3.67	–5.91	–5.37	0.54
$C_{58}Ir$ [b]	C_{2v}	7.06	3.51	–5.60	–5.26	0.34
$C_{58}Os$	C_{2v}	7.41	3.35	–5.95	–4.96	0.99
$C_{59}Pt$	C_s	6.68	3.05	–5.38	–4.68	0.70
$C_{59}Ir$ [b]	C_s	6.44	3.10	–5.12	–4.82	0.30
$C_{59}Os$	C_s	7.00	2.96	–5.56	–4.64	0.92
$C_{56}Pt_2$:***10***	C_1	7.04	3.64	–5.69	–5.20	0.49
$C_{57}Pt_2$:***11***	C_1	6.78	3.44	–5.53	–5.03	0.50

[a] Values in eV. [b] Energies for the HOMO and LUMO correspond to the energy of the α-single occupied orbital and its β-unoccupied counterpart, respectively.

already been found for Si-,[45] N- and B-doped fullerenes, and metal heterofullerenes such as $C_{59}M$ (M = Fe, Co, Ni and Rh).

For $C_{56}Pt_2$:**10** and $C_{57}Pt_2$:**11** regioisomers, the computed IPs are 7.04 eV and 6.78 eV, respectively, and the corresponding EAs are 3.64 eV and 3.44 eV. Therefore, the incorporation of new metals in the fullerene skeleton of the monoheterofullerenes hardly changes the physical properties of the cluster (Figure 5.23). The same behavior was reported for multiple-substituted $C_{60-x}N_x$ and $C_{60-x}B_x$ heterofullerenes.

5.7 CONCLUDING REMARKS

Mass spectrometric detection. Heterohedral metallofullerenes have only been detected in mass spectrometric studies and so they have not yet been characterized because of the tiny quantities involved. Two main processes have been used to synthesize them. The first method is the photofragmentation of the previously prepared exohedral $C_{60}M_n$ and $C_{70}M_n$ clusters (introduced by Branz). The second alternative route involves the laser ablation of the electrochemically deposited films C_{60}/Pt or C_{60}/Ir(CO)$_2$ (introduced by Balch). Macroscopic synthetic methods have not yet been

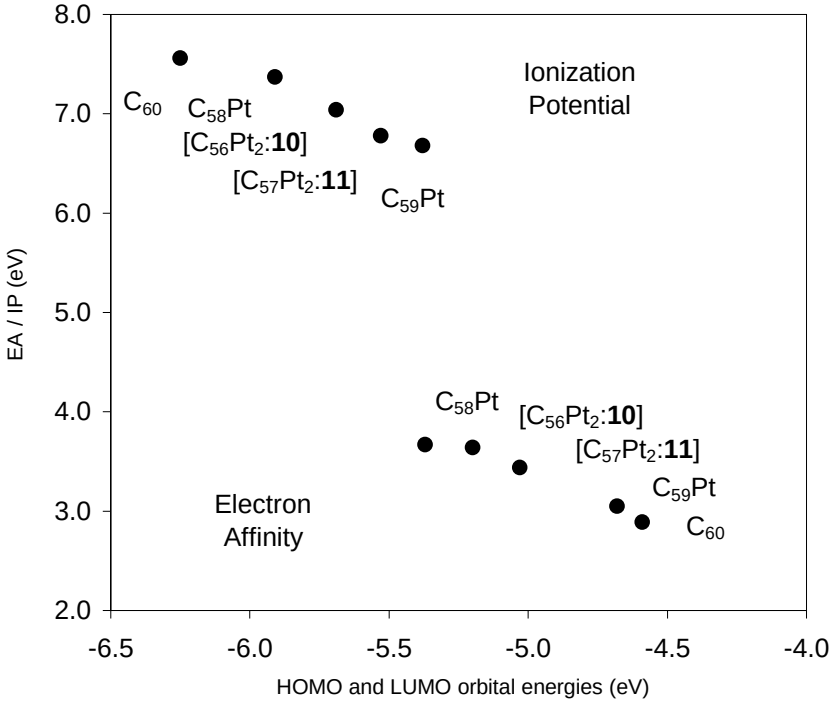

Figure 5.23 Ionizaton potentials (IPs) and electron affinities (EAs) versus HOMO and LUMO energies, respectively, for the free C_{60} and $C_{58}Pt$, $C_{59}Pt$, $C_{56}Pt_2$ and $C_{57}Pt_2$ heterofullerenes.

developed for heterohedral metallofullerenes, although for analogous non-metal heterofullerenes a modified Krästschmer-Huffman process is used satisfactorily. The new metallofullerenes obtained mainly correspond to a C_2 unit or C atom replaced by a metal in C_{60}, yielding the stoichiometries $C_{59}M$ and $C_{58}M$. The diheterofullerenes $C_{57}M_2$ and $C_{56}M_2$ (M = Pt and Ir) are observed when several substitutions occur. A common process observed during the experiments is the successive loss of C_2 units leading to the family of monoheterofullerenes $C_{59-2x}M$ and $C_{58-2x}M$. These last clusters have substantial rearrangements in the fullerene carbon framework, which means that they are more difficult to study than the previous ones.

Geometry and substitution energy (SE). When a metal substitutes a C_2 unit it becomes tetracoordinated. It does not protrude from the fullerene surface but stays within the fullerene carbon framework. This is called substitution energy (SE) which was computed to be 7.35 eV for the most stable isomer of C_{2v}-$C_{58}Pt$, a 6:6 C_2 substitution by a Pt. The other isomer corresponds to a 6:5 C_2 substitution (C_s-$C_{58}Pt$.65), which leads to an isomer that is 0.63 eV less stable. On the other hand, the tricoordinated M atom in $C_{59}M$ protrudes from the fullerene surface because there is not enough space far it to be completely enclosed (SE = 6.20 eV). The SE can be divided into two main contributions: first, the energy necessary to make the hole (hole energy) and, second, the energy involved in inserting the metal into this hole (insertion binding energy, IBE). The hole energy is highly endothermic (17.90 eV for C_{2v}-$C_{58}Pt$ isomer and 19.31 for C_s-$C_{58}Pt$.65) and determines the relative stability of the two isomers. The 6:6 C–C substitution is more favorable than the 6:5 C–C substitution because the former involves the destruction of fewer π C–C bonds. On the other hand, the IBE is an exothermic process that is slightly more favorable for the 6:5 substitution (−10.55 eV for C_{2v}-$C_{58}Pt$ and −11.33 eV for C_s-$C_{58}Pt$). However, the IBE is not capable of overcoming the greater destabilization produced in the 6:5 isomer during the hole-making process.

Metal covalent bond within the fullerene carbon framework. According to the fragment molecular orbital method, the Pt atom in the C_{2v}-$C_{58}Pt$ isomer has 18 electrons involved in the metal-carbon bond (4 σ sp^2, 4 π p_z and 10 *d*-based electrons) in the 0 oxidation state. We have used the D_{4h}-$C_{24}H_{12}Pt$ heterocompound as a feasible model for the C_{2v}-$C_{58}Pt$ monoheterofullerene, which can be taken as a general example of the metal insertion in heterofullerenes. In the D_{4h}-$C_{24}H_{12}Pt$ heterocompound, the metal-carbon bond can be separated into two contributions: σ and π. In general, the metal-carbon bond consists of two σ and two π interactions. The interaction between the sp^2 carbon ligand orbitals of the four dangling C with the d_z^2 and d_{xy} metal orbitals provides the two σ bonds. The π bond is formed through the interaction between the p_z carbon ligand orbitals and the d_{xz} and d_{yz} metal orbitals. The d_{x2-y2} metal orbital has a non-bonding character. These model bonding orbitals are slightly modified in the C_{2v}-$C_{58}M$ heterofullerene in the sense that σ and π molecular orbitals (MOs) are

allowed to mix but they retain all the main bonding characteristics of the MOs described above for the D_{4h}-$C_{24}H_{12}Pt$ heterocompound. To sum up, the highly exothermic and favorable process of the metal insertion, *ca.* –11 eV for 4 Pt–C bonds, is confirmed by the presence of four covalent metal-carbon bonding MOs.

Stability of monoheterofullerenes. $C_{58}M$ and $C_{59}M$ (M = Ir, Os, Ti) exhibit the same inertion pattern as $C_{58}Pt$ and $C_{59}Pt$. The 6:6 C_2 substitution is much easier (*ca.* 0.6 eV for all studied isomers) than the 6:5 C_2 substitution. Another conclusion is that the insertion of larger metals such as Os and Ir is favoured because they cause less cage deformation. The difference between Pt and Os incorporations is of *ca.* 2 eV. Particularly important is the correlation between the geometric parameters (cage radius and HOMA) and the substitution energy (SE): small cage radius and high HOMA values are accompanied by lower SE values, which indicates that the deformation of the cage caused by the metal insertion is essential to the stabilization of the heterofullerenes. As expected, the substitution of one C atom by a metal is a little bit more favorable (*ca.* 1 eV). It is also important to notice that the SE is significantly reduced when the cation or anion of these heterofullerenes is used, thus facilitating the formation process.

Ethylene addition, a proof of heterofullerenes. The experimental detection of substrates such as 2-butene added to the heterofullerenes $C_{58}M$ and $C_{59}M$ has confirmed the heterohedral position of the metal in these metallofullerenes. The ethylene coordinates to the metal without disrupting the fullerene structure at long M–C distances: for example, 2.447 Å for $C_{58}Pt(C_2H_4)$ compared to 2.148 Å for $(\eta^2\text{-}C_2H_4)Pt(PH_3)_2$ complexes. The binding energy (BE) is –0.70 eV for $C_{58}Pt(C_2H_4)$ and the partitioning scheme of the BE indicates that the orbital term is clearly dominated by the σ donation, instead of the π back-donation which occurs in the $(\eta^2\text{-}C_2)Pt(PH_3)_2$ complexes. In other words, the ligand to metal σ donation is more effective than the metal to ligand π back-donation at long M–ethylene distances. The geometry and the BE change significantly for the reduction and oxidation processes of these coordinated heterofullerenes.

Stability of polyheterofullerenes. When two Pt atoms replace two C_2 units, or one C_2 unit and one C atom in C_{60}, a priori, multiple regioisomers are possible. Calculations carried out on numerous regioisomers of $C_{57}Pt_2$ and $C_{56}Pt_2$ clearly show that the metals occupy neighbouring positions in the most stable structures. Metal substitution deforms the fullerene carbon framework and partially destroys the fullerene aromaticity. This is the *key* factor in determining the stability of these disubstituted clusters. Indeed, it is much easier to make a big hole that permits the incorporation of two Pt atoms in the carbon cage than two smaller holes in two opposite sites of the fullerene. The structures with two neighbouring Pt atoms retain the greatest number of C–C bonds; this aspect is another important factor that determines the stability of the cluster. In addition, clusters with short Pt–Pt contacts may contain weak metal-metal interactions, which also favour the stability of the cluster but which are not a fundamental stability element. The 6:6 substitutions are preferred to the 6:5 substitutions, as we have seen in monoheterofullerenes. In our opinion, these results go beyond the particular cases of the $C_{57}Pt_2$ and $C_{56}Pt_2$ regioisomers and we believe that the present conclusions can be extended to any transition metal derivative. Calculations performed on the ionic species of the Pt-derivatives and on some Ti homologues confirm the hypothesis that disubstituted C_{60} fullerenes should contain the heteroatoms in adjacent sites. The behavior of larger fullerenes such as C_{70} should be similar although in this case the curvature of the fullerene could also be important, as previously shown in monosubstituted species.

Chemometric tools. Partial least squares (PLS) was the technique satisfactorily used to analyze the interdependencies among all the factors that govern the stability of these diheterofullerene clusters. We conclude that no factor by itself is capable of explaining the relative stability but that the combination of topological factors such as Pt–Pt separation, number of C–C bonds, substituted C–C bond type and number of heterorings can satisfactorily describe the general trends of the relative stability. Although the curvature and the increase in the cage can affect isomer stability, we have been able to predict the trends of the REs of the regioisomers of $C_{81}Pt_2$, a doped fullerene from the free D_{2d}-C_{84}:**23** fullerene. We used a PLS regression model from the analogous $C_{57}Pt_2$ data to predict the stability of

the $C_{81}Pt_2$ heterofullerene. This is probably our greatest contribution to metallofullerene research.

Physical properties. Doping with metals enhanced the redox properties of C_{60}: smaller ionization potentials and higher electron affinities are found for the heterohedral metallofullerenes. However, the incorporation of new metals in the fullerene skeleton of the monoheterofullerenes hardly changes the physical properties of the clusters.

REFERENCES AND NOTES

[1] Krätschmer, W.; Lamb, L. D.; Fostiropoulos, K.; Huffman, D. *Nature* **1990**, *347*, 354. Muhr, H. J. ; Nesper, R. ; Banhart, F. ; Zwanger, M. *Abstract, International Winterschool on Electronic Properties of Novel Materials : Fullerides and Fullerols*, **1995**, Tyrol.

[2] Clemmer, D. E.; Hunter, J. M.; Shelimov, K.B.; Jarrold, M. F. *Nature* 1994, *372*, 248. Shelimov, K. B.; Clemmer, D. E.; Jarrold, M. F. *J. Phys. Chem.* **1994**, *98*, 12819.

[3] Branz, W.; Billas, I.M. L.; Malinowski, N.; Tast, F.; Heinebrodt, M.; Martin, T. P. *J. Chem. Phys*. **1998**, *109*, 3425.

[4] Billas, I. M. L.; Branz, W.; Malinowski, N.; Tast, F.; Heinebrodt, M.; Martin, T. P.; Massobrio, C.; Boero, M.; Parrinello, M. *NanoStruct. Mat.* **1999**, *12*, 1071.

[5] Poblet, J. M.; Muñoz, J.; Winkler, K.; Cancilla, M.; Hayashi, A.; Lebrilla, C. B.; Balch, A. L. *Chem. Comm.* **1999**, 493.

[6] Balch, A. L.; Costa, D. A.; Winkler, K. *J. Am. Chem. Soc.* **1998**, *120*, 9614.

[7] Hayashi, A.; de Bettencourt-Dias, A; Winkler, K.; Balch, A. L. *J. Mater. Chem.* **2002**, *12*, 2116.

[8] Kong, Q.; Shen, Y.; Zhao, L.; Zhuang, J.; Qian, S.; Li, Y.; Lin, Y.; Cai, R. *J. Chem. Phys.* **2002**, *116*, 128.

[9] Hayashi, A.; Xie, Y.; Poblet, J. M.; Campanera, J. M.; Lebrilla, C. L.; Balch, A. L. *J. Phys. Chem. A* **2004**, *108*, 2192.

[10] Hirsch, A.; Nuber, B. *Acc. Chem. Res*.**1999**, *32*, 795; Chen, Z.; Ma, K.; Chen, L.; Zhao, H.; Pan, Y.; Zhao, X.; Tang, A.; Feng, J. *J. Mol. Struc. (Theochem)* **1998**, *452*, 219.

[11] Chen, Z.; Zhao, X.; Tang, A. *J. Phys. Chem. A* **1999**, *10*3, 10961.

[12] Chen, Z; Reuther, U.; Hirsch, A.; Thiel, W. *J. Phys. Chem A* **2001**, *105*, 8105.

[13] Jiao, H.; Chen, Z.; Hirsch, A.; Thiel, W. *Phys. Chem. Chem. Phys.* **2002**, *4*, 4916.

[14] Turker, L. *J. Mol. Struc. (Theochem)* **2002**, *593*, 149.

[15] Jiao, H.; Chen., Z. Hirsch, A. Thiel, W. *J. Mol. Mod.* **2003**, *9*, 34.
[16] Billas, I. M. L.; Massobrio, C.; Boero, M.; Parrinello, M.; Branz, W.; Tast, F.; Malinowski, N.; Heinebrodt, M.; Martin, T. P. *J. Chem. Phys.* **1999**, *111*, 6787.
[17] Ding, C. G.; Yang, J. L.; Cui, X. Y.; Chan, C. T. *J. Chem. Phys.* **1999**,*111*, 8481.
[18] Ding, C. G.; Yang, J. L.; Han, R.; Wang, K. *Physical Review A* **2001**, *64*, 43201.
[19] Billas, I. M. L.; Massobrio, C.; Boero, M.; Parrinello, M.; Branz, W.; Tast, F.; Malinowski, N.; Heinebrodt, M.; Martin, T. P. *Comput. Mat. Sci.* **2000**, *17*, 191.
[20] Kong, Q.; Zhuang, J.; Xu, J.; Shen, Y., Li, Y. ; Zhao, L.; Cai, R. F. *J. Phys. Chem A* **2003**, 107, 3670.
[21] (a) Ziegler, T.; Rauk, A. *Teor. Chim. Acta* **1977**, *46*, 1. (b) *Inorg. Chem.* **1979**, *18*, 1558.
[22] (a) Morokuma, K. *J. Chem. Phys.* **1971**, *55*, 1236. (b) Kitaura, K.; Morokuma, K. *Int. J. Quantum. Chem.* **1976**, *10*, 325.
[23] Albright, T. A. *Tetrahedron* **1982**, *38*, 1339.
[24] (a) Kruszewski, J.; Krygowski, T. M. *Tetrahedron Lett.* **1972**, *3839*. (b) Krygowski, T. M. *J. Chem. Inf. Comput. Sci.* **1993**, *33*, 70.
[25] Krygowski, T. M.; Cyranski, M. K. *Chem. Rev.* **2001**, *101*, 1385.
[26] Fowler, P.W.; Manoloupoulus, D. E. *An Atlas of Fullerens*, Oxford University Press, Oxford, **1995**.
[27] (a) Restivo, R. J.; Ferguson, G.; Kelly, T. L.; Senoff, C. V. *J. Organomet. Chem*. **1975**, *90*, 101. (b) Koster, R.; Seidel, G.; Kruger, C.; Muller, G.; Jiang, A.; Boese R. *Chem. Ber.* **1989**, *122*, 2075. (c) Lundquist, E. G.; Folting, K.; Huffman, J. C.; Caulton, K. G. *Organometallics* **1990**, *9*, 2254. (d) Wakefield, J. B.; Stryker, J. M. *Organometallics* **1990**, *9*, 2428**.** (e) Einstein, F. W. B.; Yan, X.; Sutton, D. *Chem.Commun.* **1990**, 1466. (f) Lundquist, E. G.; Folting, K.; Streib, W. E.; Huffman, J. C.; Eisenstein, O.; Caulton, K. G. *J. Am. Chem. Soc.* **1990**,*112*, 855. (g) Bell, T. W.; Helliwell, M.; Partridge, M. G.; Perutz, R.N. *Organometallics* **1992**, *11*, 1911. (h) Burger, P.; Bergman, R. G. *J. Am. Chem. Soc.* **1993**, *115*, 10462. (i) Huffer, S.; Wieser, M.; Polborn, K.; Beck, W. *J. Organomet. Chem.* **1994**, *481*, 45. (j) Batchelor, R. J.; Einstein, F. W. B.; Lowe, N. D.; Palm, B. A.; Yan, X.; Sutton, D. *Organometallics* **1994**, *13*, 2041. (k) Cleary,B. P.; Eisenberg, R. *J. Am. Chem. Soc.* **1995**, *117*, 3510. (l) Aizenberg, M.; Milstein, D.; Tulip, T. H. *Organometallics* **1996**, *15*, 4093. (m) Alvarado, Y.; Boutry, O.; Gutierrez, E.; Monge, A.; Nicasio, M. C.; Poveda, M. L.; Perez, P. J. Ruiz, C.; Bianchini, C.; Carmona, E. *Chem. Europ. J.* **1997**, *3*, 860. (n) Antwi-Nsiah, F. H.; Torkelson, J. R.; Cowie, M. *Inorg. Chim. Acta* **1997**, *259*, 213. (o) Gutierrez-Puebla, E.; Monge, A.; Nicasio, M. C.; Perez, P. J.; Poveda, M. I.; Rey, L.; Ruiz, C.; Carmona, E. *Inorg. Chem*. **1998**, *37*, 4538. (p) Slugove, C.; Mereiter, K.; Trofimenko, S.; Carmona, E. *Chem. Commun.*

2000, 121. (q) Wiley, J. S.; Oldham, Jr., W. J.; Heinekey, D. M. *Organometallics*, **2000**, *19*, 1670.
[28] Nunzi, F.; Sgamelloti, A.; Re, N.; Floriani, C. *Organometallics* **2000**, *19*, 1628.
[29] (a) Cheng, P.-T.; Nyburg, S. C. *Can. J. Chem.* **1972**, *50*, 912. (b) Burns, C. J.; Andersen, R. A. *J. Am. Chem. Soc.* **1987**, *109*, 915. (c) Clark, H. C.; Ferguson, G.; Hampden-Smith, M. J.; Kaitner, B.; Ruegger, H. *Polyhedron* **1988**, *7*, 1349. (d) Camalli, M.; Caruso, F.; Chaloupka, S.; Leber, E. M.; Rimml, H.; Venanzi, L. M. *Helv. Chim. Acta* **1990**, *73*, 2263. (e) Mole, L.; Spencer, J. L.; Carr, N.; Orpen, A. G. *Organometallics* **1991**, *10*, 49. (f) Fulwood, R.; Parker, D.; Ferguson, G.; Kaltner, B. *J. Organomet. Chem.* **1991**, *419*, 269. (g) Baker, M. J.; Harrison, K. N.; Orpen, A. G.; Pringle, P. G.; Shaw, G. *J. Chem. Soc., Dalton Trans.* **1992**, 2607.
[30] Dedieu, A *Chem. Rev.* **2000**, *100*, 543.
[31] Frenking, G.; Frölich, N. *Chem.Rev.* **2000**, *100*, 717.
[32] (a) Fagan P. J.; Calabrese, J. C.; Malone, B. *J. Am. Chem. Soc.* **1991**, *113*, 9408. (b) Fagan, P. J.; Calabrese, J. C.; Malone, B. *Acc. Chem. Res.* **1992**, *25*, 134. (c) Balch, A. L.; Lee, J. W.; Noll, B. C.; Olmstead, M. M. *J. Am. Chem. Soc.* **1992**, *114*, 10984. (d) Bo, C.; Costas, M.; Poblet, J. M. *J. Phys. Chem*. **1995**, *99*, 5914.
[33] Allen, F. H. *Acta Crystallogr.* **B58**, 380-388, 2002.
[34] Alcock, N. W.; Bergamini, P.; Gomes-Carniero, T. M.; Jackson, R. D.; Nicholls, J.; Orpen, A. G.; Pringle, P. G.; Sostero, S.; Traverso, O. *J. Chem. Soc., Chem.Commun.* **1990**, *4*, 980.
[35] (a) Bader, R. W. F. Atoms in Molecules, A Quantum Theory, Clarendon Press: Oxford, U.K., **1990**. (b) Bader, R. W. F., MacDougall, P. J.; Lau, C. D. H. *J. Am. Chem. Soc.* **1984**, *106*, 1594.
[36] Bénard, M.: Rohmer, M. M.; Poblet, J. M. *Chem. Soc. Rev.* **2000**, *100*, 495.
[37] (a) Kurita, N.; Kobayashi, K.; Kumabora, H.; Tago, K. *Phys. Rev. B* **1993**, *48*, 4850. (b) Kurita, N.; Kobayashi, K.; Kumabora, H.; Tago, Ozawa, K. *Chem. Phys. Lett.* **1992**, *198*, 95. (c) Kurita, N.; Kobayashi, K.; Kumabora, H.; Tago, K. *Fullerene Sci. Technol.* **1993**, *1*, 319.
[38] Chen, Z.; Ma, K.; Pan, Y.; Zhao, X.; Tang, A.; Feng, J. *J. Chem. Soc., Faraday Trans.* **1998**, *94*, 2269.
[39] (a) Poater, J.; Fradera, X.; Duran, M.; Solà, M. *Chem. Eur. J.* **2003**, *9*, 5. (b) Poater, J.; Fradera, X.; Duran, M.; Solà, M. *Chem. Eur. J.* **2003**, *9*, 2.
[40] Massart, D. L.; Vandeginste, B. G. M.; Buydens, L. M. C.; De Jong, S.; Lewi, P. J.; Smeyers-Verbeke, J. *Handbook of Chemometrics and Qualimetrics*; Elsevier Science: Amsterdam, 1998; Parts A and B.
[41] (a) Fowler, P. W.; Manolopoulos, D. E. *An Atlas of Fullerenes*, Oxford, **1995**. (b) Zhang, B. L.; Wang, C. Z.; Ho, K. M. *J. Chem. Phys.* **1992**, *96*, 7183. (c) Wang,

X. Q.; Wang, C. Z.; Zhang, B. L.; Ho, K. M. *Phys. Rev. Lett.* **1992**, *69*, 69. (d) Wang, X. Q.; Wang, C. Z.; Zhang, B. L.; Ho, K. M. *Chem. Phys. Lett.* **1993**, *207*, 349.

[42] (a) Haddon, R. C.; Scott, L. T. *Pure Appl. Chem.* **1986**, *58*, 137. (b) Haddon, R. C. *J. Am. Chem. Soc.* **1986**, *108*, 2837. (c) Haddon, R. C.; Chow, S. Y. *J. Am. Chem. Soc.* **1998**, *120*, 10494.

[43] Lichtenberger, D. L.; Nebesny, K. W.; Ray, C. D.; Huffman, D. R.; Lamb, L. D. *Chem. Phys. Lett.* **1991**, 176, 203.

[44] Yang, S. H.; Pettiette, C. L.; Concienciao, J.; Cheshnowsky, O. ; Smalley, R.E. *Chem. Phys. Lett.* **1991**, *139*, 233.

[45] Lu, J.; Luo, Y.; Huang, Y.; Zhang, X.; Zhao, X. *Solid State Comm.* **2001**, *118*, 309.

CHAPTER 6

$M(PH_3)_2$ EXOHEDRAL METALLOFULLERENES

Since organometallic complexes of fullerenes were first prepared, many transition metals exohedral to the fullerene cages have been synthesized and structurally characterized. They are known as exohedral metallofullerenes. The first well-defined transition-metal derivative of C_{60}, $C_{60}(t\text{-}BuC_5H_5N)_2OsO_4$, was reported by Hawkins in 1991. Subsequently, a variety of exohedral metallofullerenes were synthesized because they are easy to make, isolate and characterize. Theoreticians have made numerous calculations to fit the geometry, and explain the isomerism and the addition patterns. So, unlike the two previous metallofullerenes, these fullerenes have already been studied by many researchers. We shall do our best not to be repetitive. We focus on making reliable calculations with basis set superposition error (BSSE) corrections for $M(PH_3)_2$ (M = Pt, Pd, Ni) units added to C_{60}, C_{70} and higher fullerenes such as C_{84} isomers. We also discuss aspects that have not been fully solved before such as (1) the pyramidalization effect on the strength of the fullerene-metal bond and (2) the prediction of the most reactive site of each fullerene from the characteristics of the C–C bonds.

After an introduction to previous experimental and theoretical work (section 6.1), the nature of the fullerene-metal interactions is explored through the Dewar-Chatt-Duncanson model (section 6.2). In section 6.3 we perform calculations with a large basis set to obtain reliable fullerene-metal binding energies (BE). We use additional calculations with several alternative strategies to reduce the computational effort when much higher systems

*need to be calculated. The basis sets need not be of such good quality to fit the geometry well, although they must be relatively large if the BE are to be reliable. Section 6.4 studies the addition of multiple metal units $M(PH_3)_2$ (M = Pt, Pd, Ni) to the C_{60} surface. The pyramidalization angle (θ_p) of carbons is introduced as a valuable parameter for determining the stability of the final complexes. Complementary calculations are performed on C_{70}, D_{2d}-C_{84}:**23** and D_2-C_{84}:**22** fullerenes in order to determine the relationship between curvature, C–C bond type and the strength of the fullerene-metal bond (section 6.5). The BE between the $Pt(PH_3)_2$ unit and the fullerene is almost independent of the cage size and the number of metals coordinated to the fullerene surface. Contrarily, the curvature and C–C bond type are fundamental for the strength of the coordination bond. Finally, we analyze the correlation between the characteristics of the reactive C–C bonds and the strength of the future fullerene-metal (section 6.6). The C–C bonds are characterized by the Mayer bond orders (MBO), the bond lengths and their pyramidalization angles.*

6.1 INTRODUCTION

6.1.1 Experimental part

Organometallic derivatives of fullerenes have been synthesized and structurally characterized since the beginning of fullerene coordination chemistry.[1] Reviews of all the work on the reactivity of fullerenes toward transition metal compounds have already been published.[2] The addition of the $M(PR_3)_2$ (M = Pt, Pd, Ni; R = Et, Ph) units to the most common fullerene, C_{60}, was reported before the additions to other fullerenes.[3,4] With an excess of $M(PEt_3)_4$ the hexaaddition product $(\eta^2\text{-}C_{60})\{M(PEt_3)_2\}_6$ (M = Pt, Pd) was obtained.[5] Monoaddition Vaska-type complexes was also synthesized and characterized for C_{60}[6] and the higher fullerenes C_{70}[7] and C_{84}.[8] Multiple additions are also possible but they often lead to a mixture of products. Nevertheless, some double addition products of C_{60} and C_{70} were well determined: $(\eta^2\text{-}C_{60})\{Ir(CO)Cl(PMe_2Ph)_2\}_2$,[9] $(\eta^2\text{-}C_{60})\{Ir(CO)Cl(PR_3)_2\}_2$ (R = Et, Me)[10] and $(\eta^2\text{-}C_{70})\{Ir(CO)Cl(PMe_2Ph)_2\}_2$.[11] In conclusion, most synthesized exohedral metallofullerenes are based on electron-rich transition metals, such as those in group VIII. In particular, several $(\eta^2\text{-}C_{60})M(PR_3)_2$ complexes of the Ni, Pd and Pt triad with R = Et, Ph were synthesized and the Pd and Pt complexes were structurally characterized. It is important to notice that the reactions which lead to these exohedral complexes are reversible, so, the thermodynamic product is always found.

These exohedral metallofullerenes are synthesized in solution and one of their notable features is the ease with which many of them can be made, and the ready isolation of crystalline derivatives, which can be examined by X-ray crystallography. This technique has been of great value in determining both the structures of the fullerene cages and the location of the metal units. NMR spectroscopic observations that focus for example, on ^{31}P spectra of metals bound to phosphines or ^{13}C spectra of fullerenes have also proven to be useful structural techniques. UV/vis absorption spectra and infrared spectroscopy are also spectroscopic techniques that can be used for characterization.

Although all the carbons in C_{60} are chemically equivalent, two different C–C bond types can be distinguished for the 6:6 and 6:5 ring

junctions: pyracylene and corannulene C–C bond types, respectively (***A*** and ***D*** types in Appendix A.2, respectively). So far, metals have only been attached to electron-rich pyracylene 6:6 C–C bond types. For the multiple metal additions, an extended Hückel analysis of the (η^2-C$_{60}$)Pt(PH$_3$)$_2$ complex revealed a slight preference for the second addition to occur at the opposite 6:6 C–C bond. It was also experimentally corroborated for the double addition of iridium compounds.[12] The hexaaddition derivatives of platinum and palladium have almost T_h symmetry, each one of the metals being bound to a 6:6 C–C bond, as in the (η^2-C$_{60}$){Pt(PPh$_3$)$_2$}$_6$ complex. Only one isomer obeys the isolated pentagon rule (IPR) for the C$_{70}$.[13] This structure, which has a D_{5h} symmetry, has five types of carbons that form nine layers. Eight types of C–C bonds connect these carbons, four of which occur at 6:6 ring junctions: Ca–Cb, Cc–Cc, Ce–Ce and Cd–Ce (Figure 6.1 and Appendix A.4). The first two C–C bonds are pyracylene types while the third is a pyrene type (***A*** and ***C*** types in Appendix A.1). In the (η^2-C$_{70}$)Ir(CO)Cl(PPh$_3$)$_2$ Vaska-type complex the Ca–Cb position is preferred. The reaction of C$_{70}$ with an excess of Ir(CO)Cl(PMe$_2$Ph)$_2$ produced exclusively the (η^2-C$_{70}$)Ir(CO)Cl(PMe$_2$Ph)$_2$, a double addition in two Ca–Cb bonds. Also, the reaction of C$_{70}$ with the (η^2-C$_2$H$_4$)Pt(PPh$_3$)$_2$ led to the four adducts: the (η^2-C$_{70}$){Pt(PPh$_3$)$_2$}$_n$ where n = 1-4. For the tetraaddition complex, the first two additions take place at the Ca–Cb bonds, at opposite ends of the fullerene, whereas the next two additions occur at the Cc–Cc bonds, also on opposite sides of the cage.[14] The structure of the C$_{84}$ fullerene is more complex because it has 24 IPR isomers. It shall therefore be discussed in detail below. Theoretical calculations indicate that isomers **22** and **23** of symmetries D_2 and D_{2d}, respectively, have the lowest energies.[15] Both isomers can be converted into each other through the Stone-Wales transformation.[16] ^{13}C NMR studies on C$_{84}$ confirm the presence of two isomers in a 2:1 mixture favorable to the D_2-C$_{84}$:**22** isomer.[17] However, the X-ray diffraction of the (η^2-C$_{84}$)Ir(CO)Cl(PPh$_3$)$_2$ complex, synthesized from the addition of an excess of Ir(CO)Cl(PPh$_3$)$_2$ to a mixture of C$_{84}$ isomers, showed that the prevalent geometry of the fullerene portion corresponds to the D_{2d}-C$_{84}$:**23** structure, but that the residual presence of organometallic complexes from the other isomer can not be avoided. The D_{2d}-C$_{84}$:**23** isomer has 19 different sets of C–C bonds (Figure

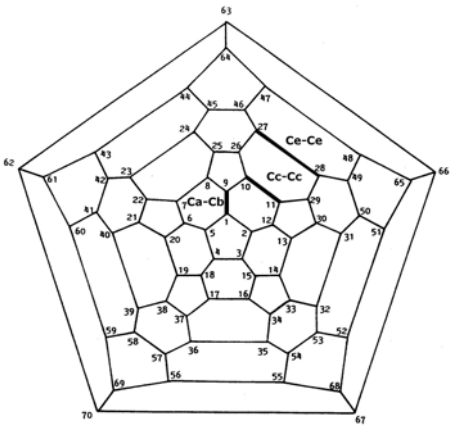

(a) Schlegel diagram of D_{5h}-C_{70}:**1**

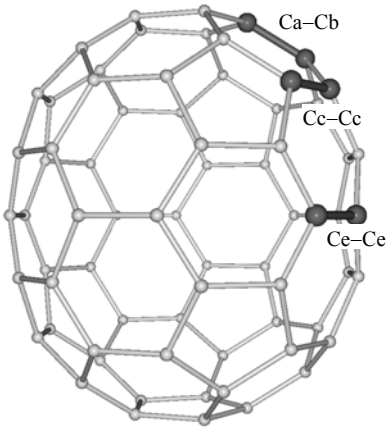

(b) Structure of D_{5h}-C_{70}:**1**

Figure 6.1 Schlegel diagram (a) and molecular structure (b) of the D_{5h}-C_{70}:**1** that incorporate the different set of C–C bonds studied. The D_{5h}-C_{70} molecule is formed by five different carbons situated in nine layers, and eight distinct set of C–C bonds. Of the four 6:6 C–C bond types, Ca–Cb, Cc–Cc, Ce–Ce and Cd–Ce, only two are of pyracylene types (***A*** type), Ca–Cb and Cc–Cc. Ce–Ce is of pyrene type (***C*** type) and Cd–Ce is of ***B*** type (See Appendix A.4). The bold lines show the C–C bonds where the $Pt(PH_3)_2$ units are added. Ca–Cb in (b) is the C1–C9 in (a). Cc–Cc in (b) is the C10–C11 in (a). Ce–Ce in (b) is the C27–C28 in (a).

6.2 and Appendix A.8) whereas the D_2-C_{84}:**22** isomer shows more variability: 32 different sets of C–C bonds (Figure 6.3 and Appendix A.7). According to the X-ray diffraction, Ir atoms are coordinated to C32–C53 bond —a pyracylene type— in the Vaska-type complex abovementioned. Note, that all metal additions in the three free fullerenes take place at pyracylene 6:6 C–C bond types.

6.1.2 Theoretical part

Earlier quantum chemistry calculations at the Hartree-Fock level on (η^2-C_{60})$\{M(PH_3)_2\}_n$ (M = Pd, Pt; n = 1, 2, 6) complexes showed that the hemisphere of the C_{60} cage which is furthest from the platinum coordination is essentially unperturbed by the metal addition.[18,19] The computed

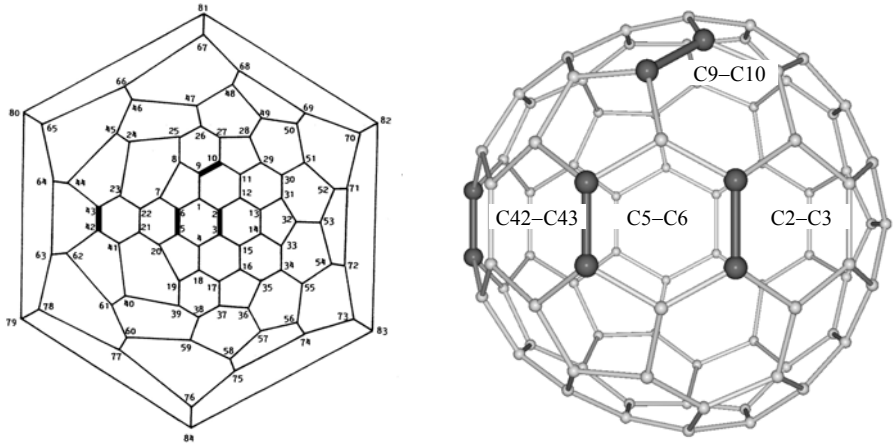

(a) Schlegel diagram of D_{2d}-C_{84}:**23** (b) Structure of D_{2d}-C_{84}:**23**

Figure 6.2 Schlegel diagram (a) and molecular structure (b) of the D_{2d}-C_{84}:**23** isomer that incorporate the different set of C–C bonds studied. We used the same atom numbering outlined in reference 40. Both drawings have the same orientation to facilitate comparison. The bold lines show the C–C bonds which have Pt(PH$_3$)$_2$ units attached.

geometries for these complexes at the HF level are in reasonably good agreement with experimental X-ray data but the calculated binding energies (BE) between the metal and fullerene cages are unreliable at that computational level because the electronic correlation effects are considerable. More recently, Sgamellotti made a detailed analysis of the fullerene-metal bond in the (η^2-C_{60})M(PH$_3$)$_2$ complexes for M = Ni, Pd, Pt.[20,21] Since complex formation causes only a local structural deformation of the fullerene cage, the pyracylene model was proposed for substituting C_{60} in the fullerene-metal interaction. To our knowledge, no quantum chemistry calculations of the organometallic derivatives of higher fullerenes have been reported yet. Dedieu made an in-depth discussion about the DE of the ethylene complexes of Pd and Pt such as (η^2-C_2H_4)M(PR$_3$)$_2$ (M = Pd, Pt).[22] These complexes are experimentally well-known and appear very often as key intermediates in a variety of reactions that are mediated or catalyzed by transition metals.

Litchtenberger systematically examined the bond between a palladium atom or a silver (I) ion and C_{60} at five different sites on the

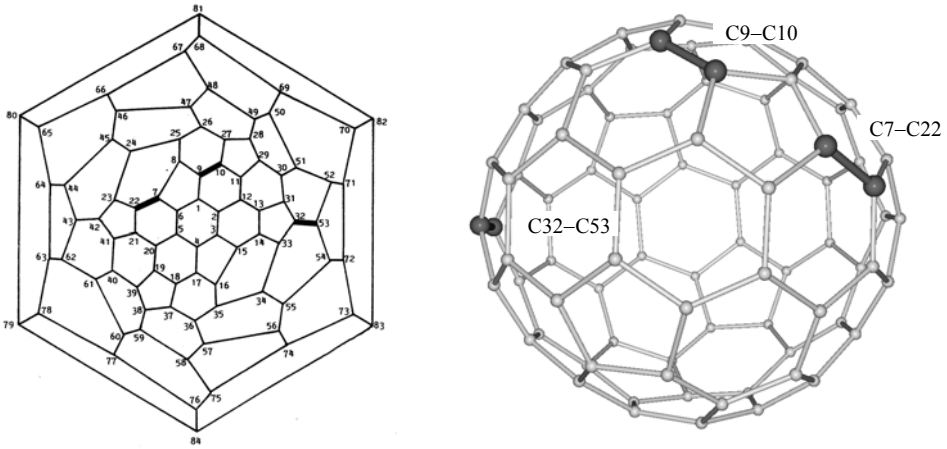

(a) Schlegel diagram of D_2-C_{84}:**22** (b) Structure of D_2-C_{84}:**22**

Figure 6.3 Schlegel diagram (a) and molecular structure (b) of the D_2-C_{84}:**22** isomer that incorporate the different set of C–C bonds studied. We used the same atom numbering outlined in reference 40. Both drawings have the same orientation to facilitate comparison. However, both drawings represent two distinct enantiòmers. This is possible because the D_2-C_{84}:**22** isomer is a chiral molecule. So both drawings are connected symmetrically by a mirror plane. The bold lines show the C–C bonds which have $Pt(PH_3)_2$ units attached.

fullerene surface. He concluded that only η^2 and η^5 coordination are favored but the former is always preferred to the latter.[23] Even so, the transition-metal fragment in most organometallic complexes is bound to the fullerene in a η^2 coordination. Recently calculations carried out at the semiempirical PM3 level on a series of $C_{60}M(C_nH_n)$ and $C_{70}M(C_nH_n)$ complexes have suggested that it is possible to stabilize η^6 coordination complexes of C_{60} and C_{70} using appropriate transition-metal fragments.[24] The interaction between a transition-metal complex and a π system in a η^2 coordination is generally described by the Dewar-Chatt-Duncanson model.[25]

The structures for these addition products suggest that a high fullerene curvature significantly enhances the reactivity of the fullerene, and facilitates the addition of the functional groups. Accordingly, in C_{70}, the metal atom is added to the most pyramidalised carbons and in the organometallic complex the pyramidalization of these atoms increases significantly.[26] The relationship between the local atomic structure and the

chemical reactivity of fullerenes was characterized by Haddon using the pyramidalization angle (θ_p) of carbons.[27] The regiochemistry will be dominated not only by the pyramidalization angles but also by the bond orders and bond lengths. Without doubt a positive correlation between π-bond order and the BE for the complexes is expected.

6.2 COORDINATION BOND BETWEEN THE FULLERENE CAGE AND THE METAL UNIT

6.2.1 Structure of (η^2-C$_{60}$)Pt(PH$_3$)$_2$

The first calculations dealt with (η^2-C$_{60}$)Pt(PH$_3$)$_2$ as a model of the η^2 coordination of the Pt(PPh$_3$)$_2$ unit to the C$_{60}$ fullerene: (η^2-C$_{60}$)Pt(PPh$_3$)$_2$. Ph groups are modelled by hydrogen atoms. This structure was the first transition-metal complex to have direct bonds to C$_{60}$ and also the first of this family of complexes to be determined by X-ray diffraction. So, a full understanding of the metal bond established in the (η^2-C$_{60}$)Pt(PH$_3$)$_2$ complex can be representative of the metal bond in the exohedral metallofullerenes studied in this chapter. The fullerene-metal bond in these transition-metal complexes can also be also easily understood by comparing the bonding characteristics in the analogous complexes of ethylene and tetracyanoethylene (TCNE): (η^2-C$_2$H$_4$)Pt(PH$_3$)$_2$ and (η^2-C$_2$(CN)$_4$)Pt(PH$_3$)$_2$. In all the transition-metal fullerene complexes characterised, fullerenes act as electron-deficient polyalkenes because their physical and chemical properties have similar values to those found for polyalkenes such as TCNE. For instance, the experimental electron affinity of C$_{60}$, 2.7 eV,[28] is very close to that of TCNE, the experimental and theoretical values of which are 2.88 eV[29] and 3.51 eV, respectively. Table 6.1 lists the calculated electron affinities (EAs) and ionization potentials (IPs) of the three ligands. According to the calculated values of the EAs, C$_{60}$ and TCNE have electron attracting character —positive values— whereas C$_2$H$_4$ has a negative value of the EA, which indicates non electron attracting character. In consequence, only C$_{60}$ and TCNE are expected to accept electrons easily. The similarity between the C$_{60}$ and TCNE complexes can also be seen in geometrical aspects: the Pt–C bond length in the (η^2-C$_{60}$)Pt(PH$_3$)$_2$ complex (2.139 Å) is closer to that of the corresponding (η^2-C$_2$(CN)$_4$)Pt(PH$_3$)$_2$

complex (2.136 Å) than to that of the ethylene complex (2.148 Å). This similarity also appears in the coordinated C–C bond lengths and the Pt–P bond lengths. It is therefore worth comparing the electronic structure of the fullerene complexes with that of the ethylene and TCNE complexes. The special stabilization when the metal unit is attached to the fullerene is corroborated by the high HOMO-LUMO gaps for these complexes: 1.38 eV for (η^2-C_{60})Pt(PH_3)$_2$, 4.00 eV for (η^2-C_2H_4)Pt(PH_3)$_2$ and 3.37 eV for (η^2-$C_2(CN)_4$)Pt(PH_3)$_2$. It shall also be interesting to compare this series of model complexes with the previously calculated platinum complex: (η^2-C_2H_4)C_{58}Pt (named C_{58}Pt(C_2H_4) in Chapter 5).[30] This is a monoheterofullerene with an ethylene coordinated to the Pt atom and, unlike the exohedral metallofullerenes shown in this chapter, the Pt atom takes part of the fullerene unit and not part of the ligand.

Some brief comments should be made about the different possible conformers of these M(PH_3)$_2$ exohedral metallofullerenes. The most important feature of these exohedral complexes is that the metal diphosphines are η^2 coordinated to a 6:6 C–C bond. All the X-ray structures available for metal diphosphine fullerene complexes align the 6:6 C–C edge in the MP_2 plane rather than perpendicular to it, just as the corresponding ethylene complexes do. All geometry optimizations on the fullerene complexes were therefore performed in the parallel orientation with imposed C_{2v} symmetry constraints. It is important to point out that the most stable conformer is that in which the hydrogens in the metal unit are eclipsed; other conformers have only slightly different relative energies.

The optimised geometries of these first three complexes are collated in Table 6.1. Metal addition causes a similar distortion in all the complexes: (1) a lengthening of the C–C bond lengths from the free ligand to the complex by about 0.086-0.127 Å and (2) a pulling away the C–C edge from the fullerene surface, which is shown in the increase in the pyramidalization angle of the coordinated carbons from the free ligand to the complex: 8.42°, 6.66° and 3.69° for ethylene, TCNE and fullerene complexes, respectively. Notice that the carbons of free ethylene and TCNE are not pyramidalized. The addition reaction is accompanied by the formation of σ and π Pt–C bonds and a partial breaking of the π bond of the C=C bond of the fullerene. This indicates that the coordinated carbons will increase their sp^3 character in the complex. The Pt–C bond lengths were determined to be 2.139 Å,

Table 6.1 Description of A-B interactions, A is a ligand and B is a molecule containing a metal atom. A-B is a stable complex [a]

A-B		(η^2-C_2H_4)-$C_{58}Pt$	(η^2-C_2H_4)-$Pt(PH_3)_2$	(η^2-$C_2(CN)_4$)-$Pt(PH_3)_2$	(η^2-C_{60})-$Pt(PH_3)_2$
A-B	Pt (in B)–C (in A)	2.447	2.148	2.136	2.139
	Pt (in B)–P (in B)	--	2.294	2.297	2.297
	C–C	1.373	1.432	1.507	1.495
	θ_p [b]	2.89	8.42	6.66	15.36
	P–Pt–P ang.	--	106.4	99.9	106.3
	Elect transf. B $\rightarrow$ A	–0.166	0.316	0.846	0.688
A	θ_p	0.00	0.00	0.00	11.67
	C–C	1.334	1.334	1.380	1.397
	MBO [c]	1.821	1.821	1.486	1.342
	Electron affinity [d]	–1.82 (–1.6) [f]	–1.82 (–1.6) [f]	3.51 (3.2) [g]	2.89 (2.7) [h]
	Ionization potential [d]	10.51 (10.5) [i]	10.51 (10.5) [i]	11.12 (11.8) [j]	7.56 (7.6) [k]
BE [e]		–0.70	–0.89	–1.39	–0.96

[a] Distances in Å, angles in º and energies in eV. [b] The carbons of the free alkene are not pyramidalised (θ_p = 0.00°) but the carbons of the free C_{60} have a θ_p = 11.67°. [c] Mayer bond order (MBO). [d] The experimental values are shown in parenthesis. [e] The binding energy (BE) is the energy difference between the optimized A–B adduct and the two relaxed A and B fragments. [f] Burrow, P. D.; Jordan, K. D. *Chem. Phys. Lett.* **1975**, *36*, 594. [g] Chowdhury, S.; Kebarle, P. *J. Am. Chem. Soc.* 1986, *108*, 5453. [h] Yang, S. H.; Pettiette, C. L.; Concienciao, J.; Cheshnowsky, O.; Smalley, R.E. *Chem. Phys. Lett.* **1991**, *139*, 233. [i] Lias, S. G.; Bartmess, J. E., Liebman, J. F.; Holmes, J. L.; Levin, R. D.; Mallard, W. G. Gas-Phase Ion and Neutral Termochemistry, *J. Phys. Chem.* Ref. Data Vol. 17, Suppl. No. 1, **1998**. [j] Stafast, H.; Bock, H. *Tetrahedron* **1976**, *32*, 855. [k] Lichtenberger, D. L.; Nebesny, K. W.; Ray, C. D.; Huffman, D. R.; Lamb, L. D. *Chem. Phys. Lett.* **1991**, 176, 203.

2.136 Å and 2.148 Å for (η^2-C_{60})$Pt(PH_3)_2$, (η^2-$C_2(CN)_4$)$Pt(PH_3)_2$ and (η^2-C_2H_4)$Pt(PH_3)_2$, respectively, and are a measure of the strength of the ligand-metal bond. From the structural information available, one can conclude that coordination in C_{60} and TCNE will be stronger than in ethylene. On the

other hand, the Pt–C bond lengths in the (η^2-C_2H_4)C_{58}Pt complex were computed to be much longer (2.447 Å) which indicated that the metal bond is weaker than the other types of fullerene-metal complexes. Specifically, in the most important model molecule, the (η^2-C_{60})Pt(PH_3)$_2$, the results of the geometry optimization of the complex give an evidence of a local structural deformation of the C_{60} unit, mainly localized in the interaction region. The C–C bond directly bound to the metal fragment increases in length by 0.098 Å and the pyramidalization angle increases from 11.67° in the free fullerene to 15.47° in the complex. Despite this, the opposite side of the fullerene remains almost unperturbed. The P–Pt–P angle reduces from its free value of 180° up to 106.3° in the complex and this change and the modification in the Pt–P bond lengths can be taken as a measure of the distortion of the Pt(PH_3)$_2$ unit.

6.2.2 The Dewar-Chatt-Duncanson model

The most widely accepted model for the patterns of (η^2-C_{60})M bonds is that proposed by Dewar, Chatt and Ducanson. It involves forming a σ-donation bond from the π C–C orbitals of the ligand to the metal and a π-back-donation bond from the metal *d*-orbitals to the π* C–C orbitals of the ligand. Thus, the π C–C bond of the ligand is weakened by the σ-donation which means that the energy of the π* C–C orbital decreases, so it can easily accept electrons from a back-donating *d*-orbital of the metal. The π interaction should be dominant for a d^{10} metal, and show a certain tendency to electron charge transfer from the metal to the C–C bond. On the other hand, the key point to bear in mind is the remarkable tendency of fullerenes to accept electrons. The combination of both effects leads to two different cases: (1) a considerable electron charge transfer from the *d* metal orbitals to the fullerene ligand for (η^2-C_{60})Pt(PH_3)$_2$ (0.688 *e*), for (η^2-$C_2(CN)_4$)Pt(PH_3)$_2$ (0.846 *e*) and for (η^2-C_2H_4)Pt(PH_3)$_2$ complex (a lower value of 0.316 *e*); and (2) an electron charge transfer from the ethylene ligand to the *d* metal orbital of the (η^2-C_2H_4)C_{58}Pt monoheterofullerene (0.086 *e*) (Table 6.1). These values are calculated from the Mulliken net charges. The amount of electron charge transfer in C_{60}-metal and TCNE-metal complexes is about twice that

in the ethylene-metal complex. This gives us complementary ideas about the strength of the ligand-metal bonds.

The BE is the energy difference between the optimized A–B complex and the two relaxed A and B fragments. The DE is defined as –BE. The order of the BE for the complexes is: (η^2-C$_2$(CN)$_4$)Pt(PH$_3$)$_2$ > (η^2-C$_{60}$)Pt(PH$_3$)$_2$ > (η^2-C$_2$H$_4$)Pt(PH$_3$)$_2$ > (η^2-C$_2$H$_4$)C$_{58}$Pt. The BE for the fullerene-metal was calculated as –0.96 eV and found to be higher than the corresponding ethylene-metal, –0.89 eV, but lower than the TCNE-metal, –1.39 eV. To separate the contributions from the σ donation and π back-donation, we analysed the ligand-metal bond DEs by using the extended transition method developed by Ziegler and Rouk,[31] which is an extension of the Morokuma's well-known decomposition.[32] The DE can be decomposed into several contributions: ΔE_{DE}, ΔE_{ST}, ΔE_{ORB}. More details about this decomposition can be found in subsection 4.2.4. ΔE_{ORB} term may be broken up into contributions from the orbital interactions within the various irreducible representations of the overall symmetry group of the system, according to the decomposition scheme proposed by Ziegler. The σ donation takes places in the a_1 representation whereas the π back-donation takes place in the b_1 representation. The decomposition for all model complexes is shown in Table 6.2.

A detailed comparison of the decomposition of the BE confirms that the coordinated bond between C$_{60}$ and the Pt(PH$_3$)$_2$ unit is qualitatively more similar to electron-deficient alkene complexes such as TCNE than ethylene. The BE for (η^2-C$_2$(CN)$_4$)Pt(PH$_3$)$_2$ is 0.50 eV higher than for (η^2-C$_2$H$_4$)Pt(PH$_3$)$_2$ and 0.43 eV higher than for (η^2-C$_{60}$)Pt(PH$_3$)$_2$. The term responsible for these energy differences is ΔE_{ORB}. Specifically, these are due to the π back-donation since σ donation remains almost constant (*ca.* 1.4-1.5 eV) for all complexes. The π back-donation in the C$_{60}$ and TCNE complexes is much larger than in the ethylene complex. It is clear that the contribution to the ΔE_{ORB} term from the π back-donation dominates over that from the σ donation in this kind of exohedral metallofullerenes. The π back-donation changes from –2.68 eV for (η^2-C$_2$H$_4$)Pt(PH$_3$)$_2$ to –4.69 eV for (η^2-C$_2$(CN)$_4$)Pt(PH$_3$)$_2$. Finally, note that the highest destabilization of ΔE_{DE} and ΔE_{ST} values for (η^2-C$_2$(CN)$_4$)Pt(PH$_3$)$_2$ are not enough to neutralize the high stabilization produced by the π back-donation and consequently it has the

Table 6.2 Decomposition of the binding energy (BE) for series that represents A-B interactions [a]

A-B		*(η^2-C_2H_4)-$C_{58}Pt$* [b]	*(η^2-C_2H_4)-$Pt(PH_3)_2$*	*(η^2-$C_2(CN)_4$)-$Pt(PH_3)_2$*	*(η^2-C_{60})-$Pt(PH_3)_2$*
ΔE_{DE}	*Metal unit*	0.14	0.54	1.34	0.38
	Lligand	0.07	1.11	0.75	1.14
	Total	0.21	1.65	2.09	1.52
ΔE_{ST}	ΔE_{Pauli}	4.72	9.00	9.31	9.17
	ΔE_{elstat}	–3.20	–7.11	–6.34	–6.55
	Total	1.52	1.89	2.97	2.62
ΔE_{ORB}	$\Delta E_{a1}(\sigma)$	–1.58	–1.53	–1.34	–1.39
	ΔE_{a2}	–0.03	–0.02	–0.08	–0.04
	$\Delta E_{b1}(\pi)$	–0.73	–2.68	–4.69	–3.41
	ΔE_{b2}	–0.09	–0.20	–0.34	–0.26
	Total	–2.43	–4.43	–6.45	–5.10
ΔE_{INT}		–0.91	–2.53	–3.48	–2.48
BE [c]		–0.70	–0.89	–1.39	–0.96

[a] Values in eV. [b] In Chapter 5 is named $C_{58}Pt(C_2H_4)$ (see ref. 30). [c] The binding energy (BE) is the energy difference between the optimized A–B adduct and the two relaxed A and B fragments.

highest BE of the complexes studied. That the BE is stronger for C_{60} than ethylene is in line with Morokuma and Borden's previous findings,[33] that the strain (in C_{60}) decreases the π^* orbital energy and increases π back-donation.

The different reactivity of the series: (η^2-C_2H_4)$Pt(PH_3)_2$, (η^2-C_{60})$Pt(PH_3)_2$ and (η^2-$C_2(CN)_4$)$Pt(PH_3)_2$ can be predicted using the Mayer bond order (MBO) of the free C–C bonds. A strong C–C bond with a high π-bond order should increase the σ donation and the π back-donation, and consequently, the BE between both fragments. This argument is completely reliable for ligands with similar electron affinities such as fullerenes and electron deficient alkenes (*e.g.* TCNE) but not for ethylene. The MBO for

the 6:6 C–C bond of C_{60} is computed to be 1.342 and for ethylene 1.821, but even so, the BE for the latter is much lower than for the former by 0.07 eV. This can be explained by taking into account that C_{60} and $C_2(CN)_4$ have a more attracting electron character (higher EA) than ethylene, while the ionization potentials are similar (Table 6.1).

Now let us turn our attention to the (η^2-C_2H_4)C_{58}Pt complex. The geometrical coordination of the various complexes led us to expect that it would be the least stable. Indeed, –0.70 eV of BE compared to –0.96 eV for the fullerene-metal bond. The consequence is a longer Pt–C distance and no elongation of ethylene C–C bond lengths. This can be attributed to the almost non-existent π back-donation from the metal atom to the ethylene in this complex. Although the σ donation is the same as that of the other Pt complexes (≈ 1.5 eV) and even the ΔE_{ST} and ΔE_{DE} terms are more favorable to the (η^2-C_2H_4)C_{58}Pt formation than in the other complexes, all these terms are not enough to counteract the lack of π back-donation. This weak π back-donation can be explained from two points of view: (1) there are no *d* metal orbitals available to connect to π* C–C of the ligand because they are involved in the bond of the fullerene carbon framework (Chapter 5); (2) the electron donor character of the such monoheterofullerenes as free fullerenes is weak. The EA of the C_{58}Pt, 3.67 eV, is even higher than that of C_{60}, so the π back-donation from C_{58}Pt to ethylene is not favoured at all, unlike the (η^2-C_{60})Pt$(PH_3)_2$ complex where the π back-donation represents the electron charge transfer from the Pt$(PH_3)_2$ unit to the C_{60} fullerene. So, for all the Pt complexes studied, except (η^2-C_2H_4)C_{58}Pt, the bonding contribution from the π back-donation dominates over that from the σ donation.

6.3 MONOADDITION COMPLEXES OF C_{60} AND ETHYLENE

6.3.1 Pt complexes

The addition of a Pt$(PH_3)_2$ unit to C_{60} in a 6:6 C–C bond generate a certain distortion in the fullerene cage, mainly in the interacting region (Figure 6.4). As a result, the coordinated C–C bond increased to 1.495 Å in the complex. This computed distance only slightly differs with the X-ray

value reported for (η^2-C_{60})Pt(PPh_3)$_2$, 1.502 Å. The deviations of the computed Pt–P and Pt–C bond lengths from the experimental values were found also very small as Table 6.3 shows.

The DE of (η^2-C_{60})Pt(PH_3)$_2$ to give the fullerene and the metal unit was computed to be 0.96 eV, a relatively high energy that stresses the stability of the organometallic derivatives of C_{60}. The hypothetical isomer with the metal linked to a 6:5 C–C bond was also studied. This isomer is 0.51 eV less stable than the observed cluster with the metal atom bonded to a 6:6 C–C bond. In agreement with the lower cage-metal interaction in the 6:5 complex, the Pt–C bond distance in this isomer is 0.042 Å longer than in the 6:6 complex and the P–Pt–P angle is somewhat greater: 112.5º and 106.3º in the 6:5 and 6:6 complexes, respectively.

The (η^2-C_{60})Pt(PR_3)$_2$ monoaddition complex is prepared through the substitution reaction:

(6.1) $$(\eta^2\text{-}C_2H_4)Pt(PR_3)_2 + C_{60} \rightarrow (\eta^2\text{-}C_{60})Pt(PR_3)_2 + C_2H_4$$

Reaction 6.1 is exothermic by only 0.07 eV with a triple-ζ + polarization (TZP) Slater basis set for all atoms. So, whereas the DE for the fullerene complex is 0.96 eV, the corresponding value for the ethylene precursor is 0.89 eV. This difference seems very small and in fact the DE of the ethylene-metal has been reported to be 0.99 eV at NL-DFT+QR level[34] and 1.22 eV at the CCSD(T) level.[35] It still remains some discrepancy with the experimental calorimetric studies for (η^2-C_2H_4)Pt(PPh_3)$_2$ which leads to an estimation of 1.56 ± 0.17 eV for the DE of C_2H_4–Pt.[36] Rosa et al. have shown that the basis set superposition errors (BSSE) are very small when these relatively large basis sets are used. In transition-metal complexes the BSSE has been estimated to be typically between 0.04-0.08 eV with TZP basis set[37] and therefore this correction at this level of computation can be neglected. The calculated BSSE was also found in this order of magnitude for our complexes using TZP Slater basis set: 0.05 eV for (η^2-C_{60})Pt(PH_3)$_2$ and 0.02 eV for (η^2-C_2H_4)Pt(PH_3)$_2$. All geometries and BE for the above mentioned exohedral metallofullerenes with different basis set are collated in Table 6.3. Notice that all BE do not include BSSE corrections but this term is listed near the BE values.

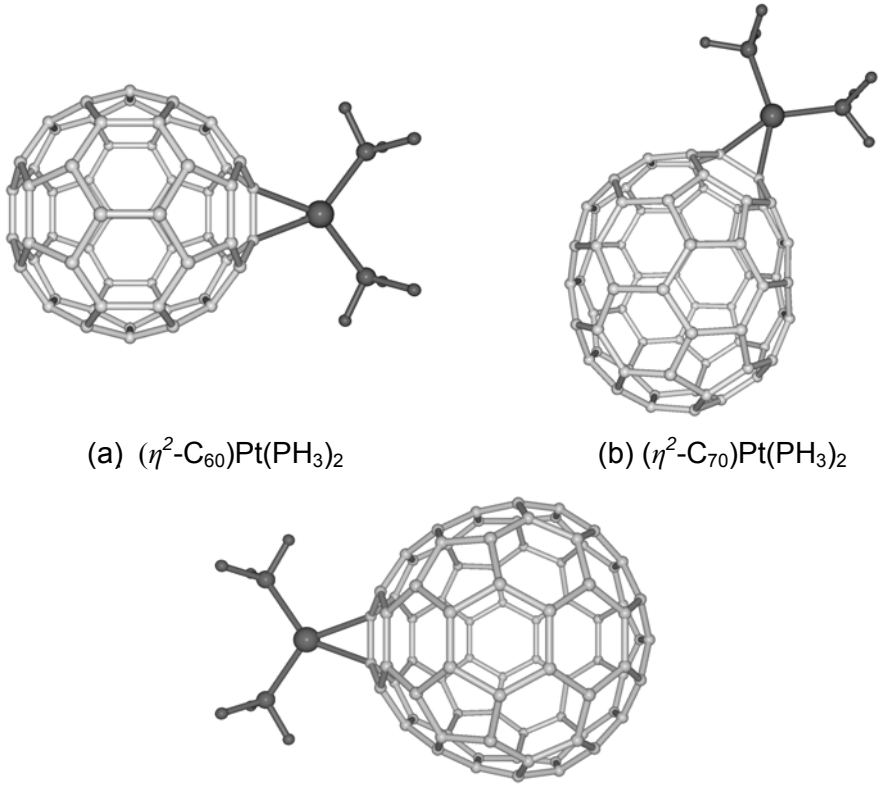

Figure 6.4 The structure of the most stable isomers of (η^2-C$_{60}$)Pt(PH$_3$)$_2$, metal unit linked to the 6:6 C–C bond type (a); (η^2-C$_{70}$)Pt(PH$_3$)$_2$, metal unit linked to the Ca–Cb bond (b), and (η^2-C$_{84}$)Pt(PH$_3$)$_2$, metal unit linked to the C42–C43 bond (c).

With the perspective of studying larger fullerene-metal systems than those reported herein, we analyzed the effect of the basis set on the DE and geometries. If the C$_{60}$ is described by a double-ζ + polarization (DZP) Slater basis set and the Pt moiety by a TZP the geometry hardly changes but the DE increases up to 1.41 eV, whereas the corresponding value for ethylene precursor is 0.92 eV. Furthermore, higher BSSE corrections were obtained when the DZP Slater basis set were used for the ligand (fullerene/ethylene): 0.37 eV for fullerene-metal complex and 0.10 eV for ethylene-metal

Table 6.3 DFT geometries and binding energies (BE) for the (η^2-C_{60})$Pt(PH_3)_2$ complex and for the (η^2-$C_{14}H_8$)$Pt(PH_3)_2$ and (η^2-C_2H_4)$Pt(PH_3)_2$ model complexes [a]

Molecule	*Basis set*	*Pt–P*	*Pt–C*	*C–C*	*BE* [b]	*BSSE*
(η^2-C_{60})$Pt(PPh_3)_2$ [c,f]		2.278	2.130	1.502	--	--
(η^2-C_{60})$Pt(PH_3)_2$ [e,g]	TZP	2.297	2.139	1.495	–0.96	0.05
	C(DZP); C,P,H,Pt(TZP)	2.293	2.120	1.504	–1.07	0.09
	C(DZP); P,H, Pt(TZP)	2.297	2.137	1.495	–1.41	0.37
(η^2-$C_{14}H_8$)$Pt(PH_3)_2$ [d,g]	TZP	2.271	2.065	1.528	–1.21	0.08
	C, P, H (DZP);Pt(TZP)	2.277	2.112	1.503	–0.95	0.29
(η^2-C_2H_4)$Pt(PPh_3)_2$ [c,f]		2.268	2.111	1.434	--	--
(η^2-C_2H_4)$Pt(PH_3)_2$ [e,g]	TZP	2.294	2.148	1.432	–0.89	0.02
	C, H (DZP); Pt, P, H(TZP)	2.294	2.147	1.431	–0.92	0.10

[a] Bond lengths in Å, angles in º and energies in eV. [b] The BE (binding energy) is equal to the –DE (dissociation energy). [c] ref. 3. [d] ref 21. [e] This study. [f] X-ray. [g] DFT.

complex. The discrepancy observed in the DE motivated us to check a mixed basis set for the fullerene cage. That is, the reactant pyracylene unit described by a TZP and the rest of the fullerene cage by a DZP. In these conditions, the X-ray geometry is well reproduced (Table 6.3) and the DE was now computed to be 1.07 eV, only 0.11 eV higher than that found with the large TZP Slater basis set; the BSSE correction is also quite small, 0.09 eV. It should also be pointed out that the energies of the frontier orbitals are very similar to those found with the TZP basis: with the mixed basis, the HOMO and LUMO energies are –5.97 eV and –4.64 eV; while the corresponding values with the largest basis set are –5.54 eV and –4.16 eV, respectively. This point is very important for describing the chemical properties of the complex.

An alternative process has been proposed by Sgamellotti and co-workers. They have used a pyracylene unit as model for the C_{60} cage in the (η^2-C_{60})$Pt(PH_3)_2$ to reduce the size of the system. When a DZP basis set is used for carbon, phosphorous and hydrogen and a TZP basis set is used for

Table 6.4 DFT geometries and binding energies (BE) for (η^2-C$_{60}$)M(PH$_3$)$_2$ and (η^2-C$_2$H$_4$)M(PH$_3$)$_2$ (M = Pd, Ni) [a]

Molecule	Basis set	*M–P*	*M–C*	*C–C* [b]	*BE*
(η^2-C$_{60}$)Pd(PPh$_3$)$_2$	X-ray	2.323	2.105	1.447	--
(η^2-C$_{60}$)Pd(PH$_3$)$_2$	TZP	2.348	2.175	1.467	–0.88 [d]
	C, P, H (DZP); Pt (TZP) [c]	2.378	2.180	1.464	–1.00 [e]
(η^2-C$_2$H$_4$)Pd(PH$_3$)$_2$	TZP	2.309	2.168	1.404	–0.74 [f]
(η^2-C$_{60}$)Ni(PH$_3$)$_2$	TZP	2.166	1.965	1.480	–1.73 [g]
	C, P, H (DZP); Pt (TZP) [c]	2.222	1.989	1.470	–1.70 [h]
(η^2-C$_2$H$_4$)Ni(PH$_3$)$_2$	TZP	2.146	1.987	1.410	–1.55 [i]

[a] Bond lengths in Å, angles in º and energies in eV. [b] The C–C distances in the free C_2H_4 and C_{60} are 1.334 Å and 1.397 Å, respectively. [c] From ref. 20. [d] BSSE = 0.05. [e] BSSE = 0.35. [f] BSSE = 0.02. [g] BSSE = 0.10. [h] BSSE = 0.35. [i] BSSE = 0.05.

platinum, the DE for (η^2-C$_{14}$H$_8$)Pt(PH$_3$)$_2$ is 0.95 eV but with a large BSSE of 0.29 eV, although if a TZP basis set is used to describe all atoms the DE becomes 1.21 eV and a BSSE of only 0.08 eV (Table 6.3). However, the geometry of the monoaddition complex is not properly reproduced even if this larger basis set is used: the angle P–Pt–P is always overestimated and the Pt–C bond length is predicted to be 0.065 Å shorter.

6.3.2 Pd and Ni complexes

The BE for C_{60} and ethylene complexes of Pd and Ni are tabulated in Table 6.4. The BE increases in the order Pd < Pt < Ni and fullerene complexes are always slightly more stable than ethylene complexes. The computed values are –0.88 and –1.73 for (η^2-C$_{60}$)M(PH$_3$)$_2$ complexes where M = Pd, Ni, respectively. Also the BSSE for the larger basis set was computed to be quite small, a maximum of 0.10 eV. The X-ray structure for (η^2-C$_{60}$)Pd(PPh$_3$)$_2$ is available but has not yet been reported for the nickel diphosphine complex. The geometry parameters of the (η^2-C$_{60}$)Pd(PH$_3$)$_2$

Table 6.5 Comparison of the various calculated and experimental BE of (η^2-C_2H_4)M(PH_3)$_2$ (M = Pt, Pd, Ni) ethylene complexes [a]

Method	*Pt*	*Pd*	*Ni*	*Ref.*
DFT-TZP	–0.89	–0.74	–1.55	This work
MP2 [b]	–1.07	–0.91	–1.52	19
CCSD(T) [c]	–1.22	–0.91	--	35
NL-DFT+QR [d]	–0.99	–0.86	--	34
Exp.[e]	–1.56	--	–1.30	36

[a] Values in eV. [b] Møller-Plesset. [c] Coupled cluster single, double and triple. [d] Nonlocal DFT quasirelativistic. [e] Estimated from calorimetric studies of the (η^2-C_2H_4)M(PPh_3)$_2$ complex

complex in the present results are slightly better than those reported by Sgmelloti, who used a basis set of less quality. In our calculations, the maximum deviation of the bond lengths was 0.07 Å (Table 6.4). The BE with the poorer basis set were reported by Sgmelloti to be –1.00 eV for (η^2-C_{60})Pd(PH_3)$_2$ and –1.70 eV for (η^2-C_{60})Ni(PH_3)$_2$, but if we take into account the BSSE corrections (not negligible in these cases) the values become –0.65 eV and –1.35 eV, respectively. Hence, a large basis set must be used if reliable BE are to be calculated.

On the other hand, the BE of –0.74 for the (η^2-C_2H_4)Pd(PH_3)$_2$ was underestimated in comparison with the –0.86 eV at the NL-DFT+QR level and –0.91 eV at the CCSD(T) level. Several values are reported for (η^2-C_2H_4)Ni(PH_3)$_2$ and they almost coincide with the calculated value: 1.55 eV in the present study and 1.52 eV at the MP2 level. These results are listed in Table 6.5. Unlike the (η^2-C_2H_4)Pt(PH_3)$_2$ complex, the BE for the (η^2-C_2H_4)Ni(PH_3)$_2$ matches the experimental value quite well and is only 0.25 eV bellow it. Once we calculated the BE for the ethylene and C_{60} complexes, we were able to evaluate the formation energies of the fullerene complexes from the ethylene complexes using equation 6.1 where R = H. The reaction energy is slightly exothermic in all cases following the order Pt < Pd < Ni: –0.07 eV for Pt, –0.14 eV for Pd and finally –0.17 eV for Ni.

The longest M–C distance was found in the C_{60} complex of Pd (2.175 Å) and the shortest in the C_{60} complex of Ni (1.966 Å). An intermediate distance of 2.139 Å was found for the analogous Pt complex.

These values suggest a strength of the ligand-metal bond in the following order: Pd < Pt < Ni like BE. However, this order is different if the geometrical distortion of the pyracylene patches is taken into account: Pd < Ni < Pt. This distortion is measured by the coordinated C–C bond lengths: 1.467 Å, 1.480 Å and 1.495 Å for the C_{60} complexes of Pd, Ni and Pt, respectively. Also, the cage radius increases slightly for all three complexes in the same order: Pd < Ni < Pt. Indeed, the fact that the degree of distortion of the fullerene complex of Pt is higher than that of Ni would suggest a reversed order for the strength of fullerene-metal bonds: Ni < Pt. But we have seen in the previous paragraph that the BE follows another order. This dichotomy has already been observed for olefins[38] and fullerene complexes and rationalised on the basis of the relaxation energies of the metal fragments.

6.4 POLYADDITION COMPLEXES OF C_{60}

6.4.1 Energy and geometry considerations of Pt complexes

To analyze how the multiple addition affects the BE, the series of complexes $(\eta^2\text{-}C_{60})\{Pt(PH_3)_2\}_n$ with n = 2, 4 and 6 were fully optimized. The metal units are spread further as possible to the C_{60} surface, minimizing the steric repulsion among the metal units. Several years ago, we demonstrated that the interaction is highly local and that the loss of the first platinum group in the $(\eta^2\text{-}C_{60})\{Pt(PH_3)_2\}_2$ is only slightly more favorable than the loss of the platinum group from the monoaddition derivative. The calculations that were carried out at the Hartree-Fock level, however, gave very low absolute energies (0.44 eV for the monoadduct). To check these results, we reanalyzed at the DFT level the series of complexes above mentioned with the large basis set, TZP for all atoms. Again, the optimized geometries at the present DFT level are in excellent agreement with the X-ray data available (Table 6.6). For example, for the hexaaddition complex, in which the platinum atoms are arranged in an octahedral array around the fullerene core, the computed C–C bond length is 1.487 Å while the X-ray value for $(\eta^2\text{-}C_{60})\{Pt(PEt_3)_2\}_6$ is 1.497 Å. This good agreement is also confirmed in the Pt–P and Pt–C bonds lengths where the deviations are *ca.* 0.04 Å. The deviations found at the HF level were a bit more important, *ca.*

Table 6.6 Geometric properties and fullerene-metal binding energies (BE) for (η^2-C_{60}){$Pt(PH_3)_2$}$_n$ (n = 1, 2, 4, 6) [a]

n [b]	*Sym*	*Pt–P*	*Pt–C*	*Δ(C–C)* [c]	*P–Pt–P*	*final* θ_p [d]	*BE* [e]	*BE per group* [f]
1	C_s	2.293	2.181	0.078	112.5	15.47	–0.45	–0.45
1	C_{2v}	2.297	2.139	0.098	106.3	15.36	–0.96	–0.96
2	D_{2h}	2.289	2.131	0.103	108.2	15.36	–0.80	–0.88
4	D_{2h}	2.288	2.150	0.094	107.7	15.07	–0.82	–0.85
6	T_h	2.289	2.153	0.090	108.1	14.88	–0.73	–0.81

[a] Bond lengths in Å, angles in º and energies in eV. [b] All C–C bonds are pyracylene type except the first row which is a corannulene type. [c] Difference between the original bond in the free C_{60} and in the complex. [d] Pyramidalization angle (θ_p) for the carbons attached to metal unit in the complex. The θ_p for the free C_{60} is 11.67º. [e] For n = 4 and n = 6, the binding energy (BE) is estimated from the reaction energies (η^2-C_{60}){$Pt(PH_3)_2$}$_{n-2}$ + 2{$Pt(PH_3)_2$} → (η^2-C_{60}){$Pt(PH_3)_2$}$_n$ and the tendency observed from n = 2 to n = 1. [f] The BE per group is calculated from the reaction: C_{60} + n{$Pt(PH_3)_2$} → (η^2-C_{60}){$Pt(PH_3)_2$}$_n$, BE per group = ΔE/n; ΔE, reaction energy. BSSE = 0.05-0.07 eV.

0.05 Å.[19] The Pt–C distances slightly increase as the number of metals on the fullerene surface increases. Thus, the Pt–C bond length is 2.139 Å for the monoadduct and 2.153 Å for the hexaadduct. The pyramidalization angle of the coordinated carbons to the metal augments and the maximum distortion appears in the monoaddition complex. When metals are successively added to the fullerene core the pyramidalization angle of the coordinated carbons decreases (Table 6.6 and Figure 6.5).

The present DFT calculations fully confirm that the addition of one metal group to the C_{60} only slightly reduces the ability of the carbon cluster to accept a second metal. The reaction energy for the process

(6.2) (η^2-C_{60}){$Pt(PH_3)_2$}$_2$ → (η^2-C_{60})$Pt(PH_3)_2$ + $Pt(PH_3)_2$

is found to be 0.80 eV, which is only 0.17 eV smaller than for the DE of the monoaddition complex. Thus, the BE per group is –0.88 eV for n = 2. Because of the low symmetry of the pentacoordinated complex the energy associated to the loss of the first metal group in the hexaadduct complex was not determined. Nevertheless, we calculated the reaction energy for the process

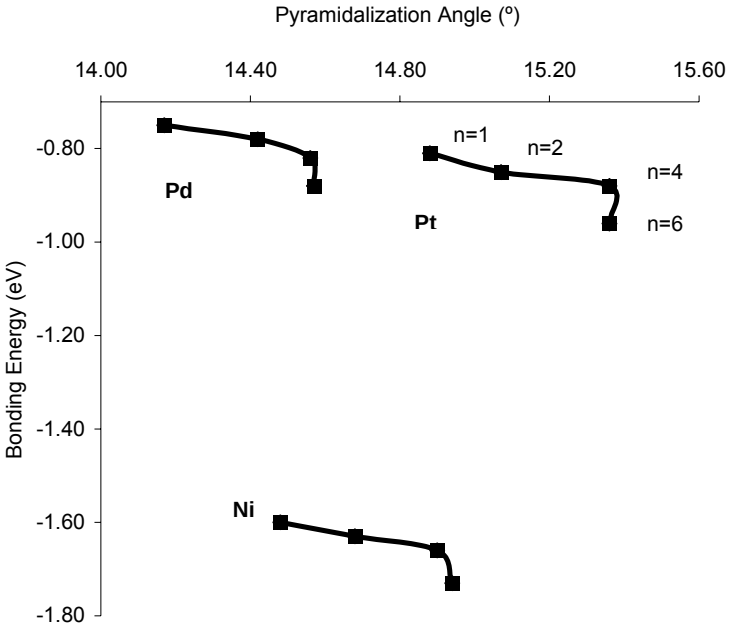

Figure 6.5 Correlation between the binding energy (BE) and the pyramidalization angle (θ_p) for (η^2-C$_{60}$){M(PH$_3$)$_2$}$_n$ (M = Pt, Pd, Ni; n = 2, 4, 6).

(6.3) $$(\eta^2\text{-C}_{60})\{\text{Pt(PH}_3)_2\}_6 \rightarrow (\eta^2\text{-C}_{60})\{\text{Pt(PH}_3)_2\}_4 + 2\{\text{Pt(PH}_3)_2\}$$

which is 1.45 eV. The tendency of the DE when going from n = 1 to n = 2 suggests that the loss of the first metal group in the (η^2-C$_{60}$){Pt(PH$_3$)$_2$}$_6$ should be almost ~ 0.64 eV ($C_{60}M_6 \rightarrow C_{60}M_5$ for short), whereas the dissociation process from $C_{60}M_5$ to $C_{60}M_4$ is estimated to be ~ 0.81 eV. The same strategy was followed for n = 4 and n = 3. The energy involved in the $C_{60}M_4 \rightarrow C_{60}M_2$ process is equal to 1.63 eV, which yields estimated values of ~ 0.73 eV and ~ 0.90 eV for $C_{60}M_4 \rightarrow C_{60}M_3$ and $C_{60}M_3 \rightarrow C_{60}M_2$, respectively. All these energies are clearly larger than the energy involved in the coordination of a platinum atom to a 6:5 ring junction, 0.45 eV. Consequently, the metal addition always takes place at the 6:6 C–C bond. To remove the six groups from the fullerene surface requires 4.84 eV, a considerable amount of energy that shows how stable these highly coordinated fullerenes are. The BE per group in the complexes (η^2-

Table 6.7 Geometric properties and fullerene-metal binding energies (BE) for (η^2-C_{60})$\{Pd(PH_3)_2\}_n$ (n = 1, 2, 4, 6) [a]

n	*Sym*	*Pd–P*	*Pd–C*	*Δ(C–C)* [b]	*P–Pd–P*	*final* θ_p [c]	*BE per group* [d]
1	C_{2v}	2.348	2.175	0.070	106.7	14.57	–0.88
2	D_{2h}	2.330	2.165	0.071	107.6	14.56	–0.82
4	D_{2h}	2.320	2.155	0.070	109.9	14.42	–0.78
6	T_h	2.320	2.181	0.063	110.2	14.17	–0.75

[a] Bond lengths in Å, angles in º and energies in eV. [b] Difference between the original bond in the free C_{60} and in the complex. [c] Pyramidalization angle (θ_p) for the carbons attached to metal unit in the complex. The θ_p for the free C_{60} is 11.67º. [d] The binding energy (BE) per group is calculated from the reaction: $C_{60} + n\{Pd(PH_3)_2\} \rightarrow (\eta^2\text{-}C_{60})\{Pd(PH_3)_2\}_n$, BE per group = ΔE/*n*; ΔE, reaction energy. BSSE = 0.05-0.06 eV.

$C_{60})\{Pt(PH_3)_2\}_n$ range from –0.96 for n = 1 to –0.81 for n = 6. The maximum number of metal groups coordinated to the C_{60} is probably imposed by the steric effects of the bulky PEt_3 ligands.

6.4.2 Pd and Ni complexes

The addition of one metal group to the C_{60} reduces only slightly the ability of the carbon cluster to accept a second metal. So, like other studies, we confirm that the interaction is highly local. However, when the number of metal groups coordinated to the fullerene increases, the BE per group decreases slightly. Indeed for Pd complexes, the BE per group ranges from –0.88 eV (n = 1, monoaddition) to –0.75 eV (n = 6, hexaaddition) (Table 6.7). For the Ni complexes the decrease was calculated to be same (Table 6.8).

The geometrical distortion caused by the polyaddition of $M(PH_3)_2$ (M = Pd, Ni) units to the C_{60} fullerene is similar to that caused by Pt units. The M–C distance increases when the number of metal units increases because the M–C bond weakens: 2.175 Å for the monoadduct (η^2-C_{60})$Pd(PH_3)_2$ and 2.181 Å when six $(PH_3)_2Pd$ units are added. The Pd double addition complex has a special stabilization, as evidenced by the Pd–C distance, which is a little shorter than the distance in the monoaddition complex. This is also observed for Pt complexes. The

Table 6.8 Geometric properties and fullerene-metal binding energies (BE) for (η^2-C_{60}){$Ni(PH_3)_2$}$_n$ (n = 1, 2, 4, 6) [a]

n	*Sym*	*Ni–P*	*Ni–C*	*Δ(C–C)* [b]	*P–Ni–P*	*final* θ_p [c]	*BE per group* [d]
1	C_{2v}	2.166	1.965	0.083	105.7	14.94	–1.73
2	D_{2h}	2.139	1.966	0.083	106.8	14.90	–1.66
4	D_{2h}	2.163	1.968	0.078	108.3	14.68	–1.63
6	T_h	2.165	1.977	0.074	107.4	14.48	–1.60

[a] Bond lengths in Å, angles in º and energies in eV. [b] Difference between the original bond in the free C_{60} and in the complex. [c] Pyramidalization angle (θ_p) for the carbons attached to metal unit in the complex. The θ_p for the free C_{60} is 11.67º. [d] The binding energy (BE) per group is calculated from the reaction: $C_{60} + n\{Ni(PH_3)_2\} \rightarrow (\eta^2\text{-}C_{60})\{Ni(PH_3)_2\}_n$, BE per group = $\Delta E/n$; ΔE, reaction energy. BSSE = 0.07-0.10 eV.

deformation in both fragments is less important in polyaddition complexes than in single- addition complexes: the P–M–P angle increases when several metals are added to the fullerene surface. For instance, the P–M–P angle is computed to be 106.7º in the (η^2-C_{60})$Pd(PH_3)_2$ complex and 110.2º in the hexaaddition complex. In the fullerene cage, the polyaddition is accompanied by the less important effect of the C–C edge pulling away from the fullerene surface. The fact that the C–C for the polyaddition complexes (0.063 Å for Pd and 0.074 Å for Ni in the (η^2-C_{60}){$M(PH_3)_2$}$_6$) increases less than the C–C bonds lengths in the monoaddition complexes (0.070 Å for Pd and 0.083 Å for Ni) confirms this idea (Tables 6.7 and 6.8).

6.4.3 Pyramidalization of carbons attached to the metal unit

The most important effect in the fullerene cage is the change in the pyramidalization angle of the carbons attached to the metal units. The degree of pullout may be indicated by the increase in the pyramidalization angle. The pyramidalization angle for free C_{60} is equal to 11.67º for all atoms and increases in all C–C bonds coordinated to a metal unit. Metal attachment causes an increase in the pyramidalization angle in the local interaction area because it pulls the C–C bond away from the edge. When metals are added successively to the fullerene cage the BE and

pyramidalization angle decrease slightly. The higher the pyramidalization angle produced by these metal additions in the coordinated C–C, the more stable the complex obtained will be. The pyramidalization angle, and therefore the distortion, is higher in the monoaddition complexes than in the rest. In this respect, Figure 6.5 shows a clear positive correlation between the BE per added group and the pyramidalization angle for all series of polyaddition exohedral metallofullerenes. It should be pointed out that although the decrease in the BE is very small, the change in the pyramidalization angle is sensitive. For instance, pyramidalization angles ranges between 15.47º and 14.88º for the series (η^2-C_{60}){$Pt(PH_3)_2$}$_n$ n = 1, 2, 4, 6. Ni and Pd complexes follow the same trend: that is to say, the pyramidalization angle in the hexaaddition complexes (14.17º for Pd and 14.48º for Ni) is lower than in the monoaddition complexes (14.57º and 14.94º, respectively). After the metal additions, the most pyramidalised carbons are those attached to the metal units. All these features can be attributed to decrease in the π* orbital energy of the coordinated C–C bond which, in turn, leads to an increase in the π back-donation from the *d* metal orbitals to the fullerene.

6.5 MONOADDITION COMPLEXES OF C_{70} AND C_{84}

Our analysis of the (η^2-C_{70})$Pt(PH_3)_2$ and (η^2-C_{84})$Pt(PH_3)_2$ complexes showed us how to evaluate the effect that the fullerene curvature and the different types of the C–C bonds have on the strength of the bond between the metal unit and the fullerene cage. The C_{70} and C_{84} are less spherical than C_{60} and their cages have carbons with different pyramidalization angles. The curvature of these higher fullerenes is different on each part of the fullerene surface.

6.5.1 C_{70}

Table 6.9 Geometric properties and binding energies (BE) for (η^2-C_{70})Pt(PH$_3$)$_2$ and (η^2-C_{84})Pt(PH$_3$)$_2$ [a]

Cage	*C–C bond* [b]	*Sym.*	*Pt–C*	*Δ(C–C)* [c]	*initial* θ_p [d]	*final* θ_p [d]	*BE* [e]	*BSSE* [f]
C_{70}	Ca–Cb	C_s	2.140	0.104	11.92	15.66	–1.04	0.05
	Cc–Cc	C_s	2.142	0.097	11.49	15.25	–0.95	0.05
	Ce–Ce*	C_{2v}	2.183	0.115	8.60	12.69	–0.22	0.05
D_{2d}-C_{84}:***23***	C42–C43	C_{2v}	2.175	0.088	10.80	14.35	–1.00	0.11
	C9–C10	C_2	2.152	0.079	10.68	14.34	–0.91	0.08
	C5–C6	C_s	2.163	0.076	10.98	14.53	–0.83	0.08
	C2–C3*	C_s	2.165	0.098	7.67	11.94	–0.33	0.08
D_2-C_{84}:***22***	C9–C10	C_1	2.164	0.082	10.73	14.26	–0.94	0.09
	C32–C53	C_2	2.148	0.082	10.71	14.48	–0.82	0.08
	C7–C22	C_1	2.153	0.079	10.91	14.64	–0.80	0.08

[a] Bond lengths in Å, angles in º and energies in eV. [b] All are pyracylene C–C bond types except those marked with * which are pyrene types (Figure 6.1 for C_{70} and Figure 6.2 and 6.3 for C_{84}). [c] Difference between the bond distance in the free fullerene and in the complex. For the free D_{5h}-C_{70}, Ca–Cb: 1.398 Å, Cc–Cc: 1.392 Å and Ce–Ce: 1.469 Å; for D_{2d}-C_{84}:**23**, C42–C43: 1.375 Å, C9–C10: 1.369 Å, C5–C6: 1.377 Å and C2–C3: 1.461 Å; for the D_2-C_{84}:**22**, C9–C10: 1.373 Å, C32–C53: 1.369 Å and C7–C22: 1.377. [d] Pyramidalization angle for the coordinated carbon bond in the free fullerene (initial θ_p) and in the complex (final θ_p). [e] Binding energy (BE). [f] Basis set superposition error (BSSE)

The C_{70} is more curved at the poles and flatter at the equator. The Ce carbons at the equator of the molecule are the least pyramidalised with θ_p = 8.60º, whereas the Ca and Cb carbons at the poles have the highest pyramidalization angle, 11.92º. The pyramidalization angle of the other carbons is between these values. To determine the dependence of the fullerene-metal BE on the fullerene curvature, we studied the coordination of the Pt(PH$_3$)$_2$ unit to the Ce–Ce, Cc–Cc and Ca–Cb bonds (Figure 6.1 and Appendix A.4). Like in C_{60}, the computed and experimental[39] geometries for the free C_{70} are in excellent agreement. The computed bond lengths of the pyracylene Cc–Cc and Ca–Cb bonds, 1.392 Å and 1.398 Å (Table 6.9),

respectively, are similar to those of the 6:6 C–C bonds in C_{60}. The Ce–Ce bond lengths of 1.469 Å corresponds to a 6:6 ring junction abutted by two hexagons, corresponding to a pyrene type. According to a Hückel analysis the π-bond order follows the same trend as pyramidalization angle. The highest π-bond orders are in the poles, Ca–Cb and Cc–Cc bonds, while the equator is more aromatic with low π-bond order in the Ce–Ce bond.[40]

When a $Pt(PH_3)_2$ unit is linked to the Ca–Cb bond, the deformation of the fullerene cage and the geometry of the $Pt(PH_3)_2$ unit is similar to that observed in the C_{60} derivative (compare Tables 6.3 and 6.9). So, in the optimised organometallic complexes the C–C bonds are lengthened and pulled away from the fullerene surface increasing the pyramidalization angle between 3-4º. The structure of this complex is given in Figure 6.4b. In consonance with this similarity in the geometries, both complexes differ in the BE to give the fullerene cage and the metal unit in only 0.08 eV more favorable to C_{70} addition. When a metal unit coordinates the fullerene through the Cc–Cc bond, the complex is somewhat less stable and the BE is –0.95 eV, 0.09 eV lower than for the most stable isomer. The DE for the complex in which the metal unit is linked to the carbons at the equator is only 0.22 eV. This lower energy is because of the different nature of the 6:6 Ce–Ce bonds (pyrene type) and the smaller pyramidalization angle of the Ce carbons. Note that this later energy is even smaller than that found for the C_{60} derivative with the metal unit coordinated to the 6:5 C–C bond. On the other hand, the relatively short Pt–C bond lengths, 2.183 Å, do not reveal the significant instability of the isomer with the metal unit bound to a Ce–Ce bond.

6.5.2 C_{84}

Balch and co-workers demonstrated that the addition of $Ir(CO)Cl(PPh_3)_2$ to a benzene solution of a mixture of C_{84} isomers yielded the $(\eta^2\text{-}C_{84})Ir(CO)Cl(PPh_3)_2$ complex. The X-ray analysis of this system showed that the fullerene cage corresponds to the D_{2d}-C_{84}:**23** isomer. However, the separation of C_{84} isomers that was achieved through crystallization of the $(\eta^2\text{-}C_{84})Ir(CO)Cl(PPh_3)_2{\cdot}4C_6H_6$ adduct was not complete. Examination of the residual electron density within the fullerene portion of the adduct indicated that another isomer of C_{84} was probably

present. It could be the most stable and experimentally found D_2-C_{84}:**22** isomer. At this level of computation, D_2-C_{84}:**22** isomer is slightly more stable than D_{2d}-C_{84}:**23** isomer by 0.05 eV. According to the Taylor numeration, the coordination of the iridium atom takes place at the C42–C43 bond,[41] one of the three distinct pyracylene C–C bond types of the D_{2d}-C_{84}:**23** isomer (C5–C6, C9–C10 and C42–C43, Figure 6.2). These three bonds have the shortest C–C distances (~ 1.37 Å) and the highest pyramidalised carbons of all 6:6 C–C bonds ($\theta_p \approx 11.0^o$). Moreover, according to Hückel calculations the pyracylene C–C bonds have the highest π-bond order. So, in accordance with these criteria, the pyracylene types should be the most reactive. On the other hand, the pyrene C–C bond types contain the longest 6:6 C–C bonds (~ 1.46 Å) and the corresponding carbons have small pyramidalization angles (~ 8º). Appendix A.8 describes the 19 distinct C–C bonds for the D_{2d}-C_{84}:**23** isomer. These geometrical parameters suggest that pyrene types should be the least reactive of the 6:6 C–C bonds. To evaluate the strength of the fullerene-metal bond we studied the coordination of the Pt(PH$_3$)$_2$ unit to the three pyracylene 6:6 C–C bond types and to the C2–C3 bond, one of the three pyrene 6:6 C–C bond types. The addition to the latter will allow us to establish an energy range for the 6:6 C–C bonds. The BE values in Table 6.9 fully confirm that the most reactive site corresponds to the C42–C43, the coordination position observed by Balch in the (η^2-C_{84})Ir(CO)Cl(PPh$_3$)$_2$ Vaska-type complex. The BE of –1.00 eV is only somewhat lower than that found at the same level of computation for the C_{60} and for the most reactive site in the C_{70}. The structure of the organometallic complex linked to the C42–C43 bond is given in Figure 6.4c. The BE for the other two pyracylene C–C bond types (C9–C10 and C5–C6) are –0.91 and –0.83 eV, respectively. Clearly, the pyrene C–C bond types are much less reactive since the BE associated to the coordination of a Pt(PH$_3$)$_2$ unit to C2–C3 is only –0.33 eV, a value similar to that determined for the 6:5 C–C bond in C_{60}. Also, the BSSE was calculated for exohedral complexes of C_{70} and C_{84}, giving a small range of values between 0.05 and 0.11 eV. The most reactive sites according to Hückel calculations, bond lengths and pyramidalization angles of the D_2-C_{84}:**22** isomer were tested. These correspond to the three pyracylene 6:6 C–C bond types: C9–C10, C32–C53 and C7–C22. See Appendix A.7 for a

Table 6.10 Mulliken net charges for several $Pt(PH_3)_2$ exohedral metallofullerenes

Fullerene cage	*C–C bond* [a]	*Metal Number*	C_2 [b]	*Pt*	$Pt(PH_3)_2$ Mulliken [c]
C_{60}	6:5	1	–0.632	0.292	0.614
	6:6	1	–0.656	0.330	0.688
	6:6 [d]	2	–0.688	0.327	0.649
	6:6 [d]	4	–0.676	0.294	0.559
	6:6 [d]	6	–0.670	0.281	0.512
C_{70}	Ca–Cb	1	–0.676	0.326	0.698
	Cc–Cc	1	–0.646	0.336	0.689
	Ce–Ce	1	–0.662	0.243	0.561
D_{2d}-C_{84}:**23**	C42–C43	1	–0.589	0.312	0.664
	C9–C10	1	–0.604	0.330	0.659
	C5–C6	1	–0.590	0.265	0.627
	C2–C3	1	–0.730	0.257	0.576
D_2-C_{84}:**22**	C9–C10	1	–0.595	0.300	0.660
	C32–C53	1	–0.612	0.328	0.661
	C7–C22	1	–0.614	0.288	0.658

[a] C–C bond linked to the metal (see Figure 6.1 and Appendix A.4 for C_{70} and Figure 6.2, Figure 6.3, Appendix A.7 and A.8 for C_{84}). [b] Net charge for the C_2 unit coordinated to the metal. [c] Mulliken net charges for the whole $Pt(PH_3)_2$ unit. [d] Average values.

complete description of all types of C–C bonds of the D_2-C_{84}:**22** isomer. Any of them lead to a more stable isomer than the addition of the $Pt(PH_3)_2$ unit to the C42–C43 bond in the D_{2d}-C_{84}:**23** (Table 6.9). But these calculations do not prevent the formation of organometallic complexes from the D_2-C_{84}:**22** isomer. In fact, experimentally the most stable adduct from the D_2-C_{84}:**22** could be found together with the most stable adduct from the D_{2d}-C_{84}:**23** isomer. It is interesting to remark that although the free D_2-C_{84}:**22** isomer is the most stable isomer overall, the isomer present in the most stable (η^2-C_{84})$Pt(PH_3)_2$ complex isomer comes from the D_{2d}-C_{84}:**23**

isomer. The reason of this is because the C42–C43 bond of the D_{2d}-C_{84}:**23** provide a better reactive site than the lower reactive C9–C10 of the D_2-C_{84}:**22** according to pyramidalization angle and MBO. To sum up, all data concordance with the prevalent presence of the D_{2d}-C_{84}:**23** isomer as adduct and the relation 2:1 favorable to the D_2-C_{84}:**22** isomer in the mixture of free isomers.

6.5.3 Electron charge transfer

The Dewar-Chatt-Ducanson model is appropriate for describing the (η^2-C_2)-M bond. Previous calculations illustrate that the π back-donation dominates over the σ donation in these complexes and, therefore, there is an electron charge transfer from the metal unit to the fullerene cage. According to the Mulliken charges, each $Pt(PH_3)_2$ unit coordinated to the fullerene surface transfers approximately 0.6 electron, which are practically at the carbons linked to the metal unit (Table 6.10). The electron charge transfer is similar in the three fullerene cages studied with the characteristic that the complexes with the strongest fullerene-metal bond have the highest electron charge transfers. For instance, in the series of (η^2-C_{60})$\{Pt(PH_3)_2\}_n$ (n = 1, 2, 4, 6) 0.688 *e* are transferred from the $Pt(PH_3)_2$ unit to C_{60} in the monoaddition complex while 0.512 *e* are transferred per unit in the hexaaddition complex. Notice from values of Table 6.10 that the BE between the metal unit and C_{60} appears to be strongly correlated with the amount of electron charge transferred to the carbon cluster.

6.6 PREDICTION OF THE MOST REACTIVE SITES

The bonding scheme between the $M(PH_3)_2$ units and the fullerene cages is of coordinative type. It is based on the σ donation of π-electrons from the ligand to the metal atom and on the formation of a π-bond by back-donation from the metal *d*-orbitals to the π* C–C bond orbitals. All the factors that affect the strength of the coordinated C–C bond will modify the BE between both fragments. To increase the σ donation, an electron-rich C–C double bond is required, or in other words with a high π-bond order or MBO. Alternatively, the C–C bond lengths —which are completely correlated to the MBO— can also be indicative of the strength of the

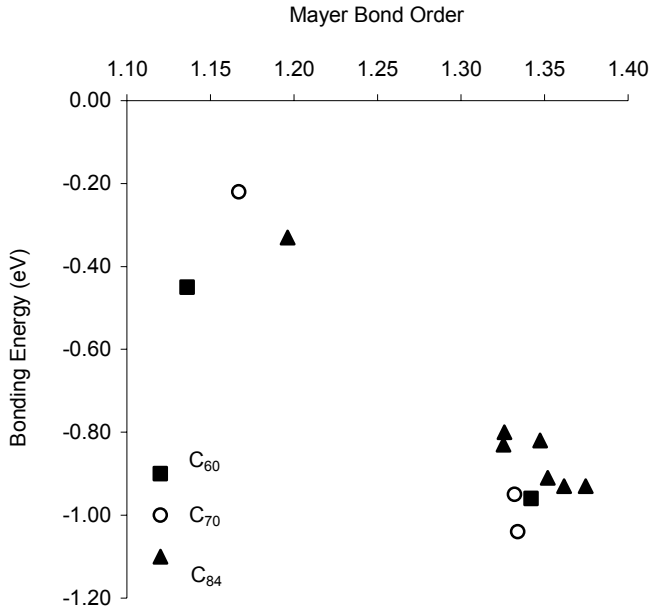

Figure 6.6 Mayer bond order (MBO) versus fullerene-metal binding energies (BE) for the C_{60}, C_{70} and C_{84} complexes

hypothetical fullerene-metal bond. Moreover, the pyramidalization angle of the free carbons can be used to estimate *a priori* this strength: the most pyramidalised carbons of the free fullerene (initial θ_p) have more sp^3 character than the less pyramidalised ones and, consequently, the interaction between them and the metal unit is more effective as some recent studies have shown.[42] This geometric parameter, then, can be used to predict the most reactive sites on the fullerene because it shows that the most pyramidalised carbons will be the most favourable sites for metal additions. In resume, the final pyramidalization angle (final θ_p) is indicative of how strong the bond is between both fragments, but the initial pyramidalization angle is also a reliable indicative parameter for this measure. Both characteristics (high pyramidalization angle and high MBO) do not always occur simultaneously because a high pyramidalization angle of the carbons is often accompanied by a long C–C bond length. Hence, the order of the BE can be estimated by taking into account only the pyramidalization angle and the MBO of the C–C bond which will react in the free fullerene. In the

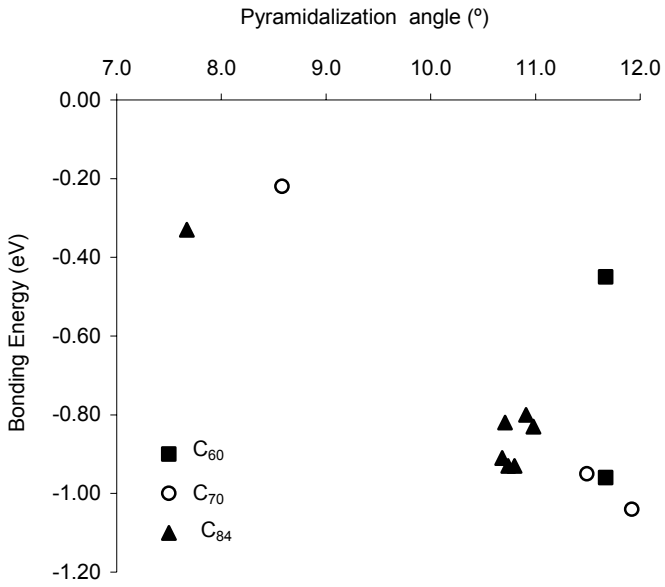

Figure 6.7 Pyramidalization angle (θ_p) versus fullerene-metal binding energies (BE) for the C_{60}, C_{70} and C_{84} complexes

most difficult cases, when both parameters are not conclusive, the final reactivity prediction will be a compromise between both parameters.

The types of all the C–C bonds, the bond lengths, the pyramidalization angles and the MBOs for all the different C–C bonds of the C_{60}, C_{70}, D_{2d}-C_{84}.**23** and D_2-C_{84}:**22** free fullerenes are given in Appendix A.2, A.4, A.8 and A.7, respectively. For a graphical representation of the different C–C bond types in the IPR fullerenes (Appendix A.1). A first inspection reveals that high MBOs and highly pyramidalised carbons are found in the pyracylene 6:6 C–C bond types (***A*** type). Hence, this C–C bond type will always tend to form the most stable complexes through metal addition reactions. On the other hand, pyrene 6:6 C–C bond types (***C*** type) show opposite features. The corannulene 6:5 C–C bond types (***D*** type) and the 6:6 C–C bonds abutted by a hexagon and a pentagon (***B*** type) have intermediate values. We correlated the BE versus the MBO in Figure 6.6, versus the pyramidalization angle in Figure 6.7 and versus the bond lengths in Figure 6.8 of the various free C–C bonds for the monoaddition complexes

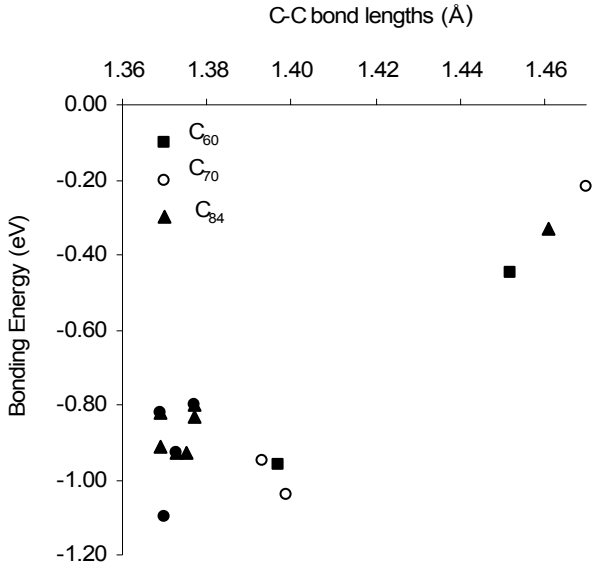

Figure 6.8 Free C–C bond distance versus fullerene-metal binding energies (BE) for the C_{60}, C_{70} and C_{84} complexes

of the C_{60}, C_{70}, D_{2d}-C_{84}:**23** and D_2-C_{84}:**22** free fullerenes. The trend is clear in Figure 6.6 and 6.7 except for the $Pt(PH_3)_2$ addition to the 6:5 C–C bond of C_{60} (square dot).

High MBOs and high initial pyramidalization angles are accompanied by more stable organometallic complexes and are a completely conclusive measure for predicting the stability of a metal unit addition to a C–C bond in a fullerene. It is important to point out that the D_{2d}-C_{84}:**23** isomer has the strongest C–C bond in the group of fullerenes above mentioned: the C42–C43 bond with an MBO of 1.375. Consequently, it seems that this isomer should be the most reactive toward addition reactions. However, it does not have the highest BE. It is found in the metal addition reaction to the Ca–Cb in C_{70}. This other C–C bond has a lower MBO, 1.334, but a much higher pyramidalization angle of 11.92° than the first one, 10.80°. Finally, we should mention that simple inspection of the bond lengths is also a good indicative parameter of the strength of the future fullerene-metal bond (Figure 6.8).

6.7 CONCLUDING REMARKS

DFT calculations were performed on the series of complexes: (η^2-C_{60}){$M(PH_3)_2$}$_n$ (M = Pt, Pd, Ni; n = 1, 2, 4, 6), (η^2-C_{70})$Pt(PH_3)_2$ and (η^2-C_{84})$Pt(PH_3)_2$ so that we could analyze how important the effect of the fullerene curvature on the BE was when mono- and polyaddition of metal units occurs. Pyracylene 6:6 C–C bonds are the most reactive sites in all the cages analyzed: C_{60}, C_{70} and C_{84}. The binding energy (BE) between the $Pt(PH_3)_2$ unit and the fullerene is almost independent of the size of the cage and of the number of coordinated metals on the fullerene surface. Contrarily, the curvature and C–C bond type determine the strength of the coordination bond. Relatively large basis sets must be used if energies are to be consistent. Finally, we investigated the correlation of the characteristics of the reactive C–C bonds of the free fullerenes with their BEs in order to obtain parameters for predicting the stability of these exohedral metallofullerenes. The main conclusions are:

Coordination bond. The $M(PH_3)_2$ metal unit is, in all cases, η^2 coordinated to a pyracylene 6:6 C–C bond type. Various possibilities of coordination on the fullerene surface have been analyzed but the η^2 coordination is always the most stable overall, indicating that the fullerene has an alkene character and not a benzenoid aromatic character. More precisely, the fullerene in these exohedral metallofullerenes acts like an electron-deficient alkene such as $C_2(CN)_4$ rather than a simple C_2H_4.

Electronic structure. The most widely accepted model for the patterns of the (η^2-C_2)-M bond is the one proposed by Dewar, Chatt and Duncanson. It involves forming a σ-donation bond from π ligand orbitals to the *d* metal orbitals and a π-back-donation bond from *d* metal orbitals to the π* C–C orbital. In these complexes, the π back-donation dominates over the σ-donation.

Monoaddition complexes of C_{60}. The metal unit is always coordinated to a 6:6 C–C bond because the coordination to a 6:5 C–C bond is very unfavorable: the BE between the fullerene and the metal unit is –0.96 eV for 6:6 coordination in contrast to –0.45 eV for 6:5 coordination.

The metal attachment lengthens the C–C bond and a pulls away the C–C edge from the fullerene surface reflected by the increment of the pyramidalization angle (θ_p). At the best level of calculation (TZP basis set for all atoms), the energy involved in the coordination of a $Pt(PH_3)_2$ unit to a C_{60} is almost the same as, or a little higher than the energy involved in the coordination of an ethylene. Also, the BE is well reproduced if the fullerene cage is described by a mixed basis set: TZP for the carbons belonging to the coordinated pyracylene and DZP for the others. The BE increases in the order Pd ≈ Pt < Ni. The basis set superposition error (BSSE) is calculated to be very small (0.05-0.10 eV) at the best level of computation, so it can be neglected. To sum up, the experimental geometries were well reproduced but in general it still appears a discrepancy between the experimental and calculated BEs for these organometallic complexes of fullerenes and ethylene.

Polyaddition complexes of C_{60}. When the number of metals attached to the fullerene cage increases, the BE decreases only slightly, which emphasizes the local nature of the fullerene-metal interaction. Also a less geometrical distortion is observed in the fragments when the polyaddition occurs: the P–M–P angle and the M–C bond lengths increase slightly. But the most important effect is the decrease in the pyramidalization angle of the coordinated C–C bond, which correlates well with the decrease in the BE per group. Recently, Melchor and coworkers showed that the curvature is a prerequisite of atomic phosphorous for bonding to polycyclic hydrocarbons and curved graphite surfaces.[43]

Monoaddition complexes of C_{70} and C_{84}. In the C_{70}, the most reactive site is that of the C–C bond with the most pyramidalised carbons in the free fullerene: the pyracylene 6:6 Ca–Cb bond. For C_{84}, two different isomers have been found experimentally (isomer **22** and **23**) but principally only the D_{2d}-C_{84}:**23** isomer formed the exohedral compound. Our calculations confirm that the most reactive site of the D_{2d}-C_{84}:**23** isomer, the pyracylene 6:6 C42–C43 bond , is a more reactive by 0.06 eV than the most reactive site of the D_2-C_{84}:**22** isomer, C9–C10 bond. It is noteworthy that the DE of the most stable monoaddition complexes of C_{70} and C_{84} is similar to that of the (η^2-C_{60})$Pt(PH_3)_2$, but the reactivity of the distinct 6:6 C–C bonds can be

quite different. Hence, for example, the addition to a pyracylene C–C bond type in C_{84} can be more favorable than to a pyrene C–C bond type by 0.67 eV, almost the same energy difference found between the most and the least reactive site in C_{70}.

Prediction parameters. We also explored the role that the pyramidalization angle of carbons plays in the nature of fullerene-metal interactions. The strain within these curved clusters and the strain release that accompanies adduct formation are important factors which will determine the strength of the fullerene-metal interaction. As was expected, the initial values of bond lengths, the pyramidalization angles and MBOs of the free C–C bonds can give us conclusive proofs on the future strength of the bond between the C–C bond and the metal unit. The correlation between these parameters and the BE for C_{60}, C_{70} and C_{84} fullerenes has been plotted to corroborate the idea.

REFERENCES AND NOTES

[1] (a) Hawkins, J. M.; Meyer, A.; Lewis, T. A.; Loren, S.; Hollander, F. J. *Science* **1991**, *252* 312. (b) Hawkins, J. M. *Acc. Chem. Res.* **1992**, *25*, 150. (c) Stephens, A. H. H.; Green, M. L. H. *Adv. Inorg. Chem*. **1997**, *44*, 1.

[2] (a) Balch, A. L.; Olmstead, M. M. *Chem. Rev.* **1998**, *98*, 2123. (b) Balch, A. L. *In the Chemistry of Fullerenes*; Taylor, R., Ed.; *Advanced Series in Fullerenes*; World Scientific Publishing Co.; Singapore, 1995; Vol. 4, p 220.

[3] Fagan, P. J.; Calabrese, J. C.; Malone, B. *Science* **1991**, *252*, 1160.

[4] (a) Lerke, S. A.; Parkinson, B. A.; Evans, D. H.; Fagan, P. J. *J. Am. Chem. Soc.* **1992**, *114*, 7807. (b) Bashilov, V. V.; Petrovskii, P. V.; Sokolov, V. I.; Lindeman, S. V.; Guzey, I. A.; Struchkov, Y. T. *Organometallics* **1993**, *12*, 991.

[5] (a) Fagan P. J.; Calabrese, J. C.; Malone, B. *J. Am. Chem. Soc.* **1991**, *113*, 9408. (b) Fagan, P. J.; Calabrese, J. C.; Malone, B. *Acc. Chem. Res.* **1992**, *25*, 134.

[6] (a) Balch, A. L.; Catalano, V. J.; Lee, J. W. *Inorg. Chem.* **1991**, *30*, 3980. (b) Vértes, A.; Gál, M.; Wagner, F. E.; Tuczek, F.; Gütlich, P. *Inorg. Chem.* **1993**, *32*, 4478.

[7] Balch, A. L.; Catalano, V. J.; Lee, J. W.; Olmstead, M. M.; Parkin, S. R. *J. Am. Chem. Soc.* **1991**, *113*, 8953.

[8] Balch, A. L.; Ginwalla, A. S.; Noll, B. C.; Olmstead, M. M. *J. Am. Chem. Soc.* **1994**, *116*, 2227.

[9] Balch, A. L. ; Lee, J. W.; Noll, B. C. ; Olmstead, M. M. *J. Am. Chem. Soc.* **1992**, *114*, 10984.
[10] Balch, A. L.; Lee, J. W.; Noll, B. C.; Olmstead, M. M. *Inorg. Chem.* **1994**, *33*, 5238.
[11] Balch, A. L.; Lee, J. W.; Olmstead, M. M. *Angew. Chem., Int. Ed. Engl.* **1992**, *31*, 1356.
[12] López, J. A.; Mealli, C. *J. Organomet. Chem.* **1994**, *478*, 161.
[13] Fowler, P. W.; Manoloupoulus, D. E. *An Atlas of Fullerens*, Oxford University Press, Oxford, **1995**.
[14] Balch, A. L.; Hao, L.; Olmstead, M. M. *Angew. Chem., Int. Ed. Engl.* **1996**, *35*, 188.
[15] (a) Zhang, B. L.; Wang, C. Z.; Ho, K. M. *J. Chem. Phys.* **1992**, *96*, 7183. (b) Wang, X. Q.; Wang, C. Z.; Zhang, B. L.; Ho, K. M. *Phys. Rev. Lett.* **1992**, *69*, 69. (c) Wang, X. Q.; Wang, C. Z.; Zhang, B. L.; Ho, K. M. *Chem. Phys. Lett.* **1993**, *207*, 349.
[16] Stone, A. J.; Wales, D. *J. Chem. Phys. Lett*. **1986**, *128*, 501.
[17] (a) Kikuchi, K.; Nakahara, N.; Wakabayashi,T.; Suzuki, S.; Shiromaru, H.; Miyake, Y.; Saito, K.; Ikemoto, I.; Kainosho, M.; Achiba, Y. *Nature* **1992**, *357*,142. (b) Manolopoulos, D. E.; Fowler, P. W.; Taylor, R.; Kroto, H. W.; Walton, D. R. M. *J. Chem. Soc., Faraday Trans.* **1992**, *88*, 3117.
[18] Koga, N; Morokuma, K. *Chem. Phys. Lett.* **1993**, *202*, 330.
[19] Bo, C.; Costas, M.; Poblet, J. M. *J. Phys. Chem*. **1995**, *99*, 5914.
[20] Nunzi, F.; Sgamellotti, A.; Re, N.; Floriani, C.; *Organometallics* **2000**, *19*, 1628.
[21] Nunzi, F.; Sgamellotti, A.; Re, N.; *J. Chem. Soc., Dalton Trans*. **2002**, 399.
[22] Dedieu, A. *Chem. Rev.* **2000**, *100*, 543.
[23] (a) Lichtenberger, D. L.; Wright, L. L.; Gruhn, N. E. Rempe, M. E. *Synth. Met.* **1993**, *59*, 353. (b) Lichtenberger, D. L.; Wright, L. L.; Gruhn, N. E. Rempe, M. E. *J. Organomet. Chem.* **1994**, *478*, 213.
[24] Jemmis, E. D.; Maniharan, M.; Sharma, P. K. *Organometallics* **2000**, *19*, 1879-1887
[25] (a) Dewar, M. J. S. *Bull. Soc. Chim. (Fr.)* **1951**, *18*, C71. (b) Chatt., J.; Duncanson, L. A. *J. Chem. Soc.* **1953**, 2939.
[26] Haddon, R. C. *Science* **1993**, *261*, 1545.
[27] (a) Haddon, R. C.; Scott, L. T. *Pure Appl. Chem.* **1986**, *58*, 137. (b) Haddon, R. C. *J. Am. Chem. Soc.* **1986**, *108*, 2837. (c) Haddon, R. C.; Chow, S. Y. *J. Am. Chem. Soc.* **1998**, *120*, 10494.
[28] (a) Yang, S. H.; Pettiette, C. L.; Concienciao, J.; Cheshnowsky, O. ; Smalley, R.E. *Chem. Phys. Lett.* **1991**, *139*, 233. (b) Lerke, S. A.; Parkinson, B. A.; Evans, D. H.; Fagan, P. J. *J. Am. Chem. Soc.* **1992**, *114*, 7807.

[29] Stephens, A. H. H.; Green, M. L. H. *Adv. Inorg. Chem.* **1997**, *44*, 1.
[30] In Chapter 5 this complex is written as $C_{58}Pt(C_2H_4)$. In Chapter 6 we use the order: ligand + metal unit, which is the order in the $(\eta^2\text{-}C_{60})Pt(PH_3)_2$ complexes. So the chemical name $C_{58}Pt(C_2H_4)$ becomes $(\eta^2\text{-}C_2H_4)C_{58}Pt$.
[31] (a) Ziegler, T.; Rauk, A. *Teor. Chim. Acta* **1977**, *46*, 1. (b) Ziegler, T.; Rauk, A. *Inorg. Chem.* **1979**, *18*, 1558.
[32] (a) Morokuma, K. *J. Chem. Phys.* **1971**, *55*, 1236. (b) Kitaura, K.; Morokuma, K. *Int. J. Quantum. Chem.* **1976**, *10*, 325.
[33] Morokuma, K.; Borden. W. T. *J. Am. Chem. Soc.* **1991**, *113*, 1912.
[34] Ziegler, T. Tschinke, V.; Baerends, E. J.; Snijiders, J. G.; Ravenek, W. *J. Phys. Chem.* **1989**, *93*, 3050.
[35] Frenking, G; Antes, I.; Böhme, M.; Dapprich, S.; Ehlers, A. W.; Jonas, V.; Neuhaus, A.; Otto, M.; Stegmann, R. Veldkamp, A.; Vyboishchikov, S. F. *In Reviews in Computational Chemistry*; Lipkowitz, K. B. Boyd, D. B. Eds.; VCH Publishers: New York, **1996**; Vol. 8, p63.
[36] (a) Mortimer, C. T. *Rev. Inorg. Chem.* **1984**, *6*,233. (b) Martinho-Simoes, J. A.; Beauchamp, J. L. *Chem. Rev.* **1990**, 629 and references therein.
[37] Rosa, A.; Ehlers, A. W.; Baerends, E. J.; Snidjers, J. G.; te Velde, G. *J. Phys. Chem*. **1996**, *100*, 5690.
[38] Nunzi, F.; Sgamellotti, A.; Re, N.; Floriani, C. *J. Chem. Soc., Dalton Trans.* **1999**, 3487.
[39] Hedberg, K.; Hedberg, L.; Bühl, M.; Bethune, D.S.; Brown, C. A.; Dorn, H. C.; Johnson. R. D. *J. Am. Chem. Soc.* **1997**, *119*, 5314.
[40] Taylor, R. *J. Chem. Soc., Perkin Trans. 2* **1993**, 813.
[41] Notice that Ir links to C32–C53 bond in reference but this C–C bond is equivalent also to C42–C43 bond according to numbering scheme proposed by Taylor for D_{2d}-C_{84}:**23** in reference 40.
[42] Park, S.; Srivastava, D.; Cho; K. *Nanotechnology* **2001**, *12*, 245.
[43] Melchor, S.; Dobado, J. A.; Larsson, J. A.; Greer, J. C. *J. Am. Chem. Soc.* **2003**, *125*, 2301.

CHAPTER 7

FINAL CONCLUSIONS

7.1 CONCLUSIONS

The characterisation of the most novel metallofullerenes up to 2004 has been theoretically and systematically discussed in various chapters of this study. Fullerenes that do not contain metals can be successfully characterized with semiempirical methods, but metallofullerenes require DFT-based methods. These methods provide an interesting framework for performing first-principle calculations of large systems more cheaply than post-HF methods. In the near future, the rapid increase in computer development and the implementation of new algorithms as well as new functionals will provide more powerful tools to scientists for studying the electronic structure of the new metallofullerenes. The way forward has already been initiated.

The vigorous start to fullerene chemistry may seem to have stopped at the end of the 1990s since several authors had already established its chemical principles. Manolopoulos et al. systematized the isomerism in the free fullerenes, and Taylor and Hirsch determined the procedure for

predicting chemical reactivity. Only the appearance of new compounds with unexpected properties and reactivity has given rise to a certain resurgence of fullerene chemistry. Two of these novel compounds are fullerenes that encapsulate a metal unit of four atoms and fullerenes that some carbons are substituted by metals. Both are metallofullerenes. From the structural point of view, metallofullerenes can be divided into three main groups, all of which have been discussed in this study: endohedral, heterohedral and exohedral metallofullerenes. The main families of compounds studied are $Sc_{3-n}M_nN@C_k$ (n = 0-3, M = Y, La; k = 68, 78, 80) (endohedral), C_xM_n (x = 56, 57, 58, 59; M = Pt, Ir, Os; n = 1, 2) (heterohedral) and (η^2-C_k){$M(PH_3)_2$}$_n$ (k = 60, 70, 84; M = Pt, Pd, Ni; n = 1, 2, 4, 6) (exohedral). The present study is a step forward in our knowledge of each of these families of compounds, and in particular, in our understanding of the metal-carbon bond, isomerism and reactivity. The DFT method proved to be an excellent computational tool for providing good geometries, for solving the intricacies of the different metal-carbon bonds, for producing experimental data (ionization potentials and electron affinities) and also for making predictions about isomerism stability and reactivity. The principal conclusions drawn about the species studied here are:

The experimental advances in each field have not been homogeneous. In consequence, the information available for each family of compounds is completely different. Whereas exohedral metallofullerenes were the first metallofullerenes to be studied in depth and their macroscopic quantities had allowed their characterisation by X-ray crystallography and other spectroscopic techniques, heterohedral metallofullerenes are still in their infancy because they have only been detected in tiny quantities by mass spectrometric studies. In the case of TNT endohedral metallofullerenes, huge advances have been made in recent years and they can now be synthesised in bulk quantities. Some of TNT endohedral metallofullerenes have been fully characterised by X-ray, IR and UV-vis techniques.

Many years studying metallofullerenes from a theoretical point of view. At first, fullerene chemistry was written about from the perspective of organic and physical chemistry and also materials science. It was not until

the middle 1990s that inorganic/organometallic chemistry began to take part. The most important characteristic of fullerenes is their ability to react as poorly conjugated and electron-deficient alkenes. Hence, fullerenes can be readily reacted with electron-rich metal species such as nucleophiles, bases, radicals or reducing agents. The perfect combination of fullerenes and metallic units has produced an endless variety of different stoichiometries for metallofullerenes. The first to be detected was the $La@C_{60}$ endohedral metallofullerene and the first to be studied was the exohedral metallofullerene $C_{60}(t\text{-}BuC_5H_5N)_2OsO_4$.

Different types of structures, different types of metal-carbon bonds. The metal units in each family of compounds are located differently in relation to the fullerene carbon framework: inside the cage, within the carbon framework and outside the cage. Each metal position is characterized by a different number of carbon neighbours and is also at different M–C bond lengths. These differences mean that the metal–carbon bond in each family of metallofullerenes has different models. The encapsulation of a trimetallic nitride template unit (TNT, $Sc_{3-n}M_nN$; n = 0-3; M = Y, La) inside the carbon cage to produce TNT endohedral metallofullerenes is explained by an ionic pair (cage-metal) model in which the TNT unit formally transfers six electrons to the cage. Classical endohedral metallofullerenes can also be explained mostly by an ionic model but when other bonding models appear when the guest is bigger or the host have not a big enough hollow (*e.g.* C_{28}). On the other hand, in heterohedral metallofullerenes, metals establish a covalent metal-carbon bond without causing oxidation to the metal. Finally, the $(MPH_3)_2$ metal units situated exohedrally to the fullerene are only coordinated in a η^2 mode to the C–C bond. However, stronger metal-carbon bonds are found in other exohedral metallofullerenes when a different metal unit is involved. For example: $\{Re(CO)_5\}_2$ and $O_2OsO_2(4\text{-}Bu^tC_5H_4N)_2$. This means that exohedral metallofullerenes can be classified as π- and σ-bonded metal-fullerene complexes. The former (studied here) are π-bonded exohedral metallofullerenes whereas the latter are σ-bonded exohedral metallofullerenes. The different strength of each metal-carbon bond can be exemplified by the magnitude and sign of the binding energies of the formation reaction of the endohedral, heterohedral and exohedral metallofullerenes: –11.60 eV for the encapsulation reaction

$Sc_3N + C_{80} \rightarrow Sc_3N@C_{80}$; 7.35 eV for the substitution reaction $Pt + C_{60} \rightarrow C_{58}Pt + C_2$; and –0.96 eV for the coordination reaction $Pt(PH_3)_2 + C_{60} \rightarrow (\eta^2\text{-}C_{60})Pt(PH_3)_2$.

Chemometric tools applied to isomerism studies. Classical methodology (which pre-determines all the isomers that are to be calculated) is used to study the isomerism in endohedral and exohedral metallofullerenes. It has been successful because the number of isomers is very limited. Nevertheless, the regioisomers of heterohedral metallofullerenes can be much more numerous: for example, the stoichiometry $C_{57}Pt_2$ has 43 distinct regioisomers. Thus, other techniques which can manage considerable amounts of data must be used if we want to understand regioisomerism in heterohedral metallofullerenes. Also, we are interested in the factors that govern the stability of isomers. As regard to this, chemometric tools have been very useful for drawing conclusions from the considerable quantities of data provided by the factors which affect the stability of regioisomers. These tools have been used not only for analysing data but also for predicting the stability of other heterofullerenes.

TNT encapsulation stabilizes fullerene isomers that are not available as free fullerenes. TNT endohedral metallofullerenes are formed by the encapsulation of a metallic nitride template inside the following cages: D_3-C_{68}:**6140**, $D_{3h'}$-C_{78}:**5**, D_{5h}-C_{80}:**6** and I_h-C_{80}:**7**. The $D_{3h'}$-C_{78}:**5** and I_h-C_{80}:**7** cages have never been detected experimentally because these cages are not the most stable IPR isomers for C_{78} and C_{80} stoichiometries. Even the C_{68} fullerene is not an IPR fullerene, which means that atom for atom it is less stable than the IPR fullerenes. So, endohedral metallofullerenes can make non-classical fullerene isomers available for study. Furthermore, on the basis of the electronic structure we predicted that no other IPR fullerenes between C_{60} and C_{84} will be capable of encapsulating a TNT unit, apart from the fullerene isomers that are already known. TNT encapsulations keep open for the non-IPR fullerenes. This is because only free fullerene isomers with a high LUMO+3-LUMO+4 gap can encapsulate and stabilize metal units that formally transfer six electrons to the cage. The only free fullerene isomers that obey this rule are the abovementioned cages.

Stability of the carbon skeleton is the principal factor that determines the regioisomer stability of the heterofullerenes. DFT calculations carried out on numerous regioisomers of $C_{57}Pt_2$ and $C_{56}Pt_2$ clearly show that the metal atoms occupy neighbouring positions in the most stable structures. Metal substitution deforms the carbon framework and partially destroys the fullerene aromaticity. This is the *key* factor in determining the stability of these disubstituted clusters. Indeed, it is much easier to make a big hole that permits the incorporation of two Pt atoms in the carbon cage than two smaller holes in two opposite sites of the fullerene. The structures with two neighbouring Pt atoms retain the most C–C bonds, which is another important factor in determining the stability of the cluster. In addition, clusters with short Pt–Pt contacts may contain weak metal-metal interactions, which also favor the stability of the cluster but are not a fundamental stability element. In our opinion, these results go beyond the particular cases of the $C_{57}Pt_2$ and $C_{56}Pt_2$ regioisomers and we believe that the present conclusions can be extended to any transition metal derivative. Calculations performed on the ionic species of the Pt-derivatives and on some Ti homologues confirm the hypothesis that disubstituted C_{60} fullerenes contain the heteroatoms in adjacent sites. The behaviour of larger fullerenes such as C_{70}, should be similar although in this case the curvature of the fullerene could also be important.

Prediction of the exohedral reactivity taking into account the full characterization of the different C–C bond types. In order to predict the exohedral reactivity of a fullerene cage such as endohedral metallofullerenes and free fullerenes, we first performed a full characterization of all C–C bond types. The fullerenes characterized were: I_h-C_{60}:**1**, D_3-C_{68}:**6140**, D_{5h}-C_{70}:**1**, $D_{3h'}$-C_{78}:**5**, I_h-C_{80}:**7**, D_2-C_{84}:**22** and D_{2d}-C_{84}:**23**. Each C–C bond type is characterized by its topology, length, pyramidalization angle and Mayer bond order. This systematization enabled us to identify which sites were most reactive to a nucleophilic addition to free fullerenes or a [4 + 2] cycloaddition to TNT endohedral metallofullerenes. They are the most pyramidalized C–C bonds that also have a high Mayer bond order. However, these features are often not found simultaneously and so the most reactive site is usually a compromise between a highly pyramidalized C–C bond with a lower pyramidalization angle, and a C–C bond with a high

Mayer bond order but a lower pyramidalization angle. The most reactive site always goes to the pyracylene 6:6 C–C bond types.

Metal doping as a tool for modifying physical properties. In general, fullerenes have relatively large electron affinities and ionization potentials, because of the presence of low-lying unoccupied and occupied orbitals, respectively. The endohedral and heterohedral functionalization can modify these physical properties because these transformations change the electronic structure of fullerenes. It is interesting to see that heterohedral and endohedral metal doping reduce the ionization potentials, making the fullerenes better electron-donor compounds. Endohedral TNT doping reduces the EA of the fullerene whereas heterohedral metal doping increases and thus improves the electron acceptor character of free fullerenes.

7.2 PERSPECTIVES

Without doubt, the main theoretical challenges in the field of metallofullerenes are provided by heterohedrals and endohedrals. To date, only simple stoichiometries have been studied: those with a single carbon atom or C_2 unit replaced by a metal atom. But other structures, which are created by the loss of C_2 units in the former, have still to be studied. There are two main experimental methods for producing heterohedral metallofullerenes: (1) Branz's method, which involves gas phase clusters: $C_{60}M_n$ and (2) Balch's method, which involves polymeric, covalently bound chains: …$C_{60}ML_n{\cdot}C_{60}ML_n$…. Depending on the production method different stoichiometries may be preferred. So Branz's method tends to produce carbon cages with an odd number of carbons whereas Balch's method produces higher yields of carbon cages with an even number of carbons. So the mechanism for forming heterohedral metallofullerenes remains unsolved. On the other hand, theoreticians are waiting for experimental evidence of metal doping in other fullerenes such as C_{70}, C_{78}, C_{80} or C_{84} which exist as free fullerenes. These fullerenes will make it possible to study the effect of substituting C–C bonds with different pyramidalization angles in the problem of the regioisomerism. Furthermore, the fact that the variability in the topology and bond strength of higher fullerenes is greater than that of the two previously studied C–C bonds of

the C_{60} will give us the final clues about the factors which govern the regioisomerism.

Apparently no more TNT endohedral metallofullerenes will be synthesized from IPR isomers between C_{60} and C_{84}. Researchers should focus on discovering new non-IPR cages which can encapsulate these TNT units. This is interesting because TNT encapsulation can make fullerene cages available that would otherwise remain unstable. To date only endohedral metallofullerenes can do this. Theoreticians should also pay greater attention to exohedral reactivity. Some progress in this area has already been made for $Sc_3N@C_{80}$. But, the exohedral reactivity of $Sc_3N@C_{68}$ and $Sc_3N@C_{78}$ complexes is almost completely unknown. Although progress in this research area is very fast, there are still many open questions concerning the electronic structure of the classical endohedral metallofullerenes such as $M_2@C_{80}$ (M = La, Ti). In the case of exohedral metallofullerenes, it seems necessary to focus on how the computational effort can be reduced before moving on to new and bigger fullerene complexes with metal units added exohedrally.

appendix

A.1 GENERAL DESCRIPTION

All different C–C bonds types in IPR fullerenes (***A***-***D*** types) and two additional types found in the non-IPR D_3-C_{68} (***E*** and ***F*** types). The bold line determines the considered C–C bond. The 6:6 ring junction in the ***A*** type is abutted by two pentagons (pyracylene C–C bond type), by a hexagon and a pentagon in the ***B*** type and by two hexagons in the ***C*** type (pyrene C–C bond type). The ***D*** type is called corannulene C–C bond type and represents a 6:5 ring junction abutted by two hexagons. The ***E*** type called pentalene C–C bond type is a 5:5 ring junction abutted by two hexagons and the ***F*** type is a 6:5 ring junction abutted by a pentagon and a hexagon. The two last types (the ***E*** and ***F*** types) are very destabilizing and only found in non-IPR fullerenes.

6:6		
Pyracylene type	--	Pyrene type
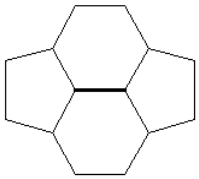	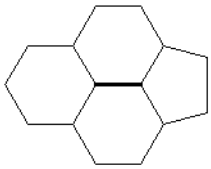	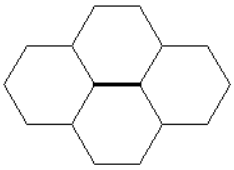
A	***B***	***C***

6:5	5:5	6:5
Corannulene type	Pentalene type	--
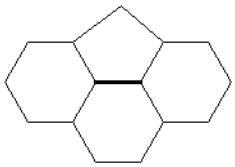	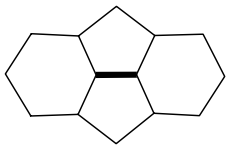	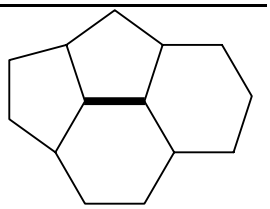
D	***E***	***F***

A.2 I_h-C_{60}:**1**

Description of the 90 C–C bonds of the I_h-C_{60}:**1** IPR fullerene divided into 2 non-equivalent sets

C–C bond [1]	*Ring junction*	*Type* [2]	*Bond lengths (Å)*	θ_p (°) [3]	*MBO* [4]
1,9/66	6:6	pyracylene, ***A***	1.397	11.67	1.342
1,2/65	6:5	corannulene, ***D***	1.452	11.67	1.136

Schlegel diagram showing the numbering system for I_h-C_{60}:**1** (a) and the structure with the C1–C9 bond marked (b)

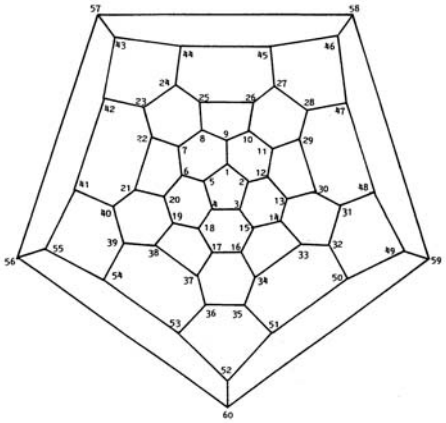

(a) Schlegel diagram of I_h-C_{60}:**1**

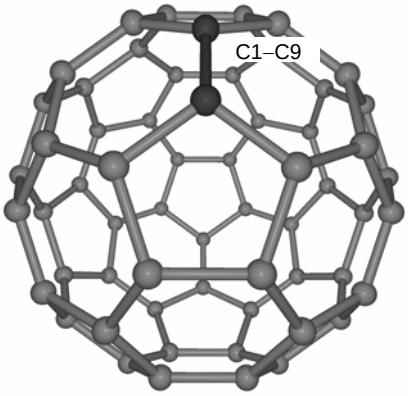

(b) Structure of I_h-C_{60}:**1**

A.3 D_3-C_{68}:**6140**

Description of 102 C–C bonds of the D_3-C_{68}:**6140** non-IPR isomer divided into 18 non-equivalent sets

C–C bond	*Ring junction*	*Type* [2]	*Bond lengths (Å)*	θ_p (º) [3]	*MBO* [4]
15,27	6:6	*pyracylene,* ***A***	1.396	11.52	1.266
23,24	6:6	***B***	1.418	9.93	1.257
14,24	6:6	***B***	1.429	9.71	1.252
12,13	6:6	***B***	1.413	9.72	1.247
11,12	6:6	***B***	1.433	10.48	1.235
21,22	6:5	***F***	1.421	13.77	1.224
1,2	6:6	***B***	1.431	9.58	1.215
2,3	6:5	corannulene, ***D***	1.433	10.90	1.210
22,23	6:5	corannulene, ***D***	1.450	11.31	1.199
13,14	6:5	corannulene, ***D***	1.443	10.54	1.194
20,21	6:5	***F***	1.424	14.49	1.185
3,15	6:5	corannulene, ***D***	1.447	11.27	1.165
2,13	6:5	corannulene, ***D***	1.449	10.14	1.159
21,42	5:5	***E***	1.436	16.20	1.156
12,22	6:6	***B***	1.446	10.27	1.151
26,27	6:5	corannulene, ***D***	1.458	11.78	1.136
14,15	6:5	corannulene, ***D***	1.438	10.80	1.133
24,25	6:6	pyrene, ***C***	1.488	8.58	1.118

Structure of the D_3-C_{68}:**6140** non-IPR isomer showing the numbering system

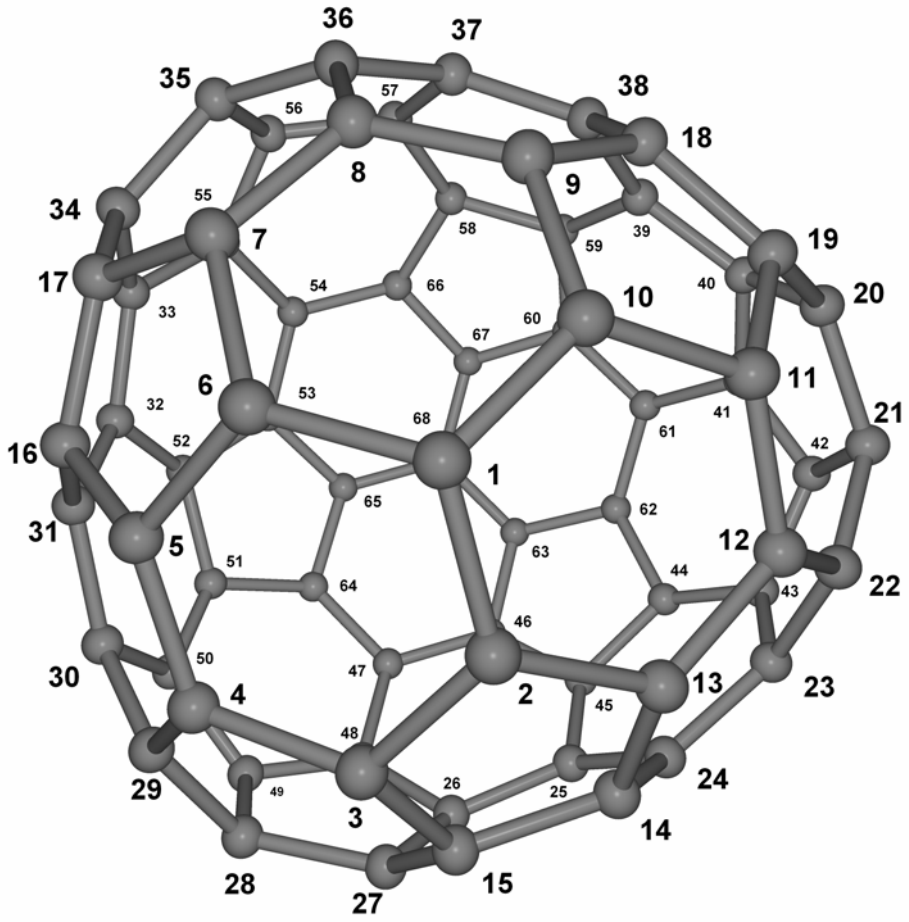

A.4 D_{5h}-C_{70}:**1**

Description of 105 C–C bonds of the D_{5h}-C_{70}:**1** IPR isomer divided into 8 non-equivalent sets

C–C bond [1]	*Ring junction*	*Type* [2]	*Bond lengths (Å)*	θ_p (º) [3]	*MBO* [4]
1,9/a,b	6:6	pyracylene, ***A***	1.399	11.92	1.334
7,8/c,c	6:6	pyracylene, ***A***	1.393	11.49	1.332
21,40/d,e	6:6	***B***	1.421	9.43	1.246
21,22/d,d	6:5	corannulene, ***D***	1.438	10.28	1.219
23,24/e,e	6:6	pyrene, ***C***	1.470	8.60	1.167
6,7/b,c	6:5	corannulene, ***D***	1.448	11.73	1.140
1,2/a,a	6:5	corannulene, ***D***	1.451	11.85	1.138
7,22/c,d	6:5	corannulene, ***D***	1.446	10.88	1.138

Schlegel diagram showing the numbering system for D_{5h}-C_{70}:**1** (a) and structure with the C1–C9/Ca–Cb bond marked (b)

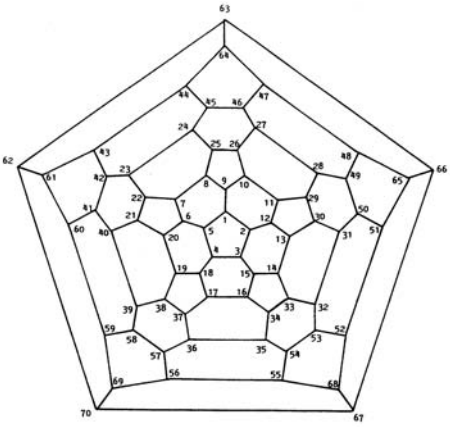

(a) Schlegel diagram of D_{5h}-C_{70}:**1**

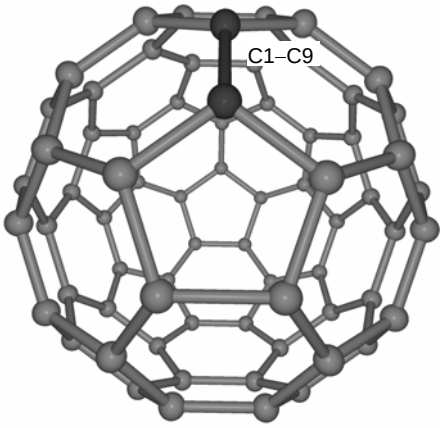

(b) Structure of D_{5h}-C_{70}:**1**

A.5 $D_{3h'}$-C_{78}:**5**

Description of the 117 C–C bonds of the $D_{3h'}$-C_{78}:**5** IPR isomer divided into 13 non-equivalent sets

C–C bond [1]	*Ring junction*	*Type* [2]	*Bond lengths (Å)*	θ_p (º) [3]	*MBO* [4]
1,2	6:6	pyracylene, ***A***	1.392	11.67	1.392
27,28	6:6	pyracylene, ***A***	1.372	10.47	1.373
22,23	6:5	corannulene, ***D***	1.414	10.49	1.293
7,21	6:6	***B***	1.419	9.63	1.283
23,24	6:6	***B***	1.423	9.56	1.221
8,24	6:6	***B***	1.424	9.48	1.214
10,26	6:6	***B***	1.436	9.65	1.205
7,8	6:5	corannulene, ***D***	1.443	10.39	1.195
10,11	6:6	pyrene, ***C***	1.470	8.63	1.163
1,6	6:5	corannulene, ***D***	1.443	11.67	1.158
1,9	6:5	corannulene, ***D***	1.446	11.15	1.129
22,42	6:5	corannulene, ***D***	1.451	10.57	1.111
23,44	6:5	corannulene, ***D***	1.470	10.31	1.090

Schlegel diagram showing the numbering system for $D_{3h'}$-C_{78}:**5** (a) and structure with the C1–C2 bond marked (b)

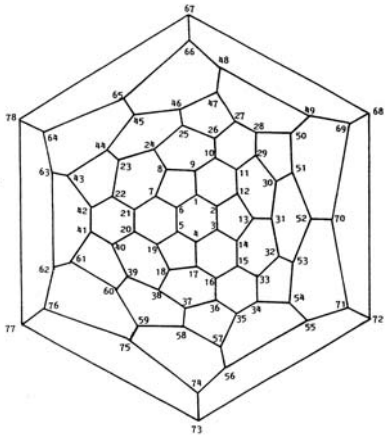

(a) Schlegel diagram of $D_{3h'}$-C_{78}:**5**

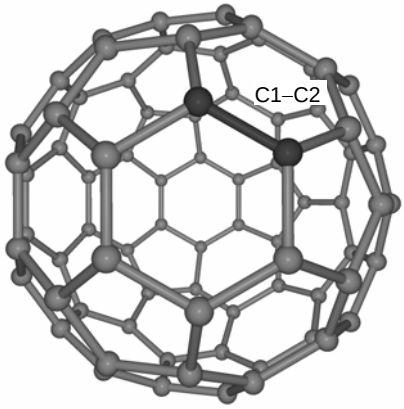

(b) Structure of $D_{3h'}$-C_{78}:**5**

A.6 I_h-C_{80}:**7**

Description of the 120 C–C bonds of the I_h-C_{80}:**7** IPR isomer divided into 2 non-equivalent sets [5]

C–C Bond [1]	*Ring junction*	*Type* [2]	*Bond lengths (Å)*	θ_p (°) [3]	*MBO* [4]
1,9/66	6:6	***B***	1.428	9.62	1.209
1,2/65	6:5	corannulene, ***D***	1.438	10.58	1.194

Schlegel diagram showing the numbering system for I_h-C_{80}:**7** (a) and structure with the C1–C9 bond marked (b)

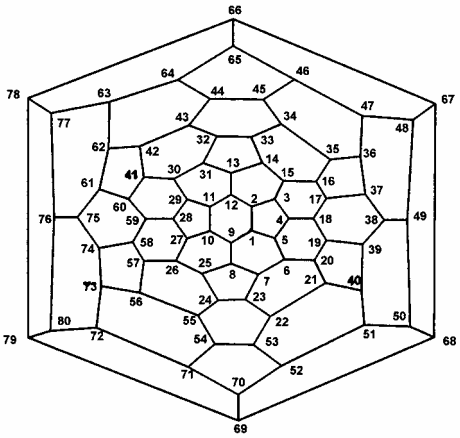

(a) Schlegel diagram of I_h-C_{80}:**7**

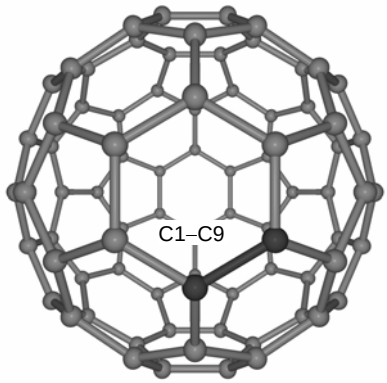

(b) Structure of I_h-C_{80}:**7**

A.7 D_2-C_{84}:**22**

Description of the 126 C–C bonds of the D_2-C_{84}:**22** IPR isomer divided into 32 non-equivalent sets

C–C bond [1]	*Ring junction*	*Type* [2]	*Bond lengths, Å*	θ_p (º) [3]	*MBO* [4]
9,10	6:6	pyracylene, ***A***	1.373	10.73	1.362
32,53	6:6	pyracylene, ***A***	1.369	10.71	1.347
7,22	6:6	pyracylene, ***A***	1.377	10.91	1.326
23,24	6:6	***B***	1.418	9.31	1.321
8,25	6:6	***B***	1.418	9.27	1.318
12,13	6:6	***B***	1.416	9.67	1.266
11,29	6:5	corannulene, ***D***	1.425	10.38	1.249
2,3	6:6	***B***	1.421	9.59	1.261
26,47	6:6	***B***	1.409	8.82	1.255
27,28	6:5	corannulene, ***D***	1.427	10.28	1.243
30,31	6:6	***B***	1.427	9.34	1.252
3,4	6:5	corannulene, ***D***	1.426	10.54	1.239
39,40	6:6	***B***	1.414	8.88	1.253
26,27	6:6	***B***	1.426	9.38	1.248
1,2	6:6	***B***	1.423	9.59	1.248
11,12	6:6	***B***	1.423	9.69	1.244
13,31	6:5	corannulene, ***D***	1.430	10.73	1.226
7,8	6:5	corannulene, ***D***	1.431	10.86	1.178
24,25	6:6	pyrene, ***C***	1.463	7.67	1.190
14,33	6:5	corannulene, ***D***	1.431	10.94	1.169
2,12	6:6	pyrene, ***C***	1.469	8.64	1.154
24,45	6:6	pyrene, ***C***	1.466	7.76	1.152
25,26	6:6	pyrene, ***C***	1.465	7.81	1.155
31,32	6:5	corannulene, ***D***	1.443	10.74	1.138

Continue					
23,42	6:5	corannulene, ***D***	1.445	10.84	1.128
10,27	6:5	corannulene, ***D***	1.439	10.80	1.130
10,11	6:5	corannulene, ***D***	1.444	10.78	1.125
8,9	6:5	corannulene, ***D***	1.449	10.76	1.121
1,9	6:5	corannulene, ***D***	1.450	10.63	1.124
13,14	6:5	corannulene, ***D***	1.452	10.80	1.122
28,29	6:5	corannulene, ***D***	1.454	9.79	1.110
3,15	6:5	corannulene, ***D***	1.453	10.73	1.111

Schlegel diagram showing the numbering system for D_2-C_{84}:**22** (a) and structure with the C9–C10 bond marked (b)

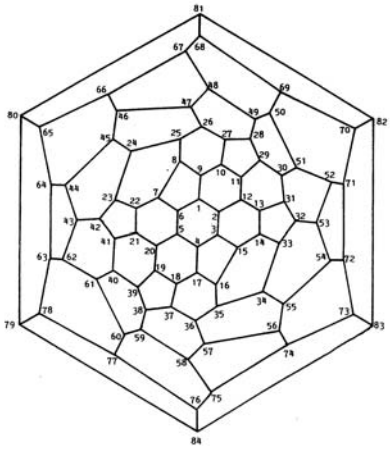

(a) Schlegel diagram of D_2-C_{84}:**22**

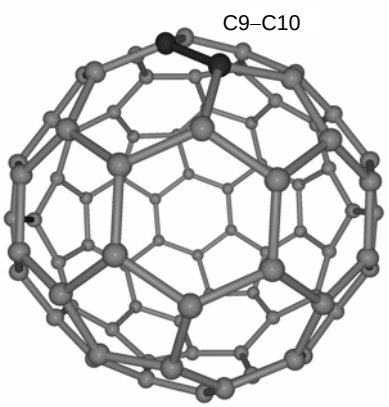

(b) Structure of D_2-C_{84}:**22**

A.8 D_{2d}-C_{84}:**23**

Description of the 126 C–C bonds of the D_{2d}-C_{84}:**23** IPR isomer divided into 19 non-equivalent sets

C–C bond [1]	*Ring junction*	*Type* [2]	*Bond lengths (Å)*	θ_p (°) [3]	*MBO*
32,53	6:6	pyracylene, ***A***	1.375	10.80	1.375
9,10	6:6	pyracylene, ***A***	1.369	10.68	1.352
5,6	6:6	pyracylene, ***A***	1.377	10.98	1.325
1,2	6:6	***B***	1.419	9.32	1.314
7,22	6:6	***B***	1.416	9.68	1.265
12,13	6:6	***B***	1.413	8.80	1.255
13,31	6:5	corannulene, ***D***	1.424	10.16	1.255
11,12	6:6	***B***	1.427	9.30	1.249
21,41	6:6	***B***	1.423	9.67	1.244
7,8	6:5	corannulene, ***D***	1.428	10.67	1.234
2,3	6:6	pyrene, ***C***	1.461	7.67	1.196
1,6	6:5	corannulene, ***D***	1.431	10.97	1.176
21,22	6:6	pyrene, ***C***	1.468	8.73	1.156
2,12	6:6	pyrene, ***C***	1.465	7.78	1.154
1,9	6:5	corannulene, ***D***	1.445	10.83	1.128
5,20	6:5	corannulene, ***D***	1.453	10.81	1.115
23,43	6:5	corannulene, ***D***	1.446	10.71	1.117
8,9	6:5	corannulene, ***D***	1.444	10.70	1.132
13,14	6:5	corannulene, ***D***	1.456	9.71	1.099

Schlegel diagram showing the numbering system for D_{2d}-C_{84}:**23** (a) and structure with the C32–C53 bond marked (b)

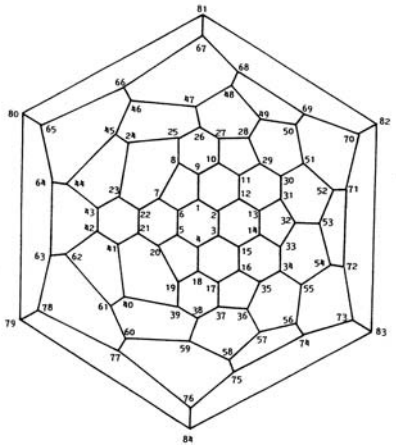

(a) Schlegel diagram of D_{2d}-C_{84}:**23**

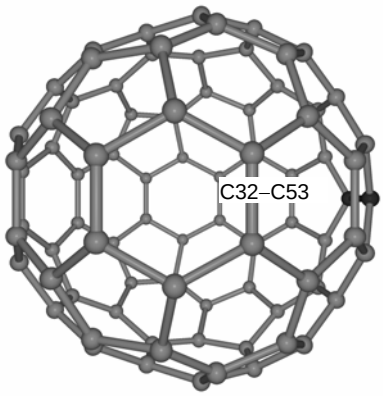

(b) Structure of D_{2d}-C_{84}:**23**

REFERENCES AND NOTES

[1] Systematic numeric system from reference Taylor, R. *J. Chem. Soc., Perkin Trans. 2* **1993**, 813.
[2] See A.1 for a schematic representation of the different motifs: pyracylene ***A***, ***B***, pyrene ***C***, corannulene ***D***, pentalene ***E*** and ***F*** types.
[3] Average pyramidalization angle of each carbon atom in the carbon bond.
[4] Mayer Bond Order (MBO).
[5] Average values from a D_{2h} symmetry used in the calculation.

index of figures

index of tables

general index

agraïments

Tot gran viatge té una tripulació que surt a navegar faci mala mar o resplendeixi el sol més paradisíac. He d'agrair els que em van guiar inicialment en aquest viatge, quan jo ja era mariner sense vaixell esperant al port: la Rosa, el Ricart, el Joan, la Mar, l'Anna i especialment els capitans que m'embarcaren a la seva flota: en Josep Maria Poblet i en Carles Bo. Sempre recordaré amb nostàlgia la constància del primer i les mirades a l'horitzó del segon. A cada mariner se li assignava un vaixell i després d'un temps inspeccionant l'estribord i el babord tots acabàvem a la sala de màquines. La meva flota estava plena de vaixells, alguns ja portaven anys navegant i d'altres començaven, com jo. Tots els vaixells havíem salpat amb les veles esteses dins una mar immensa de color blau. Mentre navegàvem no ens veiem gaire però sempre recordarem les nits sota la embriagadora lluna a coberta o al camarot, al port, o alguna illa dita Sevilla i/o Barcelona o a la ciutat. Bons mariners sense dubte: el Xavi, el Jose, el Joan Miquel, el Jorge, l'Anaval, el Paco, l'Alfred, el Gerard, el Jesuset, l'Isa, l'Esther, l'Helena, la Susanna, el David, l'Elias i la Núria. Tots érem peculiars: alguns els hi agradava més muntar veles que navegar i d'altres tenien molta experiència en la navegació. Alguns passaven més temps a terra que a mar i d'altres sempre d'illa en illa. De tots ells en tinc un granet. Els mariners Elias i Núria eren del mateix escamot que el meu, de fet, vàrem salpar plegats. Quantes tempestes i alegries junts! Sempre teníem temps per anar a esvalotar el galliner del port! Ara crec que toca el de la ciutat, oi? Què faria un vaixell sense uns bons oficials de manteniment? Pregunteu-li al capità James S. Hook! Doncs, res. Quantes vegades ens han salvat d'un naufragi segur! El Jose, el Joan i l'Elisenda! Gràcies per mantenir els vaixells en bones condicions. D'altres portaven el paperam amb la cort (Yolanda) o bé revisaven el complex estilisme marcat per l'època (John). Quan portaves moltes dies de navegació sense tornar a port podies perdre't. A vegades era bo perdre't per la mar i deixar-te endur per alguna tempesta que de ben segur a algun lloc nou et portava. En aquestes escapades vaig acabar a tres illes força interessants: *Bath*, *Exeter* i *Sussex*. En cada illa vaig aprendre coses diferents. Ara penso que tothom hauria de tenir l'oportunitat de visitar-ne alguna, d'illa. No cal ser en *Robinson Crusoe* per fer-ho! La primera illa la vaig trepitjar molt cautelosament sense saber què i qui em

trobaria. Quin mariner seria jo sense les tècniques de navegació turques de *Bath*? Ebru, Yudum i Mete, molta sort *and see you later*! A l'illa de *Bath* vaig també forjar l'amistat amb un mariner de terra endins: el Pedret. *Una Pizza, please! We need a change*! A *Exeter* vaig fer una parada curta però profitosa, necessitava una mica de coco de platja: la Rosa, l'Helena i la Rakel em van acompanyar. Quines andorranes! Finalment en l'última illa vaig conèixer els natius. Fins i tot em van allotjar. Una forta abraçada per la càlida acollida de la família de la Doreen: Hugh, Suzanne, Ethan, Owain i Lydia. *I was like a brother*! *Thank you*! Tot i les aventures dignes d'un *Indiana Jones*: Arribada d'un *keimpa* a Sussex, a la recerca de les bases perdudes de Newcastle, el congrès fantasma d'Exeter, el projecte *Hirsch-Erlangen*: si tu no vols jo vinc, ful·lerens a *Methyl Tydfil* i la *Hadrian's Wall*?, el pis cinquè, *London* la no-capital, els trens sense rumb per la hispània ulterior, per què tres catalans no es troben a la mateixa hora i el mateix lloc?, el *Sherlock Holmes* de Lewes, de *James Bond* a l'Opera de *Glyndebourne*, creuer pel mississipí baètic ... i un llarg etcètera al final sempre vaig tornar a casa. Així doncs, tot mariner té uns dies a alta mar i altes a terra ferma. A terra ferma aprofitava per copsar l'opinió que sovint la llunyania de la mar no em deixava veure. Quant he après de la Montse, la Neus de Tarragona, el Carles i la Cruset de Reus, el Pedret de Montbrió, el Benito de Valls, el Pepe de Cambrils, el Xiquelo de la Ràpita, el Saki de l'Hospi, el Toni d'Orta, la Brezo de Tarragona, la Salla dels Omells de na Gaia, el Saura de Llorenç, el Nino de Bellvei, el Norber de l'Arboç i el Jaume de Santes Creus. Alguns eren amb mi al port a l'inici del viatge. Moltes gràcies a tots! Un que sempre trobava quan tornava era el Gerard. Gràcies per sempre ser-hi! Jo era d'aquells que quan sortia del port i anava a la ciutat, sempre tenia temps per anar a esvalotar-la. Quines estones més maques amb la gent de EL MARGE i el SEP: el Mariano, la Rosa, la Sílvia, el Joan, el Jaume de la Bisbal, l'Andreu i el Joan del Vendrell, la Laura de Masarbonés i el Marc de Llorenç. Els vostres granets mouen muntanyes. A casa del mariner però es coïa tot! A casa era on sempre tenia el refugi i tothom a qualsevol hora m'esperava o em feina la cassola. Quins pares! Sempre al peu del canó, més de terra que no pas de mar! Però il·lusionats que el fill anés a mar! I el meu germà sempre tant treballador fent niuet! Els meus cosins sempre m'esperaven quan tornava a casa amb el sarró: l'Albert i la Montse. Una abraçada a la meva àvia, la padrina, que em va veure

iniciar en aquest món i la meva tieta! I sobretot una mirada de futur als cosinets més xics: el Robert, la Marta, els dos Arnaus, l'Aida, la Núria, la Laia i al Roger. Endavant! Entre tant de tràfec, l'Elena m'ha revifat l'ésser humà tant el de muntanya com el de mar, una abraçada i a volar! Però, és clar, fins i tot la mar es pot fer petita si observes atentament allò que vols! A poc a poc vas agafant el rumb i substitueixes els cops de timó per unes bones veles. Jo vaig veure un dia un far molt i molt llunyà i allí em vaig dirigir. Vaig pujar-lo i aquí sóc: ben il·luminat amb unes bones vistes cap a un munt de fars i mars més! On és el proper viatge? i la resta de mariners? Mires enrere i veus el trajecte, ha valgut la pena el camí, oi! Moltes gràcies!

Octubre de 2004
La Bisbal del Penedès / La Masó
Campa xic / *Little* Campa

viatges

Estada al Departament de Química de la Universitat de Bath (Gran Bretanya). Juliol i agost del 2000. Tutor: Dr. Andrew Burrows. Síntesi de fosfines.

Participació en la XVIIena REUNIÓ DE LA XARXA DE QUÍMICA TEÒRICA DE CATALUNYA celebrada a Tarragona el 4 i 5 de juliol del 2001.

Participació i presentació del pòster: "A DFT study of Organometallic Derivatives of Fullerenes, Jordi Muñoz, Josep M. Campanera, Jordi Vázquez, Carles Bo and Josep M. Poblet" en el FIGIPS: MEETING IN INORGANIC CHEMISTRY celebrat entre el 15 i el 20 de juliol de 2001 a Barcelona.

Estada al Departament de Química de la Universitat d'Exeter (Gran Bretanya). Agost del 2001. Tutor: Dr. Craig Butts. Reaccions fotoquímiques de ful·lerens.

Participació i presentació de la comunicació. "Enllaç en els endohedres $Sc_3N@C_x$ x = 68, 78 i 80, Josep M. Campanera, Carles Bo, Marilyn M. Olmstead, Alan L. Balch i Josep M. Poblet" en la XVIIIena REUNIÓ DE LA XARXA DE QUÍMICA TEÒRICA DE CATALUNYA que tingué lloc a Barcelona els dies 8 i 9 de juliol de 2002.

Participació i presentació del pòster: "Bonding within the endohedral fullerenes $Sc_3N@C_x$ x = 68,78 and 80, Josep M. Campanera, Carles Bo, Marilyn M. Olmstead, Alan L. Balch and Josep M. Poblet" a l'ESPA2002: ELECTRONIC STRUCTURE: PRINCIPLES AND APPLICATIONS, celebrat a Sevilla de l'11 al 13 de Setembre de 2002.

Estada al Departament de Química de la Universitat de Sussex (Brighton, Gran Bretanya). Maig-Setembre de 2003. Tutors: Roger Taylor i Malcom Heggie. Analysis of polyaddition levels in *i*-Sc_3NC_{80}.

Participació en la Nanotec'03: NANOTECHNOLOGY IN CARBON RELATED MATERIALS celebrat a la Universitat de Sussex a Brighton (Gran Bretanya) entre el 27 i el 30 d'agost de 2003.

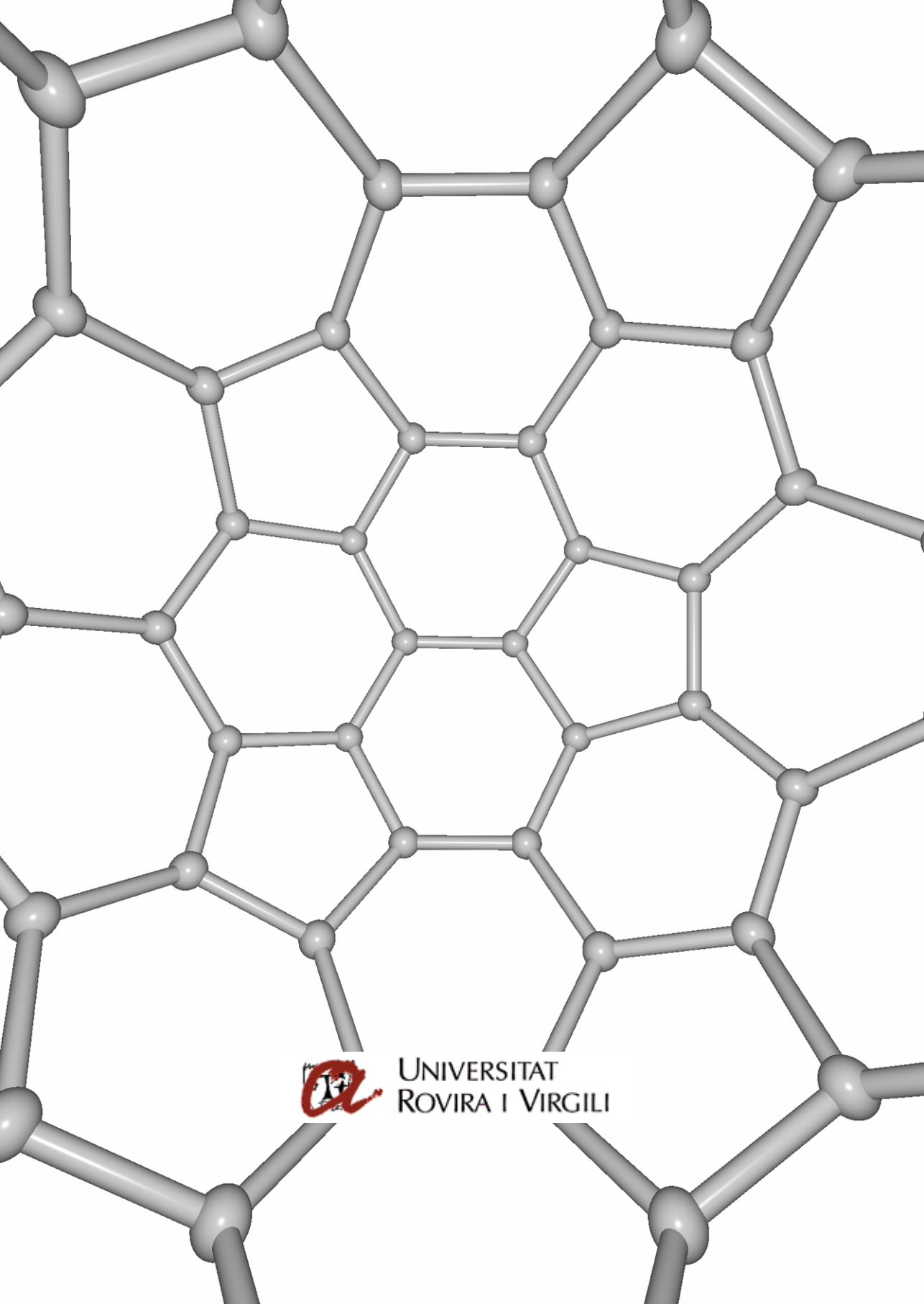

UNIVERSITAT
ROVIRA I VIRGILI